Computational and Empirical Thermal Modelling of a Proposed SOFC Stack Housing Design

THE UNIVERSITY OF
WAIKATO
Te Whare Wānanga o Waikato

A thesis submitted in partial fulfilment
of the requirements for the degree of

Doctor of Philosophy

in Materials and Process Engineering

by

Basil Fenton

March, 2004

To my family

Jewel, Ryan and Sonya.

Abstract

Solid oxide fuel cells (SOFC) generate electricity cleanly, efficiently and quietly. There has been much effort in commercialising planar and large tubular SOFCs in the past two decades. Some research has involved modelling the mass, thermal and electrical energy flows in SOFC stack designs. Due to increased thermo-mechanical strength, a mini-tubular configuration offers quicker start up than planar designs, higher power densities than large tubular designs, and the potential for easier sealing.

A stack housing design that bundled the small tubular fuel cells inside a three-way heat exchanger was proposed. Effluent fuel from the fuel cells was combusted to form an integrated burner. The air required is supplied by natural convection generated from the exhaust and hot gasses flowing up a flue (chimney). Experimental trials were done with a fabricated test rig (verification cell) to assess the stack housing design when operated with hydrogen-air. Temperature profiles data were collected to investigate the effect of varying fuel flow rate, chimney dimensions, and insulation.

Code was written for the finite element program ANSYS® to model the verification cell. This included a simple model for the flame in the verification cell. Robustness of the model was investigated by varying software settings, and comparing predicted temperature profiles with measured temperature profiles for varying fuel flow rates, chimney dimensions, and insulation.

The verification cell operated successfully on hydrogen-air but the temperature was not high or uniform enough to support a fuel cell stack. Using insulation increased temperatures and produced a more uniform temperature distribution. Increasing flue length increased temperatures marginally but increasing flue width decreased temperatures by 10%.

A simple model for the hydrogen flame was used as the heat source in the verification cell to predict temperature profiles for a given set of flow rates and operating conditions. Temperature profiles could be correlated with flow rate within 10% of actual data for the air and exhaust manifolds, but accuracy was not translated for other fuel flow rates. The benefits and drawbacks of the ANSYS® program for modelling the SOFC stack are discussed and recommendations on further research given.

Acknowledgements

I would like to thank Dr Nigel Sammes for the opportunity to conduct research in the emerging field of ceramic fuel cell technology, and for his academic support, and guidance throughout the course of this work.

A special thanks to Assoc. Prof. Keven Broughan for spending many hours attempting to enlighten me on the world of differential equations (I am recovering).

I would like to convey my sincere appreciation to Assoc. Prof. Janis Swan for spending an inordinate amount of time revising this thesis and enabling its completion.

I would like to convey my appreciation and love to my family, especially my wife Jewel, and children, Ryan and Sonya, I thank you all for your loving support and endless patience, for it has taken so long (the pain and anguish of puberty pails in comparison).

Thanks to Reinder Boersma for providing me with the concept of a system to develop a model upon, and Rhys Foster for assisting with the evolution of the modelling code.

My fellow research students and friends, Dr G. Tompsett, Dr M. Brown, Dr C. Hatchwell, Dr R. Phillips, Dr M. Phillipps, Dr M. Glanvill, M. Henderson, Dr B. Maclean, Tuti Aranui, Russel Cross, Tracy Murray, Paul Dixon, to any other person whom I have failed to mention, for their helpful advice on aspects of this work. Additional mention for R. Foster, Dr G. Tompsett, Dr. M. Brown and E. Fenton for proof reading parts of this thesis.

I would also like to praise the UOW staff whom I have worked beside for the past 5 years, Jijian Lu, Lesly Falconer, Yuangi Zhang, Alf Harris, Dave Wild, Assoc. Prof. Alan Langdon, Assoc. Prof. Janis Swan, and staff of the Department of MAPE, School of Science Computer support, the Glass blowing unit, and the Electronics and Engineering workshops.

This work has been assisted by funding from the New Zealand Foundation for Research in Science and Technology.

Table of Contents

CHAPTER THREE
Verication Cell – Design and Operation

CHAPTER FOUR
Modelling Method and Models: ANSYS® and Verification Cell Model

CHAPTER FIVE
Results and Discussion

CHAPTER SIX
Modelling Results and Discussion

CHAPTER SEVEN
Conclusions and Recommendations

APPENDICIES

List of Tables

List of Figures

Preface

The fuel cell produces power cleanly and efficiently and is becoming a practical option for power generation. Although fuel cell technology was demonstrated by Sir William Grove in 1839, it was not commercialised until the 1960s when an alkaline fuel cell (AFC) was used in the American manned space programme.

The global effort on fuel cell development has been stimulated by the same reasons for fuel cell technology as used in the space programme, - it is light, relatively safe and quiet. Other technologies such as conventional battery technology, and solar and wind generation are too bulky, and nuclear power is considered unsafe. Fuel cell developments have also been driven by socio-economic factors and environmental concerns about global warming and the need to reduce carbon dioxide emissions. Utility industries are intended in reducing emissions and improving commercial competitiveness. This can be done by increasing power generation efficiency. Modern society also wants reduce its reliance on the finite energy deposits (oil, coal) by developing renewable energy sources.

In the 1970s and 1980s, American and Japanese companies put substantial effort into developing fuel cell technologies, with European interest picking up in the 1990s. The solid oxide fuel cell (SOFC) is one fuel cell technology being developed. Thermal management is an important parameter for effective and efficient operation. This thesis investigates two approaches to thermal modelling of a novel mini-tubular SOFC stack housing design. The pertinent design features are combusting the fuel cell off-gas (unused fuel) in an integrated burner, made from concentric tubes, which also enhance heat transfer between incoming process air and fuel, by natural convection and the outgoing combustion exhaust gases. A flue (chimney) in the fuel cell stack draws process air through the system by buoyancy induced natural convection. This thesis investigates heat flow in the proposed stack-housing design and how various operating conditions affect this flow.

Chapter 1 introduces SOFC technology, describes the components and their functions, describes the principles of SOFC operation, and describes different cell

and stack designs. Development and modelling a mini-tubular fuel cell is reviewed. This chapter concludes with the scope of the work and the thesis questions.

Chapter 2 provides an overview of literature on modelling SOFC, beginning with modelling research, and the fundamental equations for the models. This chapter also includes relevant aspects of hydrogen combustion and flame phenomena.

The experimental and modelling methods used in this research are outlined in Chapter 3 and 4. Fabricating the experimental verification cell and its operation are given in Chapter 3 along with characterising the hydrogen flame. Chapter 4 overviews the modelling program ANSYS®, then gives a detailed description of the model and module codes developed. It concludes with a description of the approach that could be taken to model a fuel cell stack.

Chapter 5 presents and discusses the temperature profiles obtained in the experimental rig. In Chapter 6, data from computer modelling are set out, discussed and compared with the experimental data. Conclusions drawn in Chapters 5 and 6 are summarised in Chapter 7. Questions posed in Section 1.6.1 are answered and recommendations for future work are given.

A list of abbreviations, notes on ANSYS®, and some of the computer model codes are given in the Appendices.

CHAPTER ONE

CHAPTER ONE

Introduction:

Solid Oxide Fuel Cell Operation and Design

1.1 Fuel Cells

The primary components of the fuel cell are similar to those of the battery: it has electrode, (anode or fuel electrode and cathode or air electrode), separated by an oxygen (or hydrogen) ion-conducting (electronically insulating) electrolyte. The main difference between a fuel cell and a battery is that the fuel and the oxidising agent are replenished at the electrodes as power is produced. Thus, the fuel cell is an electrical generator whilst the battery is an electrical storage device.

Materials used in active components of the solid oxide fuel cell (SOFC) are the result of two decades of electrochemical and materials science research.[1] The electrodes are often fabricated using ceramo-metallic materials, or cermets (an intimate mixture of ceramic and metal). The conventional anode material is a porous, electronically conducting nickel cermet and the corresponding cathode is a mixed conducting perovskite, principally strontium-doped lanthanum manganite. The gas manifold and interconnect components are made from high temperature metal alloys (inconel) and/or dense ceramics (lanthanum chromite). The electrolyte is typically yttria-stabilised zirconia (YSZ), which requires high temperatures (800-1000°C) to achieve sufficiently high ionic conductivity for useful cell operation.

Five main fuel cell technologies are currently being developed: SOFC, AFC, MCFC (Molten Carbonate), PAFC (Phosphoric Acid) and PEMFC (Proton Exchange Membrane or Polymer).[2,4] These types of fuel cells have different mechanisms for conducting the charge within the electrolyte, are made from different materials and operate at different temperatures.

Many SOFC designs have been described[1-5] with the most established (tubular, planar, and monolithic) being developed commercially. The tubular design is well advanced towards commercial production but the planar design is a viable contender due, in part, to improved production techniques. Bossel[5] suggested that other designs are often included in modelling activities for comparative purposes rather than as viable designs.

The mini-tubular (or micro-tubular) SOFC was developed during the 1990s.[6,7] It is based on a single tubular cell, typically 2-4 mm in diameter. These tubes are significantly smaller than the established Siemens-Westinghouse tubular designs.[8] The smaller tube geometry can withstand rapid heating,[6] offering potential for assembling SOFC generators with faster start-up times than conventional SOFC generators. Their improved thermal shock resistance is due to the thinner ceramic wall, tubular geometry, and the fabrication method, (i.e. extruding a plastic mass).

The thermo-mechanical strength of mini-tubular fuel cells has been further extended by using a different sealing method than used for planar stacks. The mini-tubular fuel cell has been installed in small systems with the zirconia tubes extending beyond the hot zone into the cooler zone. This allows low temperature seals to be used. The longer current paths in mini-tubular fuel cells, which result in significant ohmic losses, still needs to be addressed.[9]

1.2 SOFC Components and Operation

The active component of a SOFC is often referred to as the PEN (Positive Electrode, Electrolyte, Negative electrode). When placed in a circuit, the PEN is an electrochemical cell. When the SOFC is operating, fuel and oxygen are combined within it, generating electricity, heat and exhaust gases via an electrochemical reaction. The electricity flows through an external circuit and is available for useful work (Figure 1.1).

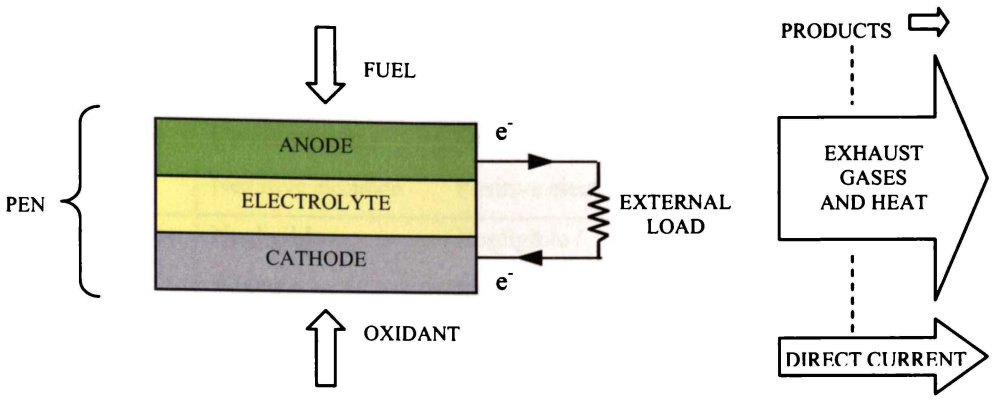

Figure 1.1 Diagram of fuel cell operation.

To achieve a desired power output, cells are connected electrically in series and/or parallel bundles. Fuel and oxidant gases are supplied through channels or manifolds. The channels may also be part of an interconnect or by-polar plate that connects the bundles of cells mechanically and electrically. This collection of components forms the stack (Figure 1.2a). A complete SOFC power generation system contains many more components: air and fuel pre-heating equipment, air movers, control and power conditioning electronics, fuel gas flow controllers, fuel processors, and possible fuel storage. These system components are called the Balance of Plant (BOP).

(a)

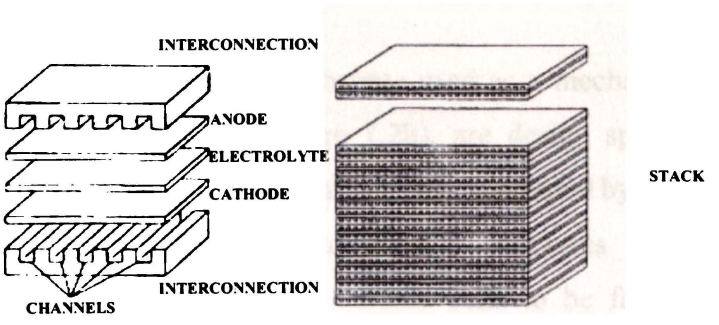

(b)

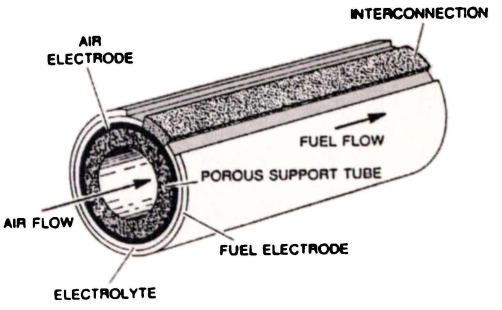

Figure 1.2 a) Planar stack with interconnect[11] and b) early Westinghouse tubular cell with interconnect and porous support tube.[12]

Table 1.1 SOFC components and material requirements

	Anode	Cathode	Electrolyte	Interconnect
Alternative name	Fuel electrode Negative electrode	Oxidant electrode Positive electrode	Separator Membrane	Bipolar Plate
Ionic-conductivity	Negligible / Mixed	Negligible / Mixed	High	None
Electronic-conductivity	High	High	Negligible	High
Porous	Yes	Yes	No	No
Chemical stability in:	Fuel and Products	Oxidant	Fuel, Oxidant and Products	Fuel, Oxidant and Products

All SOFC designs have common components with slight variations depending on SOFC geometry, function and/or the operating conditions: current collectors, gas (fuel, exhaust and oxidant) manifolds, seals and structural components. The interconnect, for example, functions as a gas manifold/channel and current collector while providing structural/load bearing support in the planar stack design (Figure 1.2a). In contrast, the interconnect in a tubular design (Figure 1.2b) has the same functions as the planar interconnect but does not function as a gas manifold.

Some components, such as the porous substrate used as a mechanical support in a early Westinghouse tubular design (Figure 1.2b), are design specific. A similar porous substrate is used in a segmented design being developed by Mitsibushi Heavy Industries (Figure 1.6a). The substrate support structures provide increased mechanical strength, which allows more durable cells to be fabricated. Further designs of SOFCs and stack configurations are reviewed in Section 1.3.

Developing the materials for fabricating SOFC components are described in the literature.[1-5]

1.2.1 Operating Principles

Yyttria stabilised zirconia (ZrO_2-Y_2O_3) has been identified as the optimal electrolyte. It is made by doping pure ZrO_2 with an aliovalent oxide to stabilise the fluorite crystal structure of ZrO_2. Substituting a trivalent cation Y^{3+} for the host lattice cation

Zr^{4+} releases several oxide-ion sites, increasing the oxygen vacancy concentration. Ionic conductivity is improved so oxygen ions can be conducted at high temperatures with a conductivity approaching that of a liquid electrolyte (0.02 at 800°C, 0.1 $S.cm^{-1}$ at 1000°C). The fluorite structure is stable from room temperature to 1000°C, making YSZ physically (morphologically) more stable than pure zirconia.

The mass transport processes occurring in a fuel cell running on hydrogen fuel and atmospheric oxygen begin with oxygen, $D(O_2)$, and hydrogen, $D(H_2)$, gases diffusing into the porous cathode and anode respectively (Figure 1.3). An electrical connection between the two electrodes provides the path for electrons to be supplied from the anode to the cathode. The oxygen molecules dissociate and ionise at the cathode-electrolyte interface. The charged oxygen ion, O^{2-}, transfers charge through the electrolyte by ionic conduction, $D(O^{2-})$, to the anode-electrolyte interface. The oxygen ion is consumed when hydrogen is oxidised to form water, which diffuses through the anode into the fuel stream, $D(H_2O)$.

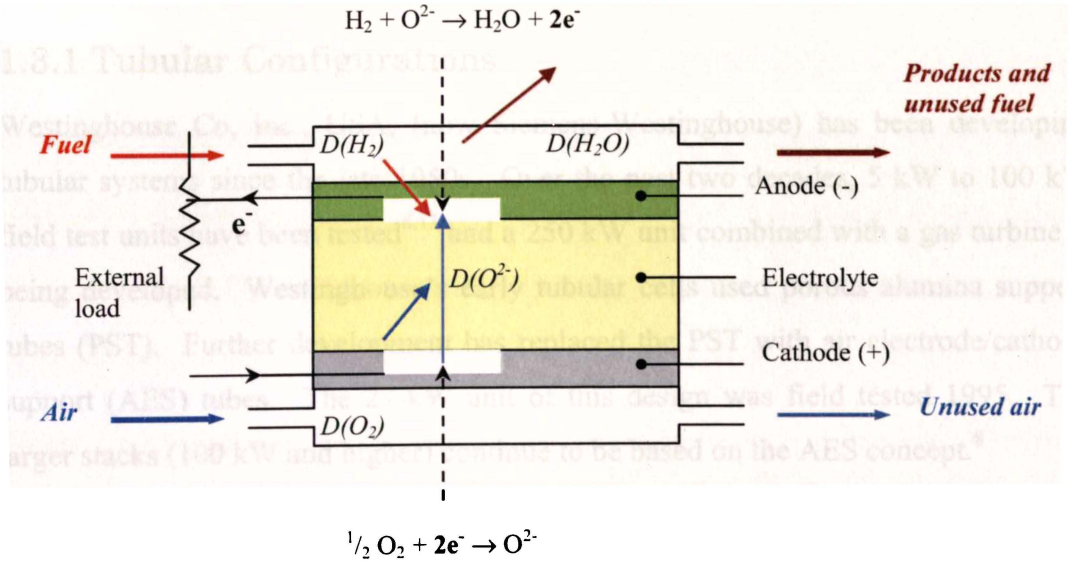

Figure 1.3 Schematic illustrating the principle of fuel cell operation, including mass transport processes.

The high operating temperatures allow fuel gases to reform within the SOFC so a wide range of fuels can be used. The reforming process reduces hydrocarbon fuels to useful hydrogen (H_2) and carbon monoxide (CO) for direct use within the fuel cell. Readily available non-precious materials such as nickel are used as catalysts to

facilitate the chemical reactions. When a hydrocarbon fuel is premixed with steam or air, the reforming reaction can occur directly on the fuel electrode. The energy that can be obtained from the electrochemical reaction depends on the concentration of reacting species and is described by Nernst's law.

1.3 SOFC Designs

The solid state components in a SOFC have been fabricated to various design strategies. The dominant designs are based on tubular, planar and monolithic cell geometries. More exotic structures have been reported. Many can be described as being segmented, with cells aligned in so-called fuel-flow series. Segmented cell stacked arrangements are commonly tubular. The differences between SOFC designs, other than shape, include the method of electrical interconnection, the sealing between fuel and oxidant gas flows, and electrical losses within the cells. This section describes the main designs currently being developed. The examples presented demonstrate different cell geometry and stack configurations.

1.3.1 Tubular Configurations

Westinghouse Co, Inc., USA, (now Siemens-Westinghouse) has been developing tubular systems since the late 1950s. Over the past two decades, 5 kW to 100 kW field test units have been tested[8,13] and a 250 kW unit combined with a gas turbine is being developed. Westinghouse's early tubular cells used porous alumina support tubes (PST). Further development has replaced the PST with air electrode/cathode support (AES) tubes. The 27-kW unit of this design was field tested 1995. The larger stacks (100 kW and higher) continue to be based on the AES concept.[8]

Recent Siemens-Westinghouse cell designs are bundled vertically and connected electrically by nickel felt interconnects (Figure 1.4a & b). The main advantage of the Siemens Westinghouse design is that it is has no seals. The tubular cells have closed ends and air is injected into the end of the cells through alumina tubes (Figure 1.4b). This eliminates the need for high temperature gas-tight seals. The fuel gas is feed external to the closed end cells and the injected air on the inside of the tubular cell is

heated by the reacting cell. During the 1990s, cell length has increased from 30 cm to 150 cm, with a diameter of 2.2 cm.

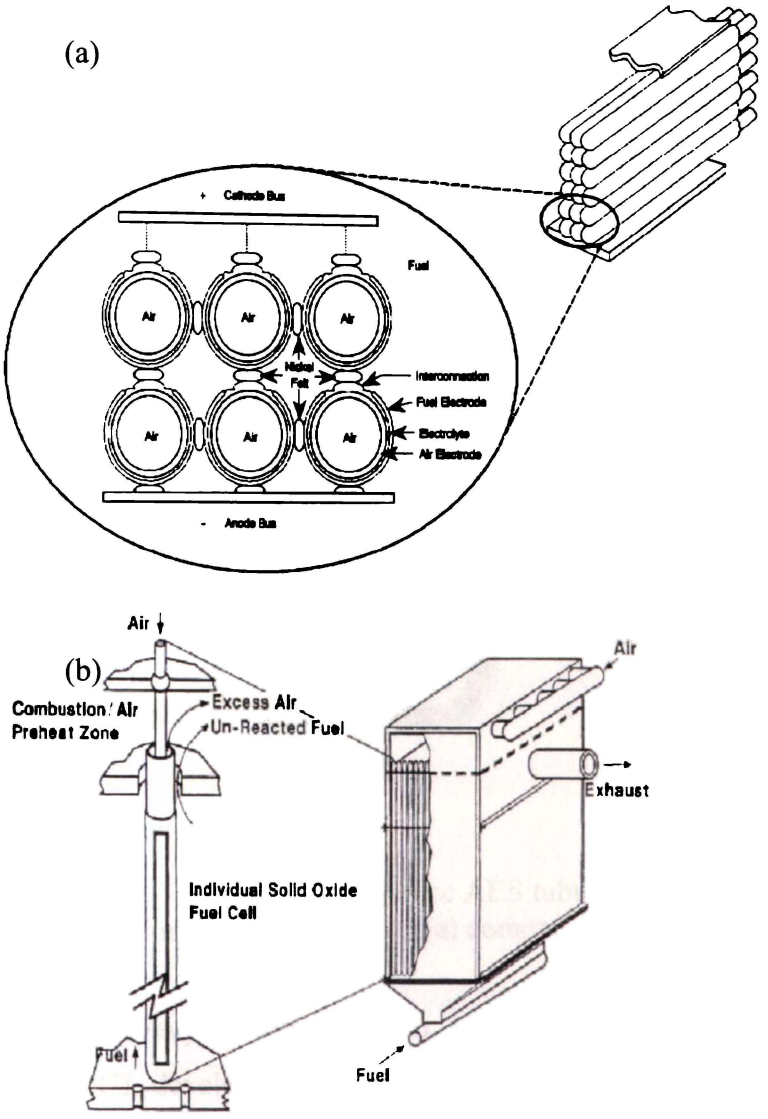

Figure 1.4 Siemens Westinghouse AES tubular design, a) method of current collection,[2] and b) gas manifold design with air injector and capped tubular cell illustrating the seal-less concept[2]

There are several disadvantages associated with the Siemens-Westinghouse design:

- The AES tube is extruded from expensive cathode material.
- The fabrication method is complex and expensive, with the electrolyte layer being applied using the electrochemical vapour deposition (EVD) process.
- Packing large tubular cells into stacks gives low volumetric power density.

- The long current paths around the circumference of cells to the interconnect increases ohmic losses.

Singhal[14] discussed progress on fabrication costs and ohmic losses due to the long current paths. Lower cost raw materials for the cathode (i.e. lower purity) are being tested and a new flat tubular design with lower cell resistance, which offers higher power density (HPD), is being investigated (Figure 1.5).

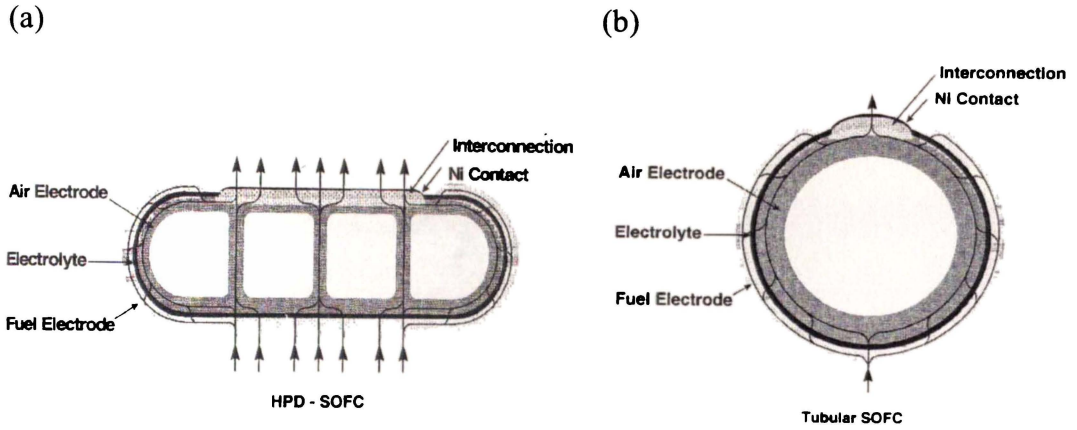

Figure 1.5 Siemens Westinghouse AES tubular design illustrating current paths in new HPD- SOFC (a) compared to traditional tubular design (b).[14]

Mitsubishi Heavy Industries (MHI), together with Electric Power Development Co. Ltd (EPDC), developed a segmented tubular-cell in the past decade.[15,16] In this design (Figure 1.6a), many short cells are fabricated onto a common porous support. The cells are connected in electrical series and produce a tube stack. The short cells provide short current paths, giving lower resistive losses than a long tubular cell.[17] Systems from 1 kW to 23 kW (Figure 1.6b) have been built and tested. As in Siemens-Westinghouse designs, these stacks operate at elevated pressures.

(a)

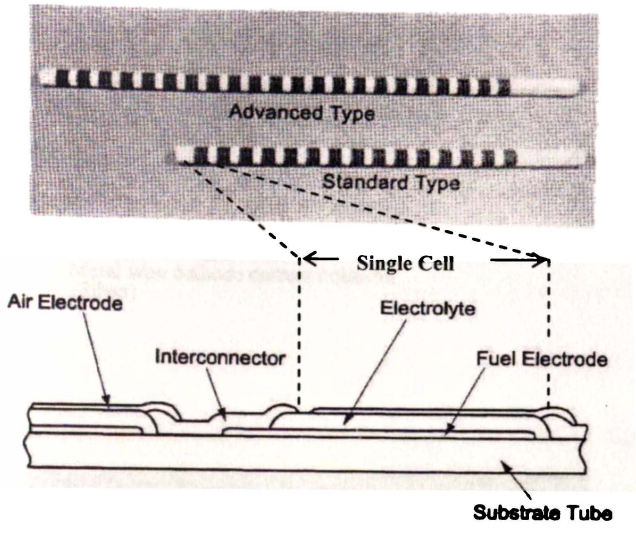

(b)

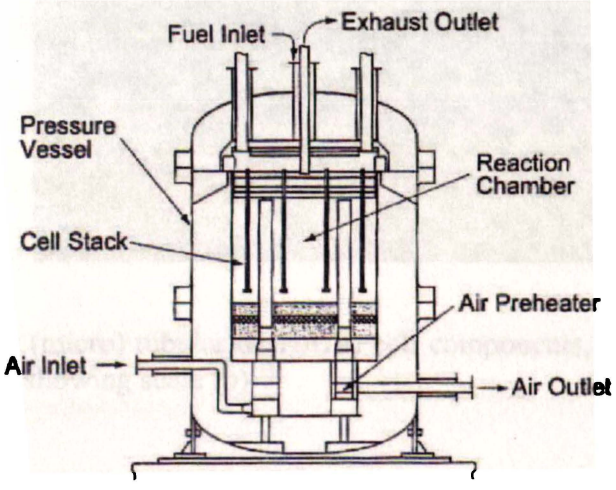

Figure 1.6 MHI segmented tubular design, a) photograph and diagram of segmented tubular cell configuration, and b) schematic of pressurised 10 kW module (stack).[16]

Mini-tubular based systems overcome some problems of the Siemens-Westinghouse designs. Cell fabrication is simple with the anode electrode layer applied on the interior of the extruded electrolyte tube and the cathode electrode applied to the exterior (Figures 1.7a and 1.7b) using conventional spray or slurry techniques. Developments in mini-tubular fuel cell technology are discussed in Section 1.4.

(a)

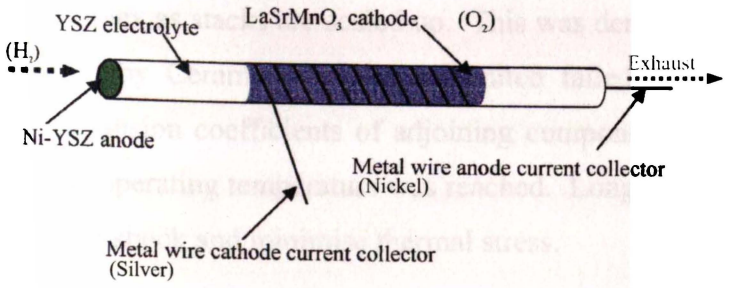

(b)

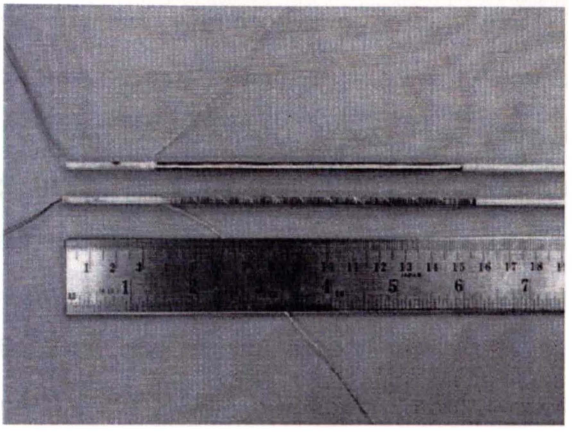

Figure 1.7 Mini (micro) tubular design, a) cell components,[18] and photograph of cells showing scale (b).[18]

1.3.2 Planar Configurations

Conventional planar designs are based on an arrangement of bipolar or flat plate components and are common in other fuel cell technologies such as MCFCs and PEMFCs. These designs offer simplicity in stacking cells, managing gas flows, and current collection. Stacking the single cells reduces the electrode-electrode and cell-cell current paths. This means that ohmic losses (polarisation) are lower and power densities are higher than in conventional tubular technologies. Being able to use traditional ceramic processing techniques such as tape casting to fabricate the electrolyte and slurry, screen, and plasma spraying for the electrodes allows the components to be mass produced.

Problems associated with planar technology include gas sealing, making components from compatible materials, and removing heat effectively. These requirements are increasingly more complex as stacks are scaled up. This was demonstrated when the 25-kW stack produced by Ceramic Fuel Cells Limited failed[20] because material mismatch (thermal expansion coefficients of adjoining components) resulted in the stack failing before the operating temperature was reached. Longer start-up times are needed to avoid thermal shock and minimise thermal stress.

In another variation of the planar SOFC, the planar cell and bipolar plates are circular plates, which allow the same fabrication technology for planar designs to be used. There is a central gas channel, which offer opportunities for managing gas flow (manifolding). The Sulzer-Hexis[21] design (Figure 1.8) uses a multifunctional metallic interconnector (current collector), which manifolds the air and fuel gas streams. Using high temperature metallic alloys means the manifold can be an effective heat exchanger, and incoming and outgoing gas temperatures can be balanced. This gives the design name, HEXIS (Heat Exchanger Integrated Stack). Another variation of the circular planar stack (Figure 1.9) is being developed by Technology Management, Inc. (TMI).[22] Other companies working on circular planar technology include Fuji Electric and Ztek. Honeywell, MHI, CFCL, Global Thermoelectric, and other companies in Japan and Europe are developing conventional planar technology.

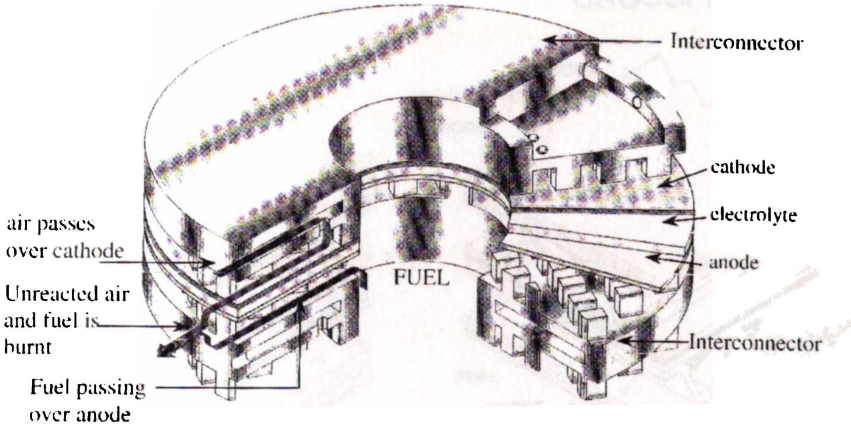

Figure 1.8 Sulzer-Hexis circular planar design, showing cell, gas, manifold and interconnect arrangement.[21]

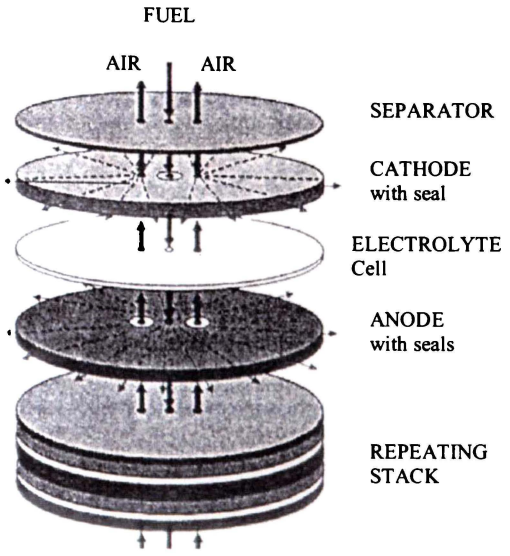

Figure 1.9 TMI circular planar design.[22]

1.3.3 Other SOFC Configurations

The monolithic design is similar to planar designs except it has a corrugated cell arrangement (Figure 1.10). These corrugations enable the PEN to function as gas distribution channels. Because the active surface area is increased, higher power densities are possible. The interconnect can also be reduced (less mass) because gas channelling is no longer required within the interconnect. This reduces ohmic losses and increases power density.

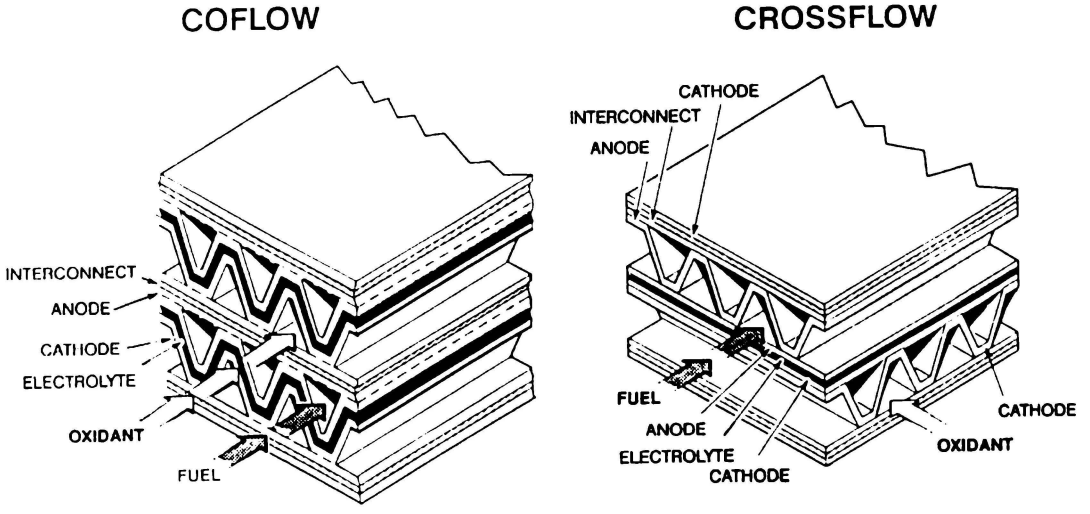

Figure 1.10 Monolithic (MSOFC) coflow configuration with corrugated PEN, and crossflow configuration with corrugated electrodes only (Allied-Signal Aerospace Company, now merged with Honeywell).[23]

The following examples, together with those already described, indicate the range of SOFC configurations investigated over the past two decades:

1. Honeycomb concept, developed by ABB.[24]
2. Mono-block layer (MOLB) SOFC concept, developed by Chubu Electric Power Company, Inc. and MHI.[25]
3. Integrated planar (IP)-SOFC, developed by Rolls-Royce.[26]

The Honeycomb concept is not being actively pursued at present, the MOLB has been under development since 1990, and the IP-SOFC is a newer concept. The common problems of sealing, thermo-mechanical compatibility, and fabrication have been associated with developing these experimental SOFC structures. In summary, the high operating temperatures continue to impose stringent requirements on fuel cell components, materials and compatibility.

1.3.4 Integrated Systems and Fuel Reforming

Efficiency and power density can be improved by integrating thermally dependent components with the fuel cell. For instance, efficiency increases if components are enclosed within the fuel cell stack housing so waste heat from operating the fuel cells can be used to preheat process gases. There is an extra saving in electrical efficiency if external compressors, pumps, etc, are not required to move mass between the fuel cell stack housing and external components to recover heat. The heat exchangers, burners and fuel reformers are commonly integrated into SOFC systems.

Waste heat recovered from electrochemical reactions within a SOFC can be used to reform a wide range of hydrocarbon fuels. The main reforming schemes are:

- **External reforming**, carried out external to the stack. Typically the heat to drive the process is supplied by an external heat source.
- **Indirect (integrated) internal reforming**, where the reformer is included within the hot envelope of the stack, allowing waste heat from the stack to be readily used by the reforming process.
- **Direct internal reforming**, where fuel is reformed within the fuel plenum and anode chamber. If reforming occurs only in the anode chamber, it is termed *in-situ* reforming.

Several chemical processes can be used to reform hydrocarbon fuels for SOFC use. Direct hydrocarbon oxidation or dry reforming (Equation 1.1) predominantly reforms fuel directly on the anode. This is the most efficient reforming process as most of the heat of reaction can be converted to electricity. It has the disadvantage of carbon deposits, which deactivate the anode by blocking active sites. If significant carbon deposits occur, carbon migration and graphite formation within the anode structure can occur, which can give mechanical degradation with the anode cracking and/or de-laminating from the electrolyte. The effect of various dopants (additives) in the anode are being investigated to reduce carbon deposition. Gadolinia-doped ceria-gold electrode is one example. [27]

$$CH_4 \Leftrightarrow C + 2H_2 \qquad (1.1)$$

Steam reforming (Equation 1.2) is the most commonly used process in the chemical process industries. Steam is added to fuel gas in specified quantities to produce hydrogen and carbon monoxide mixtures. The reaction is strongly endothermic. When coupled with a SOFC, efficiencies are improved. However, a separate source of heat is required at start up to obtain the temperature required in the reformer. Furthermore, water purity and the quantity of steam added must be carefully controlled. Because the equipment used for steam reforming increases overall size and cost of a fuel cell system BOP, steam reforming is suited to larger systems.

$$CH_4 + H_2O \Leftrightarrow CO + 3H_2 \qquad (1.2)$$

For smaller systems, catalytic partial oxidation (CPO or CPOX), using high temperature catalysts such as nickel based materials, is an effective alternative to steam reforming (Equation 1.3). Because the CPOX reaction is exothermic, it essentially is self-starting and does not require a water supply. Therefore, minimal extra equipment is required. However, CPO is not as efficient as steam reforming because some of the fuel is being oxidised.

$$CH_4 + \tfrac{1}{2} O_2 \Leftrightarrow CO + 2H_2 \qquad (1.3)$$

Other fuel processing routes include auto-thermal reforming (which uses both steam and oxygen or air), and using anode exhaust gases recycled back into the fuel stream.

Because recycling provides some of the ingredients (steam) for the reforming process, no external steam supply is required. However, high-temperature recycle fans or compressors may be needed.

Other fuels being investigated for fuel cells include gas from biomass (biogas), liquid fuels such as methanol and diesel, and coal. Each fuel has specific processing requirements. To achieve efficient reforming, a thermal equilibrium is required. Therefore the temperature, heat flux and species concentrations need to be constant.

1.4 Mini-Tubular Design and Development

In the early 1990s, the concept of a ceramic fuel cell that could withstand rapid heating and was easy to fabricate evolved. Developing mini-tubular fuel cells (Figure 1.7a and b) has advanced through studies at Keele University (United Kingdom) and the University of Waikato (New Zealand). The following section gives an overview of these studies.

1.4.1 Concept

The small tubular fuel cell was designed to satisfy several constraints. The new device could be heated to 1000°C in minutes rather than hours. The smaller diameter tubes improved cell packing, thus increasing the active cell area per volume, which increased power density. The tube could be readily sealed against gas leaks, with the potential for cold seals away from the hot zone. Finally, the tubes could be fabricated using conventional, inexpensive extrusion techniques.

The novel attributes of the smaller zirconia tubular cell were demonstrated by Kendall and Sales's [6] work in the early 1990s. Thermal shock testing, using a jet of cold gas was used to measure the thermal shock resistance and thermo-mechanical properties of planar sheets of zirconia, and 2- and 5-mm diameter zirconia tubes. Samples were made from the same batch of YSZ and were tested in a furnace at 1000°C. The mini-tubular structure withstood large thermal gradients without fracturing. The planar sheet samples cracked within the cooled region on the planar sheet because thermal shrinkage produced large tensile stresses. In ceramic

structures, any physical flaws in high stress regions are points for crack initiation and propagation, and were thought to be the mechanism that made the planar sheets fail.

1.4.2 Development

Kendall *et al.*[29-39] investigated several prototype systems made from small SOFC tubes. An integrated system was proposed for residential use.[29,30] Efficiency could be increased by using waste heat from the fuel cell to heat water, which was termed a combined heat and power (CHP) system. Data from trials of the prototype fuel cell systems showed that the cells could withstand rapid heating and moderate thermal cycling. Durability under rapid-cycling whilst running on natural gas was then tested in small concept systems of 16 tubes[29] and 9 tubes.[30] The mini-tubular cells survived realistic operating conditions from ignition, through start-up to steady state operation and shutdown. The control strategy, control system, and BOP were also addressed.[30]

In 1997, operation of a 200-tube reactor was reported.[31,32] The tubes were fabricated using a colloidal route rather than the previous viscous processing route.[6] A silicone elastomer (RTV) was used to seal the tubes into the cold manifold and the rest of the tube containing the cell was passed through thermal insulation into the hot zone. The tubes had excellent mechanical properties and reasonable electrical performance. However, performance was lower when the cells were tested in a stack. It was concluded that the 80°C temperature variation over the active region of the cells was the cause. It was suggested that a more efficient heat exchanger would improve thermal distribution and allow a 1000-tube reactor to be constructed.

Testing a 1000-tube reactor[33,34], the largest system built and tested by Kendall and co-workers, was reported in 1998. The design (Figure 1.11) consists of cells mounted vertically in a furnace type enclosure with a blower (not shown) supplying air for the cathode side of the cells. The reactor operated on natural gas/air premix. The air is consumed in the partial oxidation of natural gas preventing coking (carbon deposits) within the fuel cells. The reactor delivered 200 W_e of electricity and 20 kW of heat for heating, and survived a temperature start-up ramp rate of 200°C per minute. This stack had a specific power output of 82 mW cm^{-2} (at 850°C) compared with an average single cell specific power of 142 mW cm^{-2} (at 800°C). Irregular fuel

gas supply, non-uniform temperature distribution, and electrical resistances in the inter-cell connections were given as likely reasons for the decrease in specific power output between the single cell and 1000-cell stack.

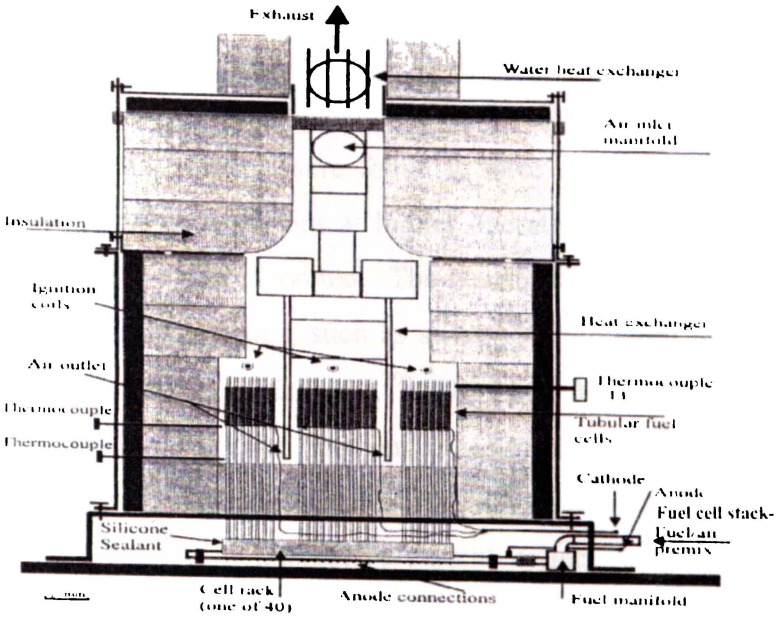

Figure 1.11 1000-tube reactor.[19]

Using micro-SOFC devices on a smaller scale have been suggested.[35,.36] They include application to microelectronics, using propane/butane as a fuel. Micro-hybrid vehicles, such as an electric golf trolley, bicycles and tricycles, are some of the theoretically proposed examples. These systems would use readily available fuels, with the potential to use alternative fuels such as biogas.[37,38]

The tubular cells are prone to electrical losses through in-plane resistance along the length of the cell. Observations reported by Kilbride[9] include a drop in specific cell resistance for increasing cell length. Larger diameter current collecting wires delivered improved performance, and thermal cycle testing with silver wire current collectors showed no degradation after 50 cycles between 200 and 900°C at 25°C min^{-1}. Testing using base metal wire (e.g., nimonic 90) current collectors showed significant degradation, due to increased contact resistance of the wires to the cathode, caused by oxidation of the alloys at higher temperatures. The Nernst potential is dependant on the fuel utilisation, decreasing with increasing cell length, as the oxygen partial pressure increases in the fuel stream. To determine if the drop in cell performance was due to an increase in the in-plane resistance or a fuel

utilisation effect, fuel utilisation was set very low (high fuel flow rate). It was shown that the magnitude of this effect when compared with in-plane resistive losses becomes significantly less with low fuel utilisation.

Hatchwell *et al.*[39] applied a $LaCoO_{3-\delta}$ coating to an nimonic 90 wire (an interconnect material), and compared the performance of this current collector to silver wire and painted silver strips. Silver strips were found to have similar performance to the silver wire, but for continuous periods at higher operating temperatures, the silver strips were concluded to have evaporated. The possibility that the silver may have been removed by other mechanisms, such as silver ion migration into the cathode, was not explored (Van Herle and McEvoy).[39b] The $LaCoO_{3-\delta}$ coating reduced losses by lowering the contact resistance between the current collecting wire and the cathode but performance was still significantly below that of the silver current collector wire. Performance of alternative current collectors was improved, if a variety of perovskites and cermet coatings consisting of Ag-$La_{0.8}Sr_{0.2}CrO_3$ (Ag-LSC) and LSC to alloy interconnects based on ducrolloy ($Cr5Fe1Y_2O_3$) where applied.[40]

1.4.3 Modelling

The ohmic losses from electrical resistance to current flow through the cell components have been quantified by Boersma *et al.*[41,42] An electrical equivalent circuit was derived and model equations were solved using the computer program MathCad™. The losses resulting from in-plane electricity conduction (Figure 1.12) in the tubular SOFCs were calculated. The calculated results were partly corroborated with experimental data and previously reported work.[9] Losses were found to be significant, with cell output improving only marginally with increasing cell length beyond 100 mm. Therefore, there is a limit on the length of cells (100 mm) or method by which they are connected (interconnect) within the stacks. Greater lengths can be obtained by stacking tube segments in series, producing a segmented tubular stack configuration.

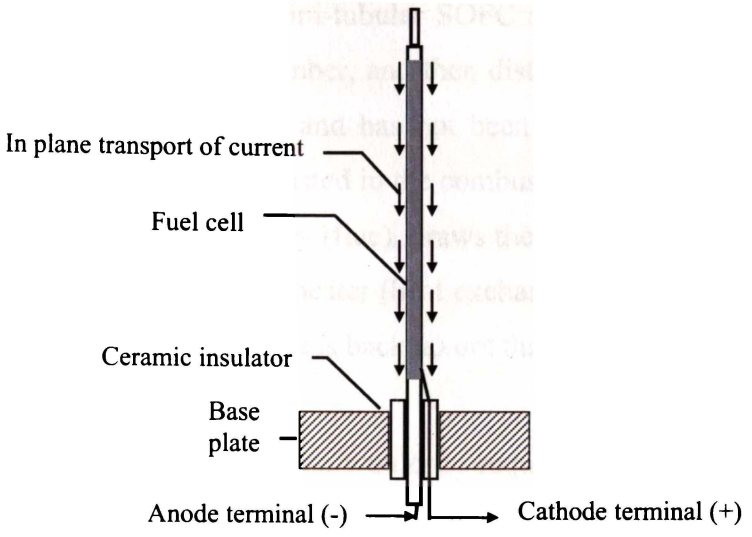

Figure 1.12 Current paths along the length of a mini-tubular SOFC.[41]

A more comprehensive approach is presented by Cooper *et al.*[43] A mathematical model is presented which takes into account the reaction and transport processes in a loaded tubular SOFC (constant current is drawn) running on methane. Results were obtained using matched asymptotic expansions to find the flow-field, the mass fractions of species, and the electrical power output. These results were confirmed by numerical methods and compared to experimental data. The model predicted the effect of the parameters investigated. Preceding studies were presented by Copcutt *et al.*[44], using matched asymptotic expansions applied to a planar SOFC configuration. Billingham *et al.*[45] further refined this model to include the planar system under load.

The mass and energy balance of a proposed integrated SOFC system (Figure 1.13) was reported by Boersma *et al.*[46] The system is similar to that proposed by Möbius[47] where cathode air supply is drawn through the system by natural convection, which is described as a "chimney effect". The system temperature is characterised as a function of the distance between the heat exchanger walls and the length of the heat exchanger paths. The impact on power output, and fuel and oxidant air, inlet temperatures are examined in a related paper.[48] The modelling suggested that up to a 2 kW system is feasible.

Fuel is fed into the integrated mini-tubular SOFC system (Figure 1.13), through a fuel tube, to a pre-reforming chamber, and then distributed into the fuel cells. Any fuel that passes through the cell and has not been electrochemically consumed is mixed with cathode air and combusted in the combustion section. The draft, induced by the heat flowing up the chimney (flue), draws the exhaust gases down the outside of the fuel cell chamber, to a pre-heater (heat exchanger) which heats incoming fuel and air, and finally exhausts the gases back up out through the chimney.

An exhaust bypass or extraction fan would be required for start up until sufficient heat is in the stack housing to induce buoyancy driven flow, enabling exhaust and cathode air to be drawn through the system. Sammes[51] has filed a patent on this mini-tubular SOFC stack design. Kendall,[49,50,52] and Kilbride [50,52] have filed earlier patents related to mini-tubular SOFC technology.

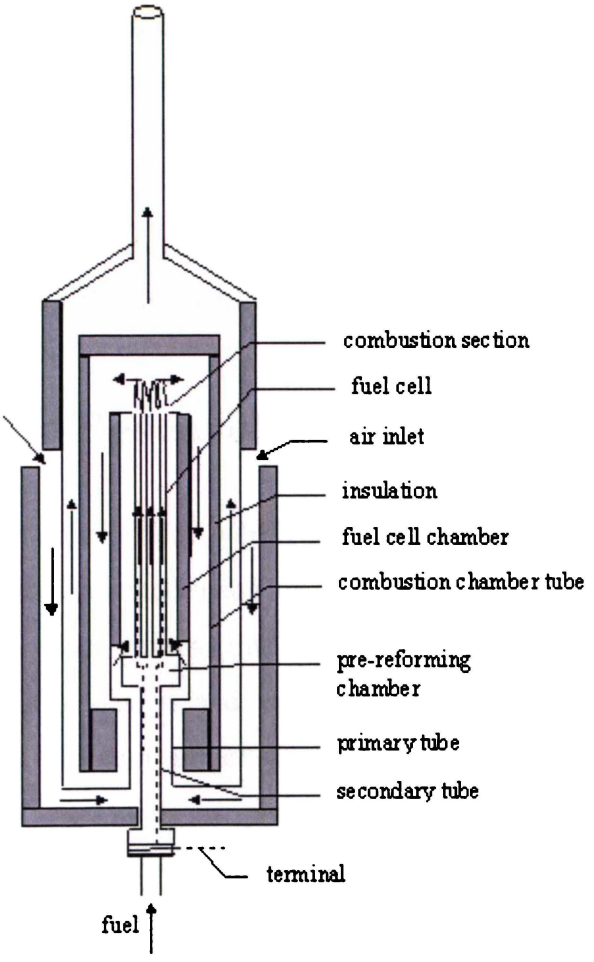

Figure 1.13 Diagram of a proposed, integrated mini-tubular SOFC.[46]

1.5 Summary

The SOFC is an efficient electrochemical converter of fuel to high quality electricity. Further efficiency gains are realised through the utilisation of the heat by-product for combined heat and power applications, including co-generation. The prospect of operating on readily available hydrocarbon fuels combined with the low pollution characteristics of fuel cell technology, gives rise to an increasingly attractive product. Study of planar and large tubular designs appear extensively in the literature, with many other designs also published. Improved performance through higher power densities, and fabrication techniques, wherein, high temperature material issues still dominate, often guide developers along their respective paths.

The mini-tubular SOFC can be fabricated using inexpensive extrusion techniques to produce tubes with increased thermo-mechanical strength. The increased strength enables shorter start up times than conventional SOFC systems, as the mini-tubular cells can withstand larger temperature gradients. Several demonstration prototypes have been built and tested. Modelling has been undertaken at the cell and stack levels. Study of electrical losses in the cell current collection is one area of interest, while a proposed 2-kW stack, which operates on a free convection principle, has been proposed and is the focus of this work.

1.6 Scope of the Research

A computer model with experimental verification and characterisation was used. The computer model is implemented using the software program ANSYS®.[10] The experimental approach involves constructing a test rig (verification cell) to simulate the proposed stack housing design and exploring how varying fuel flow rate, chimney dimensions and insulation affect temperature distribution through the rig. Modelling is restricted to determining an approximate temperature distribution of the proposed stack housing before fuel cell operation. Active SOFC components (operating fuel cells) have not been included in the results presented.

1.6.1 Research Questions

1. Can the stack housing design for a SOFC system, proposed by Boersma *et al.*[46] be implemented and, if so, what is the steady state temperature profile of a typical configuration?

2. How does the temperature profile of the system vary with changes in rig geometry?

3. Is it possible to model the system so that the predicted temperature profile agrees with the measured temperature profiles?

These research questions have been further refined as objectives in Chapters 3 and 4.

REFERENCES - Chapter One

1 J. Larminie and A. Dicks, *Fuel Cell Systems Explained*, John Wiley & Sons, Ltd., Published in England, **2000**, Chps 4-6.

2 J. H. Hirschenhofer, D. B. Stauffer, R. R. Engleman, and M. G. Klett, *Fuel Cell Handbook*, 4th edn, *Parsons Corporation, Reading, PA 19607 for U.S. Department of Energy, DOE / FETC-99 / 1076*, CDROM, November **1998**, Chps 3-6.

3 K. Kordesch and G. Simader, *Fuel Cells and Their Applications*, VCH Verlagsgesellschaft mbH, *Weinheim;VCH Publishes, Inc, New York; NY (USA)*, Published in Germany, **1996**, Chp 4.

4 N. Q. Minh, *J. Am. Ceram. Soc.* 76, No.3, **1993**, pp. 563-588.

5 U. Bossel, *Facts & Figures, The IEA programme of R, D, & D on Advanced Fuel Cells*, Annex II: Modelling and Evaluation of Advanced Solid Oxide Fuel Cells. Swiss Federal Office of Energy, Operating Agent Tack II, Berne, April **1992**.

6 K. Kendall and G. Sales, in *2nd Int. Conf. Ceramics in Energy Applications*, Inst. of Energy, London, **1994**, p. 55.

7 M. Prica, R. Copcutt and I. Kilbride, in *Proc. 2st Eur. SOFC Forum,* (ed. B. Thorstensen), Vol. 1, Oslo, Norway, **1996**, pp. 393-402.

8 R. A. George, *J. Power Sources* 86, **2000**, pp. 134-139.

9 I. P. Kilbride, *J. Power Sources* 61, **1996**, pp. 167-171.

10 ANSYS, Inc.,Southpointe, 275 Technology Drive, Canonsburg, PA 15317, USA
The Internet; [http://www.ansys.com].

11 J. Yuan, M. Okni, and B. Sunden, in *Solid Oxide Fuel Cells VI*, (eds. S. C. Singhal and M. Dokiya), Vol. PV 99-19, The Electrochemical Socity, Inc., Pennington, NJ, USA, **1999**, p. 1100.

12 N. Q. Minh, *J. Am. Ceram. Soc.* 76, No.3, **1993**, p.575.

13 S. E. Veyo, in *Fuel Cell Seminar Abstracts*, Nov. **1998**, pp. 457-460.

14 S. C. Singhal, in *Solid Oxide Fuel Cells VI*, (eds. S. C. Singhal and M. Dokiya), Vol. PV 99-19, The Electrochemical Socity, Inc., Pennington, NJ, USA, **1999**, pp. 39-51.

15 S. Kaneko, T. Gengo, S. Uchida, and Y. Yamauchi, in *Proc. 2nd Int. Sym. Solid Oxide Fuel Cells*, (eds. F. Grosz, P. Zegers, S. C. Singhal, and O. Yamamoto), Athens, Greece, **1991**, pp. 35-42.

16 H. Mori, H. Omura, N. Hisatome, K. Ikeda, and K. Tomida, in *Solid Oxide Fuel Cells VI*, (eds. S. C. Singhal and M. Dokiya), Vol. PV 99-19, The Electrochemical Socity, Inc., Pennington, NJ, USA, **1999**, pp. 52-59.

17 N. Q. Minh, *J. Am. Ceram. Soc.* 76, No.3, **1993**, p. 577.

18 C. E. Hatchwell, **1999**, "Fabrication and Properties of Thin-Walled SOFC Electrolyte Tubes", *D. Phil. Thesis, University of Waikato*, pp. 25, 91.

19 T. Alston, K. Kendall, M. Palin, M. Prica, and P. Windibank, *J. Power Sources* 71, **1998**, p. 272.

20 B. Godfrey and K. Foger, in *Solid Oxide Fuel Cells VII*, (eds. S. C. Singhal and H. Yokokawa), Vol. PV 2001-16, The Electrochemical Society, Inc., Pennington, NJ, USA, **2001**, pp. 120-124.

21 R. Diethelm, E. Batawi, and K. Honegger, in *Proc. 4th Eur. SOFC Forum,* (ed. A. J. McEvoy), Vol. 1, Lucerne, Switzerland, **1994**, pp. 183-192.

22 M. A. Petrik, C. E. Milliken, R. C. Ruhl, and B. P. Lee, in *Fuel Cell Seminar Abstracts*, Nov. **1998**, pp. 124-127.

23 N. Q. Minh, T. R. Armstrong, J. R. Esopa, J. V. Guiheen, C. R. Horne, F. S. Liu, T. L. Stillwagon, and J. J. Van Ackeren, in *Proc. 2nd Int. Sym. Solid Oxide Fuel Cells*, (eds. F. Grosz, P. Zegers, S. C. Singhal, and O. Yamamoto), Athens, Greece, **1991**, pp. 93-98.

24 M. Wetzko, A. Belzner, F. J. Rohr, and F. Harback, *J. Power Sources* 83, **1999**, pp. 148-155.

25 Y. Sakaki, A. Nakanishi, M. Hattori, H. Miyamoto, H. Aiki, and K. Takenobu, in *Solid Oxide Fuel Cells VII*, (eds. S. C. Singhal and H. Yokokawa), Vol. PV 2001-16, The Electrochemical Society, Inc., Pennington, NJ, USA, **2001**, pp. 72-77.

26 M. J. Day, in *Proc. 4th Eur. SOFC Forum,* (ed. A. J. McEvoy), Vol. 1, Lucerne, Switzerland, **1994**, pp. 133-140.

27 O. A. Marina and M. Mogensen, *App. Catalysis*, Vol. 189, **1999**, pp. 117-126.

28 Omitted.

29 K. Kendall and M. Prica, in *Proc. 1st Eur. SOFC Forum,* (ed. U. Bossel), Vol. 1, Lucerne, Switzerland, **1994**, pp. 163-170.

30 K. Kendall and T. W. J. Longstaff, in *Proc. 2nd Eur. SOFC Forum,* (ed. B. Thorstensen), Vol. 1, Oslo, Norway, **1996**, pp. 195-202.

31 M. Prica and K. Kendall, in *Proc. of The 2nd Int. Meeting of Pacific Rim Ceramic Societies*, (eds. P. Walls, C. Sorrell and A. Ruys), Vol. 2, The Australasian Ceramic Society, CDROM, **1996**, Sym. 20. pp. 382-396.

32 M. Prica, T. Alston and K. Kendall, in *Solid Oxide Fuel Cells V*, (Edss. U. Stimming, S. C. Singhal, O. Yamamoto and H. Tagawa), Vol. PV 97-40, The Electrochemical Socity, Inc., Pennington, NJ, USA, **1997**, pp. 619-625.

33 K. Kendall, M. Prica, and T. Alston, in *Proc. 3rd Eur. SOFC Forum,* (ed. P. Stevens), Nantes, France, **1998**, pp. 113-121.

34 T. Alston, K. Kendall, M. Palin, M. Prica, and P. Windibank, *J. Power Sources* 71, **1998**, pp. 271-274.

35 K. Kendall and M. Palin, *J. Power Sources* 71, **1998**, pp. 269-270.

36 G. A. Tompsett, C. Finnerty, K. Kendall, T. Alston, and N. M Sammes, *J. Power Sources* 86, **2000**, pp. 376-382.

37 J. Staniforth and K. Kendall, *J. Power Sources* 71, **1998**, pp. 275-277.

38 J. Staniforth and K. Kendall, in *Solid Oxide Fuel Cells VI*, (eds. S. C. Singhal and M. Dokiya), Vol. PV 99-19, The Electrochemical Society, Inc., Pennington, NJ, USA, **1999**, pp. 603-611.

39 C. E. Hatchwell, N. M. Sammes, and K. Kendall, Cathode current-collectors for a novel tubular SOFC design, *J. Power Sources* 70, **1998**, pp. 85-90.

39b J. Van Herle and A. J. McEvoy, J.of Physics and Chemistry of Solids, Vol. 55 (4), **1994**, pp. 339-347.

40 N. M. Sammes, R. J. Boersma, C. Hatchwell, and K. Kendall, in *Proc. 3rd Eur. SOFC Forum,* (ed. P. Stevens), Nantes, France, **1998**, pp. 495-505.

41 R. J. Boersma, N.M Sammes, and C. J. Fee, in *Proc. of the 5th Annual New Zealand Engineering and Technology Postgraduate Conference*, Published by College of Sciences, Massey University, November **1998**, pp. 233-239.

42 R. J. Boersma, N.M Sammes, and C. J. Fee, in *Proc. of the 12th International Conference on Solid State Ionics, Extended Abstracts*, Greece, Published by International society for solid-state ionics, June **1998**, p. 207.

43 R. J. Cooper, J. Billingham, and A. S. King, *J. Fluid Mech.*, **2000**, 411, pp. 233-262.

44 R. C. Copcutt, A. C. King, A. J. McDonald, and J. Billingham, in *Proc. 2st Eur. SOFC Forum,* (ed. B. Thorstensen), **1996**, pp. 237-246.

45 J. Billingham, A. C. King, R. C. Copcutt, and K. Kendall, *SIAM J. Appl. Math.* **2000**, 60, pp. 574-601.

46 N. M. Sammes and R. J. Boersma, C. Fee, in *Solid Oxide Fuel Cells VI*, (eds. S. C. Singhal and M. Dokiya), Vol. PV 99-19, The Electrochemical Socity, Inc., Pennington, NJ, USA, **1999**, pp. 1109-1124.

47 H. H. Moebius and B Rohland, US patent 3,377,203, **1968**.

48 R. J. Boersma, N. M. Sammes, and C. Fee, *J. Power Sources* 86, **2000**, pp. 369-375.

49 K. Kendall, Br. Patent Appl. No. GB94/00549, **1994**.

50 K. Kendall and I. Kilbride, Br. Patent Appl. No. 9612389.8, **1996**.

51 N.M. Sammes, Int. Patent Appl. No. PCT/NZ98/00151,**1998**

52 K. Kendall and I. Kilbride, European Patent Publication, #EP0907978, **1999**.

CHAPTER TWO

CHAPTER TWO

Solid Oxide Fuel Cell Modelling:

Description and Literature Overview

2.1 Introduction

The combination of the many different materials (with differing properties) used to construct the various SOFCs components together with their complex design (which makes it difficult to monitor or measure internal operating parameters) makes modelling attractive. Accurate models allow design and process optimisation to be done more quickly, easily and are less expensive than building prototypes.

Most work on SOFC modelling has focussed on investigating the effect of temperature distributions, chemical concentration gradients, and coupled electrical potentials. Earlier modelling activities were predominantly for steady state operating conditions but transient (unsteady state) modelling has become more popular due partly to increased computer power.

In this chapter, the fundamental equations defining the SOFC, which can be used in SOFC modelling, are developed. The techniques and methods to apply and solve models along with the recurring themes in SOFC modelling are presented. Combustion and flame phenomena are discussed. The summary compares published research with this work.

2.2 The SOFC – Governing Equations

Fuel cell models use the laws of conservation of mass and energy, describing mass and energy (thermal and electric) flow with electrochemical reactions in an operating fuel cell.

2.2.1 Levels of Modelling

Selman[1] categorised SOFC models by the design stage (Table 2.1). At one end, modelling begins with fuel cell component materials (molecular or micro modelling) and expands from electrode, to cell, to stack, to broader system models. Other activities include modelling thermal stresses[2] on components, current collection networks[3], power control strategy simulations[4] and fuel reforming processes[5].

Table 2.1 Levels of modelling (Selman[1])

Level	SOFC Component, and Purpose of Model
Molecular	Cell Materials. Help define material properties, such as ionic conductivity of electrolyte materials and diffusion of doped electrode materials.
Electrode	Electrode-Electrolyte and Electrode-Gas interfaces. Assist in predicting electro-chemical characteristics at the gas-electrode and electrode-electrolyte interfaces, and hence predict diffusion and electron-transfer reactions (electrode polarisation's).
Cell	Cell (PEN) or Repeat Unit cell (which may consist of the cell and the interconnect, for example). Used to describe performance of single cells or unit cell/modules in terms of voltage and current (V-I curve, or polarisation curve). Often measured as a function of temperature and/or gas composition.
Stack	Connected Cells, or Modules (may include gas and electrical interconnection). Performance of cells due to location within the stack or module configuration, typically expressed in terms of power output and thermal losses and often requires a three dimensional (3D) approach. Output measured as a function of temperature and/or gas composition.
System	Stack and BOP (fuel pre-treatment, air and fuel pre-heaters, power electronics). Predicts overall system efficiency in terms of heat, mass and momentum. A stack model will be included as one element (or input). Used to increase overall system efficiencies and to estimate capital and operating costs.

The modelling approach used in this thesis is at the stack modelling level. The information obtained can be used to investigate thermal efficiencies of proposed stack housings.

2.2.2 Electrode Reactions

Fuel cells are commonly run on hydrogen and methane (main constituent of natural gas). The electrochemical reactions occurring at the electrodes can be represented by

half reactions. Oxygen is reduced at the cathode, forming an oxygen ion and releasing a pair of electrons into the current collector. Hydrogen and/or carbon monoxide is oxidised at the anode to form water and/or carbon dioxide.

Cathode	$\frac{1}{2} O_2 + 2e^-$	$\rightarrow$	O^{2-}	(2.1)
and Anode	O^{2-}	$\rightarrow$	$\frac{1}{2} O_2 + 2e^-$	(2.2)
	$\frac{1}{2} O_2 + H_2$	$\rightarrow$	H_2O	(2.3)
	$\frac{1}{2} O_2 + CO$	$\rightarrow$	CO_2	(2.4)

Hydrogen and carbon monoxide from a hydrocarbon fuel (e.g. methane) undergoes one or more of the following reforming reactions:

$CO + H_2O$	$\Leftrightarrow$	$CO_2 + H_2$		(2.5)
$CH_4 + H_2O$	$\Leftrightarrow$	$CO + 3H_2$		(2.6)
$2CO$	$\Leftrightarrow$	$C + CO_2$		(2.7)
$CH_4 + \frac{1}{2} O_2$	$\Leftrightarrow$	$CO + 2H_2$		(2.8)
CH_4	$\Leftrightarrow$	$C + 2H_2$		(2.9)

Equations 2.5–2.8 are the shift, steam reforming, Boudouard, and CPOX (catalytic partial oxidation) reactions respectively and Equation 2.9 is direct oxidation of methane.

2.2.3 Gibbs and Nernst Equations

The power P_c, for a fuel cell is the product of the cell voltage V and current I,

$$P = V I \tag{2.10}$$

The electronic potential or electromotive force (EMF) is directly related to the Gibbs free energy change, ΔG, for a given chemical reaction. Complete oxidation of hydrogen and methane gives the following Gibbs free energy change at standard conditions:[6]

$$H_2 + \frac{1}{2} O_2 \rightarrow H_2O_{(l)}, \quad -\Delta G = 237.3 \text{ kJ mol}^{-1} \tag{2.11}$$

$$CH_4 + 2O_2 \rightarrow CO_2 + 2H_2O_{(l)}, \quad -\Delta G = 818.4\ kJ\ mol^{-1} \tag{2.12}$$

Under standard conditions*, $\Delta G°$, is called standard free-energy change. The ΔG, which indicates the maximum net work from a reaction, can be calculated for any reaction mixture. A negative ΔG indicates a reaction will proceed.

Gibbs free energy, enthalpy, H, and entropy, S, of a chemical reaction are related:

$$\Delta G° = \Delta H° - T.\Delta S \tag{2.13}$$

The electric potential or Gibbs voltage, E, of a cell is related to ΔG:

$$E = -\frac{\Delta G}{n_e F} \tag{2.14}$$

where: $E = (V_{rev,c} - V_{rev,a})$, $V_{rev,c}$, and $V_{rev,a}$ are the reversible electrode potentials for the cathode and anode, n_e is the number of electrons per atom involved in the reaction and F is Faraday's constant (96,487 Coulombs per gram mole/electron) linking electrical and chemical units.

During fuel cell operation, the Gibbs voltage for the cell, E, is modified for non-standard conditions such as oxygen partial pressure and fuel type and properties. This is the Nernst potential, E_N, (Equation 2.15) and represents the electrodes at equilibrium, which is the theoretical open circuit voltage. The Nernst potential assumes the quotient of current carried by the oxygen ion through the electrolyte and the total current is unity ($t_i \approx 1$, where t_i is the ionic transport or transference number).

$$E_N = E^o - \frac{RT}{2F} \ln\left(\frac{P_{H_2O}}{P_{H_2}\left(P_{O_2}\right)^{0.5}}\right) \tag{2.15}$$

* 298.15 K, 101 kPa

2.2.4 Electric Potential Balance and Losses

When the fuel cell is under load, losses in the form of heat occur. These losses are attributed to ohmic resistances (IR) occurring wherever current flows throughout the solid structure, and to electrode over-potentials ($\eta_{anode} + \eta_{cathode}$). These losses or over-potentials at the electrodes are also seen as polarisations, irreversibilities, or more generally, voltage drops. The over-voltage is the sum of over-potentials of the two electrodes of the cell and the ohmic losses, and is the difference between the cell voltage and open-circuit voltage (OCV) while current is flowing. The actual voltage or potential balance E, observed for a cell under load is given by:

$$E = E_N - IR - (\eta_{anode} + \eta_{cathode}) \tag{2.16}$$

The over-potentials for each electrode are further defined:

$$\eta = \eta_{kin} + \eta_{dif} + \eta_{reac} \tag{2.17}$$

where: η_{kin} is the kinetic over-potential (activation polarisation)

η_{dif} is the diffusion over-potential (concentration polarisation)

η_{reac} is the reaction over-potential (concentration polarisation).

The voltage-current relationship for a cell under load is used to characterise cell performance (Figure 2.1). At low current, the kinetic over-potential is the voltage expended during a chemical reaction to transfer electrons to and from the electrode and decreases with increasing temperature. The voltage losses for most of the voltage-current curve is attributed to IR losses. At high currents, the diffusion over-potential is added to the activation and IR losses, and is the decrease in voltage resulting from a limited supply of reactants, or conversely removal of products, from the electrodes. The reaction over-potential and diffusion over-potential are related. Thus, an increasing product-reactant ratio at the surface of the anode further increases the drop in potential difference of the cell.

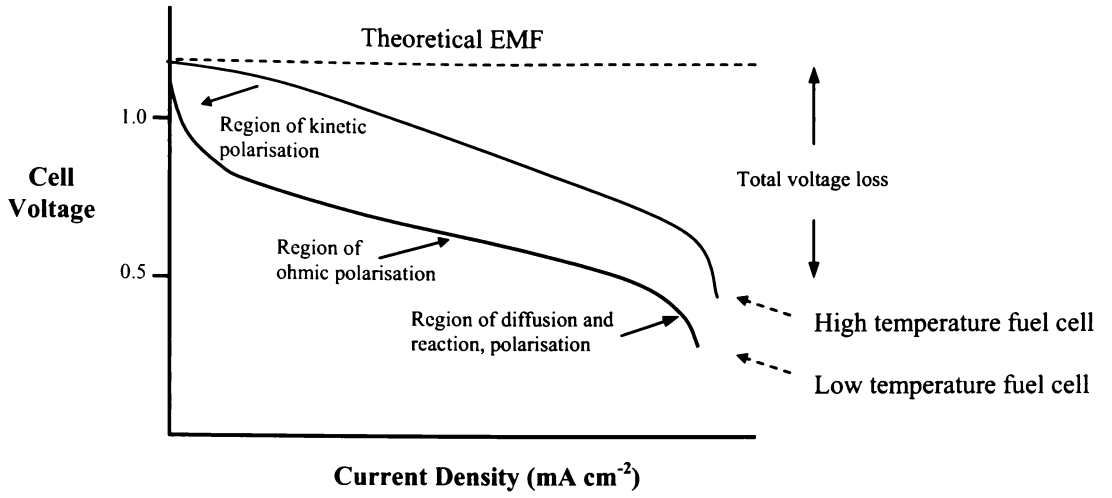

Figure 2.1 Theoretical and actual voltage-current curve characteristics for low- and high-temperature fuel cells.

2.2.5 Mass and Energy Balance

Fick's law describes molecular diffusion, which depends on concentration gradients:

$$N_i = -cD_{i-j}\nabla x_i + x_i(N_i + N_j) \tag{2.18}$$

where: D_{i-j}, is the diffusion coefficient of a species i in a binary mixture of species j; c is the molar density in a binary mixture; x_i is the mole fraction of species i in species j; and N_j is the molar flux of species j. For an air electrode in air, i = O_2, j = N_2 and $x_i = 0.21$. Current density, j, is also related to the molar flux of each species in a cell and described by Faraday's law:

$$j = n_e F N_i \tag{2.19}$$

The flux of each species depends on stoichiometry. The following relationship occurs for the reaction between hydrogen and oxygen (Equation 2.11):

$$2N_{O_2} = N_{O_{2^-}} = N_{H_2O} = N_{H_2} \tag{2.20}$$

Equation 2.19 indicates the minimum fuel required for a SOFC stack under load. For real operating conditions, the cell is run at higher fuel flow rates (fuel efficiency of 50-80%) to ensure the cell is not damaged by oxidation (see to Section 2.2.7).

To model energy flows and temperatures throughout the SOFC, the interactions between solid components and gaseous states in the form of losses and heat sources must be considered. Newton's law of cooling describes heat flow between two components such as oxygen/fuel and the solid components in an SOFC :

$$q = h(T_{solid} - T_{gas}) \tag{2.21}$$

where q is the heat flux, h is the heat transfer coefficient and T is temperature of a body. The enthalpy, H_W, is:

$$H_W = C_{pi} N_i T_{gas} \tag{2.22}$$

where C_{pi} is the specific heat of species i.

The energy balance for the solid region of the fuel cell:

$$\frac{\rho_s Cp_s \partial T_s}{\partial t} = \frac{\left(\lambda_{cf,x} \partial^2 T_s\right)}{\partial x^2} + \frac{\left(\lambda_y \partial^2 T_s\right)}{\partial y^2} + \frac{\left(\lambda_{cf,z} \partial^2 T_s\right)}{\partial z^2} + \Phi \tag{2.23}$$

where: subscript s denotes solid, λ_{cf}, effective conductivity of solid and Φ is a heat source term:

$$\Phi = q_s + \frac{\left(h_f (T_f - T_s) A_f\right)}{\partial V} + \frac{\left(h_a (T_a - T_s) A_a\right)}{\partial V} \tag{2.24}$$

where: h is the heat transfer coefficient, A is respective area of fuel (f) or air (a) electrodes, and q_s is the heat generated by the oxidation reaction (a) and ohmic heating (b):

$$q_s = \overbrace{\frac{-T_{solid} \Delta S_i}{2F}}^{(a)} + \underbrace{j^2 \rho_{eff} z_{cell}}_{(b)} \tag{2.25}$$

where q_s (Equation 2.25) is the is the heat source and ΔS_i is the change in entropy of species i. Fourier's law gives the relationship between q and the gradient of temperature:

$$q = -\lambda \nabla T \tag{2.26}$$

where λ is the thermal conductivity. Other equations are required when considering different modes of heat transfer such as radiant heat transfer.

These standard equations are used to describe and solve mass and energy flows and are implemented in the ANSYS® program (Appendix D2). The way the equations are applied to solve a problem (domain) depends on the analytical or numerical method used. The fundamental equations provide the basis for developing a set of model equations that can be solved numerically after appropriate boundary conditions are applied. For example, equations for cell voltage and temperature at the anode can be derived from current and heat balances, Ohm's and Fourier's laws:

$$\nabla^2 U = 0 \tag{2.27}$$

$$-\lambda \nabla^2 T = \sigma \nabla U \cdot \nabla U \tag{2.28}$$

The boundary conditions depend on the region being investigated. At the anode/fuel interface, for example, the boundary condition for cell temperature is given by:

$$\nabla T = h_{fuel}(T_{solid} - T_{fuel}) \tag{2.29}$$

2.2.6 Temperature, Pressure, and Gas Composition

The cells in a stack operate under non-homogenous (unsteady) conditions. The effect of temperature and pressure on the electric potential can be derived from Equations 2.13 and 2.14:

$$\left(\frac{\partial E}{\partial T}\right)_P = \frac{\Delta S}{nF} \tag{2.30}$$

$$\left(\frac{\partial E}{\partial P}\right)_T = -\frac{\Delta V}{nF} \tag{2.31}$$

The reaction between hydrogen and oxygen has negative entropy so the electric potential drops. However, performance increases at the higher temperature because reaction rates at the electrodes improve and electrolyte resistance decreases. A typical cell (voltage-current) performance curve is shown in Figure 2.2.

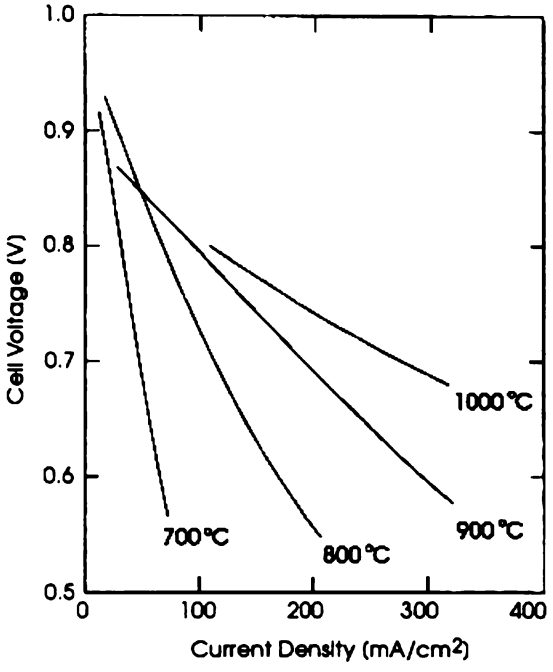

Figure 2.2 Effect of temperature on cell performance. [11]

Increasing pressure improves electric potential and has been reported for a Seimens-Westinghouse AES cell (air electrode support).[8] The effect of increasing pressure on cell performance has been approximated:

$$\Delta V_P = 59 \log \frac{P_2}{P_1} \tag{2.32}$$

where ΔV (mV), P_1 and P_2 are different cell pressures.

Achieving uniform thermal and chemical distribution over the active cells, within a stack is paramount for long term and efficient operation of an SOFC. If temperature is not uniform throughout the stack (or within a cell), higher fuel utilisation (consumption) will occur in regions of higher temperature for two reasons. Firstly, gas viscosity increases with temperature, gas flow decreases at higher temperatures and less fuel is available. Secondly, conductivity of the electrolyte (YSZ) improves with increasing temperature. The anode may oxidise if fuel is depleted while the cell is under load, with the possibility of physical damage. If there is insufficient oxidant at the cathode, electric potential decreases but the electrodes are not physically damaged. Sira and Ostenstad [9] reported that the conventional cross-flow planar stack design suffers from large thermal gradients induced by the cooler fuel and air flows entering at the inlets.

Fuel utilisation can be adjusted to obtain a specific performance. Hartvigsen *et al.*[10] developed a performance map for natural gas operation that allows optimum operating conditions to be identified as a function of power and efficiency requirements.

2.2.7 Summary

SOFCs can be modelled using equations that describe mass flow into a fuel cell and the amount of intrinsic thermal and electrical energy carried by the mass. Mass transfer through the electrodes is by diffusion and kinetic relationships that quantify oxygen reduction, and fuel oxidation. The power output, or current produced, by the system (SOFC stack) is related to the mass consumed. The system's overall thermal characteristics are a balance of mass flow, thermal losses to surroundings and heat sources (electrochemical and resistive heating). The potential drop experienced by the system is due to ohmic losses, irregular temperature profiles, and variation in fuel and oxidant composition and pressure.

2.3 Computer Modelling Techniques

Simple problems, such as heat conduction in a metal rod, can be solved analytically. Numerical methods* are becoming widely used mainly because low-cost high-speed computing is available. Complex problems typically require solution over an irregular domain where thermal properties are temperature, and/or position dependant, and boundary conditions are non-linear.

The common numerical methods are based on discrete elements such as finite element (FE), finite difference (FD) and finite volume (FV). These methods involve dividing the modelled domain into smaller components, referred to as elements. Joining sets of points, referred to as nodes, forms the elements. The interconnection between the nodes forms the mesh (Figure 2.3). These methods allow complexities of a problem to be retained commonly at the expense of accuracy. Therefore, these techniques are essentially approximate solution methods.

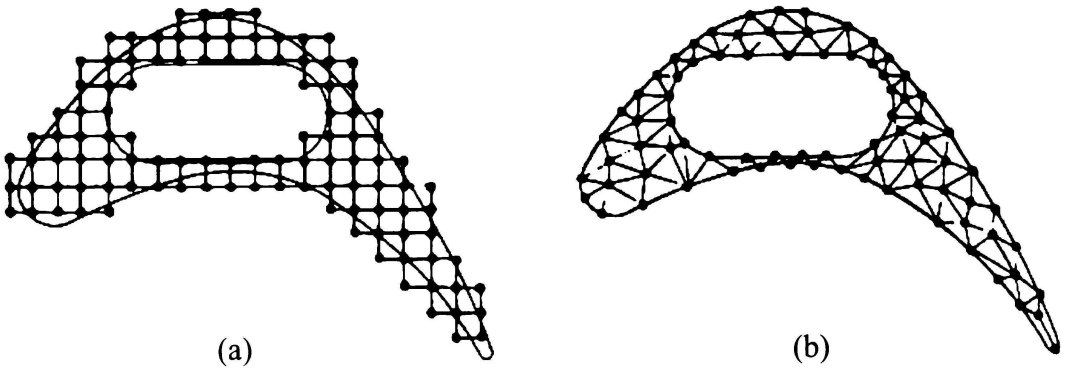

Figure 2.3 a) Finite difference and b) finite element discretizations of a turbine blade profile.[12]

2.3.1 Finite Difference

The FD method was originally performed manually, with difference equations written for an array of grid points. Computers allow an increase in grid points,

* In this thesis, numerical modelling has been used inter-changeably with computer (or computational) modelling.

improving accuracy. FD becomes difficult to use with irregular geometries and unusual boundary conditions.

2.3.2 Finite Element

The FE method is used widely for modelling structural mechanics, heat conduction and computational fluid dynamics (CFD), and offers improved flexibility for complex geometries. The method involves dividing the problem domain into small pieces or elements (Figure 2.3b). In two-dimensional problems, the elements are triangular or tetragonal. The unknowns are solved at each element using approximating (or interpolation) functions, which are defined in terms of the values of the unknown field variables at the nodes (i.e. describes the behaviour of the physical properties on to each element).

2.3.3 Finite Volume

This technique uses an arbitrarily selected volume to solve the values of conserved variables averaged across the volume. The values of the conserved variables are located within the volume element and not at the nodes or surfaces. Therefore, boundary conditions can be applied non-invasively. FV can be applied to non-structured meshes.

2.3.4 Other Methods

The SOFC computer models available are largely custom-coded packages in programming languages such as C and Fortran. Other software programs have been used for a more object-orientated programming environment (easier to use) for assembling problems. These range from spreadsheets (Microsoft® Excel), to mathematical notebooks (MATLAB®[14] and MATHEMATICA[15]). There are also specific programs using computational fluid dynamic (CFD) programs such as FLUENT[16] and STAR-CD[17] and generic FEM programs such as ANSYS® and COSMOS™.[18] However, there is little published information on using these generic FEM programs to model SOFCs.

2.4 Modelling Trends – Overview

This section briefly overviews the SOFC modelling literature since the early 1990s. The primary interest of this thesis is to model temperature distribution and mass flow so the effect of changing design features can be investigated. A selected number of papers, which focus on the aspect to be studied, are reviewed in this thesis.

2.4.1 Areas of Interest

Nearly all models developed have a thermal, a mass, an electrical, and an electrochemical aspect, as demonstrated when developing models for a SOFC stack (Table 2.2).

Table 2.2 SOFC stack modelling parameters and model outputs

Parameter	Model Output	(Comments)
Thermal	Bulk electrolyte conductivity	(increases with temperature)
	Catalytic and electrochemical reactions	
	Reaction kinetics and reforming issues	
	Performance and efficiency, fuel in, heat in and heat loss	
	Fuel utilisation	
	Thermo-mechanical stresses	(increase)
	Hot spots, (localised heating)	
	Material compatibility	
	Transient characteristics, start up times and thermal stresses	
	Ohmic losses	(increase)
Mass Flow	Current density	
(Chemical Composition)	Fuel utilisation	(throughout the stack)
	Performance and efficiency	
	Thermal distribution due to flow (component) configuration	
	Thermal distribution	
Electrical	Current density	
	Performance and Efficiency	(of current collection & cell)
	Ohmic losses and heat generation	
	Load	
Electrochemical	Couples thermal, mass flow and electrical parameters	
	Electric potential	
	Steady state and transients	

2.4.2 Planar

Most SOFC modelling is based on planar cells. Models for single cells up to unit cell arrangements with interconnect and gas channelling have been reported. Typically comparisons are made between three different gas flow (channel) configurations - cross-, co-, and counter-flow. Vayenas *et al.*[20] used a simple 2D, steady state approach that highlights the benefit of high power densities in a cross-flow monolith configuration over conventional designs. The model predicted species conversion, temperature distribution and thermodynamic energy conversion efficiency. Radiation transfer was not considered (a simplification used often in early modelling).

Ahmed *et al.*[21] developed a thermal-hydraulic model for a monolithic solid oxide fuel cell (cross-flow). They used geometric data (cell and interconnect and channel dimensions), material data (physical properties of all solid materials in unit cell) and process data (feed gas composition, temperature, pressure, etc, of feed and oxidant gases, applied load, etc). The model was simulated with humidified hydrogen and simulated coal gas for fuel feeds, and air for the oxidant. One conclusion was that increasing the air inlet edge (relative to the fuel inlet edge) decreased pressure drop and hence parasitic losses from the cathode air blower.

Arato and Costa[22] modelled a monolithic SOFC to predict temperature and current density to load, under adiabatic and non-adiabatic conditions. Increased temperature gradients and decreased cell power was predicted for the non-adiabatic conditions.

Yentekakis *et al.*[23] developed models for cross-, counter-, and co-(concurrent) configurations and reported that performance of the co-flow configuration was better than counter and cross-flow configurations. Ferguson's[24] work demonstrated that co-flow gave better performance under similar operating conditions. The IEA (International Energy Agency)[25,26] discussed these models in 1992-1994.

A 3-D, time dependent simulation (Achebach.[5,27]) of various planar configurations, which included the effect of radiation but assumed uniform mass flow across all channels, indicated that the counter-flow configuration had the highest cell

efficiency, co-flow had the most uniform current density, and cross-flow had the largest temperature gradients (Figure 2.4). The model was extended to simulate a 2-D stack and to compare ceramic and metallic interconnects (Figure 2.5). About 22% of the heat loss from the metallic interconnects was radiant heat compared with 7 % for the ceramic interconnects. Achebach[28] also investigated the effect of increasing mass flow throughout the stacks by 300-400%. Manifold size was an important factor but, the effect on performance was less than 1%, with a temperature rises of 20K.

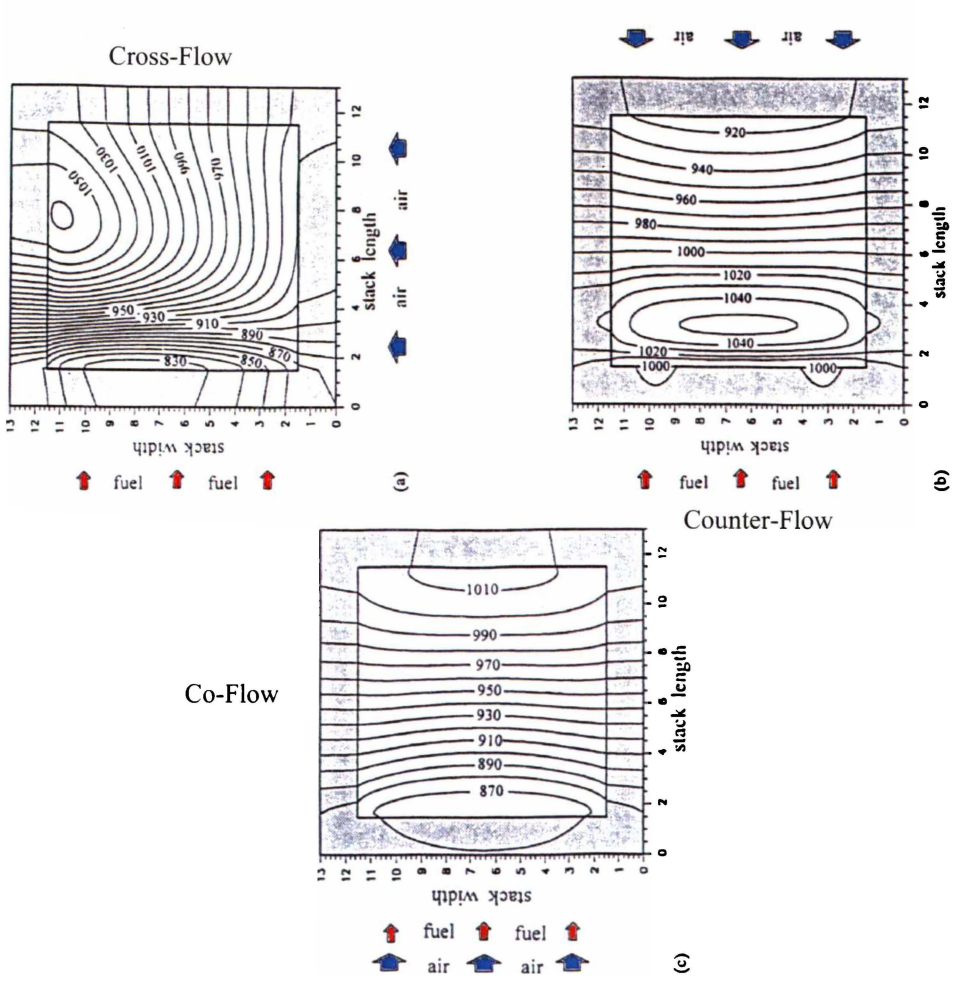

Figure 2.4 Thermal distributions for cross-, counter-, and co-flow planar geometries.[5]

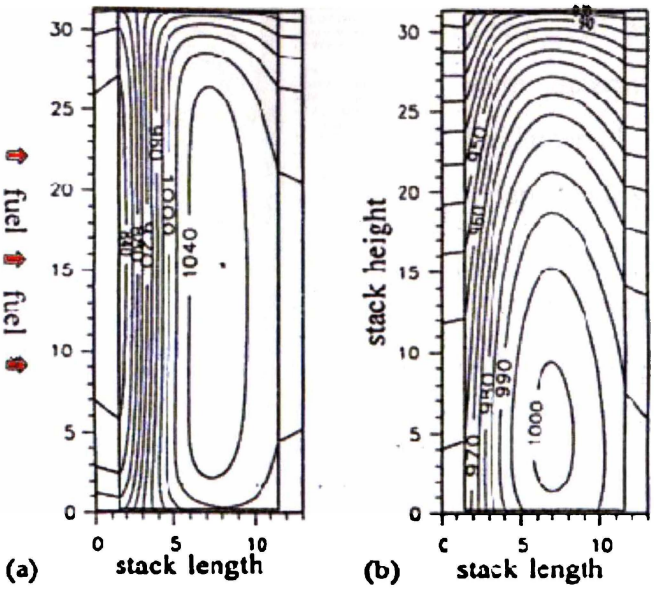

Figure 2.5 Thermal distributions for a 50-cell stack with a) ceramic, and b) metallic interconnect.[5]

Over the past 5 years, other SOFC geometries such as the SULZER HEXIS[29] have been modelled. Models are being developed for multiple-gas channels and stacks, and often include radiation and the effect of mass compositions. They increasingly are carried out using a 3-D approach (Yakabe[30]).

2.4.3 Tubular

In the early 1070s, Sverdrup *et al.*[31*] reported on a design for high-temperature SOFC batteries, with high power density. The cells were arranged with series fuel flow on a porous support. A mathematical description of the electrical characteristics of the tubular cell arrangement was given. Material properties, component dimensions and operating (or process) conditions were used to determine the ideal interconnection length between cells. The ratio of interconnection and active cell lengths for maximum power per unit volume was equal to the square root of the ratio of the interconnection and electrolyte resistivity-thickness products. The optimised interconnection length was ~0.2 cm for the segmented tubular cell.

Further modelling focused primarily on tubular cells developed by Siemens-Westinghouse.[32-34] Bessette *et al.*[32] coupled an electrochemical model with a finite

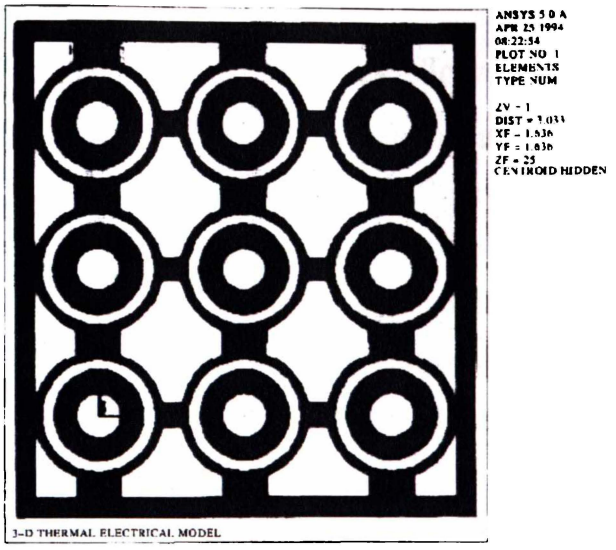

element thermal model (Figure 2.6b). All data for this model were determined from either fundamental equations or independently measured electrochemical and thermo-physical properties compared to the usual situation when data are obtained from regressing empirical SOFC performance curves. The model's predictions were within 5-7% of the experimental performance data.

Bessette *et al.*[33] used a stack model (SOFC module) of nine cells (Figure 2.6a) and found that deviations from ideal stack output was related to variations in temperature and resistance, and current flow paths. The model focussed on group cell behaviour rather than single cell performance (a common assumption in the mid-1990s). The effects of different cell failures on power output from the fuel cell stack were examined.

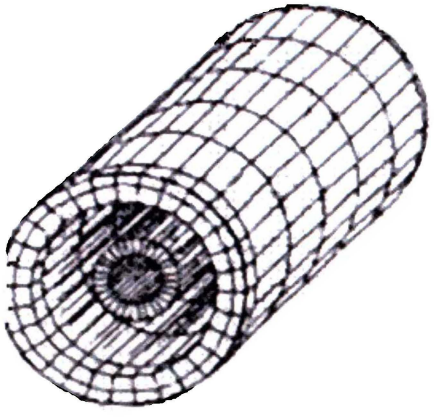

(b)

Figure 2.6 Finite element discretization of a) 3 x 3 stack module[33] and b) a tubular thermal model.[32]

* Westinghouse Research Laboratories, Pittsburgh, Pennsylvania, USA.

2.4.4 Thermal and Mass Flow

Yuan *et al.*[35] reviewed the developments in heat transfer and gas flow modelling in SOFCs. More recently, Winkler[36] reported the effect of SOFC cell geometry on mass transfer, and consequently stack design, using dimensionless numbers to describe flow in tubular, tubular-annular and planar stack designs. He proposed that higher power densities are possible when reactant gases are mixed within and around the cells, increasing mass transfer at the electrode surfaces. A tubular-helix concept was proposed to achieve increased mass transfer.

2.4.5 Coupled Models

Generic FEM modelling programs coupled with SOFC custom codes (such as electrochemical models), have been used over the past decade. Researchers use established programming tools because of fully developed Pre- and Post-programming features. Bessette *et al.*[32,33] successfully coupled electrochemical models to the generic FEM program ANSYS®. Melhus and Ratkje[36] used KAMELEON, a generic FEM program, and later KAMELEON II, which was designed to study combustion processes. Although the output is unsuitable to quantitatively design a 3D-SOFC, the data helps material selection and in optimising geometry. An example of the flexibility of generic modelling programs is shown in Figure 2.6, where mass fraction of oxygen and hydrogen in a cell are plotted, to illustrate consumption of reactants within the channels.

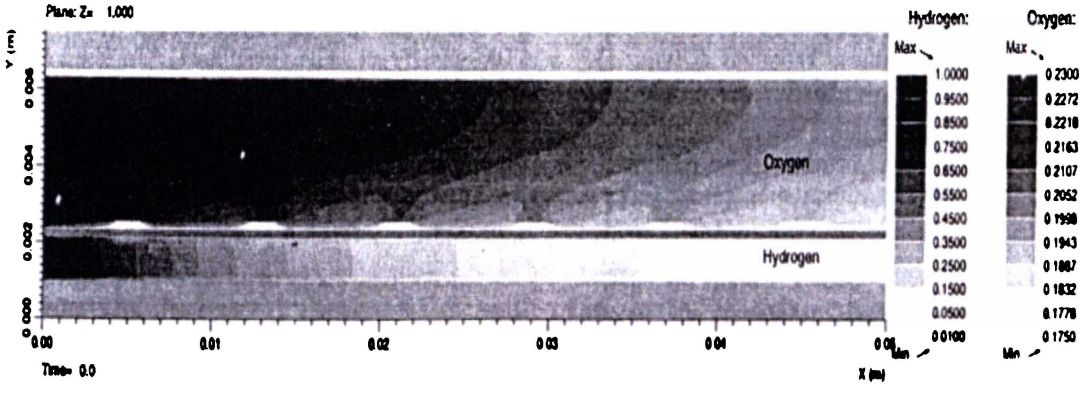

Figure 2.7 Mass fraction of oxygen (upper) and hydrogen (lower) in a single cell (kg/kg).[37]

2.5 Combustion and Flame Properties

Fuel combustion from a fuel tube or nozzle into air is a complex phenomenon to model. A non pre-mixed flame or diffusion flame occurs when the fuel and air are supplied through separate orifices. This section presents an overview of combustion, focusing on non pre-mixed hydrogen-air combustion with laminar flame behaviour. A partial treatment of combustion processes such as enthalpy of combustion (heat generation) and a general description of flame profile for modelling is given.

2.5.1 Fuel-Air Flame and Combustion

A flame consists of "spatial zones, perhaps varying with time, in which non-uniformity of velocity, temperature and composition introduce momentum, heat and mass transfer." [38] Theoretical studies of flames typically use equations that describe diffusive processes and are of the general form given by Equation 2.33. Other equations include Newton's law of viscosity, Fourier's law of heat conduction and Fick's law of species diffusion:

$$F = -D\frac{\partial C}{\partial y} \tag{2.33}$$

where: F is the flux, D is the diffusivity and C is the concentration.

While hydrogen is the primary focus of this work, the SOFC can theoretically operate on a wide range of fuels. Combustion characteristics of common fuels varies but the calculated (theoretical) flame temperature of many fuels is 2200-2300K (Table 2.3). This temperature is an upper limit because thermal losses to surroundings by radiation, thermal dilution effects of feed gases, and complex, multi-step reactions will significantly decrease the actual flame temperature.

Table 2.3 Combustion characteristics of various fuels at standard temperature and pressure

Fuel	Calculated flame temperature, K In air*	Flammability limits, % fuel gas by volume in air Lower : Upper	Maximum flame velocity ms^{-1} In air	% Theoretical air for max. flame velocity
Acetylene, C_2H_2	2905	2.5 : 81.0	2.67	83
Butane, commercial	2246	1.86 : 8.41	0.87	-
Butane, n-C_4H_{10}	2246	1.86 : 8.41	0.40	97
Hydrogen	2318	4.0 : 74.2	2.83 {3.46}#	57
Methane, CH_4	2191 {2148}#	5.0 : 15.0	0.45	90
Methanol, CH_3OH	2177	6.7 : 36.0	-	-
Natural gas	2214	4.3 : 15.0	0.30	100
Propane, commercial	2240	2.37 : 9.5	0.85	-
Propane, C_2H_8	2240 {2385}#	2.1 : 10.1	0.46	94

* Flame temperatures are calculated for the stoichiometric ratio (dissociation considered). [39]

Alternative reference.[40]

Flammability limits are well defined and important for operational and safety considerations. Acetylene and hydrogen have a wide flammability limit or composition over which flame propagation can occur. Therefore, the fuel to oxidant ratio is not critical. However, the fuel to oxidant ratio is more critical for fuels with lower flammability limits. The maximum temperature is achieved at the stoichiometric mixture. Either side of this ratio the mixture becomes fuel rich or fuel lean, which decreases flame temperature (Figure 2.8). The primary cause of a lower temperature is dilution due to excess cool fuel or oxidant streams.

The maximum flame velocity defines operational and safety procedures. More importantly for premixed fuels (i.e., fuel and oxidant mixed before combustion), is the potential for flash back, which occurs if the minimum fuel velocity is lower than the maximum flame velocity. Too much fuel may give blow-off (i.e., the flame is extinguished). However, a pure hydrogen jet diffusion flame has no blow-off limit.[41]

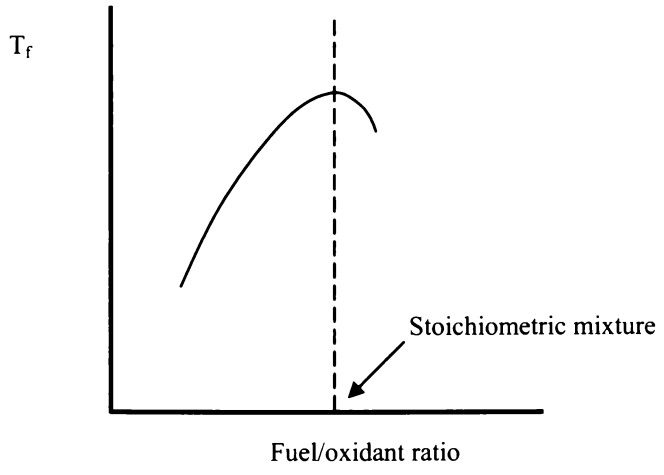

Figure 2.8 Impact of fuel to oxidant ratio on combustion temperature.[42]

2.5.2 Enthalpy and Heat Generation

Energy absorbed (released) when chemical compounds are formed is called the enthalpy of formation.* The enthalpy of reaction indicates the energy generated when fuel combusts. Together with the enthalpies of formation, the energy released for hydrogen and oxygen combustion can be calculated using thermodynamic data: [43]

$$H_{2(g)} + 0.5\,O_{2\,(g)} \rightarrow H_2O_{(g)} \qquad (2.34)$$

$\Delta H_{formation}$ for the products and reactants:

$\Delta H_{H2O\,(g)} = -241.8$ kJ mole^{-1}

$\Delta H_{H2(g)} = 0$ kJ mole^{-1}

$\Delta H_{O2(g)} = 0$ kJ mole^{-1}

Calculate $\Delta H_{rcaction}$

$\Delta H_{H2O(g)} = (1\cdot\Delta H_{H2O\,(g)}) - [(1\cdot\Delta H_{H2\,(g)}) + (0.5\cdot\Delta H_{O2\,(g)})]$

$\Delta H_{rcaction} = -241.8$ kJ mole^{-1}

Enthalpies for calculating fuel cell efficiencies are often quoted as either the high heating value (HHV) when products are in the gaseous phase, or the low heating

* Enthalpy of formation can be used for thermochemical calculations. When these include several compounds and or elements, the calculated energy is referred to as the "*enthalpy of reaction*". If the enthalpy of reaction involves one mole of a reactant (fuel) reacting with an oxidant, the resulting energy is termed the "*enthalpy of combustion*". The evolution and transfer of heat is a fundamental part of the first law of thermodynamics, which states that the total energy of any system and its surroundings is conserved

value (LHV) where products in the liquid phase. Water vapour (gas state) releases -241.8 kJ $mole^{-1}$ whilst water (liquid) has a $\Delta H_{H2O(l)}$ of -285.8 kJ $mole^{-1}$.

At constant volume and pressure, with only temperature varying significantly (the situation for a non-aerated Bunsen burner), Kirchoff's Law, which relates the rate of change of enthalpy of a reaction with temperature, can be used:

$$\Delta H_{R2} = \Delta H_{R1} + \int_{T_1}^{T_2} (pC_p - rC_p) \cdot \Delta T \qquad (2.35)$$

where ΔH_{R1} and ΔH_{R2} are the enthalpies of reaction at temperature T_1 and T_2, and p and r are products and reactants, respectively. The temperature affects enthalpy and total enthalpy in the products of combustion is less than that in the reactants. The balance is the heat liberated during combustion. For the reaction presented in Equation (2.34), the $\Delta H_{reaction}$ is -249.0 kJ $mole^{-1}$ at 1200 K.[44] An increase in temperature has only a small effect on enthalpy of combustion (~ 3%).

2.5.3 The Flame Temperature Profile

Factors determining whether the flame for a non-premixed combustion process is laminar or turbulent include diameter of the nozzle and velocity and viscosity of the issuing or injected gas. Turbulent flames are shorter because mixing is better, and are often used for rapid heating. The term space heating rate (SHR) is the rate heat is released through chemical reactions in a unit volume of reaction space.[45] The ANSYS® program uses a similar term, heat generation rate (Section 4.5.1.).

Large temperature gradients exist in the flame, especially at the outer zone. The thermal gradient is affected by oxygen diffusion from the air into the fuel and composition of combusted gases, which depend on the fuel to oxidant ratio (Figure 2.9a). In over-ventilated conditions flame shape depends on the fuel tube (Figure 2.9b curve 2). In under-ventilated conditions, flame shape depends on the airflow annulus (Figure 2.9b curve 1). The length, L of a laminar diffusion flame can be

calculated from the volumetric flow rate V, and diffusion coefficient D (oxygen in hydrogen):[50]

$$L = \frac{V}{\pi D} \tag{2.36}$$

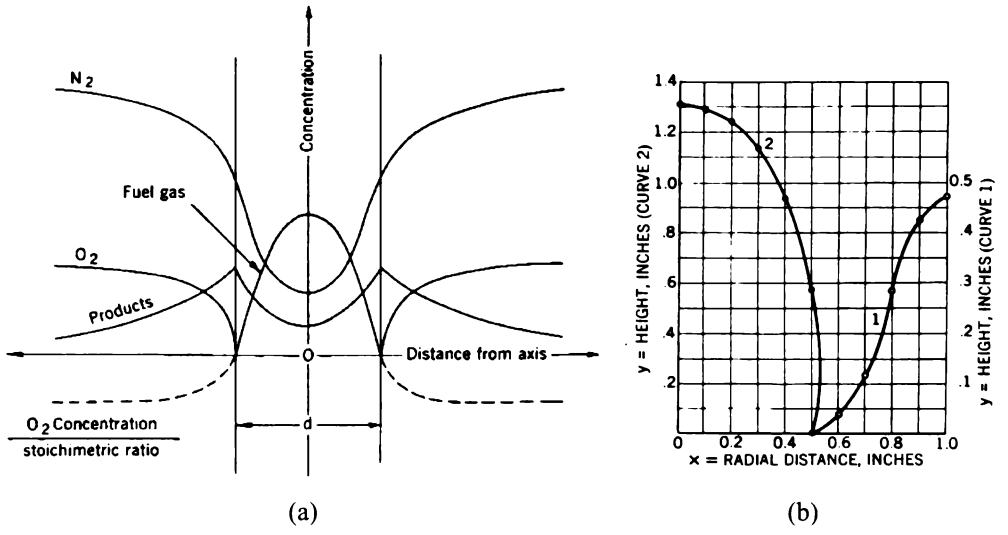

(a) (b)

Figure 2.9 a) cross section concentration profile for a laminar diffusion flame, and b) curve 1, underventilated cylindrical flame and curve 2 is an overventilated flame.[45]

Flame photography is commonly used to observe flames. Flames of hydrocarbon fuels can be photographed directly but other techniques such as floating dust particles and stroboscopic lights are required for flames from fuels with low luminosity such as hydrogen (Figure 2.10). The dust particles appear as interrupted lines in the photographs, with the length of the interruption indicating velocity. These particle tracks also indicate changes in acceleration and flow direction.

Other photographic methods rely on changes in gas density and composition due to temperature variation throughout the flame (Topler Schlieren and the Dvorak shadow methods), and the interferometer methods. Infrared spectroscopic techniques, used in conjunction with a Meker burner flame and an optical pyrometer, can be used to measure flame radiation.

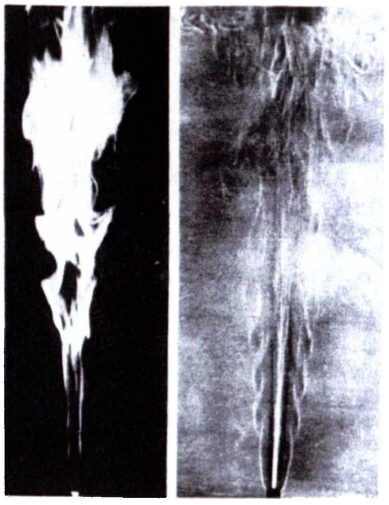

Figure 2.10 Direct a) and shadow b) photographs of a laminar, 100% butane flame (0.01-m ID burner tube, Reynolds number = 7000, 0.01 sec exposure).[46]

2.5.4 Flame and Combustion Modelling

Flame profiles can be characterised in terms of flame height, temperature, chemical composition and energy. These calculations often require empirical data such as diffusion coefficients, reactant gas compositions, flame temperature profile, and specific information on the test equipment used. Much of combustion science concentrates on large-scale or industry-focussed applications such as industrial furnaces. Combustion models generally consist of many sub models for calculating the many complex phenomena. Most models involve combustion of fuels that contain particles, so a particle field solution is required.

Before a code simulation is accepted, the modelling codes are often rigorously evaluated by comparing experimental data from different combustor geometries of various sizes. Comprehensive combustion models contain many parameters and variables, making it difficult to identify any observed lack of agreement. A review of combustion modelling[47] suggests that present combustion models require operators with appropriate training, background and specialised experience.

The correlation between combustion science and SOFC development is not strong. Winkler and Kruger[51] discuss designing and manufacturing a tubular SOFC combustion system, and concluded that using cascading tubular cells to form an

integrated burner arrangement is feasible. However, the combustion processes were not examined in detail.

2.5 Summary

The focus of the research in this thesis is at the stack modelling level. The equations describing SOFCs, and which constitute the governing equations of many fuel cell models, revolve around conserving mass, thermal and electrical energy. Modelling SOFCs has focussed on cell models, usually planar and to lesser extent, large tubular designs. Stack models are often coupled with cell models and simulated from the cell up. Iterative techniques are used to solve between the cell and stack environments.

To model an integrated burner in a fuel cell system requires information on combustion processes. Combustion modelling focuses mainly on industrial systems or very specific combustion processes and rely heavily on empirical data. Characterising a simple flame is challenging and relies on empirical data to assemble the code, solve the model, and verify the results.

REFERENCES - Chapter Two

1 R. J. Selman, *Modelling and design in SOFC scale-up, Proc. of the International Symposium on Solid Oxide Fuel Cells*, Nagoya, Japan, **1989**, pp. 212-252.

2 H. Yakabe, T. Ogiwara, I. Yasuda, and M. Hishinuma, in *Solid Oxide Fuel Cells VI*, (Eds. S. C. Singhal and M. Dokiya), Vol. PV 99-19, The Electrochemical Society, Inc., Pennington, NJ, **1999**, pp. 1087-1098.

3 N. F. Bessette II and W. J. Wepfer, *Energy Convers. Management.* 37(3), **1996**, pp. 281-293.

4 J. Padulles, G. W. Ault, and J. R. McDonald, *J. Power Sources* 86, **2000**, pp. 134-139.

5 E. Achenbach, *J. Power Sources* 49, **1994**, pp. 333-348.

6 K. Kordesch and G. Simader, *Fuel Cells and Their Applications*, VCH Verlagsgesellschaft mbH, Weinheim;VCH Publishers, Inc, New York; NY, Published in Germany, **1996**, p. 45.

7 N. Q. Minh, *J. Am. Ceram. Soc.* 76(3), **1993**, p. 573.

8 S. C. Singhal, in *Solid Oxide Fuel Cells V*, (Eds. U. Stimming, S. C. Singhal, O. Yamamoto, and H. Tagawa), Vol. PV 97-40, The Electrochemical Society, Inc., Pennington, NJ, **1997**, pp. 37-50.

9 T. Sira and M. Ostensdad, in *Proc. 3rd Int. Symp. on Solid Oxide Fuel Cells*, (Eds. S. C. Singhal and H. Iwahara), **1993**, pp. 851-860.

10 J. Hartvigsen, A. Khandkar, and S. Elangovan, in *Solid Oxide Fuel Cells VI*, (Eds. S. C. Singhal and M. Dokiya), Vol. PV 99-19, The Electrochemical Socity, Inc., Pennington, NJ, USA, **1999**, pp. 1135-1141.

11 K. Kordesch and G. Simader, *Fuel Cells and Their Applications*, VCH Verlagsgesellschaft mbH, *Weinheim;VCH Publishes, Inc, New York; NY (USA)*, Published in Germany, **1996**, p. 136.

12 K. H. Huebner, E. A. Thornton, and T. G. Byrom, *The Finite Element Method for Engineers*, 3rd Ed., John Wiley and Sons, Inc., USA, **1995**, p. 5.

13 The Internet; [http://www.engr.usask.ca/~macphed/finite/fe_resources/fe_resources.html]

14 The Internet; [http://www.mathworks.com/]

15 The Internet; [http://www.wolfram.com/]

16 The Internet; [http://www.fluent.com/]

17 The Internet; [http://www.cd.co.uk/]

18 The Internet; [http://www.cosmosm.com/]

19 M. J. Fagan, *Finite Element Analysis, Theory and Practice*, Longman Scientific and Technical, Singapore, **1992**.

20 C. G. Vayenas, P. G. Debenedetti, I. Yentekakis, and L. L. Hegedus, *Ind. Eng. Chem. Fundam.* 24, **1985**, pp. 316-324.

21 A. Ahmed, C. McPheeters, and R. Kumar, *J. Electrochem. Soc.*, Vol. 138(9), **1991**, pp. 2712-2718.

22 E. Arato and P. Costa, in *Proc. 2nd Int. Sym. Solid Oxide Fuel Cells*, (Eds. F. Grosz, P. Zegers, S. C. Singhal, and O. Yamamoto), Athens, Greece, **1991**, pp. 273-280.

23 I. V. Yentekakis, S. Neophytides, S. Seimanides, and C. G. Vayenas, in *Proc. 2nd Int. Sym. Solid Oxide Fuel Cells*, (Eds. F. Grosz, P. Zegers, S. C. Singhal, and O. Yamamoto), Athens, Greece, **1991**, pp. 281-288.

24 J. R. Ferguson, in *Proc. 2nd Int. Sym. Solid Oxide Fuel Cells*, (Eds. F. Grosz, P. Zegers, S. C. Singhal, and O. Yamamoto), Athens, Greece, **1991**, pp. 305-312.

25 SOFC Materials, Process Engineering, and Elect., Proc. 5th IEA Workshop, Julich, Germany, 2-4 March **1993**.

26 *The IEA programme of R, D, & D on Advanced Fuel Cells*, Annex II: Modelling and Evaluation of Advanced Solid Oxide Fuel Cells. Swiss Federal Office of Energy, Final Report, SOFC Stack Design Tool, Berne, November **1992**.

27 E. Achenbach, *J. Power Sources* 57, **1995**, pp. 105-109.

28 E. Achenback and U. Reus, in *Solid Oxide Fuel Cells VI*, (Eds. S. C. Singhal and M. Dokiya), Vol. PV 99-19, The Electrochemical Society, Inc., Pennington, NJ, **1999**, pp. 1125-1133.

29 P. Silberg and E. Handschin, in *Solid Oxide Fuel Cells V*, (Eds. U. Stimming, S. C. Singhal, O. Yamamoto and H. Tagawa), Vol. PV 97-40, The Electrochemical Socity, Inc., Pennington, NJ, USA, **1997**, pp. 1368-1373.

30 H. Yakabe, T. Ogiwara, I. Yasuda, and M. Hisinuma, in *Solid Oxide Fuel Cells VI*, (Eds. S. C. Singhal and M. Dokiya), Vol. PV 99-19, The Electrochemical Society, Inc., Pennington, NJ, USA, **1999**, pp. 1087-1098.

31 E. F. Sverdrup, C. J. Warde, and R. L. Eback, *Energy Conversion,* 13, **1973**, pp. 129-141.

32 N. F. Bessette II, W. J. Wepfer, and J. Winnick, *J. Electrochem. Soc.* 142(11), **1995**, pp. 3792-3800.

33 N. F. Bessette II and W. J. Wepfer, *Energy Convers. Mgmt.* 37(3), **1996**, pp. 281-293.

34 M. Suzuki, A. Hirano, T. Ioroi, Z. Ogumi, and Z. Takehara, in *Solid Oxide Fuel Cells V*, (Eds. U. Stimming, S. C. Singhal, O. Yamamoto, and H. Tagawa), Vol. PV 97-40, The Electrochemical Socity, Inc., Pennington, NJ, USA, **1997**, pp. 1359-1367.

35 J. Yuan, M. Rokni, and B. Sunden, in *Solid Oxide Fuel Cells VI*, (Eds. S. C. Singhal and M. Dokiya), Vol. PV 99-19, The Electrochemical Society, Inc., Pennington, NJ, USA, **1999**, pp. 1099-1108.

36. Winkler, *J. Power Sources* 86, **2000**, pp. 449-454.

36 O. Melhus and S. K. Ratkje, *Denki Kagaku*, **1996**, pp. 662-673.

37 A. M. Kanury, *Introduction to Combustion Phenomena*, Vol. 2: *Combustion Science and Technology*, Gordon and Breach Science Publishers, Inc., USA , **1975**, pp. 47.

38 R. H. Perry and D. W. Green Eds, *Perry's Chemical Engineers' Handbook* 7th edn., McGraw-Hill, USA, Chapt. 27, p. 26.

39 K. Kordesch and G. Simader, "Fuel Cells and Their Applications" VCH Verlagsgesellschaft mbH, *Weinheim;VCH Publishes, Inc, New York; NY (USA)*, Published in Germany, **1996**, p. 299.

40 Y. N. Shebeko, A. Y. Korolchenko, E. D. Zamishevski, A. V. Trunev, V. Y. Navzenya, and A. A. Zaitzev, *Combust. Flame*, Vol. 117, **1999**, pp. 438-440.

41 *Burner Technology*, Encyclopædia of Technology, (publisher-unknown), p. 284.

42 The NBS tables of chemical thermodynamic properties, *J. Phys. Chem. Ref. Data*, Vol. 11, **1982**, Suppl. No. 2.

43 The Internet; [http://www.crct.polymtl.ca/cgi-test/reaction]

44 A. M. Kanury, *Introduction to Combustion Phenomena*, Vol. 2: *Combustion Science and Technology*, Gordon and Breach Science Publishers, Inc., USA , **1975**, pp. 42, 138.

45 B. Lewis and G. Von Elbe, *Combustion, Flames and Explosions of Gases* 3rd edn, Academic Press, Inc., USA, **1987**, p. 482.

46 A. M. Eaton, L. D. Smoot, S. C. Hill and C. N. Eatough, *Prog. Enegy. Comb. Sci.* 25, **1999**, pp. 387-436.

47. E. R. G. Eckert, R. J. Goldstein, W. E. Ibele, S. V. Patankar, T. W. Simon, P. J. Strykowski, K. K. Tamma, T. H. Kuehn, A. Bar-Cohen, J. V. R. Heberlein, J. H. Davidson, J. Bischof, F. Kulacki and U. Kortshagen., *Int. J. Heat Mass Transfer* 42, **1999**, pp. 2717-2797.

47 L. D. Smoot, *Prog. Energy Combust. Sci.* 23, **1997**, pp. 203-232.

48 I. S. Wichman, Z. Pavlova, B. Ramadan and G. Qin, *Combust. Flame* 118, **1999**, pp. 651-668.

49 W. Winkler and J. Kruger, *J. Power Sources* 71, **1998**, pp. 244-248.

50. B. Lewis and G. Von Elbe, *Combustion, Flames and Explosions of Gases* 3rd edn, Academic Press, Inc., USA, **1987**, p. 493.

CHAPTER THREE

CHAPTER THREE

Verification Cell-Design and Operation

3.1 Introduction

This chapter outlines the design, fabrication details and operating procedure for an experimental test rig, which is termed the "verification cell". The objectives and initial design of this cell are reviewed. The resulting physical cell is described in detail, along with cell operating procedures and test parameters. The temperature profile of a hydrogen flame from the fuel tube is characterised. Flame characteristics are considered when assessing empirical and theoretical data.

3.2 Verification Cell Concept - Design

The verification cell was developed so data from a computer model could be verified. This cell is essentially a gas burner inside a heat exchanger made of concentric stainless steel tubes based on a proposed mini-tubular stack design.[1] Because of the symmetrical design, computer modelling can be simplified to a two dimensional (2D) axisymmetric approach. The life of the verification cell was expected to be low if operating temperatures are high (>800°C) so materials were selected for an intermediate temperature (<800°C) SOFC system.

3.2.1 Objectives

The following objectives were set for the verification cell:

1. To establish design feasibility and determine if air could be supplied to maintain the burner above the operating temperature, using a chimney effect (buoyancy driven flow).

2. To collect temperature profile data and compare them with data generated by the computer model.

3. To better understand real time operation of the test rig in terms of the selected design and materials (for example, the time to reach steady state from start up and thermal stability of the system).

4. To identify design features and operating conditions that significantly affect the temperature profile.

3.2.2 Design

The verification cell incorporates the design intent of Boersma *et al.*[1] but also meets the requirements of the 2D axisymmetric approach of the computer model. The initial design was drawn and refined using Solid Works® 98 Plus[2], a standard three dimensional (3D) computer aided design (CAD) and mechanical design software package that uses feature-based parametric solid modelling. The 3D cross section of the verification cell drawn in Solid Works® 98 Plus is shown in Figure 3.1a and the 2D axisymmetric representation used for the computer modelling is shown in Figure 3.1b. Computer modelling of the verification cell is described in Chapter 4.

3.3 Verification Cell Fabrication

The schematic of the verification cell (Figure 3.1) does not have sufficient detail for physical assembly and does not show the following components: support screws, screw clamps for component end caps (base plates), and various Tungsten Inert Gas (TIG) welds. These parts were as small as possible to minimise their effect on temperatures and ensure minimum differences between actual and theoretical data. For example, extra components (such as internal screws) create resistance to gas flow resistances and affect solid bulk mass properties (e.g. overall heat capacity of the test rig) but these effects are not included in the computer model.

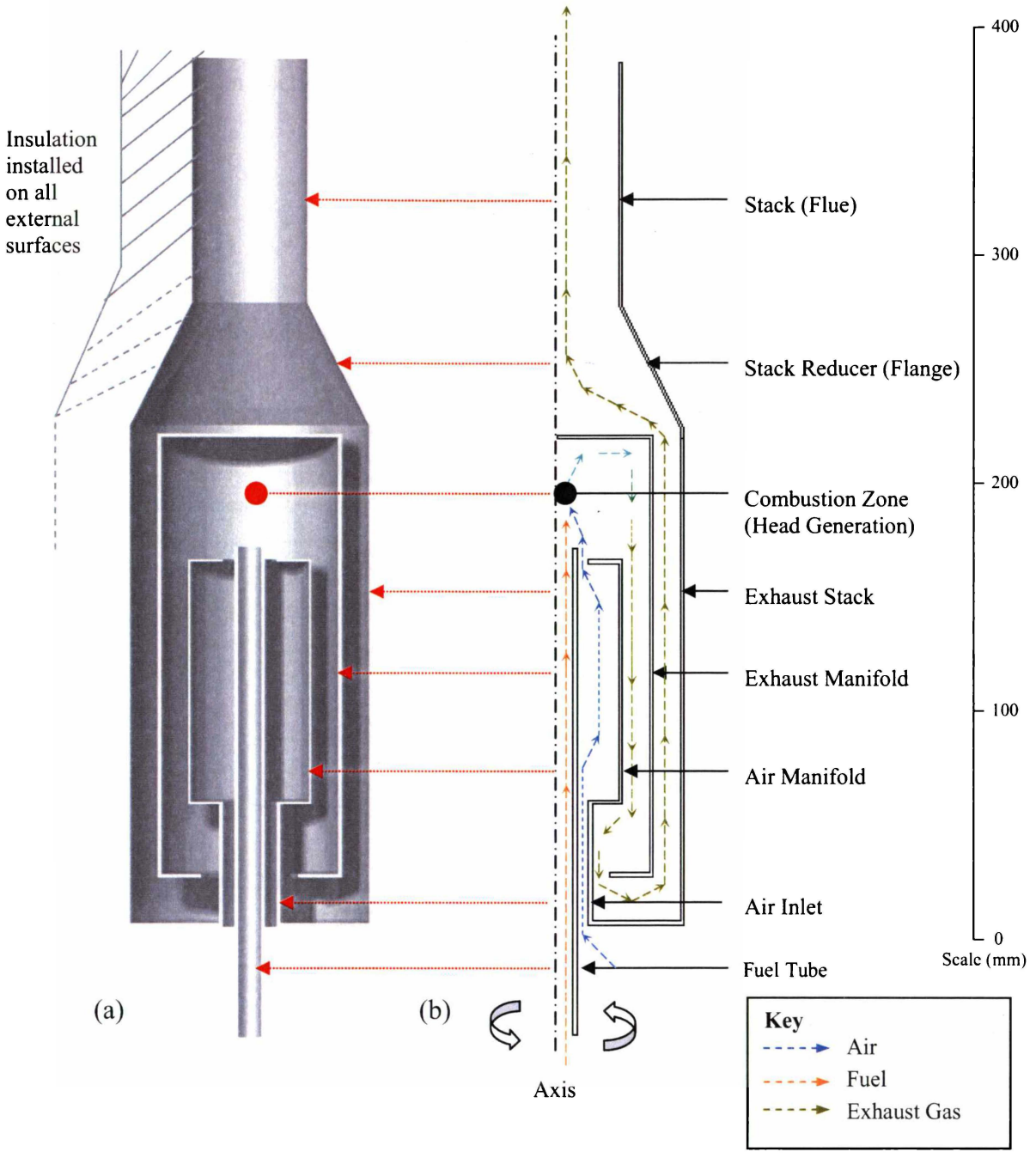

Figure 3.1 a) 3D cross section of the verification cell concept - design,
b) 2D axisymmetric representation illustrating gas flow paths.

3.3.1 Cell Design and Construction

An exploded view (Figure 3.2) illustrates how the verification cell is assembled. Each of the components are shown with attached thermocouples, and details of the screw clamps, support screws and welds in the verification cell (Figure 3.3). A

close-up of the thermocouple attachment (Figure 3.4) is shown with the discoloration of metal components due to a preliminary high-temperature test. An assembled and insulated system with the 51-mm diameter flue is shown in Figure 3.5. Further details are given in Section 3.3.4 and Chapters 4 and 6.

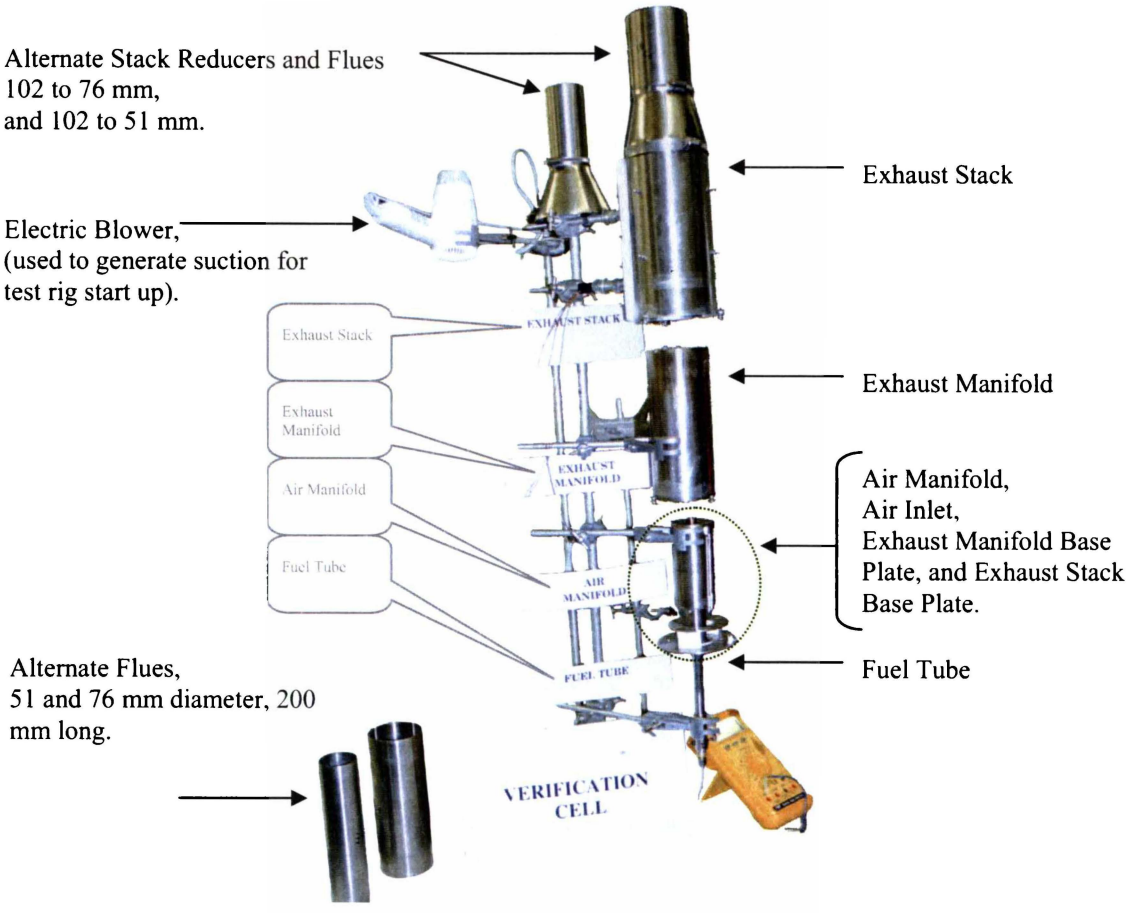

Figure 3.2 Exploded assembly view of the verification cell.

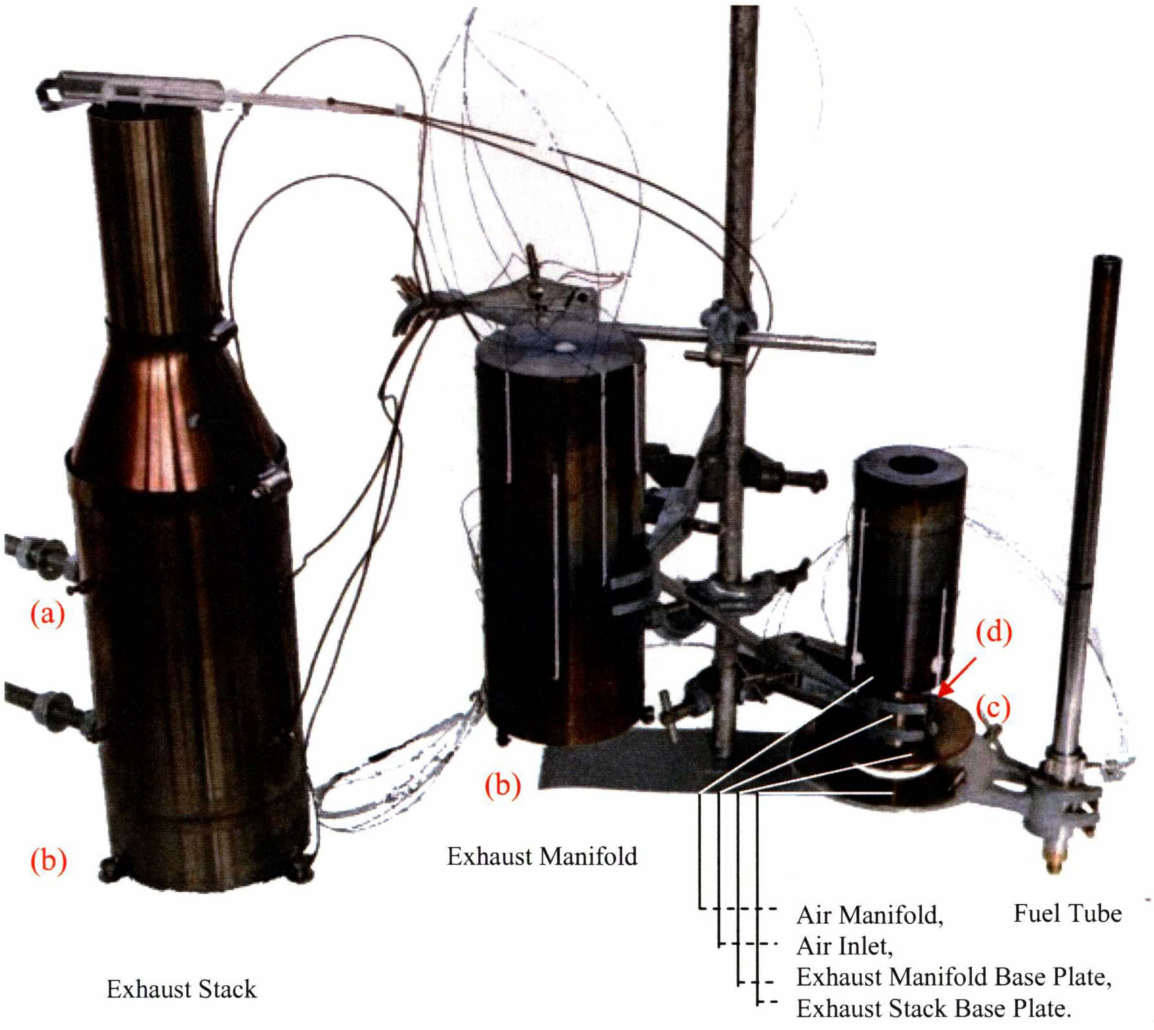

(a) Six adjustable support screws arranged in pairs around the exhaust stack at 50 mm and 150 mm and 120 degrees apart around the exhaust stack circumference. The support screws hold the exhaust manifold in place within the exhaust stack.

(b) Screw clamps consisted of 3 nuts welded to the base of the exhaust stack and exhaust manifold, with 120 degree spacing. A screw and washer were then screwed into the nut with the washer fastened the component end cap (base plate) into position.

(c) Six adjustable support screws were also located within the air inlet to guide the fuel tube into position. The arrangement of the fuel tube alignment screws was similar to that for (a).

(d) The top of the air inlet is welded to the bottom of the air manifold, and the bottom of the air inlet is welded to a 39-mm diameter flange, which is attached to the exhaust stack base plate by three screws at 120-degree intervals around the flange, and sealed with cement.

Figure 3.3 Verification cell components and design details.

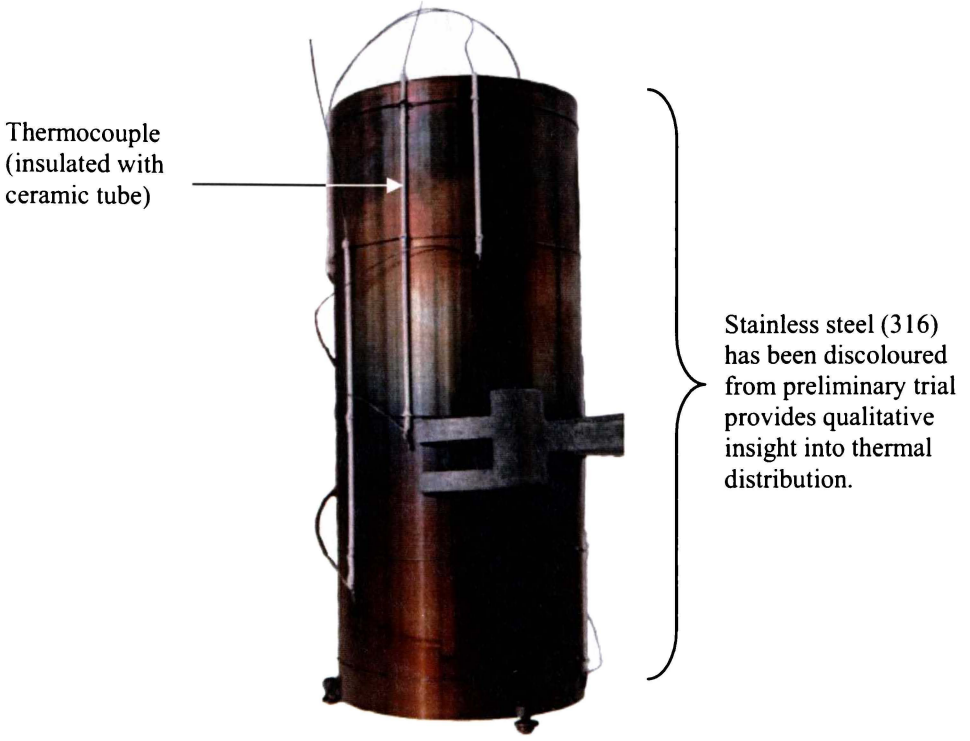

Figure 3.4 Exhaust manifold with insulated thermocouples and wiring visible.

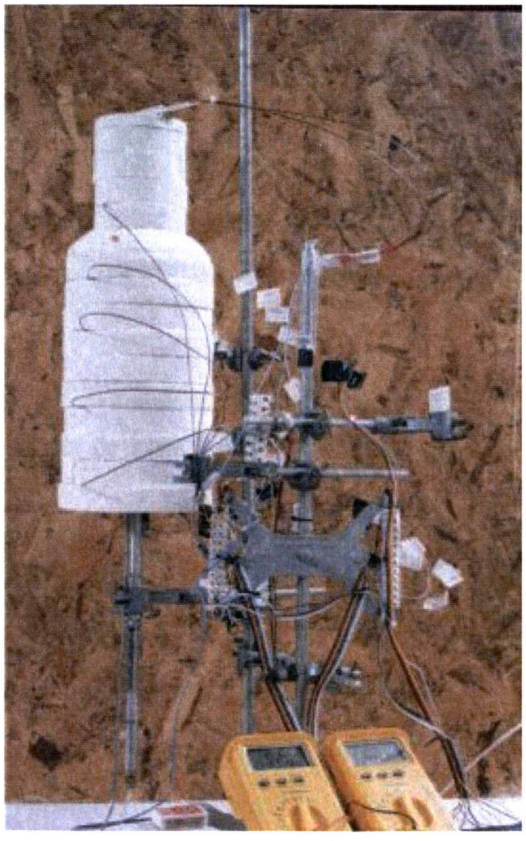

Figure 3.5 Insulated system and thermocouple test setup.

3.3.2 Materials for the Verification Cell

The following materials were used to construct the verification cell:

- All tubing for the body and all metal components were fabricated from 316 stainless steel (17% Cr, 12% Ni, 2%Mo)[3]. Concentric tubing with external diameters of 13, 25, 51, 76 and 102 mm and a nominal thickness of 1.65 mm was obtained from New Zealand Fasteners Stainless Limited (NZF Stainless). The maximum operating temperature is 800°C. Further properties of 316 stainless steel are given in Chapter 4.
- M3 x 8 (316 stainless steel) screws were used for the exhaust stack support, exhaust manifold base plate and the air inlet/fuel tube support, and M4 x 4 (316 stainless steel) screws were used for the larger exhaust stack base plate.
- Sauereisen ceramic cement (number SCC8, Scientific Instruments Services) was used as gasket material to seal components and to sheath thermocouples. The cement increased the mechanical strength and protected various components against the high temperature environment.
- Kaowool® 1260 (Thermal Ceramics New Zealand Limited), a 25-mm thick vacuum-formed board was used to insulate the test rig.
- The internal thermocouples were made from 0.38-mm standard K-Type thermocouple wire (British Driver-Harris Co. Ltd., Manchester) and were termed positive chromel, negative alumel, or chromel/alumel. The external thermocouples were glass fibre insulated, K-type wires (Radiospares Components NZ).
- The internal thermocouples were electrically isolated using 1.2-mm outer and 0.8-mm inner diameter ceramic alumina tubes (Figure 3.4).

3.3.3 Thermocouple Placement

Thermocouples were fastened by winding (chromel) thermocouple wire around each component and electrically isolated with alumina tubing where required (Figure 3.4). Thermocouples contacted the surface of the specific component and were orientated against the gas flow. Thermocouples were attached at 45 to 90 degrees around the diameter of the air and exhaust manifolds (Figure 3.6) to reduce gas flow discontinuities from upstream thermocouples and thereby reduce any impact on gas

flow and temperature distributions, and to verify the assumption of axial symmetry. Further details of thermocouple locations are reviewed in Chapter 4. Physical dimensions of the verification cell are given in Appendix C.

3.3.4 Component Function

The fuel tube in the verification cell supplies hydrogen fuel directly to the combustion zone at the top inside of the exhaust manifold. Air comes through the air inlet into the air manifold, moves to the top of the air manifold, then through the air manifold outlet into the combustion zone, which is concentric to the fuel tube and 5 mm below the fuel tube orifice (Figure 3.6). The chimney effect pulls air and exhaust gases from combustion through the system and down the inside of the exhaust manifold (outside the air manifold). The chimney effect is generated by buoyancy forces (induced draft) from heating air above the combustion zone. The heated air rises and exhausts through the flue (stack), generating the chimney effect. This is described further in Chapters 4 and 6.

3.4 Verification Cell Operation

Gas flow and temperatures were recorded while the test rig was being operated. A consistent operating procedure was used to ensure reproducible data were obtained.

3.4.1 Safety

Working with hydrogen in a confined space is hazardous so the procedures used must minimise the chance of explosions. Due to design constraints from assuming axisymmetry and other modelling considerations, an ignition system was not built into the combustion zone. Instead, the hydrogen was ignited before the fuel tube was inserted into the test rig to minimise the chance of explosion if hydrogen accumulated during a failed ignition.

An electric blower at the top of the exhaust stack/flue outlet (required for start up) provided suction and reduced the chance of hydrogen accumulating at the top of the exhaust manifold or combustion zone. This, coupled with using small-sized screws

and nuts for clamping the manifold ends, reduced any significant pressure build-up that could occur during a system malfunction.

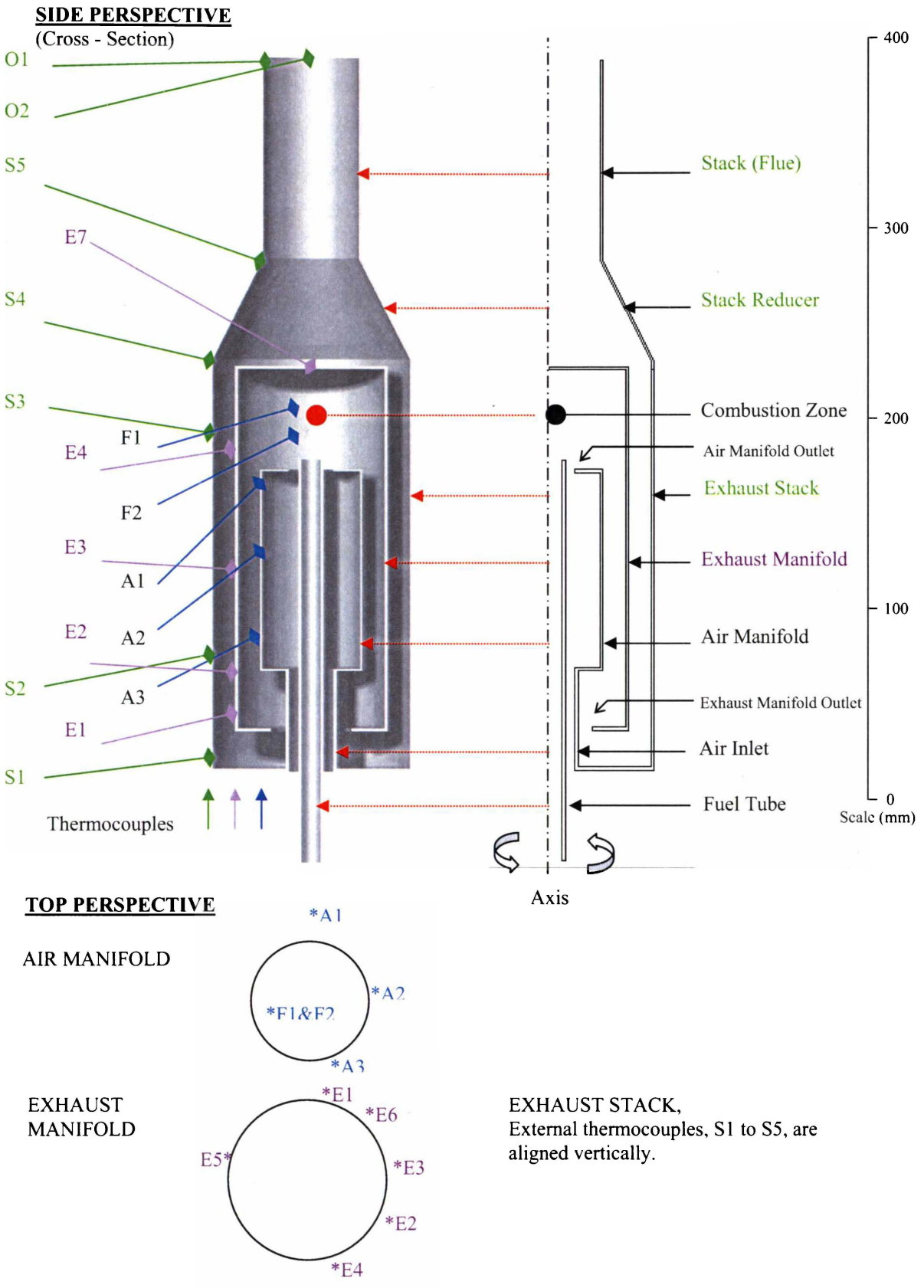

Figure 3.6 Placement of thermocouples in the verification cell.

3.4.2 Test Equipment

Platon gas rotameters were connected in parallel and used for controlling and recording the fuel flow (bottled industrial grade hydrogen, 99.5% pure). The rotameters were calibrated for hydrogen using an Altech Digital Flow Check (NIST traceable. CAT. No. 4700, Version 3.2, 3/14/95). Reading accuracy of each rotameter was ±10 mL min^{-1}. Standard temperature and pressure were assumed for recording of flow rates. As the verification cell is an open system, it is assumed that any small internal pressure variations, which could affect rotameter readings, were negligible.

Twenty-two thermocouples were routed through three bipolar selector dials and connected to three CIE 8042N K-type multimeters. Temperature data were taken in sequence from the combustion zone, air manifold, exhaust manifold, stack and exhaust outlet (i.e. following the path of combusted gas from the burner through to the exhaust outlet). There was a ±2°C difference between reading the first thermocouple (F1) to reading the last thermocouple (O2) during test rig heat-up and cool down.

3.4.3 Start Up Procedure

Each experimental test run had the following start-up procedure and operating conditions:

1. Initial system temperature of 22°C ±1°C.
2. A Remington Turbo 1250 air blower was used to apply a suction velocity* of 1.4 ±1 m s^{-1} (measured with a "Turbo Meter", Davis Instruments, USA) at the flue outlet for 10 minutes.
3. During this 'suction' time, fuel flow was set to the test rate. Preheating ensured the temperature of the test rig would be high enough to create the chimney effect, providing sufficient airflow to the burner for stable combustion.

The layout for the verification cell test rig is shown in Figure 3.7.

* Volumetric flow rates generated by the blower differ for the 51-mm and 76-mm flue configurations.

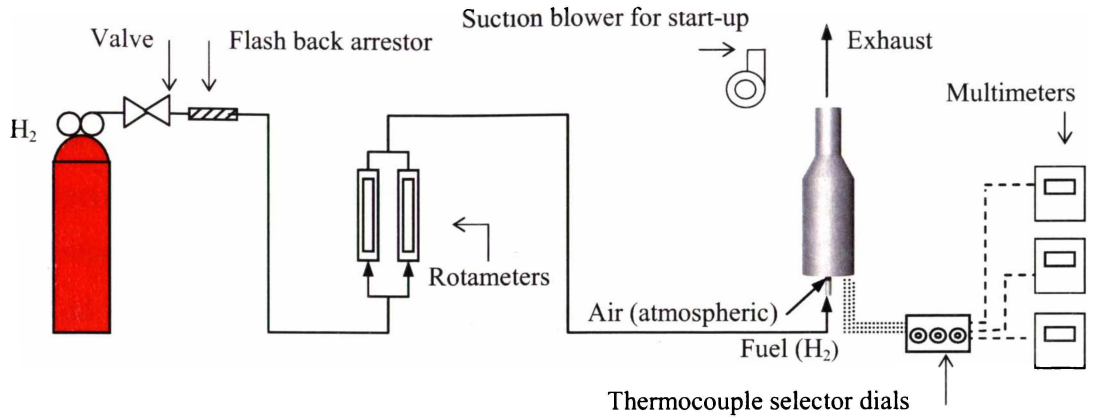

Figure 3.7 Process and instrumentation diagram for verification cell test setup

3.5 Test Parameters and Schedule

The effect of changing operating variables, such as test rig geometry, was measured as their impact on the near steady-state temperature distributions of temperatures recorded within the verification cell.

3.5.1 Operating Parameters

The effect of various fuel flow rates on the temperature while obtaining steady state, and on cooling once the fuel was turned off, was measured:

- Fuel flow rates of 400, 800, 1200 and ≥1600 mL min^{-1} on operating temperatures, recorded every 10 minutes for 60 to 80 minutes, when near steady-state was achieved.
- The cooling curve after stopping the fuel (at 800 mL min^{-1} only) was recorded every 10 minutes for 60 minutes.

3.5.2 Design Parameters

The following are the design parameters for the verification cell:

- Non-insulated or insulated externally with 25 ±5 mm of Kaowool® (Board).
- Flue height of 100 mm (standard), 200 mm and 300 mm.
- Flue width of 51 and 76 mm outer diameter.
- Restricted air inlet and exhaust outlet.

3.5.3 Test Schedule

The standard testing schedule was as follows:

1. Start-up (Section 3.4.3).
2. Operate for 60 or 80 minutes at the designated fuel flow rate, recording temperatures.
3. Add a 100-mm stack (flue) extension and equilibrate the system for 20 minutes before continuing to record temperatures.
4. Add a second 100-mm extension (total flue height of 300 mm), equilibrate the system for 20 minutes before continuing to record temperatures.
5. Repeat procedure for a different fuel flow rates, flue widths, and non-insulated or insulated systems.

The temperature of air flowing into the system 25, 75 and 100 mm from the base of the air inlet into the air manifold was recorded at all fuel flows at 60-70 minutes.

3.5.4 Factors Investigated

Experimental work investigated the following:

1. Increasing fuel flow for the non-insulated system.
2. Increasing fuel flow for the insulated system.
   Comparison of the effect of insulation*
3. Increasing flue height for 51 mm flue.
4. Increasing flue height for 76 mm flue.
5. Increasing fuel flow versus increasing flue height (51 mm flue)
   Comparison of the effect of flue width*
6. Effect of inlet and outlet flow restrictions.

Further analyses and experimental work was conducted to further characterise the system:

7. Comparing temperatures on the exhaust manifold to check for thermal axisymmetry.
8. Time taken for system to achieve steady state.

9. Temperature profile for the system cooling.
10. Effect of applying flow restrictions at the air inlet and air outlet on temperature.
11. Temperature profile of air flowing into the air manifold.

3.6 Flame Characterisation

To model the system, the temperature profile of the hydrogen flame must be known so heat generated in the system can be assessed. Therefore, the flame's temperature profile at different fuel to air ratios must be known to simulating and evaluate combustion or heat generation efficiency. The nozzle shape (fuel tube) and local conditions also influence the hydrogen flame profile.[4-7] However, the hydrogen flame is non-luminous (invisible). Two approaches were used to develop the empirical model; a combination of two thermocouple methods, and a visual (photographic) method.

3.6.1 Objectives

The two objectives for experiments on characterising the flame were:

1. To determine the effect of fuel flow on temperature profile of a hydrogen flame.
2. To assist in developing an empirical relationship for heat generation that could be applied to the verification cell model.

The heat generation module in ANSYS® requires two values to estimate heat generated from combustion: the rate of heat generated per unit volume of combusted fuel (with units of J $s^{-1}m^{-3}$ or W m^{-3}) and area of heat generation. In this research, the flame temperature profile will be used to approximate the area. The theory behind combustion, emphasising the parameters to be considered when simulating combustion, is reviewed in Section 2.5 and alternative methods for simulating the heat source are described in Section 4.5.1.

---

* From the experimental work other factors are compared.

3.6.2 Thermocouple Approach

For the thermocouple method, a custom, four-probe thermocouple array was aligned on the periphery above the fuel tube orifice (Figures 3.8a and 3.8b). The thermocouple junctions and wires in the flame zone were coated with a thin layer <0.5 mm) of cement to shield the thermocouple junctions from the reducing hydrogen flame and to reduce contamination from combustion products. Further temperature data were obtained from a thermocouple 20 mm above the fuel tube in the centre of the flame.

Thermocouples F1 and F2 were 30 and 15 mm above the fuel tube opening respectively and 6 mm from the outer diameter of the fuel tube wall. Data from the four-probe thermocouple should not be correlated with data from F1 and F2, which measure combustion zone temperature in the verification cell rather than the flame temperature profile.

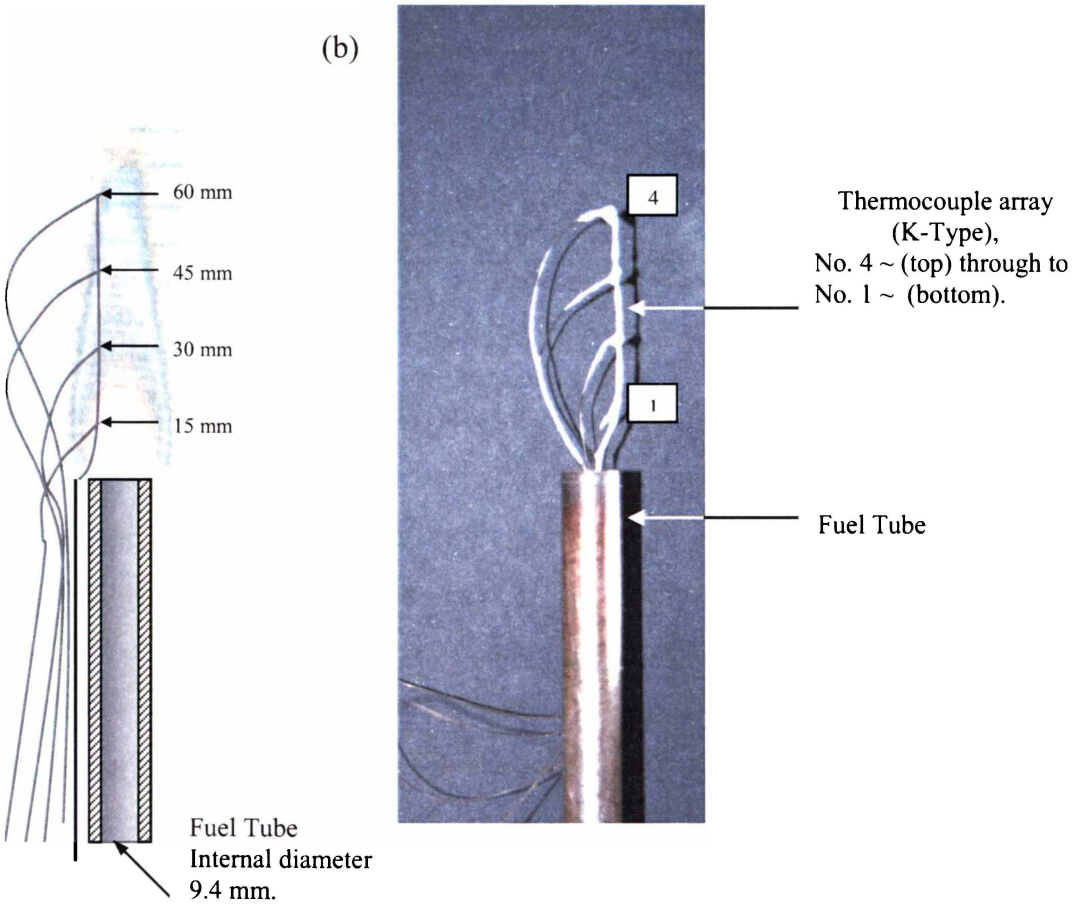

Figure 3.8 Diagram a) and photograph b) of the thermocouple array. Note: the flame profile indicated in a) is not visable because the hydrogen flame is non luminous.

3.6.3 Visual Approach (Photographic)

A 300 X 600 mm piece of nickel gauze (40 mesh) woven from 0.13-mm diameter wire was placed directly above and perpendicular to the fuel tube opening. Hydrogen was supplied to the fuel tube from a compressed gas cylinder. The hydrogen was ignited and the thermal response of the nickel gauze was photographed for fuel flows of 200 to ≥2000 mL min^{-1}. A scale attached to the side of the gauze was used to draw lines on the gauze at 10-mm intervals for dimensioning purposes. A thermocouple was placed at various locations within the flame to determine the approximate temperature distribution and supplemented data from the photographs (Figure 3.9a). The various thermal dimensions of the flame (Figure 3.9b) were measured as a function of fuel flow rate. The dimensions, abbreviations and temperature range are listed in Table 3.1. Correlation between flame dimensions, temperature and fuel flow rate were determined.

Table 3.1 Characteristic flame dimensions

Dimension Title	Abbreviation	Temperature (°C)
Flame height	FH	500 – 800
Radiant flame	RF	800 – 1200
Coolant front height	CFH	< 500
Radiant flame width	RFW	800 – 1200

3.6.4 Experimental Considerations

The following issues arise when characterising the hydrogen flame:

1. The four-probe thermocouple gives the temperature profile. However, flame distortions occur because thermocouples 2, 3 and 4 are subject to temperature and mass flow fluctuations caused by thermocouple(s) below that protrude into the fuel stream. This is discussed further in point 2 below.
2. The flame study used the nickel gauze to highlight an arbitrary flame profile rather than an absolute profile. Placing gauze across the centre of the fuel flow creates some turbulence and changes the oxygen-fuel diffusion characteristics, and hence the flames characteristics. The gauze also conducts heat from the flame.

3. The derived flame profile is for a laminar fuel stream flowing into still air and does not account for the following effect when housing the fuel tube within the verification cell:
    - Flame behaviour in a confined space (i.e. the exhaust manifold).
    - Concentric airflow entering from the air manifold-outlet.
    - Combustion of hydrogen at elevated temperatures.
    - Ratio of fuel to air.

    These complex phenomena were discussed in Chapter 2.

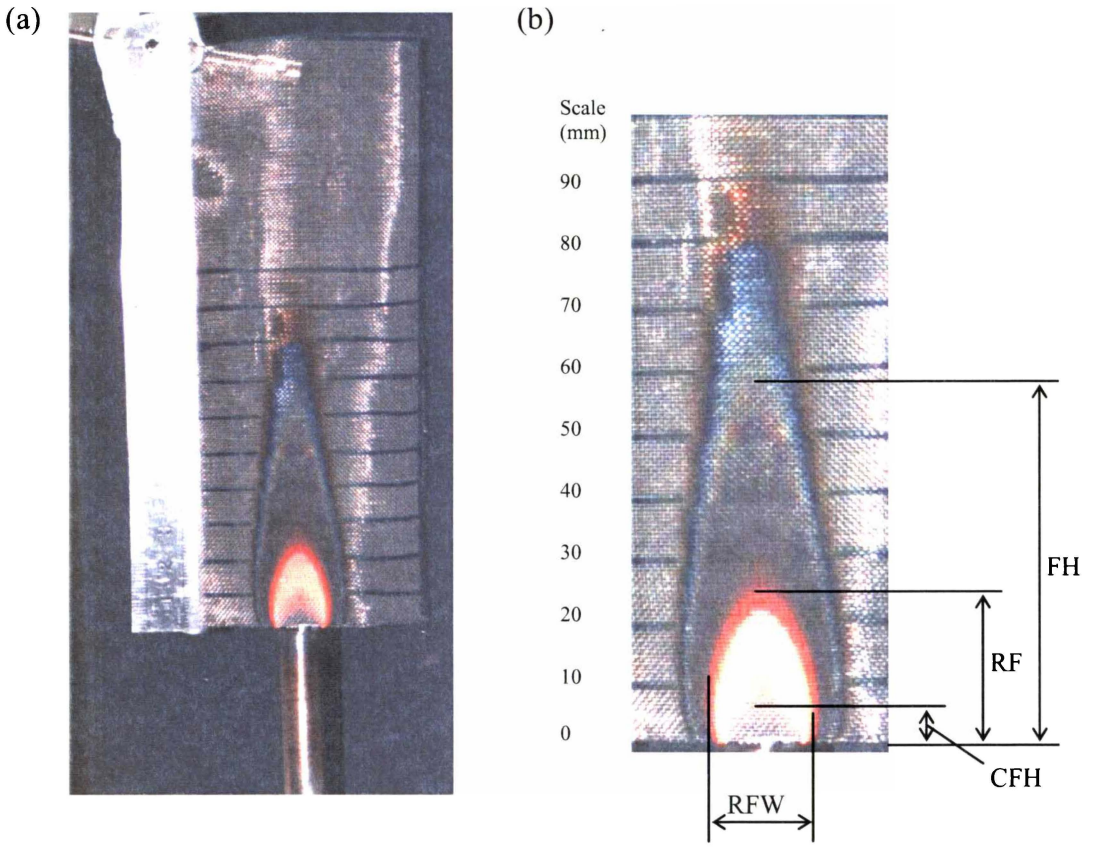

Figure 3.9 Photograph a) of expermental set-up with hydrogen flame providing an arbitrary temperature profile on nickel gauze and b) positions of characteristic dimensions taken from photographs.

REFERENCES – Chapter Three

1 R. J. Boersma, N. M. Sammes, C. Fee, *J. Power Sources* 86, **2000**, pp. 369-375.

2 SolidWorks Corporation, Concord, Massachusetts 01742, USA. [http://www.solidworks.com]

3 NZF Stainless, Hamilton, New Zealand, Product Guide, **1991**, REF 7/95.

4 A. M. Kanury, *Introduction to Combustion Phenomena*, Vol. 2: *Combustion Science and Technology*, Gordon and Breach Science Publishers, Inc., USA , **1975**.

5 A. G. Gaydon and H.G. Wolfhard, *Flames, their structure, radiation and temperature*, Chapman and Hall, 4th Ed, **1979**.

6 *North American Combustion Handbook*, North American Mfg. Co., Cleveland, Ohio 44105 USA, (Ed. R. J. Reed), 2nd Ed, **1978**.

7 *Combustion Technology Manual*, 4th Ed., Published by the Combustion Division of the Industrial heating Equipment Association, Arlington, Virginia 22209, **1988**.

CHAPTER FOUR

CHAPTER FOUR

Modelling Method and Models:

ANSYS® and Verification Cell Model

4.1 Introduction

Temperature distribution in the operating verification cell was modelled using the generic simulation software program ANSYS®[1], which uses the finite element method (FEM). Three case studies, and their underlying mathematical principles, are presented to demonstrate how the computer model described in this chapter evolved. The modelling process, including specific details of the models and modules (sub models), is described in Sections 4.4 and 4.5, and an approach to modelling a SOFC stack is proposed. Because of the size and scope of ANSYS®, an overview and the most pertinent features of the modelling process are described.

4.1.1 Objectives

The computer-modelling component had the following objectives:

1. To assess the whether ANSYS® can be used to model the proposed SOFC stack housing design, and
2. To determine if new insights into stack housing design, not easily achieved using physical models, can be obtained.

4.1.2 Help Manuals and Guides

ANSYS® has an extensive online help (Appendix D1), online Workbook examples and a Verification manual with examples. This online help, together with literature obtained from the Internet, are the primary reference resources for this chapter.

[1] ANSYS is a registered trademark of ANSYS Inc.

4.2 ANSYS®

ANSYS® has been used widely by many manufacturing industries, servicing industries, consulting firms and universities since the 1970s for a wide range of general analyses, research, and educational purposes. The broad use of ANSYS® is due partly to the scope of engineering disciplines and analysis options it offers.

This research was done using versions 5.2, and 5.4 of ANSYS® (Multiphysics, University High option). Several platforms were used including a SparcStation 20, running 64 megabytes of RAM. The program was run on a range of IBM-compatible PCs with Pentium II, 266, 350 and 400 MHz processors with up to 256 megabytes of RAM and 20 GB total disk storage, using Microsoft Windows 95, 98, or NT4 operating systems.

4.2.1 ANSYS® - Overview

ANSYS® has more than 100 element types, which can be used to analyse the following: mass, thermal, fluid, structural, electrical and magnetic properties, and mode-frequency and buckling eigenvalues under steady (static) or unsteady (transient or dynamic) state. The following can be incorporated in the simulation: 2D and 3D structures; plane, axisymmetric and 3D solids; piping systems; plates, axisymmetric and 3D shells; and non-linear problems including contact (interfaces) and cables. The effect of radiation, temperature dependency, material anisotropy, plasticity, large strain, hyperelasticity, swelling, creep, large deflections, contact and stress stiffening can also be included.

4.2.2 GUI - Graphical User Interface

The Graphical User interface (GUI), with windows, menus and dialog boxes (Figure 4.1), allow the user to build a model, enter data and run ANSYS® operations (processors or subroutines). Solutions can be monitored by displaying the convergence plot in real time.

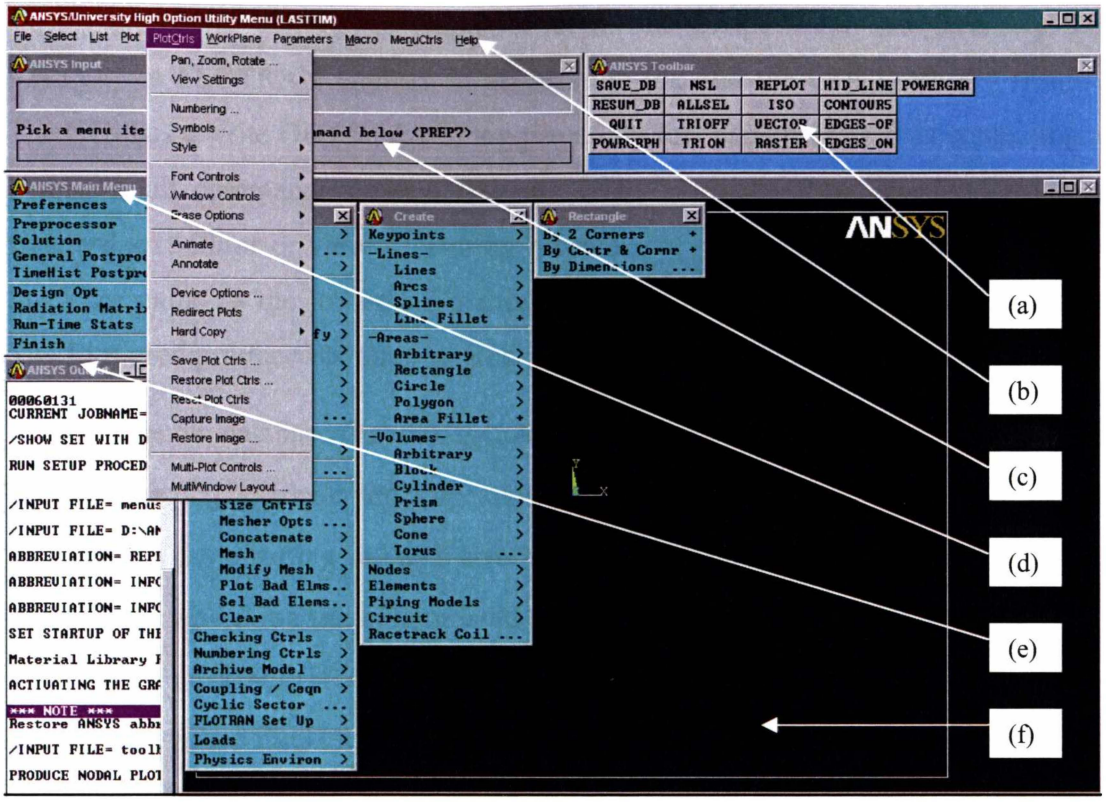

Figure 4.1 Graphical User Interface (GUI) with various menus pulled down: a) customisable toolbar, b) utility menu, c) command input window, d) main menu, e) output window, and f) graphics window.

4.2.3 APDL – ANSYS® Parametric Design Language and Batch File Processing

Design changes or model details can be changed easily and conveniently using APDL, a scripting language similar to FORTRAN 77. A model can be built by assigning numeric or alphanumeric values to parameters (variables) in the model. These can include parametric expressions involving operations between parameters (addition, subtraction, multiplication, division, exponentiation and comparison), as well as FORTRAN functions such as, ABS(x), EXP(x), LOG(x), etc*. Other features include macros (a sequence of ANSYS® commands recorded in a file), if-then-else branching, do-loops, and vector and matrix operations. The APDL is also the foundation for some of the more advanced features such as optimisation and adaptive meshing. Guidelines for parameter names and defining parameters are given in Chapter 14 of the ANSYS® Modelling and Meshing guide.

* ABS(x)=Absolute value of x, EXP(x) = Exponential of x (e^x), LOG(x) = Natural log of x (ln(x)).

Users can create batch files (input or command script files) and then use the ANSYS® or FLOTRAN engines to process the file and the GUI to review results. The GUI has a write DB (database) log file utility that can generate files containing a listing of all commands entered into the GUI. This file can be edited using a standard text editor or viewer. During a batch run, several files are generated with the same name as the job and file extensions specific to the function of each file. The files used/produced in this research include:

- jobname.db, database file with geometry, material properties, etc.,
- jobname.dbg, database file with solution information,
- jobname.err, error log file with error and warning messages,
- jobname.lgw, a log file of command operations,
- jobname.rfl, a FLOTRAN results file,
- jobname.pfl, a FLOTRAN print file with input convergence monitors, and inlet and outlet summaries.

4.2.4 FLOTRAN

The FLOTRAN software can be stand-alone or integrated into ANSYS® (and called ANSYS/ FLOTRAN, FLOTRAN CFD or Computational Fluid Dynamics) using the pre- and post-processing capabilities of ANSYS®. It offers comprehensive tools for analysing two- and three-dimensional fluid flow fields to calculate fluid flow characteristics such as pressure drop, velocity distribution, flow direction, lift and drag forces, and heating or cooling effects.

FLOTRAN has the following options: laminar or turbulent flow, thermal or adiabatic flow, compressible or incompressible fluid, Newtonian or non-Newtonian fluids, and multiple species transport. It has several solvers for the sequential solution algorithm. The Tri-Diagonal Matrix Algorithm (TDMA) is a fast, approximate solver that performs a user-defined number of iterations, through the problem domain. The exact method solvers, which use semi-direct conjugate direction methods iterating to a specified convergence criterion, can be applied to non-symmetric matrix equations and incompressible pressure equations.

4.2.5 Modelling Procedure

Several main processors (subroutines*) are used to build and analyse a model (Table 4.1). The "GUI path" refers to the menu selection order and the "Command" is typed at the command line or entered in an input batch (script) file. The procedures for implementing these routines are typically ordered in an input file or as input through the GUI, using the following steps:

1. Build the geometry — define key points, create areas, select elements, set real constants and element options
2. Define the materials — define material properties
3. Generate the mesh — set preferences, define element types, mesh the model
4. Apply loads — temperatures, heat flows, velocities, etc.
5. Obtain the solution — set the solver convergence criteria, initial conditions
6. Review the results — plot, animate, extract results, etc.

Table 4.1 Processors available in ANSYS®

Processor	Function	GUI Path	Command
PREP7	Build the model (geometry, materials, meshing, etc.)	Main Menu>Preprocessor	/PREP7
SOLUTION	Apply loads and obtain finite element solution	Main Menu>Solution	/SOLU
POST1	Review results over the entire model at specific time points	Main Menu>General Postproc	/POST1
POST26	Review results at specific points in the model as a function of time	Main Menu>TimeHistpostpro	/POST26
OPT	Improve an initial design	Main Menu>Design Opt	/OPT
AUX2	Dump binary files in readable form	Utility Menu>File>List>Binary Files	/AUX2
AUX12	Calculate radiation view factors and generate radiation matrix for thermal analysis	Main Menu>Radiation Matrix	/AUX12
AUX15	Translate files from CAD or FEA program	Utility Menu>File>Import	/AUX15
RUNSTAT	Predict CPU time	Main Menu>Run-Time Stat	/RUNSTAT

* Processors used in this research are illustrated in sample code in section 4.5 and Appendix D.

4.3 ANSYS® Examples and Modelling Equations

The following three examples illustrate the methodology and solution strategy used to develop the verification cell model. The examples include the essential phenomena being modelled, - heat exchange and buoyant flows that produce the chimney effect. The multiple species example demonstrates how the Thermal – Mass Flow (base) model can be further refined. The potential for using the multiple species simulation in a SOFC model is discussed in Section 4.6. The examples were run successfully to produce the result shown and demonstrates (verifies) the degree of fit of the ANSYS® code.

4.3.1 Buoyancy

This example demonstrates a natural convection solution where laminar flow (Figure 4.3) is due to a temperature gradient across the cavity (Figure 4.4). The ideal gas law (Equation 4.1) shows that fluid density is inversely proportional to temperature.

$$\rho = {}^{P}/_{RT} \tag{4.1}$$

where ρ = density, P = pressure, R = gas constant and T = Temperature.

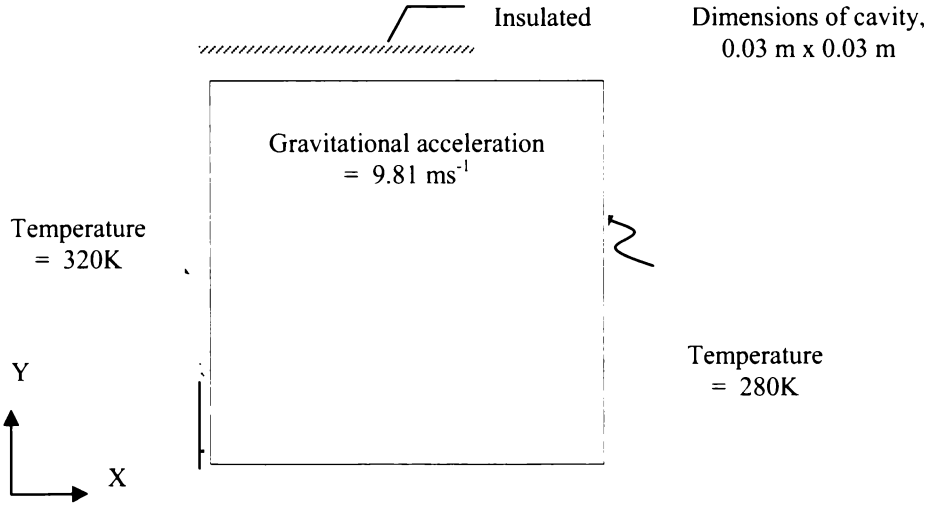

Figure 4.2 Modelling conditions for an air filled square cavity.

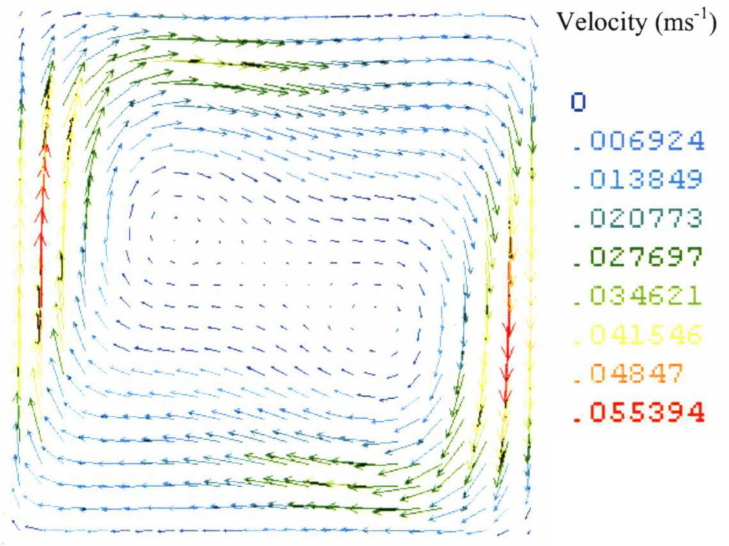

Figure 4.3 Velocity vectors for buoyancy driven flow.

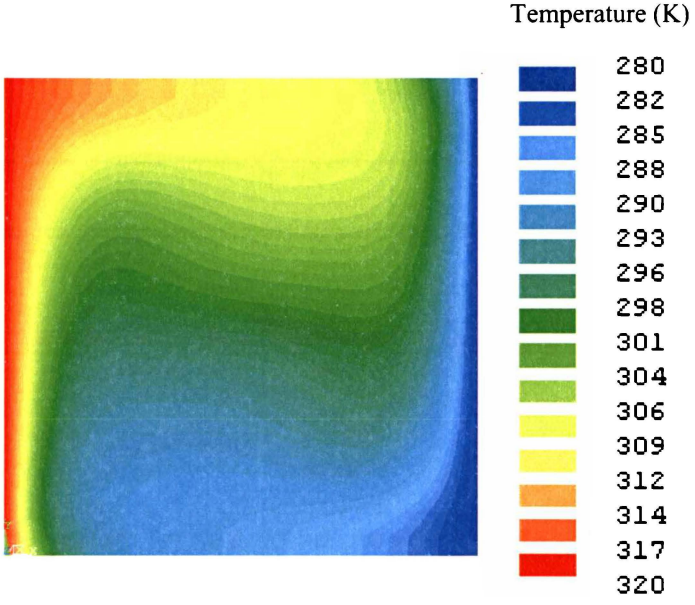

Figure 4.4 Temperature solution for buoyancy driven flow.

4.3.2 Heat Exchanger

The counter-flow heat exchanger example uses the multiple species feature but does not activate the multiple species solution option. Fluid "region one" uses properties of species A (i.e. mass fraction of A is set to 1) and "region two" uses properties of species B. Heat moves from the higher temperature in region one to the lower temperature in region two (Figure 4.7).

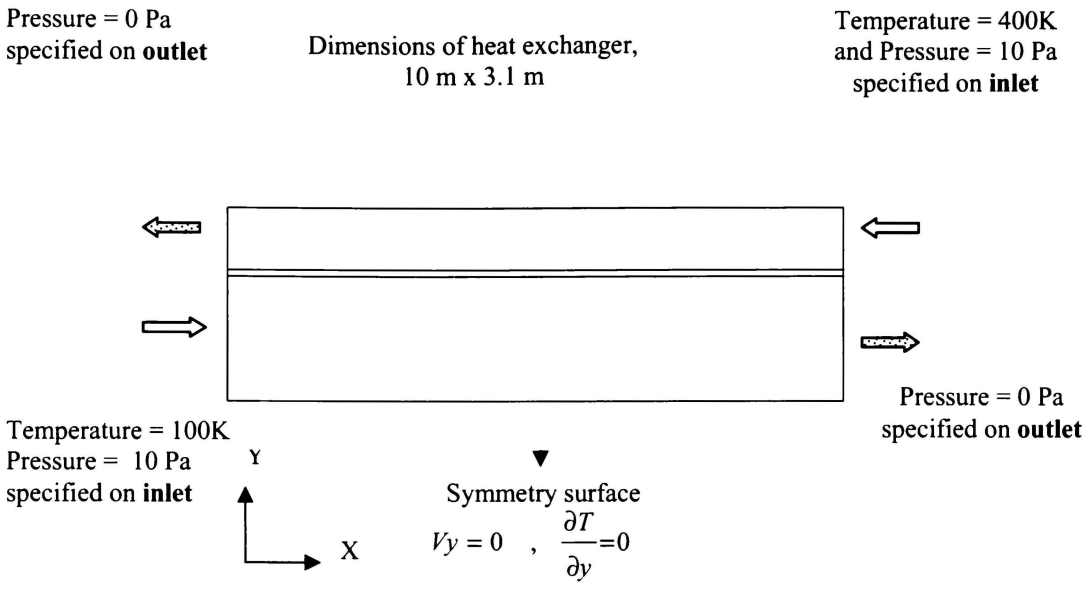

Figure 4.5 Modelling conditions for a conventional, counter flow heat exchanger.

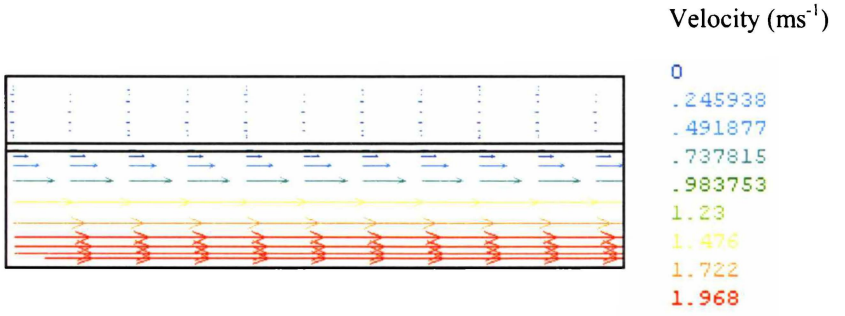

Figure 4.6 Velocity vectors for heat exchanger.

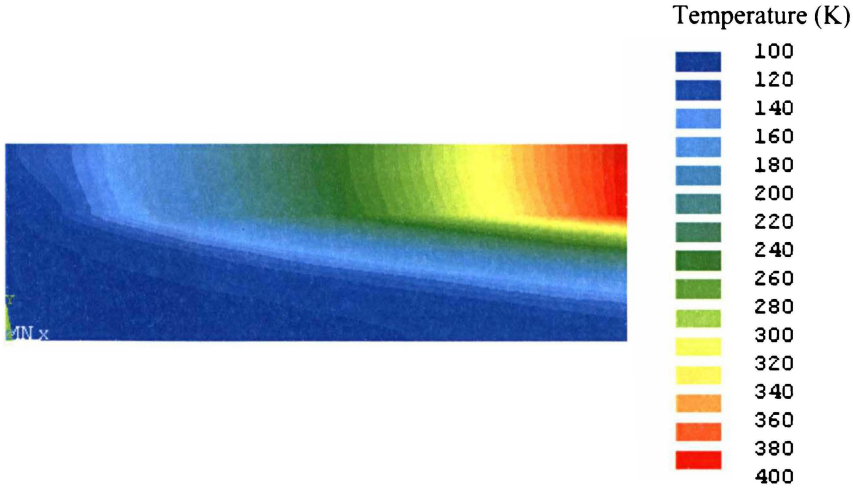

Figure 4.7 Temperature solution for heat exchanger.

4.3.3 Multiple Species

The multiple species ANSYS® module allows up to six species to be tracked in a mix of fluids. In this example, three gases at different temperatures are mixed and the solution shown as mass fraction distributions of these gases throughout the modelled domain (Figure 4.9 and 4.10). The influence of the individual gases on temperature and velocity field (Figure 4.11) can be studied.

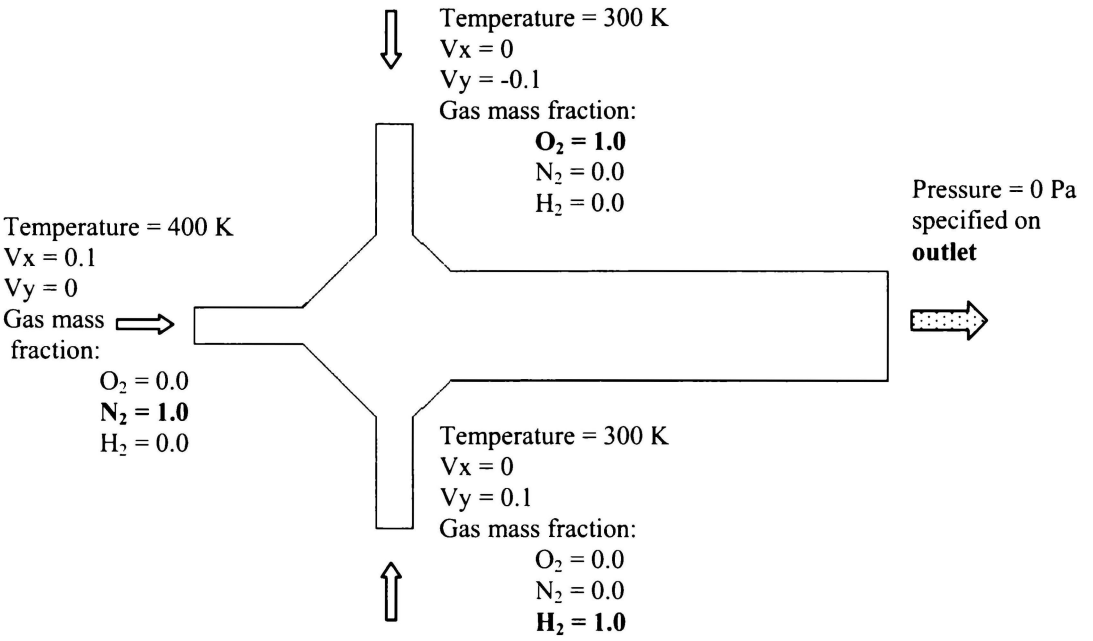

Figure 4.8 Diagram illustrating modelling conditions for analyssing three mixed gases; oxygen (O_2), nitrogen (N_2) and hydrogen (H_2).

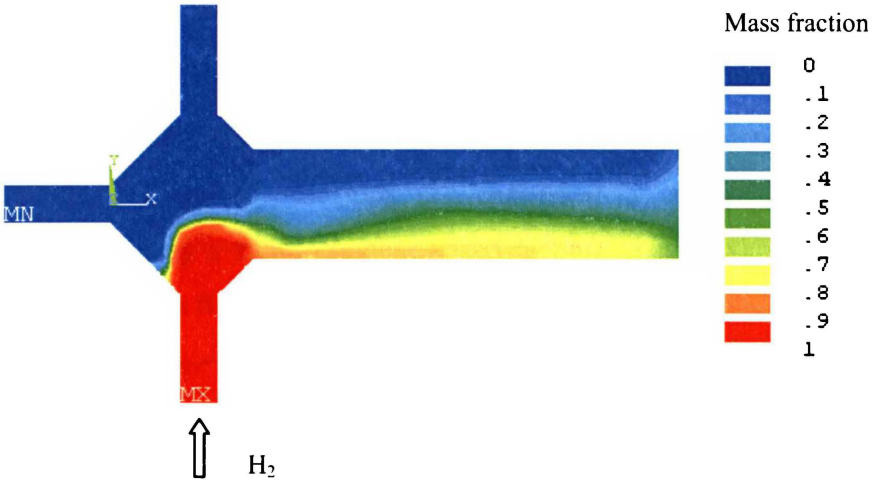

Figure 4.9 Mass fraction of hydrogen in the gas mixture.

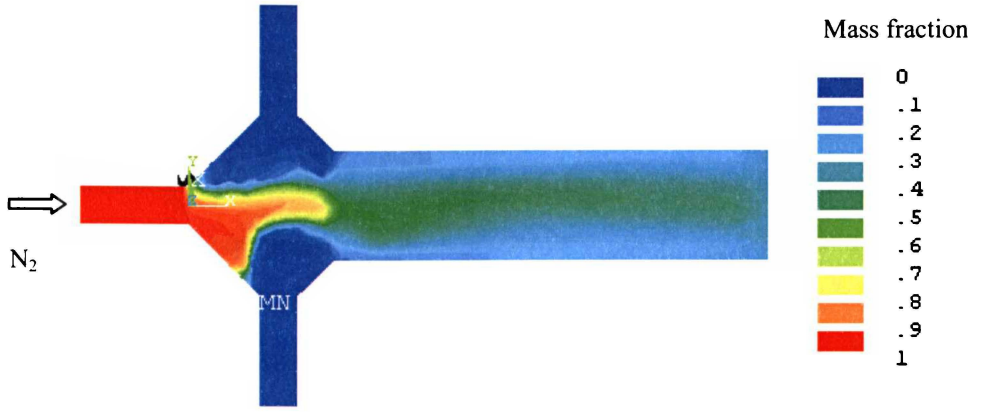

Figure 4.10 Mass fraction of nitrogen in the gas mixture.

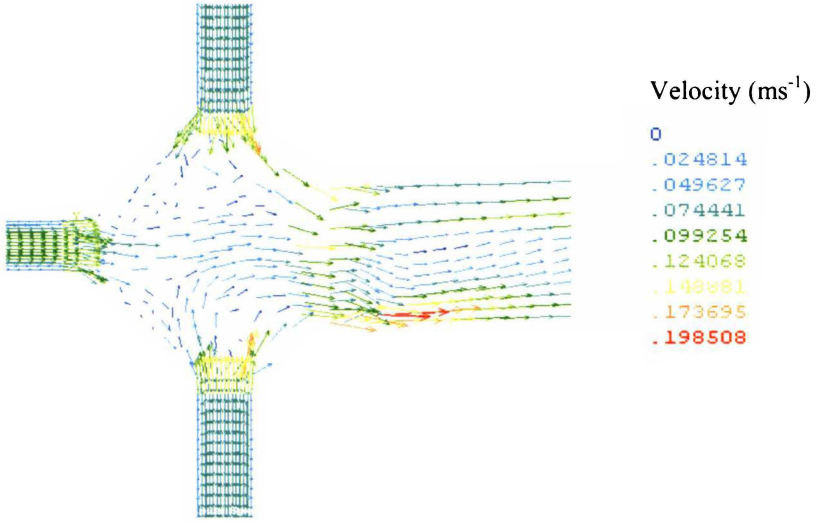

Figure 4.11 Velocity vectors for the mixed gases (magnified).

4.3.4 Modelling Equations

ANSYS® uses the laws of conservation of mass, momentum and energy to solve fluid-flow problems. These relationships are expressed as partial differential equations and discretised by a finite element based technique. ANSYS® uses the following assumptions about the fluid and the analysis:

1. Newtonian fluid behaviour
2. Single phase
3. The problem domain (geometry) remains constant
4. The problem type is uniformly of each component either laminar or turbulent, and either incompressible or compressible.

The fundamental equations in ANSYS®/FLOTRAN relevant to this research are given in Appendix D2. The equations are solved using a solution algorithm with a complete pass through all the equations, referred to as a global iteration (Table 4.2). The algorithm consists of:

1. Approximate solution for each momentum equation in a sequential fashion
2. Solving the pressure equation
3. Calculating velocities to conserve mass
4. Solving the energy equation
5. Updating the laminar properties
6. Solving the turbulence equations
7. Updating the turbulent properties.

Table 4.2 Global iteration structure[3]

SOLUTION ALGORITHM
Formulate – Solve VX equation approximately – Calculate $\hat{V}_x$
Formulate – Solve VY equation approximately – Calculate $\hat{V}_y$
Formulate – Solve VZ equation approximately – Calculate $\hat{V}_z$
Formulate pressure equation using $\hat{V}_x$, $\hat{V}_y$ and $\hat{V}_z$
Solve pressure equation for relative pressure (PRES)
Update velocities based on $\hat{V}_x$, $\hat{V}_y$, $\hat{V}_z$ and relative pressure
Formulate – Solve energy equation for temperature (TEMP)
Solve species transport equations
Update temperature dependent properties
Solve turbulence equations for ENKE and ENDS*
Update Effective Properties based on Turbulence Solution
Check Rate of Change of the Solution (Convergence Monitors)
End of Global Iteration

* Not defined in this chapter.

4.4 Verification Cell Model

This section explains the modelling procedure in detail, beginning with a description of the modelling parameters. Cell geometry or modelling domain and geometry variations with respect to design parameters, is given and material property data, the approach to meshing the domain, and properties of the FLOTRAN element type, Fluid141, are reviewed. The model loading (boundary) conditions and deriving heat transfer coefficients for the external surface of the verification cell are presented.

4.4.1 Modelling Parameters and Assumptions

Parameters (variables) and conditions that affect accuracy of modelled (numerical) results can be categorised as those that influence the computer model and physical model and those specific to the computer model. These categories need clarification so data from the computer-model (i.e. predictions) and experimental rig (empirical) can be rigorously assessed. The following factors influence the physical verification cell and the computer model:

- Design variables — additions and variations to geometry
- Operating variables — fuel flow and start up procedure
- Materials and material properties — fuel, air, stainless steel and insulation; thermal conductivity, density, etc.
- Environment — air flow and temperature around the verification cell
- Initial conditions — temperature, pressure

The computer model is also influenced by:

- Model loads — temperatures, velocities (walls) and pressures
- Element selection — fluid, thermal, etc
- Mesh properties — size, shape and quality
- Solver selection, convergence criterion and number of iterations
- Problem type — laminar, compressible, thermal, etc

The complex phenomena occurring during combustion (see Chapter 2). The physical flame properties include non-linear behaviour of mass, and heat transfer with

increasing temperature. The confined space where combustion is occurring introduces large uncertainties in modelling the heat generation at the source. Because of these inherent complexities, four significant simplifications are made in the verification cell model:

1. The heat generation zone when combusting hydrogen in air is approximated by two empirical relationships:
   a) flame area in quiescent air is a function of fuel flow (from photographic data),
   b) flame area is a function of temperature and fuel flow (from thermocouple data).
2. The Thermal – Mass Flow model solves for mixed convection uses properties of air for the fluid region as this approximates the gas mixture.
3. Disturbance in gas flow due to internal thermocouples, thermocouple-insulating tubes, and friction from component walls is neglected (i.e. assumes that overall impact on flow area in a laminar flow system is negligible).
4. The effect of radiation on temperature profile is not coupled with the Thermal – Mass Flow model.

Progress has been made to address properties of reactant and product gases (assumption 2) and to include radiation (assumption 4) as additional sub models (modules). These are called the Multiple Species Module and Radiation Module respectively, and are presented in Section 4.5. Preliminary results are presented in Chapter 6.

It is difficult to include fine geometrical detail, such as internal thermocouples, because model complexity increases. Even if successful, significant meshing errors can be introduced. Also, because the thermocouples were arranged in a non-symmetrical radial configuration, they could not be modelled axisymmetrically in two dimensions.

4.4.2 Geometry and Problem Domain

Models within ANSYS® can be built manually (direct generation) or by importing a geometry created in a computer aided design (CAD) program such as Pro/Engineer[4]

or SolidWorks®.[5] To build a solid model the geometric boundaries and size and type of the elements. Nodes and elements within the specified domain are automatically done within ANSYS®. Simulating larger, complex solids uses primitives (areas and volumes), Boolean operators between primitives, and advanced computational geometry algorithms. However, for direct generation, node location and size, type and connectivity of every element is generated manually. In this research, a combination of solid modelling, and direct generation approaches were used.

Figure 4.12 is the two dimensional representation of the verification cell (modelled domain) with component labels and abbreviations used in the batch file codes (Appendices D4 to D8). Because of rotational symmetry about the y-axis, only half the cross section is required to describe the model.

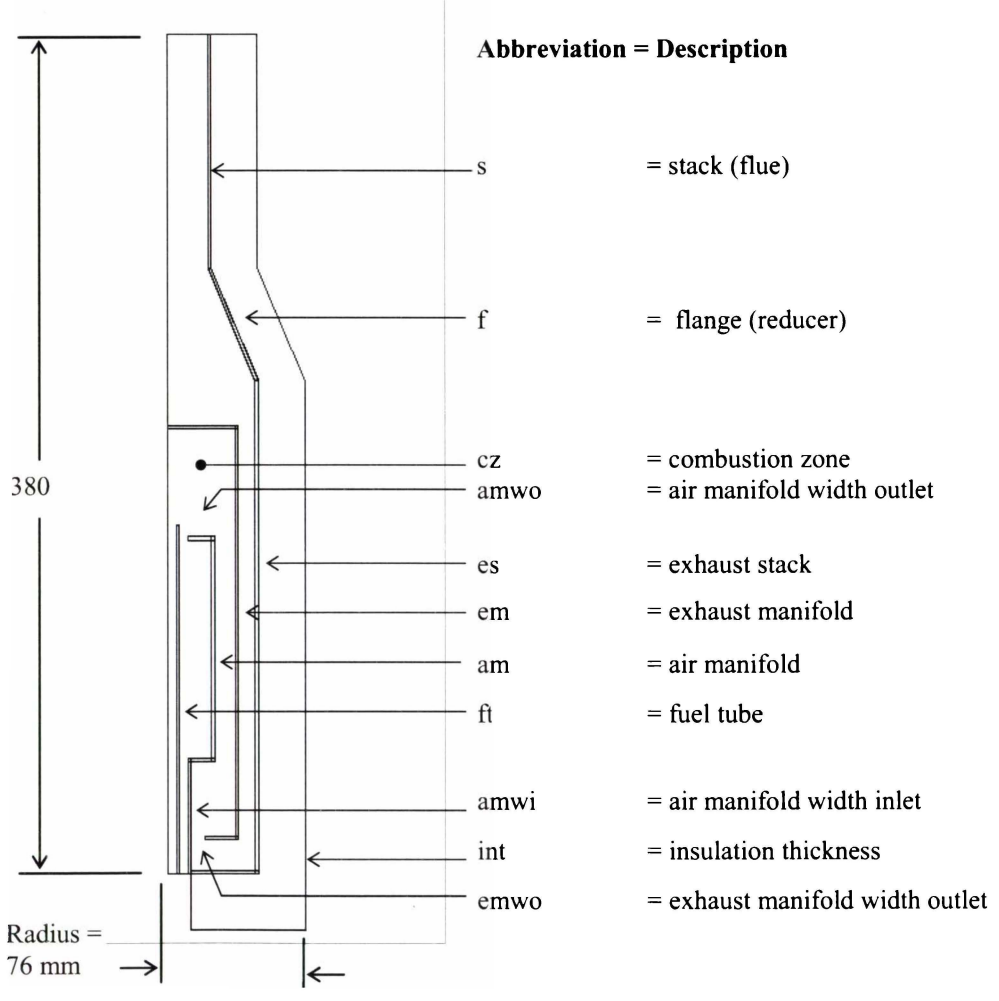

Figure 4.12 Verification cell geometry and modelling code abbreviations. (Abbreviations used in the batch files are listed in Appendix D3).

Various configurations for the physical model (Figure 4.13) were tested. Geometric changes easily generated. For example, only two parameters, *sh* (stack height) and *sw* (stack width) are required to describe the flue (Figure 4.13a-b). These can be changed independently. A new parameter, *int,* had to be coded into the batch file to account for insulation thickness. Alternatively, the insulation region could be removed and a low heat transfer coefficient boundary condition applied at the external boundary. This reduces computational solving time but extra information about the temperature profile through the insulation is not obtained.

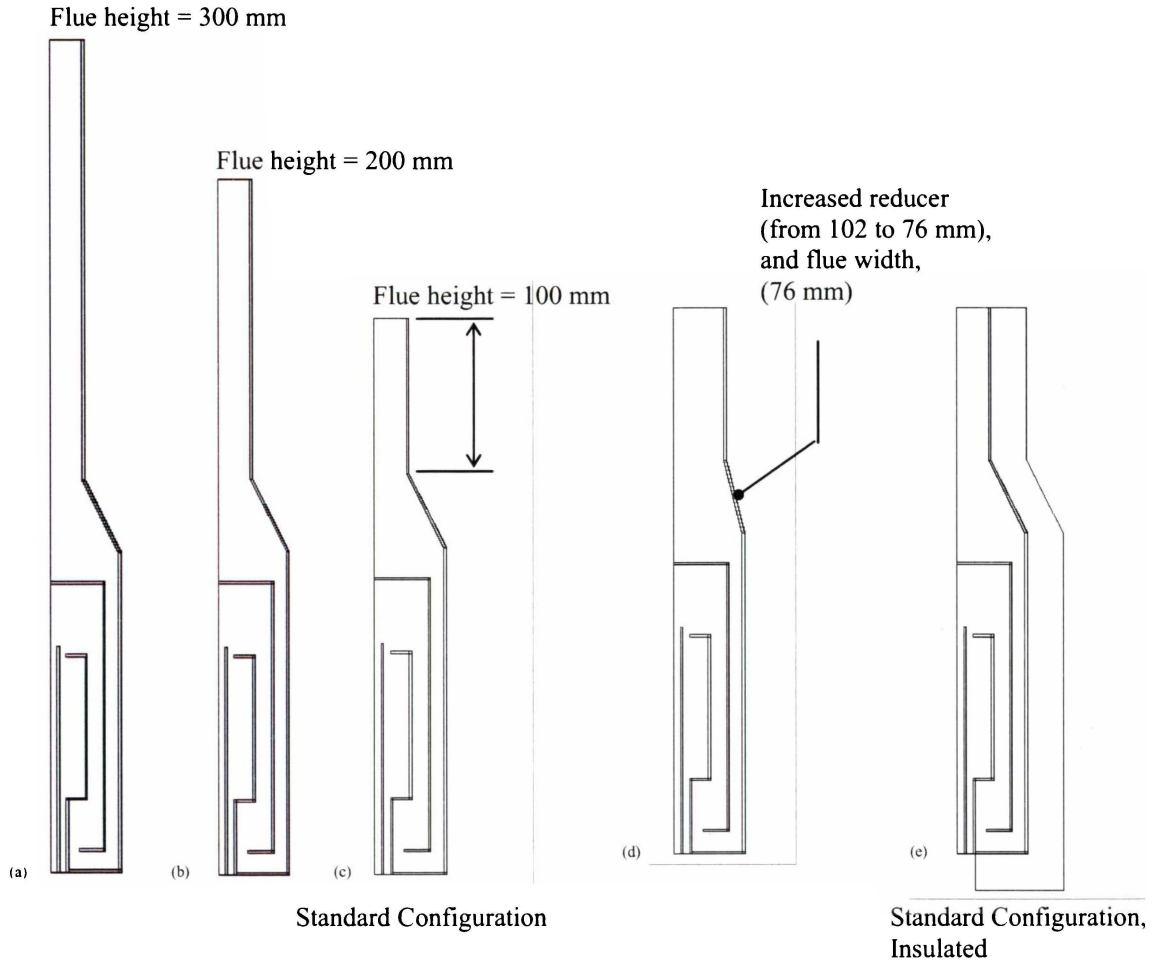

Figure 4.13 Various configurations used in the modelling; a) standard configuration (SC) with 200-mm flue extension, b) SC with 100-mm flue extension, c) SC, d) SC with flue width (reducer width) increased from 102-51 mm to 102-76 mm, and e) SC with 25-mm of insulation.

4.4.3 Material Properties

Properties of the components (Table 4.3) and the gases (Table .4.4) are needed for the simulation. Sutherlands Formula[6] (Equation 4.2) was used to predict the temperature-dependent values for thermal conductivity and air viscosity.

$$Y = \frac{C_1 T^{\frac{3}{2}}}{T + C_2} \tag{4.2}$$

where Y is the thermal conductivity or viscosity, C_1 and C_2 are equation coefficients, and T is the absolute temperature.

Table 4.3 Material properties data for modelling

Material (Property)	Value		Units	Reference
Stainless steel				7, 8
Density	7500		kg m^{-3}	
Thermal Conductivity	15	(298K)*	W K^{-1} m^{-1}	
	25	(773K)	"	
Heat Capacity	500		J kg^{-1} K^{-1}	
Emissivity	0.75			
Kaowool®				9
Density	250		kg m^{-3}	
Thermal Conductivity	0.07	(298K)*	W K^{-1} m^{-1}	
	0.07	(473K)	"	
	0.09	(673K)	"	
	0.12	(873K)	"	
	0.15	(1073K)	"	
	0.19	(1273K)	"	
Heat Capacity	1000		J kg^{-1} K^{-1}	
Air				10
Density	1.2		kg m^{-3}	
Heat Capacity	1004		J kg^{-1} K^{-1}	
Thermal Conductivity	C_1= 2.502E-3		W K^{-1} m^{-1}	
	C_2=194.44			
Viscosity	C_1= 1.4592E-6		kg m^{-1} s^{-1}	
	C_2=110.56			

*Temperature and material property data tables were used for thermal conductivity, which defines the thermal conductivity as a linear function of the temperature, between data points
Material property data is for standard temperature and pressure.

Table 4.4 Gas properties data for modelling

Temperature (K)	300	400	500	600	700	800	900	1000	1200	*Ref.
Air										11
ρ	1.177	0.883	0.705	0.588	0.503	0.441	0.393	0.352	0.295	
C_p	1.006	1.014	1.030	1.055	1.075	1.098	1.121	1.142	1.179	
k	0.026	0.034	0.040	0.047	0.052	0.058	0.063	0.068	0.078	
μ (E-06)	18.46	22.86	26.71	30.18	33.32	36.25	38.99	41.52	46.90	
Hydrogen										12
ρ	0.081	0.061	0.048	0.040	0.036	0.030	0.027	0.024	0.020	
C_p	14.31	14.48	14.52	14.55	14.61	14.70	14.83	14.99	15.37	
k	0.183	0.226	0.266	0.305	0.342	0.378	0.412	0.448	0.528	
μ (E-06)	0.896	1.082	1.264	1.424	1.578	1.724	1.865	2.013	2.262	
Oxygen										
ρ	1.284	0.962	0.770	0.641	0.550	0.481	0.430	0.385	0.321	12
C_p	0.920	0.942	0.972	1.003	1.031	1.054	1.074	1.090	1.115	
k	0.027	0.033	0.041	0.047	0.053	0.059	0.065	0.071	0.082	
μ (E-06)	20.72	25.82	30.33	34.37	38.08	41.52	44.72	47.70	53.25	
Nitrogen										
ρ	1.123	0.843	0.674	0.562	0.481	0.421	0.374	0.337	0.281	12
C_p	1.041	1.045	1.056	1.075	1.098	1.122	1.146	1.167	1.204	
k	0.026	0.033	0.039	0.045	0.050	0.055	0.060	0.065	0.076	
μ (E-06)	17.82	22.04	25.77	29.08	32.10	34.91	37.53	39.99	44.53	
Water vapour										
ρ		0.554	0.441	0.365	0.314	0.274				12
C_p		2.014	1.985	2.026	2.085	2.152				
k		0.026	0.034	0.042	0.051	0.060				
μ (E-06)		13.44	17.04	20.67	24.26	27.86				

Units: ρ (kg m^{-3}), C_p (J kg^{-1} K^{-1}), k (W K^{-1} m^{-1}), μ (kg m^{-1} s^{-1}),
*Ref. = Abbreviation for data reference.

The air density and viscosity in the model are set to vary with temperature but other properties are held constant. Only density is allowed to vary for the other gases.

4.4.4 Elements and Meshing

The Fluid141 element is the main element used in this research. Element shape is either quadrilateral with four nodes or triangular with three nodes. Degrees of freedom (DOF) include fluid velocity components, pressure, temperature, turbulent kinetic energy, turbulent energy dissipation, and fluid/gas mass fractions.

A mapped meshing procedure was used to ensure a consistent shape and number of elements in the 1.65-mm thick verification cell walls. This produced a high quality mesh. The free meshing option used for the gas and insulated regions is suitable for complex geometries but the mesh usually has lower quality than mapped meshes.

The hierarchy for assembling the model indicates which entities must be created first (from top), or deleted first (from bottom). This hierarchy is used to revise a model. The decreasing hierarchy of entities was:

1. Keypoints (and solid-model point loads, see Section 4.4.5), which allow mesh at corners in the model domain to be solved
2. Lines (and solid-model line loads)
3. Areas (and solid-model surface loads)
4. Volumes (and solid-model body loads)
5. Nodes (and nodal loads)
6. Elements (and element loads).

Aspects of the meshing operation including creation of keypoints, lines with divisions for mapped mesh, and free meshed areas are shown in Figure 4.14.

4.4.5 Boundary Conditions and Loads

Once the model domain is meshed, conditions describing the model's environment (which include boundary conditions and internally or externally applied forcing functions) are applied as loads. Four of the six ANSYS® forcing functions (DOF constraint, forces, surface loads, body loads, inertia loads, coupled-field loads) were used to simulate conditions in the verification cell (Table 4.5). The following values were used in the simulations:

fv = 0.1, 0.19, 0.29 and 0.38 ms^{-1} (400, 800, 1200 and 1600 mol min^{-1} at STP)

ft = 800 to 1400 K

htc = 5 to 10 $Wm^{-2}K^{-1}$

hg = 25E+6 to 35E+6 Wm^{-3}.

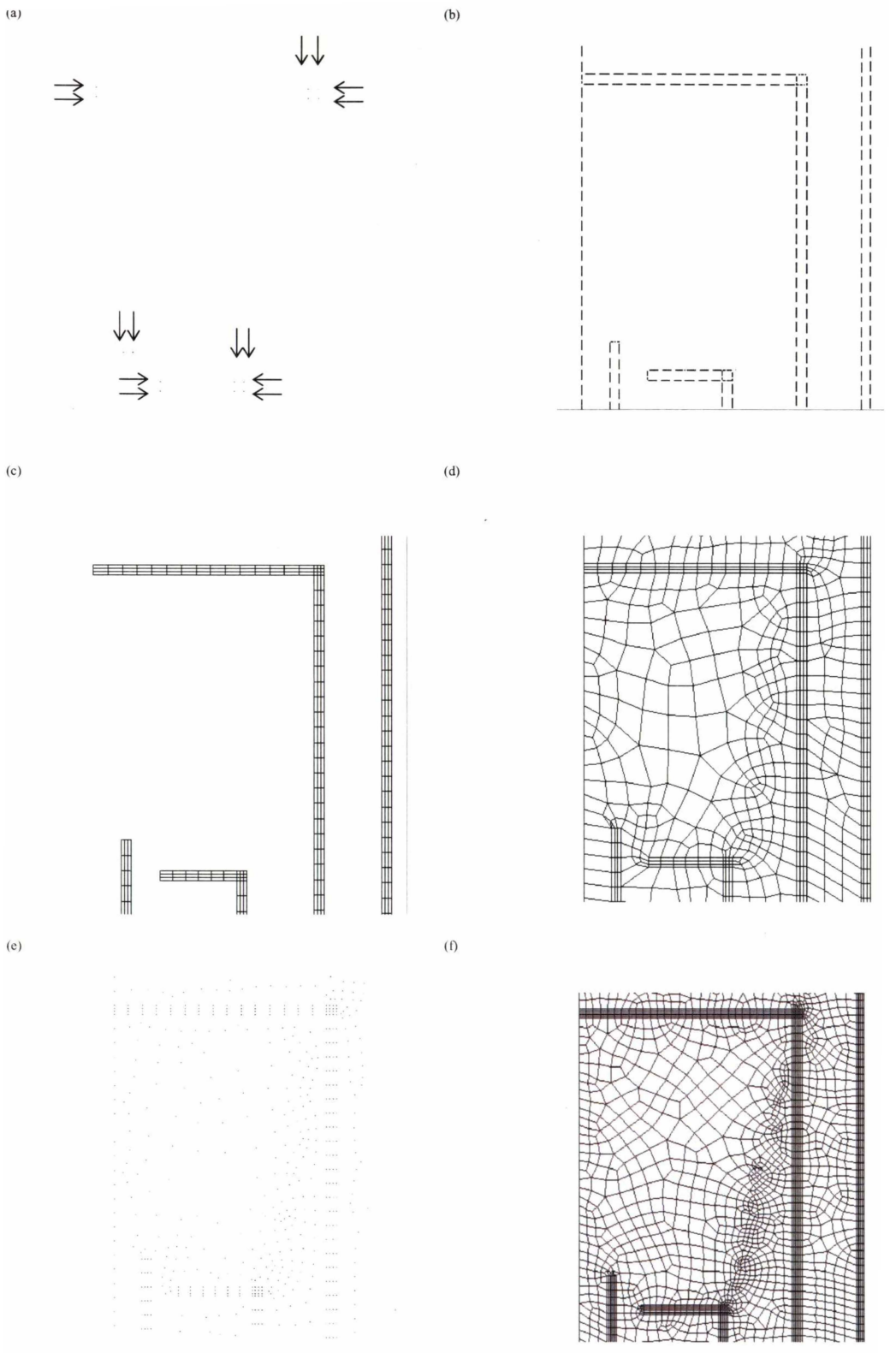

Figure 4.14 Meshing operation at the combustion zone, a) keypoints (arrows highlight keypoints), b) line with divisions, c) mapped mesh, d) free mesh, e) nodes, and f) refined mesh.

Table 4.5 Modelling loads

Category	Load	Component location	Parameter		Unit
DOF constraint	Velocity	All component walls	Vx,Vy	= 0	ms^{-1}
		Symmetry (Y-axis)	Vx	= 0	ms^{-1}
		Fuel flow, air inlet	Vy	= fv	ms^{-1}
	Temperature	Combustion zone		= ft	K
Surface loads	Film coefficient	External surface		= htc	$W\ m^{-2}\ K^{-1}$
	Pressure	Exhaust outlet		= 0	Pa
		Exhaust inlet			
Body load	Heat generation	Combustion zone		= hg	$W\ m^{-3}$
Inertial load	Grav. acel.	All		= 9.81	ms^{-2}

Vx,Vy, velocity component in x and y directions, fv = flame velocity, ft = flame temperature, htc = heat transfer coefficient (film coefficient), hg = heat generation, and grav. acel.= gravitational acceleration.

A heat transfer coefficient (or heat flux) at the boundary is required to model the effect of the surroundings on the non-insulated and insulated verification cell. The verification cell is in still air and external cooling is from natural convection. The variables used for solving the equations for natural convection problems are presented in Table 4.6.

Table 4.6 Variables for solving natural convection problems

Symbol	Variable	Dimensions*
L	Significant length	L
ρ	Fluid density	ML^{-3}
μ	Fluid viscosity	MLt
C_p	Fluid heat capacity	$Q(MT)^{-1}$
k	Fluid thermal conductivity	$Q(LtT)^{-1}$
β	Fluid coefficient of thermal expansion	T^{-1}
G	Gravitational acceleration	Lt^{-2}
ΔT	Temperature difference	T
H	Heat-transfer coefficient	$QL^{-2}(tT)^{-1}$

* L, M, Q,T,t, are dimensions of length, mass, energy, temperature and time.

Two methods can be used to calculate the heat transfer coefficient:

1. Dimensionless relations, (Equations 4.3 and 4.4),
2. Dimensionless equations, (Equations 4.9 and 4.11).

The dimensionless Nusselt number (Nu) is the ratio of conductive to convective thermal resistance of the fluid (gas) and incorporates the Prandtl number (Pr), which is the ratio of momentum and thermal diffusivities, and the Grashof number (Gr), which is the ratio of buoyancy and viscous forces in a free-convection flow system:

$$Nu = f(Pr, Gr) \tag{4.3}$$

$$Pr = \frac{C_P \mu}{k} \tag{4.4}$$

$$Gr = \frac{G\beta\rho^2 L^3 \Delta T}{\mu^2} \tag{4.5}$$

where Cp, μ, k, etc are defined in Table 4.6. The temperature difference (ΔT) is between the surface of the verification cell (t_s) and the surrounding air (t_∞). Fluid properties used in solving Equations 4.4 and 4.5 are evaluated at $t_f=(t_s+t_\infty)/2$, and $\beta=t_\infty+t_f$ for $t_\infty<t_s$ (indicating the surface is hotter than the surrounding air).

The heat transfer coefficient is influenced by the flow field and the effect of surface geometry heat transfer is described in standard texts.[12-16] A vertical cylinder of height L, and diameter D, may be considered as a vertical flat plate if:[13]:

$$\frac{D}{L} \geq \frac{35}{Gr^{0.25}} \tag{4.6}$$

The Rayleigh number (Ra=Gr.Pr) indicates which variation of the Nusselt equation to use for calculating the heat transfer coefficient. Alternatively, the Rayleigh number can be used to select experimentally determined coefficients from published tables. Because the verification cell operates in $10^4<Ra<10^9$, Equations 4.7 and 4.12 can be used.

$$\mathrm{Nu} = 0.683\mathrm{Gr}^{0.25}\,\mathrm{Pr}^{0.25}\left[\frac{\mathrm{Pr}}{(0.861+\mathrm{Pr})}\right]^{0.25} \tag{4.7}$$

$$h = \frac{Nu\ k}{L} \tag{4.8}$$

The heat transfer coefficient can be expressed as a function of the Rayleigh number using coefficients a and m (Equation 4.9). The values of the coefficients for conditions used in this research are m=0.25 and a = 0.59.

$$\mathrm{h} = \frac{\mathrm{ka(Ra)^m}}{\mathrm{L}} \tag{4.9}$$

The following simplified equation can be derived from Equation XXX. For air, water and organic liquids, b=1.37:

$$\mathrm{h} = \mathrm{b}(\Delta\mathrm{T})^{\mathrm{m}}\,\mathrm{L}^{3\mathrm{m}-1} \tag{4.10}$$

Equation 4.11 is an alternative for Equation 4.10. In this case, b = 1.42,

$$\mathrm{h} = 1.42\left(\frac{\Delta\mathrm{T}}{\mathrm{L}}\right)^{0.25} \tag{4.11}$$

For air, O_2, H_2, CO and many other inert gases, Pr is approximately constant at 0.7, even at temperatures of up to 1900K. Therefore, Equation 4.12 can be applied to calculate the Nu number of gases. Equation 4.8 can then be used to calculate h.

$$\mathrm{Nu} = 0.477\mathrm{Gr}^{0.25} \tag{4.12}$$

Table 4.7, compares the values of Pr, Gr, Nu and h calculated using Equations 4.7 to 4.12, for the conditions used in this research.

Table 4.7 Heat transfer coefficient – calculations for vertical surface in air

$T_{surface}$(K)	300	400	500	600	700	800	900	1000
$T_{fluid\ properties}$	300	350	400	450	500	550	600	650
β	0.0034	0.0029	0.0025	0.0022	0.0020	0.0018	0.0017	0.0015
ρ	1.1774	0.998	0.8826	0.7833	0.7048	0.6423	0.5879	0.4530
k	0.0262	0.030	0 0.0336	0.0370	0.0403	0.0436	0.0466	0.0495
μ (E-05)	1.9	2.1	2.3	2.5	2.7	2.9	3.0	3.2
Pr	0.708	0.697	0.689	0.683	0.68	0.68	0.68	0.682
Gr (E+08)	0.603	4.49	4.89	4.29	3.58	2.96	2.42	2.01
Nu (Eq.(4.7)	45.25	74.27	75.54	72.89	69.55	66.32	63.08	60.23
Nu (Eq.4.12)	42.03	69.42	70.92	68.66	65.63	62.58	59.52	56.77
h (Eq. 4.8)	2.96	5.58	6.35	6.75	7.02	7.23	7.35	7.46
h (Eq. 4.8)	2.76	5.21	5.97	6.36	6.63	6.82	6.93	7.03
h (Eq. 4.9)	3.13	5.89	6.72	7.15	7.44	7.66	7.79	7.90
h (Eq. 4.10)	2.80	5.54	6.53	7.21	7.74	8.17	8.55	8.88 (b=1.37)
h (Eq. 4.11)	2.90	5.74	6.77	7.47	8.02	8.47	8.86	9.21 (b=1.42)
h (average)	**2.91**	**5.6**	**6.5**	**7.0**	**7.4**	**7.7**	**7.9**	**8.1**

Units: ρ (kg m^{-3}), C_p (J kg^{-1} K^{-1}), k (W K^{-1} m^{-1}), μ (kg m^{-1} s^{-1}), h (Wm^{-2} K^{-1}). Values for constants and variables: L=0.4 m, g = 9.81 ms^{-1}, t_∞=293 K, $T_{fluid\ properties}$ = t_∞+t_f, and constant pressure. Properties data obtained from Holman[11]

When t_s < 400K, the criterion for Equation 4.6 is not fulfilled.

The mean temperatures recorded for the surface of the verification cell were between 400 and 700K. Using Equation 4.10 and data in Table 4.7; the following results were derived when length varied from 0.2 to 0.6 m:

1. L = 0.2, h = 6-9 Wm^{-2} K^{-1}
2. L = 0.4, h = 5-8 Wm^{-2} K^{-1}
3. L = 0.6, h = 5-7 Wm^{-2} K^{-1}.

Radiant heat loss from the external surfaces of the verification cell can be calculated using the radiant heat-transfer coefficient, h_r (Equation 4.13). As temperature increases, heat loss due to radiation increases.

$$h_r = \varepsilon\left[\frac{\sigma\left(T_s^4 - T_\infty^4\right)}{T_s - T_\infty}\right] \tag{4.13}$$

Where ε is the emissivity of the surface, and σ is Stefan-Boltzmann constant.

Overall heat transfer coefficient would therefore be:

$$h_t = h + h_r \tag{4.14}$$

The radiant and total heat transfer coefficients for surface temperatures of 400, 700 and 1000 K, using $\varepsilon = 0.75$ for stainless steel, and T_∞ at 293K, are:

1. T = 400, $\underline{h_r = 7}$ $\quad \therefore \underline{h_t = 13}$ $Wm^{-2} K^{-1}$
2. T = 700, $\underline{h_r = 24}$ $\quad \therefore \underline{h_t = 33}$ $Wm^{-2} K^{-1}$
3. T = 1000, $\underline{h_r = 60}$ $\quad \therefore \underline{h_t = 68}$ $Wm^{-2} K^{-1}$

4.5 Modelling Code: – Batch Files

Batch files are a collection of sub-models or modules related by the solution algorithm (Figure 4.15). In this Section, assumptions for each model and module are reviewed, beginning with the heat generation module because heat generated from combusting hydrogen in air was the most difficult phenomenon to simulate in ANSYS®. Experimental data was used to refine or recalibrate the model so as and examine the effect of other parameters

The effect of design variables was explored using the Thermal – Mass Flow (base) model, which accounts for mass (using properties of air) flow and convective and conductive heat transfer. Other gases such as nitrogen, oxygen, hydrogen and water vapour were used by including the Multiple Species module with the Thermal – Mass Flow model. The influence of gas species on temperature distribution was investigated. The value of data from the Multiple Species option is discussed at the end of this chapter.

The Radiation model was solved using ANSYS® rather than FLOTRAN because FLOTRAN and ANSYS® elements are not compatible. The method used is outlined and the underlying fundamental approach reviewed. However, because of programming constraints (results would not translate between models) the Radiation module was not coupled with the Thermal – Mass Flow model.

Model codes are listed in Appendices D4 to D8. Only the relevant components of the Multiple Species module and the Radiation module are presented.

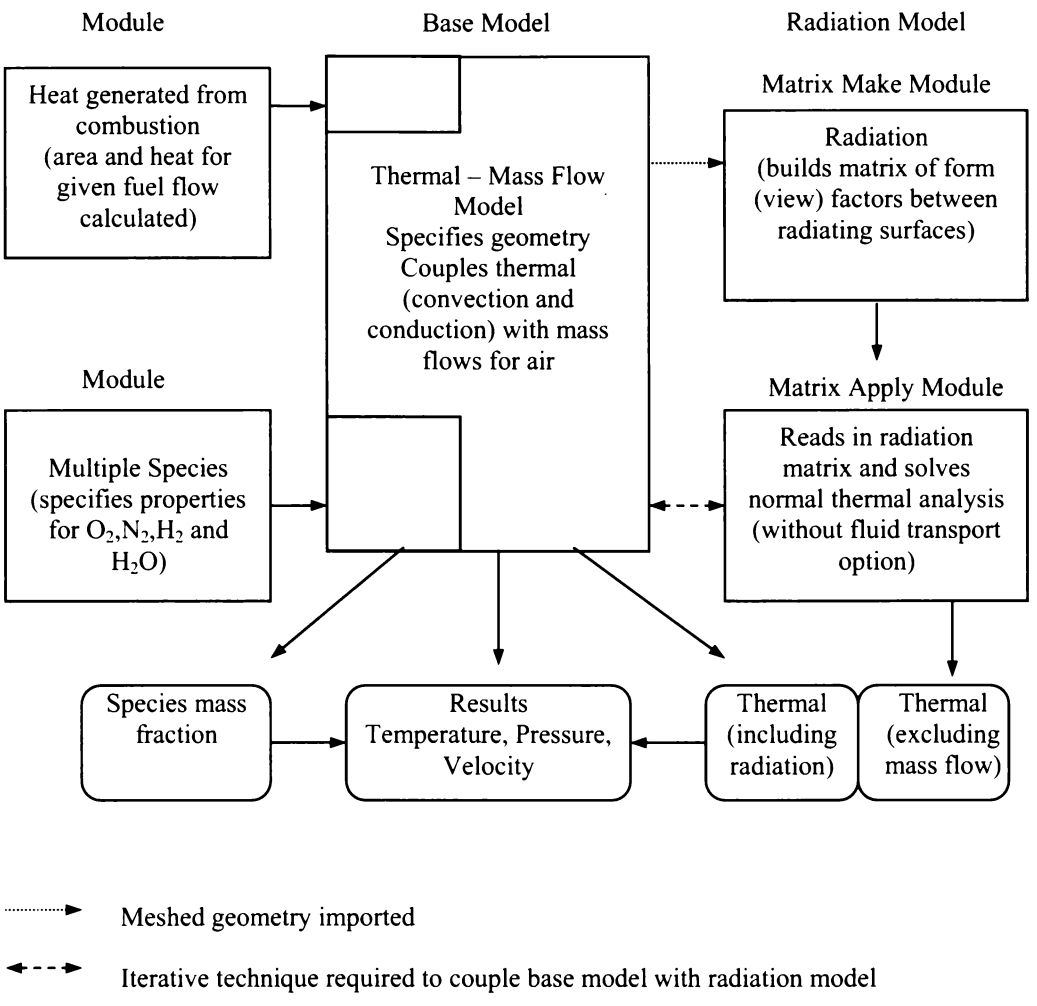

Figure 4.15 Flow diagram for model – module relationships and solution algorithm.

4.5.1 Flame and Heat Generation Module

The flame was modelled to provide an initial approach for including the flame in the verification cell and to determine limitations of the modelling software (Figure 4.6).

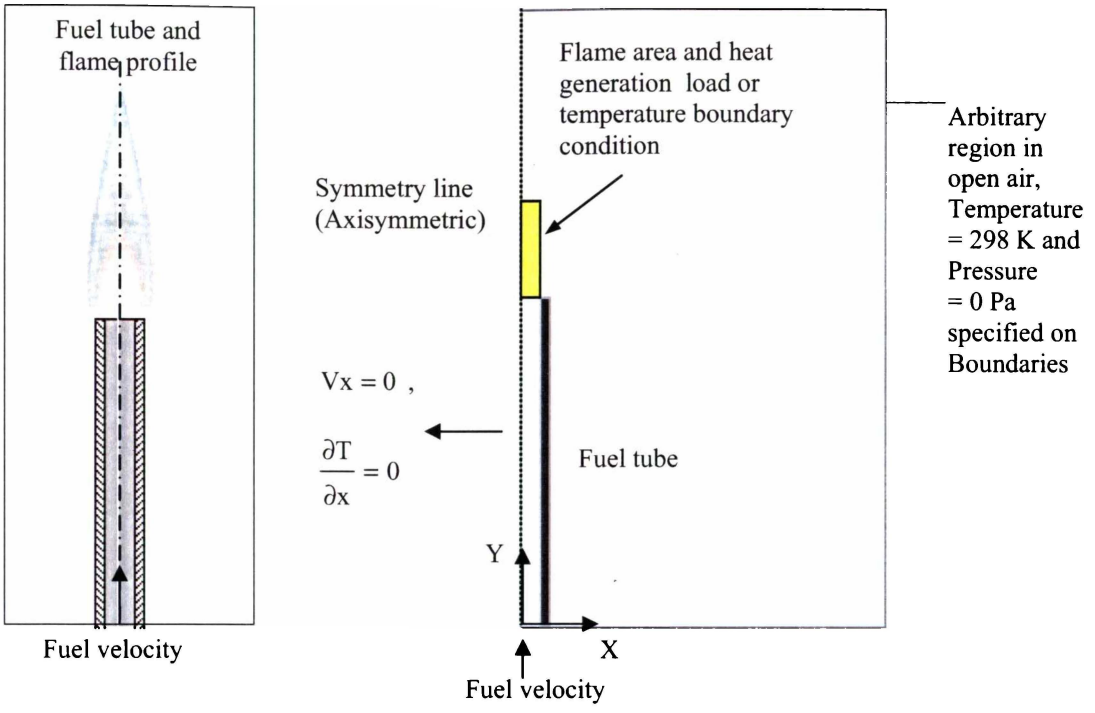

Figure 4.16 Flame profile and modelling loads for a 2D axisymmetric model of a hydrogen-air flame.

In the ANSYS® model, heat generated (heat source) from combusting hydrogen in air required a heat generation value (Wm^{-3}, or $Js^{-1}m^{-3}$). The heat originates in the combustion zone from the fuel tube (essentially an integrated burner). Data on the rate hydrogen is consumed (volume per second) and the ideal gas law can be used to calculate the theoretical maximum heat rate (enthalpy) generated. The approach taken, including the equations written into the code, by *{in brackets and italicised} is as follows:* . The abbreviations for the equations are given in Appendix D3.

1. Fuel flow rate is converted to fuel velocity (ms^{-1}):

   ((fuel flow)/((π*ftw^2)(60E+6))) (4.15)

2. Volume of hydrogen gas per second is calculated by multiplying fuel velocity by fuel tube area (m^3):

   (fv(π*ftw^2), or ((fuel flow)/(60E+6)) (4.16)

3. Theoretical maximum heating rate is derived from volume of hydrogen gas, enthalpy of reaction forming water or combusting hydrogen in air[17] (derived in Chapter 2), and the ideal gas law:

   *{HGG=(V*P)/(R*T))*H*Ce}* (4.17)

where *Ce* is a calibration factor (combustion efficiency).

4. Flame profile is simplified to a cylindrical volume and used in the 2D model using a height (czh) and a width (czw) obtained from empirical Equations 5.2 and 5.3.

   $$czh = 0.0883(fv) + 0.0044 \quad (5.2)^*$$

   $$czw = 0.0196(fv) + 0.0109 \quad (5.3)^*$$

Equation 5.2 is valid when fuel velocity <0.5 ms^{-1}. At greater flow rates, the heat generation area is above the exhaust manifold and this approximation not valid.

5. Equation 5.3 is multiplied by 0.5 to get the approximate flame radius:

   *{czw=((0.0196*fv)+0.0109))*0.5}* (4.18)

6. As the model is axisymmetric, the applied flame area is represented by a volume equal to:

   *{HGAA=(Pi*czw**2)*czh}* (4.19)

7. The product of the reciprocal of the representative volume and the theoretical maximum heat into the system gives the heat generation value to use in the model:

   *{HG=(1/HGAA)*HGG}* (4.20)

An alternative approach for modelling heat generation is to apply a temperature constraint in the approximated flame area (i.e. constrains the temperature to a specific value), which gives the following relationship:

---

* Equations (5.1), (5.2) and (5.3) are derived in Chapter 5 from experimental data.

$$T_F = -4913(fv^2) + 4003(fv) + 281 + 273.15 \qquad (5.1)^*$$

The data from several ways to model the flame profile (heat source) as a function of fuel velocity (fuel flow rate) are given Section 6.3. The following approaches were used:

1. The heat generation rate, derived from Equation 4.2, was applied to a fixed and to a calculated flame area (using Equations 5.2 and 5.3).
2. The heat generation rate over a fixed and a calculated flame area was decreased by 10% per 10% of flame dimension, from the centre-bottom up and outwards (Section 6.2).
3. The fixed temperature (DOF) constraint (Equation 5.1) was applied to a fixed and a calculated flame area (Equations 5.2 and 5.3).

These approaches were first applied in a flame study (Section 6.3) to determine validity of the simple flame model. The same flame model was then applied to the combustion zone in the verification cell.

4.5.2 Thermal – Mass Flow Model

The effect of the following variables on the verification cell were investigated:

- Compressible fluid — allowed density variations resulting in buoyant flows
- Laminar flow — low fuel velocities, fv = 0.5 ms^{-1}, Re < 430
- Thermal system — losses from system to surroundings included.

The verification cell was considered to be a laminar or mixed – laminar system, with low velocity forced fuel flow and air being drawn through the air inlet by natural convection. The Reynolds (Re) number (Equation 4.21) must be >2300 for the turbulence model. The Re number for hydrogen gas flowing through the vertical fuel tube was calculated to be 430 (298K) and 42 (1200K) at a fuel velocity of 0.5 ms^{-1}. Turbulent conditions occur when fuel velocity is >2.7 ms^{-1} Bossel[18] describes a more detailed approach for natural convection systems that combines the Re and Gr numbers.

$$Re = \frac{\rho \upsilon L_C}{\mu} \tag{4.21}$$

Where υ, is the velocity, μ, is the viscosity and L_c is the hydraulic diameter, D_h, defined by Equation (4.22). For flows in tubes, L is the diameter of the tube:

$$L_C = D_h = \frac{(\text{Cross-sectional Flow Area})}{\text{Wetted Perimeter}} \tag{4.22}$$

Although operating conditions indicate laminar flow behaviour, system geometry may allow turbulence in some regions. Therefore, simulations were done using the turbulent and non-compressible options (Section 6.2).

The steps, including the modelling code format, for the Thermal – Mass flow model were:

/TITLE, VERIFICATION CELL: THERMAL-MASS FLOW MODEL (INSULATED)

KEY
PARAMETERS
Modelling Parameters
Loading Parameters
Design and Operating Parameters (Geometry)

* <<< Heat Generation – (Permanent Module) >>>

MODELLING DOMAIN – GEOMETRY
Boolean Operation – Connects Individual Domains

MESHING
Material Properties (Assign Attributes)
Meshing

LOADS AND BOUNDARY CONDITIONS
Velocity
Thermal

FLOTRAN SETUP AND FLUID PROPERTIES

* <<< Multiple Species Module Inserted Here >>>

EXTRACTION CODE - TEMPERATURES FROM RESULT FILE

FINISH

4.5.3 Multiple Species Module

Incorporating reactant gases flowing into the system and combustion products (e.g. water vapour) improves accuracy for predicting the temperature profile. The initial temperature profile was generated using air properties and then the Multiple Species module was used to calculate mass fraction of each defined species. The temperature profile was then updated after allowing for the effect of thermal and mass flow properties of the species on flow fields (global iteration). Being able to track several different fluids simultaneously could be useful in a SOFC model (Section 4.6).

To simulate chemical species in the verification cell, mass fraction of hydrogen at the fuel inlet is set to 1. Air entering the air manifold is 0.21 oxygen, and 0.79 nitrogen. Combustion products are defined as water vapour/steam (mass fraction 0.5) generated in the combustion zone (Section 6.5).

A single momentum equation is solved for the flow field, with transport equations being solved for each species. The composite mixture (CMIX) analysis option was chosen. The properties used in the solution are calculated from the mass fraction of species as a function of space. Fluid transport is caused by momentum effects, advection and diffusion. The effect of chemical reactions between species was not included in the model.

4.5.4 Radiation Modules

The two Radiation modules use the ANSYS® element Plane55 rather than Fluid141. Because these two elements have identical mesh geometry, results and loads can be compared, transferred or manipulated between models. The Radiation Make Matrix module uses "/AUX12", a radiation matrix generator processor for generalised radiation problems where two or more surfaces are all receiving and emitting radiation (Appendix D9). A matrix of form factors (view factors) between radiating surfaces is generated and then used as a super-element (Matrix50 element type) in a thermal analysis. Hidden and partially hidden surfaces and/or a sink for radiation energy (space node) can be included. Thus, the three steps in the Radiation Make Matrix are:

1. Defining the radiating surfaces
2. Generating the radiation matrix
3. Using the radiation matrix in the thermal analysis.

The Radiation Apply Matrix module implements Step 3.

The hidden surface method was used to generate the super matrix. View factors, including all walls (radiating surfaces) of the verification cell, were then calculated. This involved overlaying the mapped mesh of the component wall (lines) regions with a Link32 element type (2D conduction bar element). The Plane55 element has the disadvantage of not including mass transport. The option that includes heat transfer from mass transport is available but can only be applied to a uniform velocity field (not applicable with this work). A space node (radiation sink) was not included. Instead temperatures of the inlets and outlets were constrained to 293K.

The following is a summary of differences between codes in the Thermal – Mass Flow model and the two Radiation modules:

1. Radiation Make Matrix module.
    - Element types Plane 55 and Link32 replace Fluid141
    - Fluid regions allocated the properties of air as no FLOTRAN set-up, property database or solution are implemented in this module
    - Link32 overlays Plane55 elements on walls (on model lines)
    - With the /AUX12 option activated, the emissivity of walls are used, matrix settings are specified, and the radiation matrix is written to a user specified file.

2. Radiation Apply Matrix module.
    - Element types Plane 55 and Matrix50 replace Fluid141

- Fluid regions allocated the properties of air
- Entire domain meshed with Plane 55 elements
- Read in radiation matrix (super-element, Matrix50)
- Thermal boundary conditions applied, heat generation replaced by temperature constraint above the flame at top of exhaust manifold top (T_F defined by Equation 5.1)
- The static solution solved.

A steady state thermal analysis is solved, with and without the radiation super-element. Data for the effect of the radiation module, over fuel flow velocities of 0.1 to 0.4 ms^{-1}, are compared with experimental and FLOTRAN derived results.

4.5.5 Further Assumptions and Modelling Notes

The following assumptions are also incorporated in the overall model:

- Not all ANSYS® and FLOTRAN commands are interchangeable.
- The radiation heat transfer coefficient is not been included in the Thermal – Mass Flow model.
- Air, hydrogen and steam are assumed to have a negligible effect on radiant heat transfer because there are no carbon or other particulates.
- The tri-diagonal matrix algorithm (TDMA) is used to obtain an approximate solution for the momentum equation and is relaxed to provide a stable solution. Consequently, conservation laws are not enforced.

The following assumptions were also incorporated in the combustion module:

- The effect of confining the flame within the combustion zone was simplified by applying the flame model with an upper fuel velocity limit (0.4 ms^{-1}).
- The Combustion Module does not consider the effect on the enthalpy through preheating fuel and air before combustion, and enthalpy is held proportional to fuel flow rate (241 kJ mol^{-1}).

- The flame has laminar behaviour for the fuel flow rates used.
- The flame is a diffusion flame so heat from the fuel combustion jet is diffusion limited.[19]
- The combustion zone from a SOFC stack is made of several smaller dispersed flames from unutilised fuel at the end of each cell, which produces a short and wide heat generation zone.

The following assumptions were also incorporated in the Thermal – Mass Flow model:

- The effect of losses due to pressure drop are not included because flow rates are low and laminar.
- Empirically-derived flame dimensions are a function of fuel flow rate. The interplay between the combustion module implemented within the verification cell and ANSYS® has not been characterised and was assumed to have a relative effect on temperature profile data for tested fuel flow rates.
- The ideal mesh for flow simulations has regular, quadrilateral elements with smaller elements in regions of high gradients (near walls, in corners and large temperature gradients).
- Temperature-dependent properties are considered constant within elements so a refined mesh will increase accuracy. A poor quality mesh may affect maximum and/or minimum values at specific locations.
- A workable mesh was obtained at the expense of mesh quality, because of the irregular domain.

The following assumptions were also incorporated for the Multiple Species module:

- The variable gas property option was not used, other than for density.
- Air composition (mass fraction of nitrogen and oxygen) was used to demonstrate how species can be tracked in an SOFC.
- Water vapour was applied as a boundary condition in the combustion zone, contrary to ANSYS® methodology, which recommends that boundary conditions should not be applied at internal nodes.

The following assumptions were also incorporated for the Radiation modules:

- The radiation module solves for view factors (i.e. radiation absorbed and emitted) of all steel wall surfaces. However, the view factors do not include radiation from combustion products (i.e. hydrogen-air flame does not emit radiation) so a temperature constraint rather than a localised heat generation was applied to the top of the exhaust manifold.
- Heat transfer through the gas regions due to mass flow is not included because radiation data could not be successfully coupled with the Thermal – Mass Flow model.

The following result/error checks were performed at the end of each run:

- ANSYS® evaluates the mesh quality (element type and mesh properties) and produces a percentage error, with the limitation that error checking is only done on models with one material. Percentage error check was not applicable for models developed for this research.
- Jobname.err, file was used to identify coding errors, Jobname.dbg file was used for checking solution convergence, and Jobname.pfl contains further information on convergence and mass and energy balances.
- Engineering judgement was used to assess relevance and accuracy of data produced by the models.

4.6 Proposed SOFC Stack Model

The proposed SOFC stack model involved coupling a specific temperature profile to performance of an operating SOFC. The first model involved retrofitting the fuel tube with a single SOFC submodel to include the thermal response of an operating (loaded) fuel cell. When the cell is loaded (current drawn), heat produced by the electrochemical reaction and ohmic heating is generated along the length of the cell. At the end of the cell, the amount of heat generated from fuel combustion has decreased directly with the amount of current drawn from the fuel cell. At higher fuel use rates (i.e., increasing fuel is used in the electrochemical reaction), burner temperature will decrease.

The strategy involved indirectly coupling an electrochemical model (custom coded) with the verification cell or finite element (FE) model. Results from each model were used as loads and/or boundary conditions in the other. The custom code can be in C or Fortran programming language and was implemented using the "user routine" option of ANSYS®. An alternative, more direct route is to generate a custom model using the APDL.

An electrochemical model coupled with a FE model was described in Section 2.4. The following approach is similar, with the aim of achieving a more realistic steady-state, start-up temperature distribution before operating the fuel cell. A common approach is to assume uniform temperature across the cell, eliminating the need to determine the actual temperature distribution.

The multiple species option in ANSYS® allows the mass fraction of individual gas species to be tracked along the length of the active cell and within the gas channels. This assists tracking feed gases and product formation and produce data on flow rates and the spacing between cells and within the stack housing. The relationship between cell potential and fuel and oxidant gas compositions at point x along the cell is given in Equation 4.23, where term a represents formation of water and Term b represents hydrogen consumption. The change in hydrogen concentration (X_{H2}) along the length of the cell can be described by a differential equation (Equation 4.24), where $j_{(x)}$ is the local current density:

$$E_N(x) = -\frac{\Delta G^o}{2F} - \frac{RT}{2F}\ln\left(\frac{N_{H2Oa,in} + \frac{I(x)}{2F}}{N_{H2a,in} - \frac{I(x)}{2F}}\right) + \frac{RT}{4F}\ln(p_{O2c}) \qquad (4.23)$$

$$\frac{dX_{H2}}{dx} = \left(\frac{1}{N_{H2}}\right)\left(\frac{j_{(x)}}{2F}\right) \qquad (4.24)$$

The electrolyte must be above a given temperature to have sufficient ionic conductivity and is important for practical reasons because damage to the fuel cell

may occur if current is drawn before a uniform temperature is achieved (which is another reason for knowing and assigning the initial temperature distribution).

A solution algorithm for the proposed SOFC model describes the relationship between the verification cell model and the electrochemical model (Figure 4.17). The electrochemical model calculates the heat sources and losses, fuel and oxidant gas consumption, and resulting power output from the fuel cell. The initial operating conditions for the electrochemical model are obtained from the verification cell model and include:

1. Initial steady state temperature, pressure and velocity profiles
2. Mass fraction of each reacting species.

The electrochemical model uses these data to:

1. Calculate heat sources (heat generated from electrochemical reaction and ohmic heating)
2. Calculate heat losses (fuel depletion and product formation, decreases burner heat output)
3. Update mass fraction of reacting species, include formation of products
4. Calculate power output of cell (voltage and current).

Once the SOFC model is refined, a stack model with multiple cells can be developed. However, multiple cell arrangement can not be modelled using a 2D axisymmetric approach. Alternative strategies include full 3D or 2D cross-sectional iterative approaches, where a slice in the horizontal plane is solved then a slice in the vertical plane is solved, etc. A 3D model, where a 15° or 30° slice is modelled, is another approach. These alternatives are beyond the scope of this thesis.

The goal for the proposed SOFC model is to study the impact of stack housing designs (geometry) on temperature distribution and consequently individual cell performance. This can be measured as individual cell power outputs, fuel cell efficiencies and fuel utilisation.

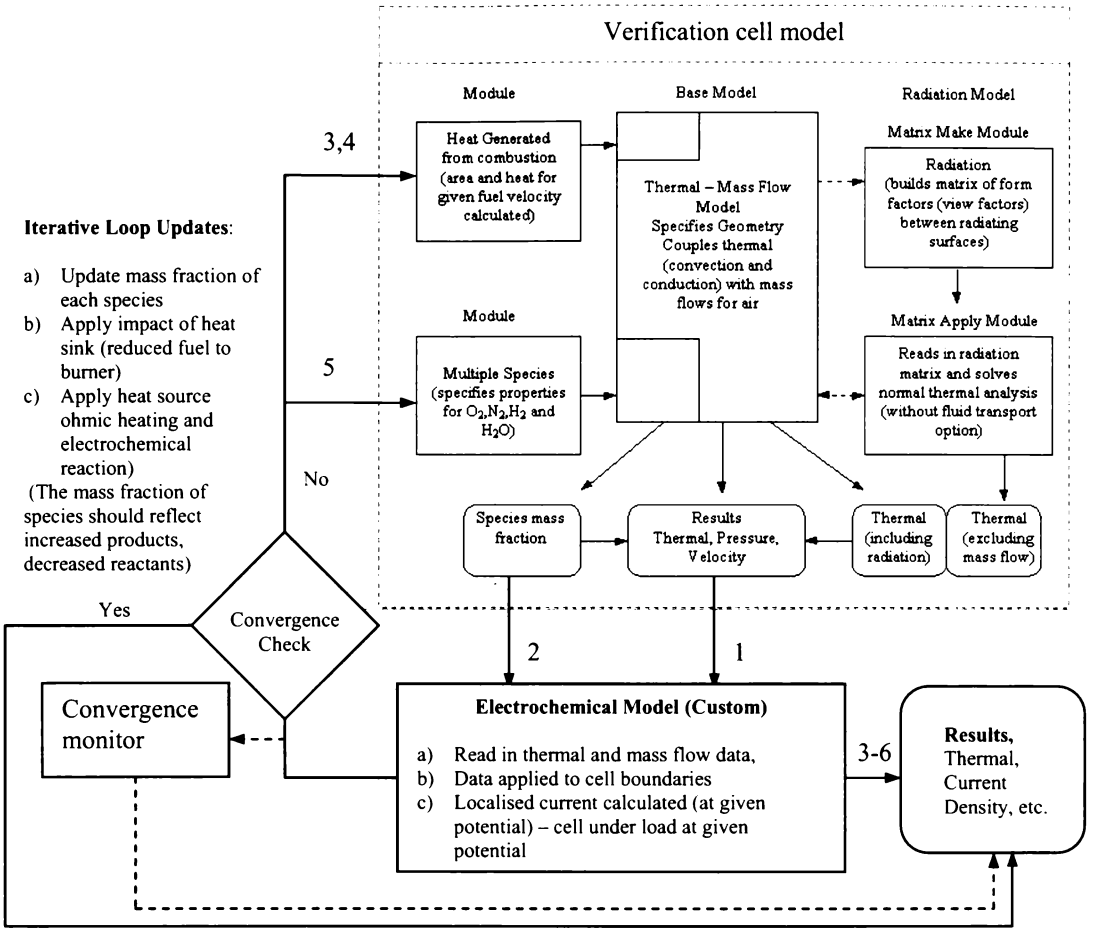

Figure 4.17 Process flow diagram for solution algorithm and, model – module relations, including proposed electrochemical module.

4.1 Summary

The functions, features and procedures for using ANSYS® (with FLOTRAN CFD) has been described. Three examples were given to highlight how ANSYS® can be used to simulate thermal fluid situations. The verification cell modelling code consists of a base model (Thermal – Mass Flow) and various modules (Combustion /flame, Multiple Species and Radiation). The information required for writing the code included verification cell geometry, properties of the materials used, creating the model mesh, and selecting the modelling parameters, assumptions, boundary conditions and loads to be used in simulations. An extension to the current modelling to include a fuel cell stack was proposed.

REFERENCES - Chapter Four

1 ANSYS, Inc, Southpointe, 275 Technology Drive, Canonsburg, PA 15317, USA. The Internet; [http://www.ansys.com].

2 The Internet; [http://www.ansys.com/VisitAnsys/index.html].

3 ANSYS® 5.4 Theory Manual, Chapter7, p. 23.

4 Parametric Technology Corporation, 128 Technology Drive, Waltham, MA 02453, USA. The Internet; [http://www.ptc.com].

5 SolidWorks Corporation, Concord, MA 01742, USA. The Internet; [http://www.solidworks.com].

6 ANSYS® 5.4 ANSYS CFD FLOTRAN Analysis Guide, Chapter 8.

7 NZF Stainless, Hamilton, New Zealand, Product Guide.

8 Materials Database Software, CMS (Cambridge Materials Selector) Version 2.02, **1994**, Granta Design Ltd. The Internet; [http://www.granta.co.uk].

9 Kaowool® Vacuum Formed Board, Product Information Sheet, Thermal Ceramics Australia Ltd.

10 ANSYS®, fluid properties data base file, floprp.ans.

11 J. P. Holman, *Heat Transfer* 8th edn., McGraw–Hill, Inc., Singapore, **1997**, p. 646.

12 D. R. Poirier and G. H. Geiger, *Transport Phenomena in Materials Processing*, TMS, USA, **1994**, p. 619.

13 J. P. Holman, *Heat Transfer* 8th edn., McGraw–Hill, Inc., Singapore, **1997**, p. 345.

14 V. L. Streeter, E. B. Wylie and K. W. Bedford, *Fluid Mechanics* 9th edn., WCB/McGraw-Hill, Singapore, **1998**.

15 N. P. Cheremisinoff (ed), *Handbook of Heat and Mass Transfer*, Vol. 1: *Heat Transfer Operations*, Golf Publishing Company, USA, **1986**.

16 J. R. Welty, C. E. Wicks and R. E. Wilson, *Fundamentals of Momentum, Heat, and Mass Transfer* 3rd edn., John Wiley & Sons, Inc, USA, **1984**.

17 B. Lewis and G. Von Elbe, *Combustion, Flames and Explosions of Gases*, 3rd edn., Academic Press, Inc., USA, **1987**, p. 700.

18 U. Bossel, *Facts & Figures, The IEA programme of R, D, & D on Advanced Fuel Cells*, Annex II: Modelling and Evaluation of Advanced Solid Oxide Fuel Cells. Swiss Federal Office of Energy, Operating Agent Tack II, Berne, April **1992**.

19 A. M. Kanury, *Introduction to Combustion Phenomena*, Vol. 2: *Combustion Science and Technology*, Gordon and Breach Science Publishers, Inc., USA, **1975**, p. 236.

CHAPTER FIVE

CHAPTER FIVE

Results and Discussion

5.1 Introduction

This chapter presents data obtained from operating the verification cell. The discussion focuses on addressing the objectives (Section 3.2.1) to assess feasibility of the design, measure temperature profiles in the cell, understand the real-time operating characteristics, and identify parameters that significantly affect design and operation of the verification cell.

5.1.1 Conventions for Data

A quick-reference thermocouple map (fold out) is given in Appendix C3 to facilitate viewing the data presented in this chapter.

The following abbreviations and conventions are used:

- The abbreviations IS (for insulated) and NI (non-insulated) are used to label temperature profiles.
- Dimensions are mm (or m). The diameter of components 13, 25, 51, 76 and 102 mm have a nominal thickness of 1.65 mm, fabricated from readily available standard size tubing (0.5, 1, 2, 3 and 4 inch).
- The conversion of the fuel flow rate (mL min^{-1}) entering the fuel tube of the verification cell to a velocity (ms^{-1}), was done for computer modelling purposes. The velocity values are used for boundary conditions in the computer modelling and have been applied in the flame characterisation work.
- Experimental temperature profiles are measured in degrees Celsius but temperature profiles generated by ANSYS® are in SI units (Kelvin).
- The standard system is 51-mm diameter, 100-mm high flue. Changes in the system configuration are shown in Figure 4.13.

- The 77-mm diameter flue has an extra thermocouple at the exhaust so data from the O1 and O2 thermocouples in the standard system (51-mm diameter flue) have been relabelled O0 and O1 respectively to produce continuous temperature profiles.
- Thermocouple E456 presented in the temperature profiles represents the average for thermocouples E4, E5 and E6.
- The non-insulated system was operated for 60 minutes rather than the 80 min for insulated systems (see Section 5.2).

5.2 Fuel Flow

The effect of increasing fuel flow rate and using insulation on temperature profiles is reported in this section. Appendix E contains supplementary temperature profile plots to the data present in this section.

5.2.1 Fuel Flow in the Non Insulated System

Thermocouples are placed in the combustion zone (F1 & F2), air manifold (A1-A3), exhaust manifold (E1-E7), exhaust stack (S1-S5) and exhaust outlet (O1, O2 plus O0 for 76-mm diameter flue). Figure 5.1 shows that after 80 minutes continuous operation, the highest temperatures occur near the combustion zone (F1 and F2) and on the top of exhaust manifold (E7). As expected, the temperature decreased beyond the combustion zone (A1-A3, and S5) and then increased as the gas moved toward the combustion zone (E1-E456, and S1-S4).

Increasing fuel flow rate by 100% (400 to 800mL min^{-1}) and 200% (to 1600mL min^{1}) increased temperatures at the air manifold by about 20% for each increase in flow rate, and temperatures at the exhaust manifold by 30 and 21% respectively.

The data is treated by assuming continuous temperature gradients across components and gases under near steady state conditions.

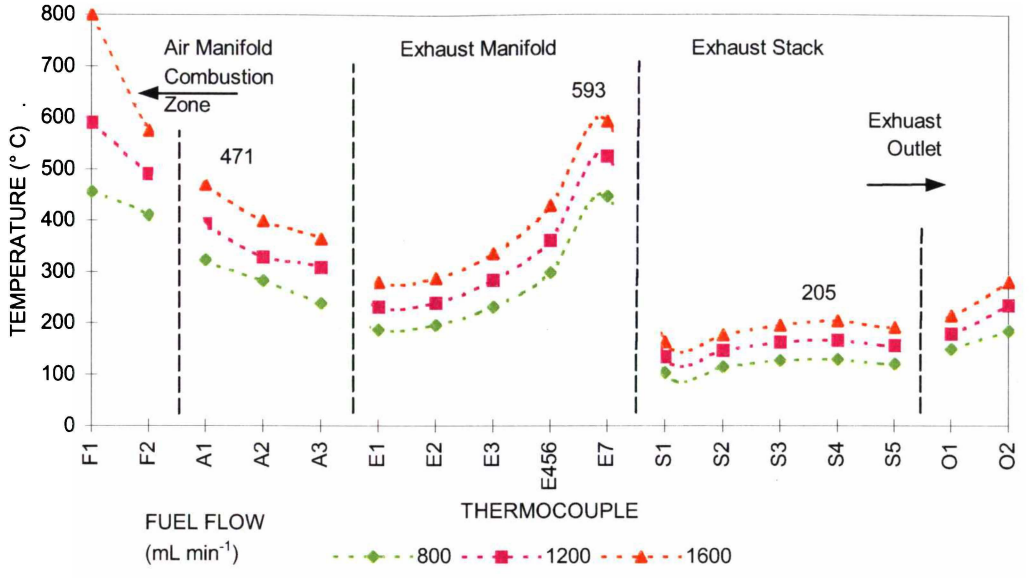

Figure 5.1 Effect of fuel flow rate on temperature profiles when operating the standard verification cell for 80 minutes.

5.2.2 Fuel Flow in the Insulated System

The effect of fuel flow rate on temperature profile in the insulated verification cell after 60 minutes continuous running are shown in Figure 5.2. Operating temperatures are 10°C lower at the air manifold and 23°C lower at the external surface of the exhaust stack than for the non-insulated system (Figure 5.1). These temperature differences are partly because the insulated cell had been running for only 60 minutes rather than the 80 minutes and partly because the Kaowool insulation has a high heat capacity (1000 J kg^{-1} K^{-1}) and low thermal conductivity (0.07 W K^{-1} m^{-1}), which increases the time needed to reach steady state. Because the non-insulated system reaches steady state more quickly than the insulated system, the standard approach was to compare data from the non-insulated system at 60 minutes with those from the insulated system at 80 min.

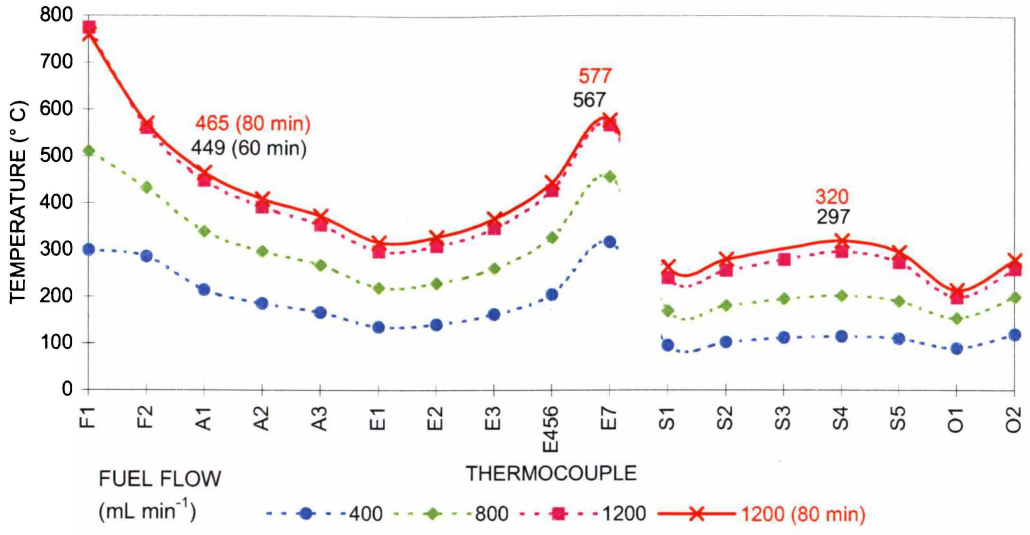

Figure 5.2 Effect of fuel flow rate on temperature profiles when operating a standard, insulated verification cell for 60 minutes (1200 mL mn^{-1}, 80 minutes).

5.2.3 Comparison of the Effect of Insulation

Using external insulation increases overall operating temperature (Figure 5.3) because it reduces thermal losses from the exhaust stack surface. The insulated system was operated for longer to reach a steady state and consequently higher temperatures at given fuel flow rates.

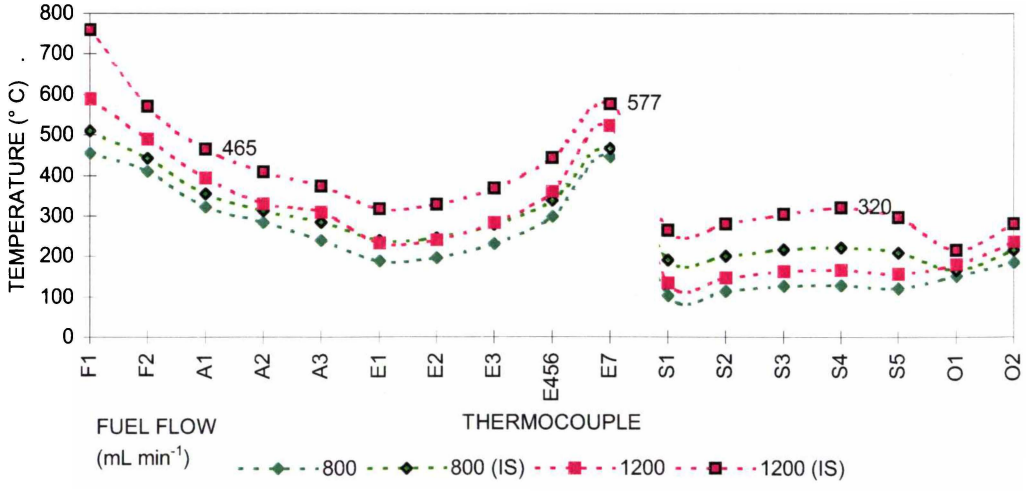

Figure 5.3 Effect of insulation and fuel flow rate on temperature profiles in the verification cell (NI operated for 60 minutes and IS for 80 minutes).

The affect (temperature differences) of insulating the verification cell are shown more clearly in Figure 5.4. At fuel rates of 800 and 1200 mL min^{-1}, insulating the verification cell increases operating temperatures by 14 and 22% respectively. Exhaust stack temperatures increase by an average of 74 and 90 % at these flow rates respectively. The effect of increasing fuel flow rate on temperature difference throughout the verification cell is similar except at thermocouple A3. This anomaly is probably caused by more air entering the system near this thermocouple.

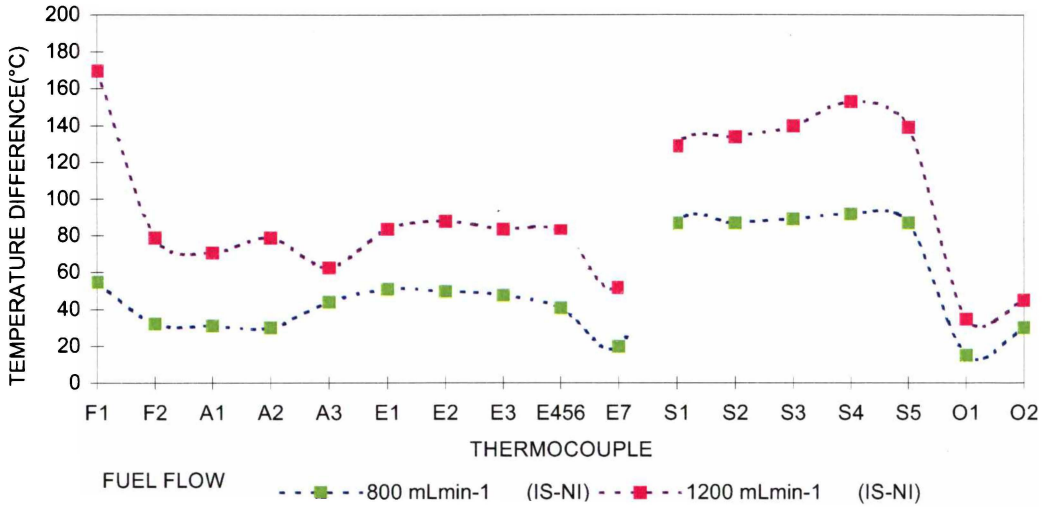

Figure 5.4 Effect of fuel flow rate on temperature difference between non-insulated and insulated systems after at 60 (NI) and 80 (IS) minutes.

5.3 Effect of Changing Flue Dimensions

The effect of varying flue height and width of the insulated standard system over a range of fuel flow rates (400, 800 and 1200 mL min^{-1}) on temperature profiles are discussed. Because the affect of flue height on temperature profiles was consistent over the fuel flow rates tested, data for other systems are only reported for the 800 mL min^{-1} flow rate.

Explanation of data labels in Figures 5.5 to 5.7. The top data label (A=446) in Figure 5.5 is the temperature at thermocouple E7 with the 100-mm high flue. The bottom point (B=427) is the temperature for the 300-mm high flue. Temperature labels in Figure 5.5 (left to right) are from thermocouples E1, E7 and S3.

5.3.1 Increasing Flue Height

Temperature in the combustion zone (F1 and F2) decreased significantly with increased flue height (300 mm). The temperature profile increased down the air manifold and part way up the exhaust manifold. There was a significant decrease ~20°C) at the top of the exhaust manifold (top of the combustion zone) and a similar temperature decrease along the exhaust stack. Temperature decreases further at the flue outlet (O1 and O2). Decreases in temperature are likely due to increased air flow but this cannot be confirmed as inlet air and exhaust flow rates were not measured because of experimental constraints. The increased air flow would also affect the flame front, extending combustion down the walls between the air and exhaust manifolds and thus increase temperature in these regions (A3, E1, and E2). This increased airflow could cool thermocouples above and near the air inlet. Air moves from the air manifold, through the air manifold outlet and into the combustion zone.

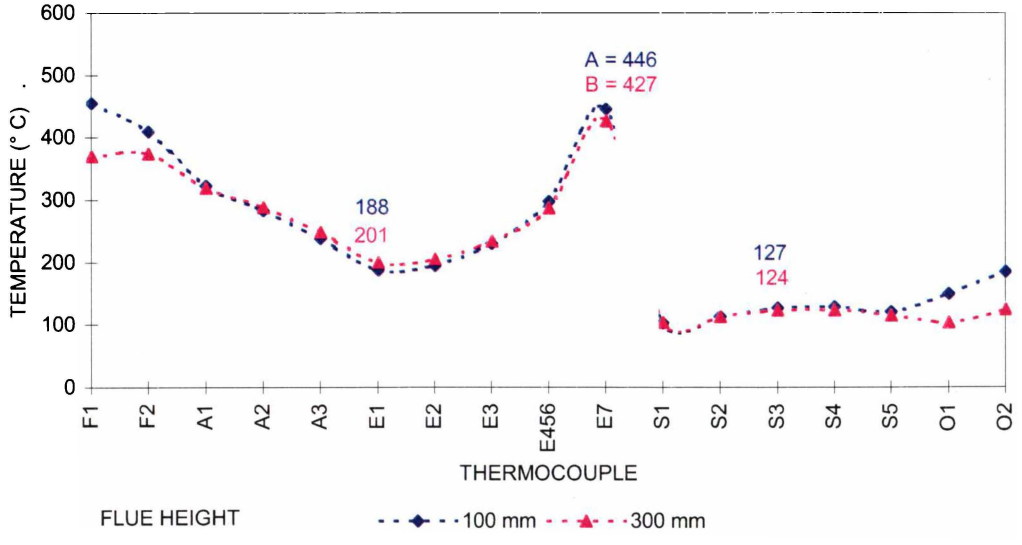

Figure 5.5 Effect of flue height on temperature profiles afer 20 minutes for the standard system at 800 mL min^{-1} fuel flow rate.

Temperature profiles in the insulated system (Figure 5.6) are similar to those in the standard system (Figure 5.5) with temperatures consistently higher.

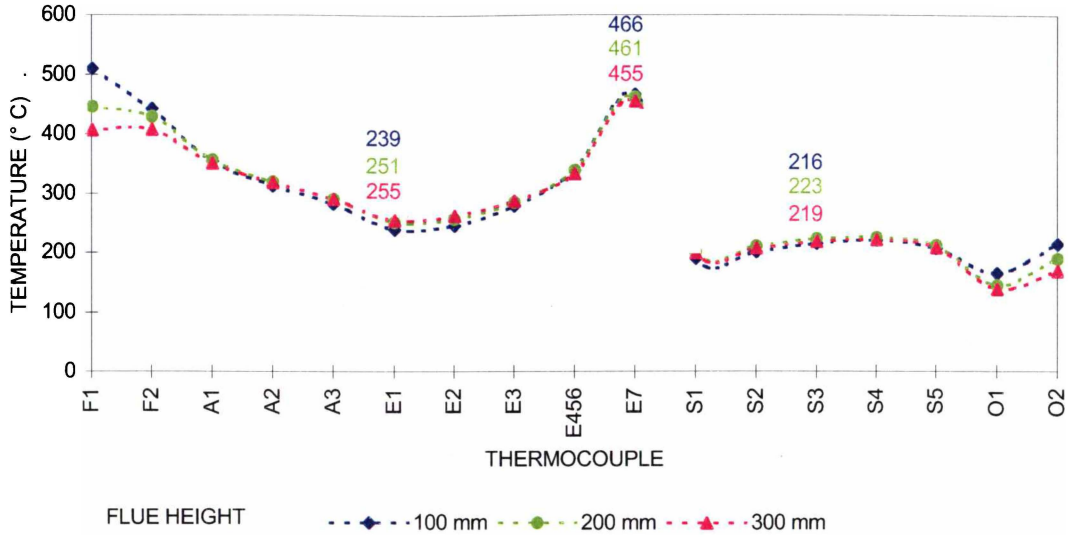

Figure 5.6 Effect of flue height on temperature profiles after 20 minutes for the insulated system with 800 mL min^{-1} fuel.

5.3.2 Increasing Height of the 76-mm Diameter Flue

The temperature decrease in the combustion zone and outlet was also observed for the 76-mm wide flue (Figure 5.7), which performed in a similar way as the 51-mm diameter flue system. Temperature increased along the solid components of the verification cell except at thermocouple E7, where temperature remained constant. Increasing chimney height increases air velocity but also increases friction losses at the chimney wall. The larger diameter flue (greater surface area) reduces friction losses but increases heat loss at the flue wall, lowering exhaust gas temperature. There is a significant radiant heat loss above the combustion zone, which becomes more exposed with increasing flue diameter. The contributing effects of flue height to that of flue width on temperature profiles could not be determined from data collected. Optimal chimney height and effect of friction losses on a similar system are reported by Boersma *et al.*[1]

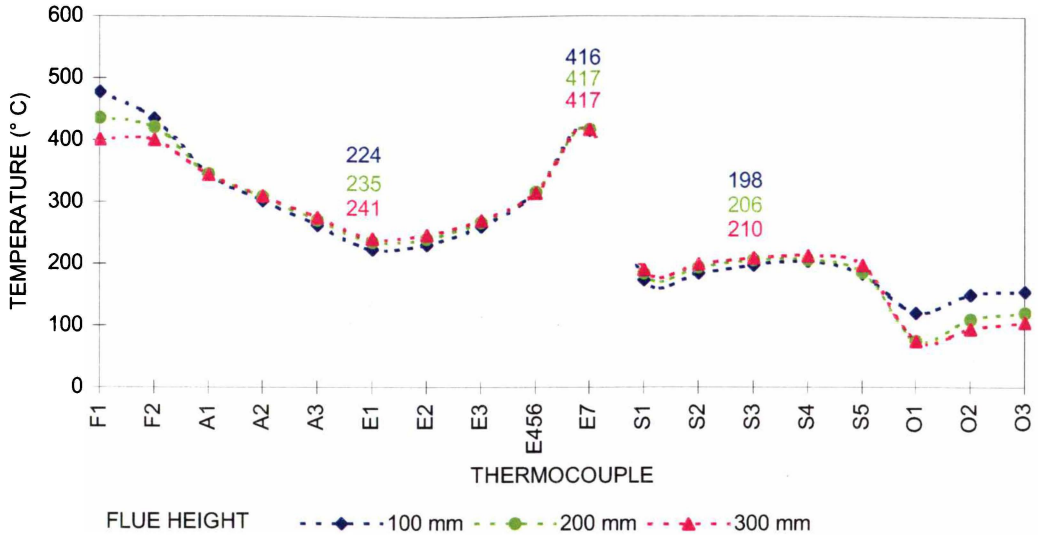

Figure 5.7 Effect of flue height (76 mm inch flue width) on temperature profiles after 20 minutes for the insulated system with 800 mL min^{-1} fuel.

5.3.3 Fuel Flow rate and Flue Height

Increasing flue height for each set fuel flow rate decreases temperature in the combustion zone and at the outlet (Figures 5.8-5.10). This data is consistent with data described in Section 5.3.1.

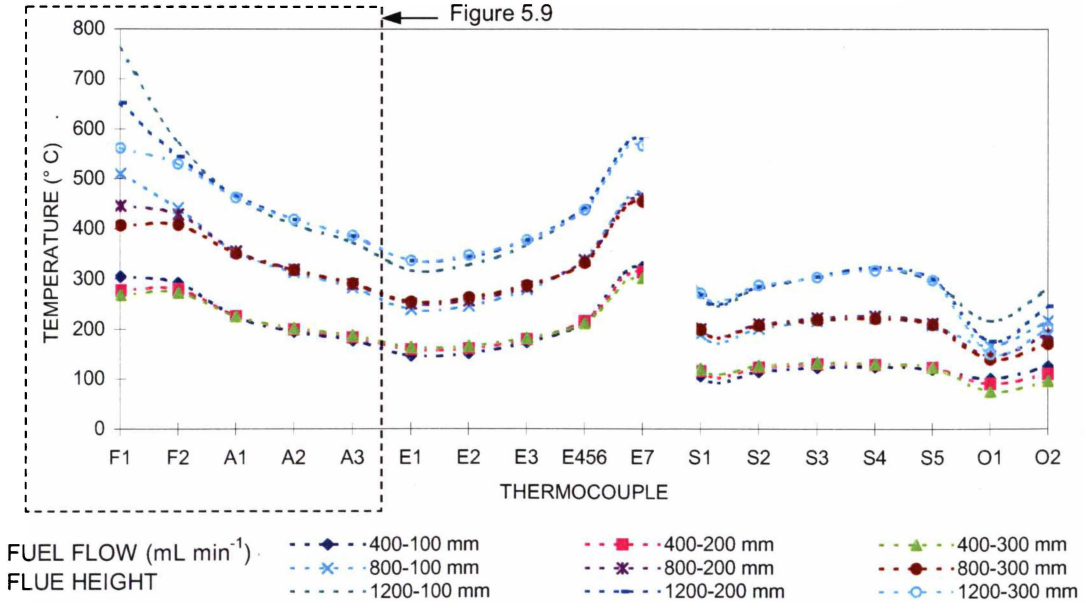

Figure 5.8 Effect of flue height and fuel flow rate on temperature profiles in an insulated standard system after 20 minutes.

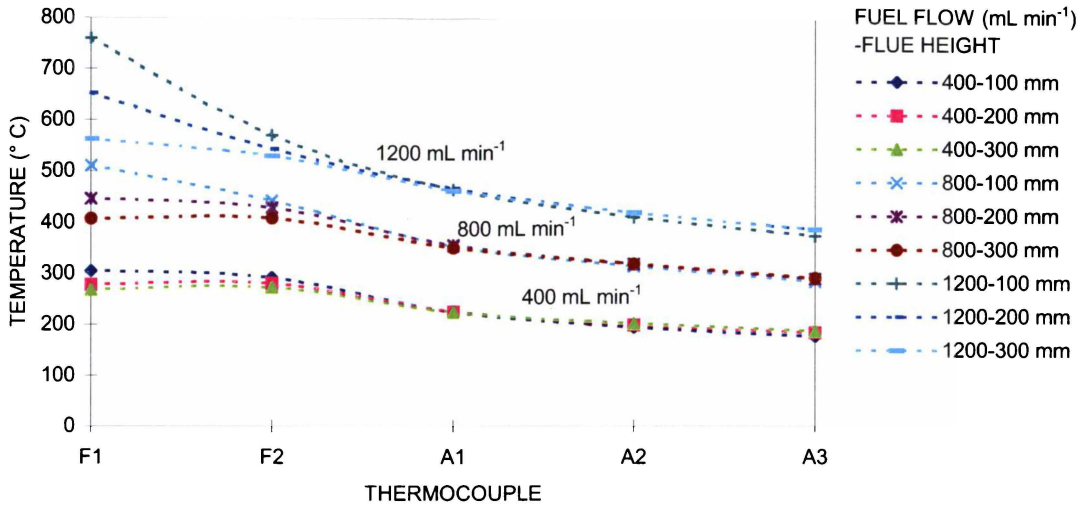

Figure 5.9 Effect of flue height and fuel flow rate on temperature profiles in the combustion zone and air manifold of an insulated standard system after 20 minutes.

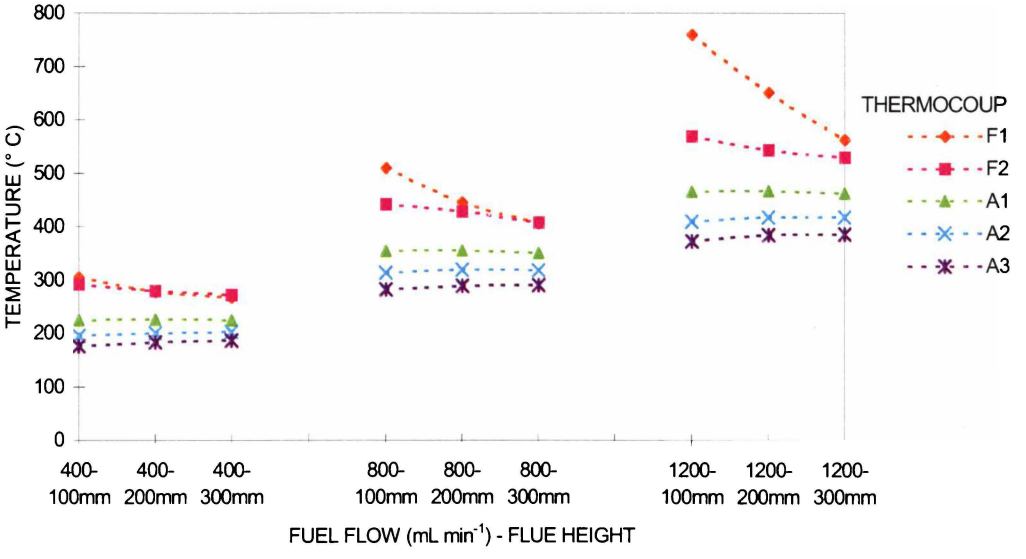

Figure 5.10 Effect of flue height and fuel flow rates on temperature at specific zones in the standard insulated system after 20 minutes.

5.3.4 Changing Flue Diameter

Increasing flue diameter decreased temperature of the entire system (Figure 5.11). The average temperatures of solid components in the verification cell decreased by 7, 8 and 9% for fuel flow rates 400, 800 and 1200 mL min^{-1} respectively. The effect of

flue diameter on temperature is pronounced above the combustion zone (E7) and at the top of the flue. Radiant heat loss from the increased surface area of the flue increases with increasing temperature. Also, it is assumed more air is drawn through the system by the chimney effect (naturally induced draft). Because air flow waas not measured, the contribution from radiation losses versus increased air flow rates could not be quantified.

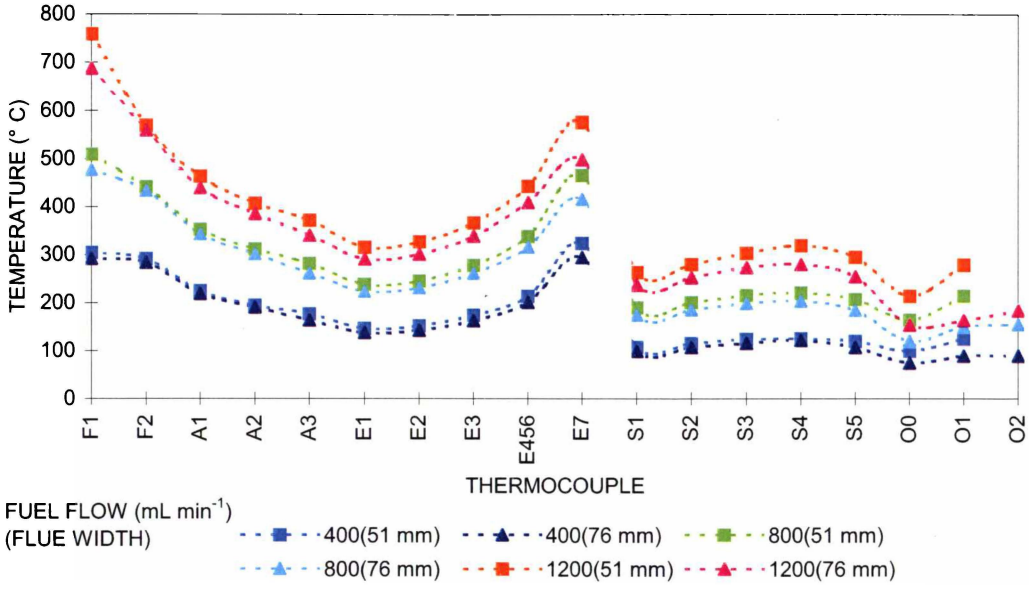

Figure 5.11 Effect of flue width and fuel flow rate on temperature profiles in the insulated 76 mm flue width system compared to the insulated standard system after 20 minutes.

5.4 Additional Analysis and Experiments

In this section, the verification cell is further characterised by investigating the degree of thermal axisymmetry at the exhaust manifold, the time required to obtain steady state, the cooling curves for various systems, the effect of restricting flows at the inlet and outlet, and the air temperature in the air manifold.

5.4.1 Thermal Axisymmetry

It was necessary to validate and measure the thermal symmetry about the central axis ("axisymmetry") of the verification cell to ensure the computer model was valid. Temperatures measured by the three thermocouples at the top of the exhaust manifold (E4, E5, E6) agreed within ±3°C except data for the standard system at

flow rates 1200 and 1600 mL min^{-1}, which varied by up to 7°C. Because of the close agreement, data from thermocouples E4, E5 and E6 are averaged and labelled E456 in the temperature profiles throughout this section. Details of variation between thermocouples E4, E5 and E6 are given in Table 5.1.

Table 5.1 Average temperatures (°C) for thermocouples E4, E5 and E6 (E456)

Configuration	TIME (minutes)							
	10	20	30	40	50	60	70	80
800 NI (51 mm)	229 (2)*	260 (2)	278 (1)	289 (1)	295 (2)	298 (2)		
1200 NI (51 mm)	269 (3)	329 (5)	341 (6)	351 (7)	357 (7)	361 (7)		
1600+ NI(51 mm)	348 (4)	388 (3)	408 (3)	421 (4)	428 (5)	429 (4)		
400 IS (51 mm)	140 (2)	167 (1)	182 (1)	193 (1)	200 (1)	205 (1)	210 (1)	214(1)
800 IS (51 mm)	226 (3)	264 (2)	289 (2)	305 (2)	317 (2)	327 (3)	333 (2)	339 (2)
1200 IS (51 mm)	307 (3)	356(3)	381 (3)	402 (2)	414 (2)	427 (2)	436 (3)	444 (3)
400 IS (76 mm)	136 (6)	158 (2)	172 (1)	181 (2)	188 (2)	194 (2)	198 (2)	201 (1)
800 IS (76 mm)	218 (0)	254 (1)	274 (1)	288 (0)	297 (1)	306 (0)	312 (1)	316 (1)
1200 IS (76 mm)	304 (2)	337 (2)	359 (2)	376 (1)	388 (1)	397 (1)	404 (1)	410 (1)

*Average temperature includes variation (error), where error represents the maximum deviation from averaged recorded temperatures for thermocouples E4, E5, and E6.

5.4.2 Steady State

The verification cell was not designed for investigating long life operation, so data were collected when the cell was near steady temperature equilibrium. Trials with the 76-mm diameter flue were operated until complete steady state was achieved (Figure 5.12). Temperatures after operating for 60 minutes could be up to 40°C lower (E1, and S1) than temperatures at steady state. Steady state is obtained more quickly near the combustion zone. For example, steady state for thermocouple E7 was achieved between 60 and 80 minutes (Figure 5.13).

The time the verification cell takes to heat up will depend on the temperature difference between heat source and the system, the mass being heated, and specific heat of the components. The verification cell contains 2.25 kg stainless steel with a specific heat of 500 J $kg^{1}K^{-1}$ and the maximum energy flux from 1600 mL min^{-1} of hydrogen is 264 W. Under these conditions, the 76-mm diameter flue will take 15, 38 and 60 minutes to heat to 227, 527 and 827°C respectively. When 0.8 kg of

insulation with a specific heat of 1000 J $kg^{-1}K^{-1}$ is added, it will take 40, 100 and 160 minutes to heat the cell to 227, 527 and 827°C respectively. These calculations assume temperatures are uniform throughout the entire system, and does not include heat transfer efficiency or thermal losses.

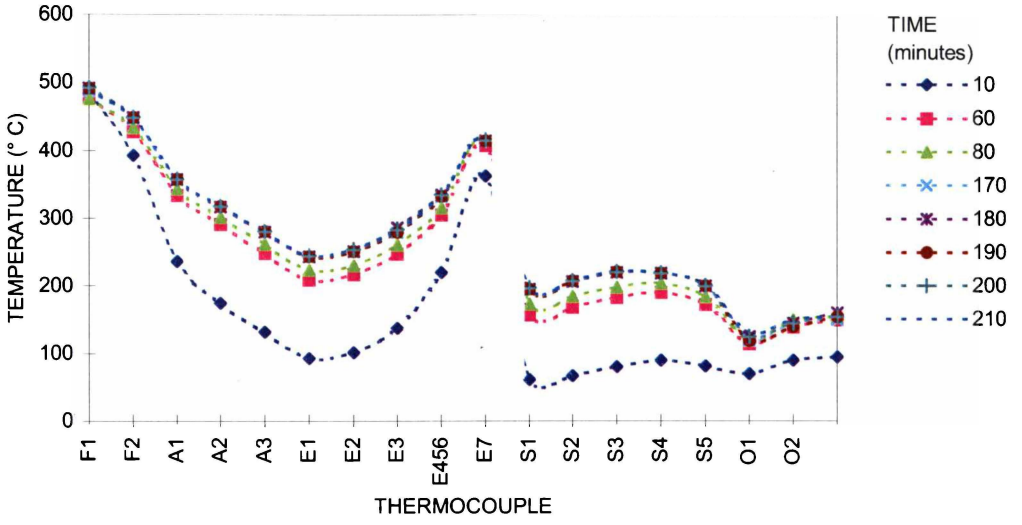

Figure 5.12 Temperature profiles over 210 minutes in the insulated system with a 76-mm diameter flue and 800 mL min^{-1} fuel flow rate.

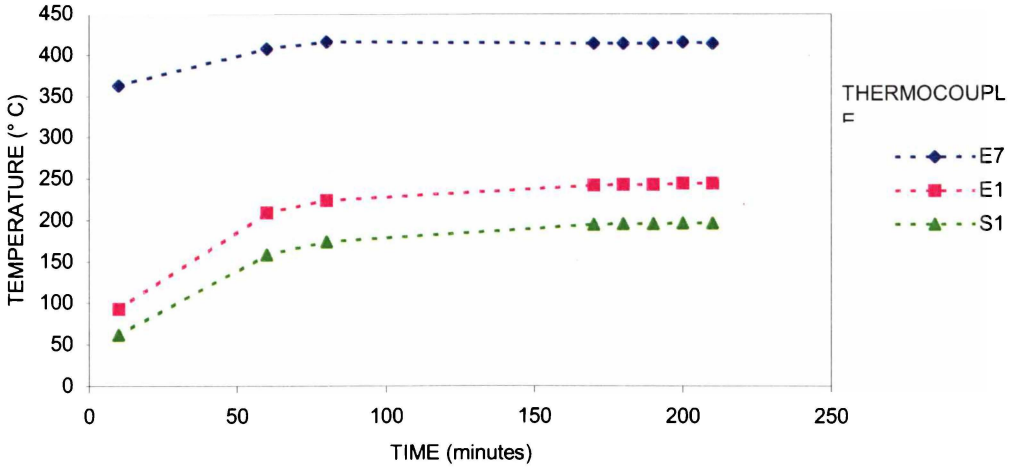

Figure 5.13 Temperature profiles over 210 minutes in the insulated system at E1, E7 and S1, with a 76-mm diameter flue and 800 mL min^{-1} fuel flow rate.

5.4.3 Cooling

The temperature difference between the temperature profile at 60 minutes, and the temperature profile at 10 minutes, from when the fuel flow was turned off, is shown in Figure 5.14. Insulating the air manifold and exhaust manifold reduced the overall cooling rate of the 51-mm width system. However, for the 76-mm width system, cooling rate increased to that equivalent to the non-insulated, 51 mm width system. The larger flue width looses more heat due to increased surface area. This leads to a reduction in temperature in all components, which is more apparent for the exhaust stack. The insulation stores heat from the exhaust stack and reduce the cooling rate at the air and exhaust manifolds. Less heat is retained by the larger diameter flue, as shown by the temperature difference when the system has been running for 60 min and 10 minutes after fuel flow was stopped (Figure 5.15). The cooling rate for the system with a 76-mm flue increased to that of the non-insulated system with a 51-mm flue.

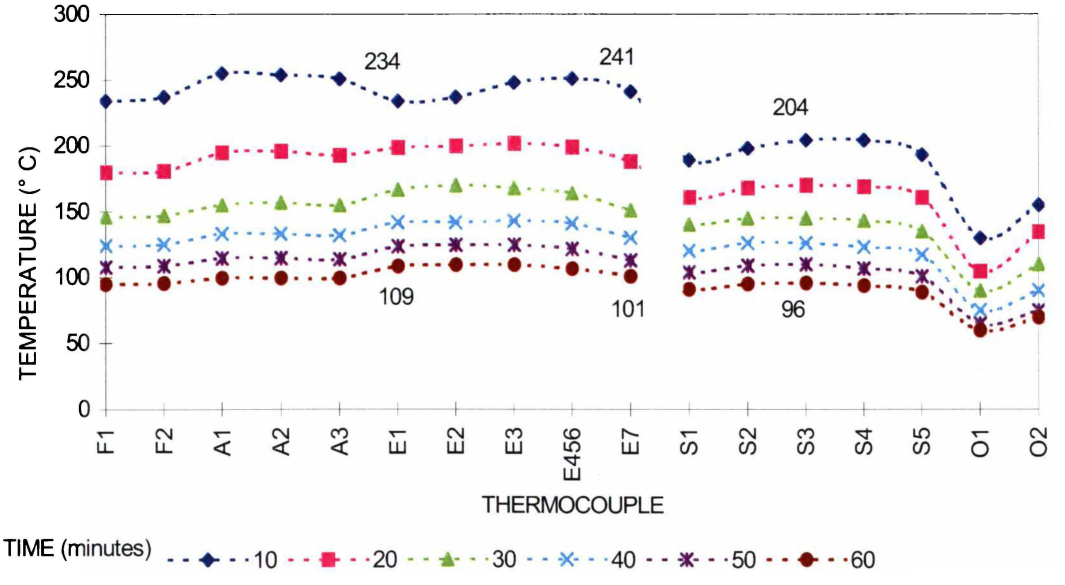

Figure 5.14 Cooling profiles for the insulated standard system over 60 minutes (10 minute intervals).

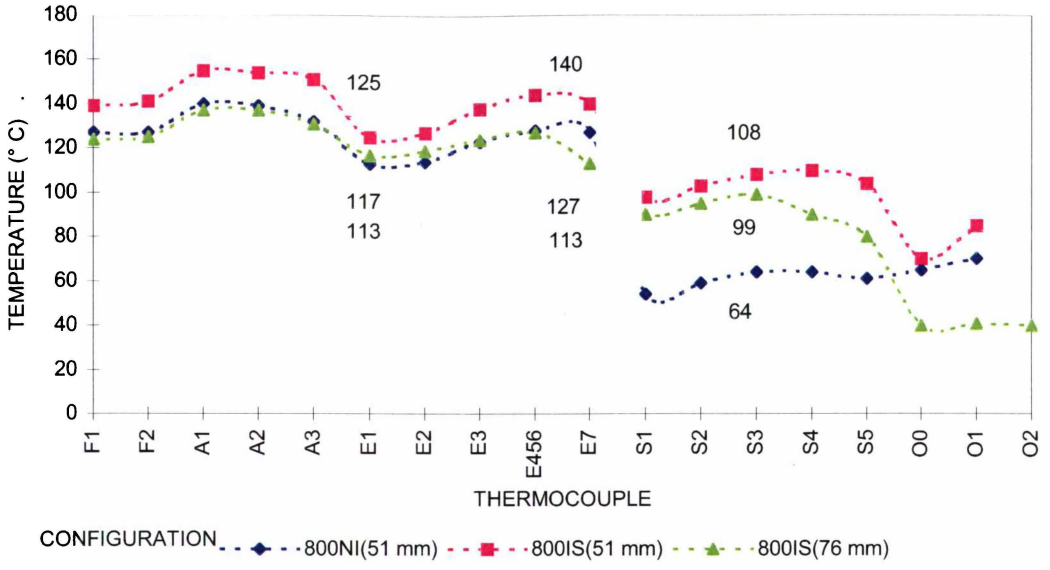

Figure 5.15 Temperature difference in cooling profiles for the standard system, insulated standard system and 76 mm width flue system, at 50 minutes.

5.4.4 Restricting Inlet and Outlet Flow

Flow was restricted by inserting a reducing aperture disc (RAD) at the inlet and/or outlet. Inserting a 20-mm diameter RAD into the air inlet reduced the cross-sectional area from 253 x 10^{-6} m^2 to 66 x 10^{-6} m^2 (75% reduction in flow area). Two different RAD sizes were used in the outlet: type A reduced outlet area to 79 x 10^{-6} m^2 (95% reduction), and type B reduced the area to 20 x 10^{-6} m^2 (99% reduction). The flow area of all gas flow paths in the verification cell are given in Table 5.2.

The ratios of flow areas between components, including the restricted flow area options, are listed in Table 5.3. These ratios indicate where flows are more constricted but do not indicate the additional contribution that bends (90-180°) in the flow path impose on the gas flow. The figures presented in Chapter 6 help to highlight the characteristic flow properties of the gases within the verification cell.

Table 5.2 Flow area of each component and between components

Inlet/Outlet	Radius (m) (Inner/Outer)	Area(m^2) (x 10^{-6})
Fuel Tube Inlet	0.0047	69
Air Inlet (& Air Manifold Width Outlet)	0.011	253
Inlet Total (Fuel Tube Inlet + Air Inlet)	...	322
Restricted Air Inlet	0.010	66
Exhaust Outlet, 51 mm diameter	0.02375	1773
Exhaust Outlet : 76-mm diameter	0.03645	4174
Restricted Type A Outlet	0.005	79
Restricted Type B Outlet	0.0025	20
Exhaust Manifold Outlet	0.02	771
Between Fuel Tube and Air Manifold	0.0047/0.02375	1646*
Between Air Manifold and Exhaust Manifold	0.02375/0.03645	2147
Between Exhaust Manifold and Exhaust Stack	0.03645/0.04915	3029

* flow area between fuel tube and air manifold = (flow area of air manifold - flow area of fuel tube)

Table 5.3 Flow area ratios

COMPONENT to COMPONENT	RATIO
Fuel to Air Inlet	= 0.27
Air Inlet / Total to Exhaust Outlet 51 mm flue width	= 0.14 / 0.18
76 mm flue width	= 0.06 / 0.08
Inlet Total to Exhaust Manifold	= 0.15
Inlet Total to Exhaust Stack	= 0.11
Inlet Total to Exhaust Manifold Outlet	= 0.42
Restricted Air Inlet to Exhaust Outlet 51 mm flue width	= 0.04
Restricted Air Inlet to Restricted Type A Outlet	= 0.84
Restricted Air Inlet to Restricted Type B Outlet	= 3.30
Air Inlet to Restricted Type A Outlet	= 3.20
Air Inlet to Restricted Type B Outlet	= 12.65

Restricting the air inlet increases temperature in the combustion zone (Figure 5.16), with 400°C increase at thermocouple F2 and a lower temperature increase for F1. This trend is opposite to that observed thus far, but is also observed for using the type A outlet restriction (Figure 5.17, profile AI+EO[A]). Reducing the outlet further with a type B restriction (Figure 5.17, profile AI+EO[B]) gave a continuous decrease in temperature. The type B restriction was outside the operational limits of the verification cell, resulting in the flame being retarded (the exhaust gases back flowed, reducing air supply to the combustion zone).

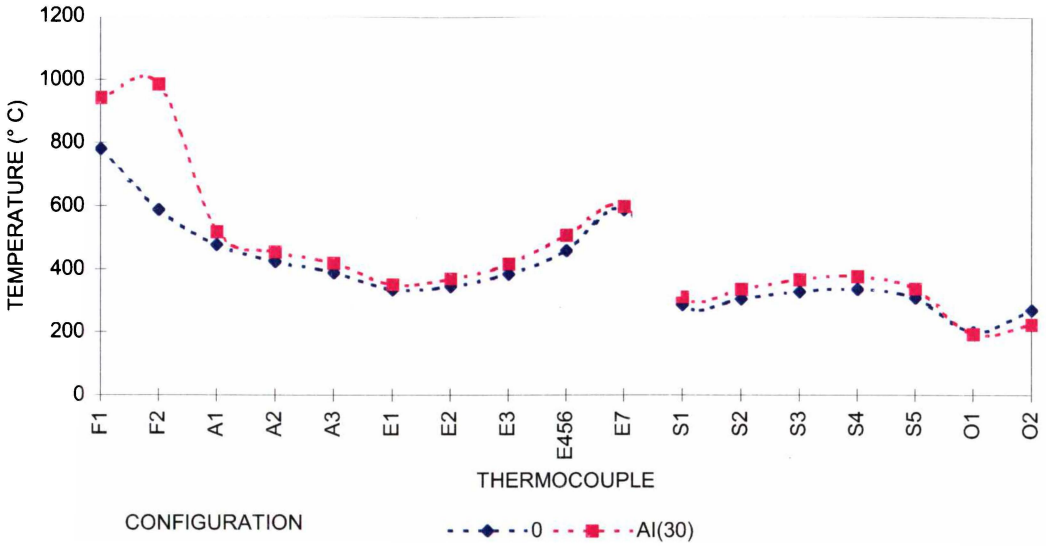

Figure 5.16 Effect of restricted air inlet AI(30) on temperature profiles afer 30 minutes for the insulated standard system at 1200 mL mL min^{-1} fuel flow rate.

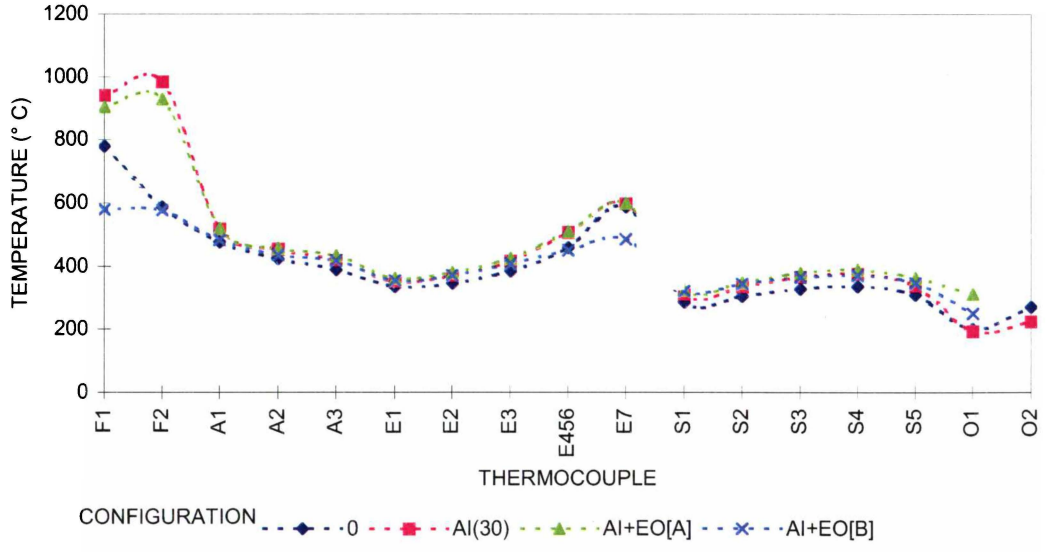

Figure 5.17 Effect of various combinations of inlet and outlet flow restrictions on the temperature profiles at 1200 mL min^{-1} fuel flow rate. Data was recorded at 30, 50 and 60 minutes respectively (cumulative time).

Increasing fuel flow rate (2000 mL min^{-1}) with outlet restriction type A further increased temperature by approximately 200°C at F2, and 100°C throughout the rest of the system (Figure 5.18, profile 2L min^{-1} EO[A]). Removing the outlet restriction significantly increased overall system temperature and decreased temperature within the combustion zone (Figure 5.18, profile 2L min^{-1}off). Thermocouple F1, which is

above F2 and close to the inside of the exhaust manifold wall, again recorded the higher temperature. Typically F1 records a higher temperature because the flame follows the inside of the exhaust manifold (combustion zone). The air flowing into the combustion zone from the air-manifold outlet cools thermocouple F2. The reversal of temperature dominance between thermocouples F1 and F2 when restrictions are applied is probably due to the reduced airflow, leading to a shortening of the flame.

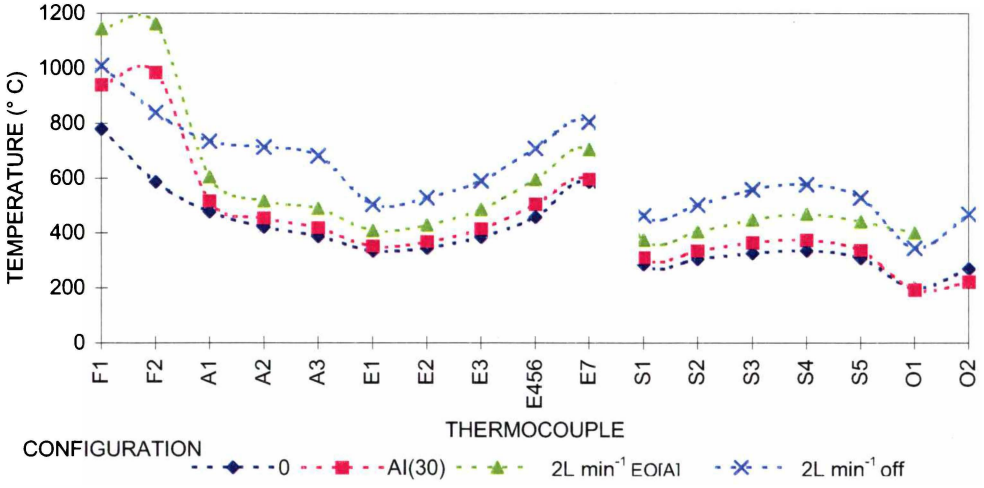

Figure 5.18 Effect of various combinations of inlet and outlet flow restrictions on the temperature profiles at 2000 mL min^{-1} fuel flow rate. Data was recorded at 30, 50 and 70 minutes respectively (cumulative time).

The potential restrictions inherent in the standard system (other than the fuel tube) are the air inlet and the exhaust manifold outlet. Modifications to restrict the flow area did not significantly effect the temperature profiles (Figures 5.16 - 5.18), indicating that the verification cell could operate even when flow areas are significantly reduced (90% reduction at outlet).

Reducing the distance between component walls (reducing the channel spacing) between the exhaust manifold and exhaust stack, will improve heat transfer throughout the system. Small flow channels effectively increase the gas velocity and consequently the heat transfer coefficient at the component walls. In contrast, there is increased surface friction with reduced component spacing, which has not been addressed in this study. It is recognised that pressure losses due to flow restricting

components will become more prevalent when modelling an SOFC system, which will include fuel cell components that will further impede fuel and air flows.

5.4.5 Air Inlet-Manifold Temperatures

The highest recorded temperature for the in-coming air was 270°C occurred half way up the air manifold (100 mm above the base of the air inlet) for the standard system, insulated with a fuel flow of 1200 mL min^{-1}. The temperatures recorded (Figure 5.19) display a trend consistent with data presented throughout this chapter; inclused insulation increases overall temperature and increasing flue width decreases temperature. This decrease in temperature supports the conclusion that more air is being drawn into the system. The nearest equivalently-placed component thermocouples are A2 and A3, 110 mm and 65 mm respectively above the base of the air inlet. The air manifold thermocouples represent the temperature of the external surface of the air manifold. The recorded temperatures for A2 and A3 are 405 and 370°C respectively, which is 110-130°C above the temperature of air flowing inside the air manifold.

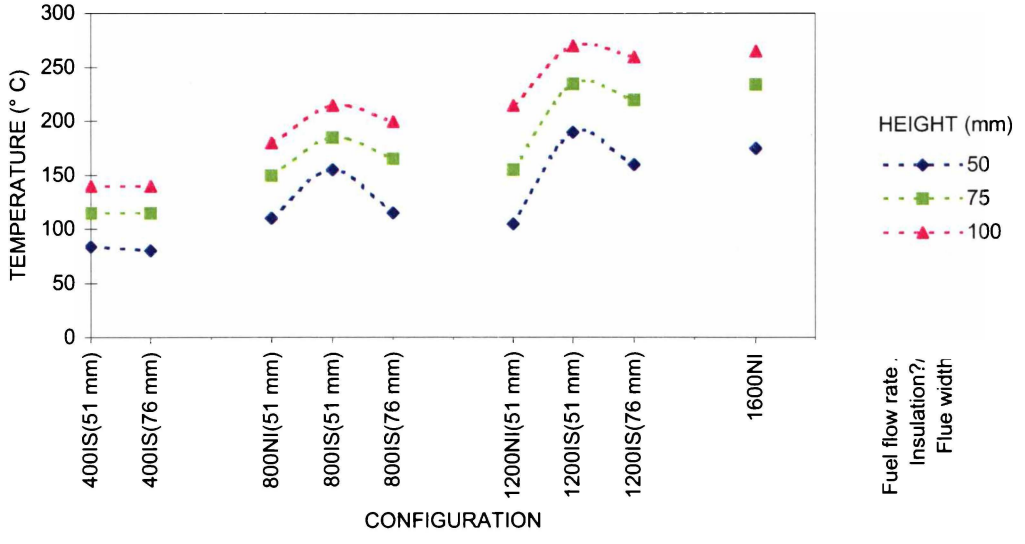

Figure 5.19 Temperature profiles for air flowing into all systems at 50, 75, and 100 mm from the base of the air inlet into the air manifold for increasing fuel flow rate, at 60 or 70 minutes.

5.5 Combustion: - Flame Characterisation

Two methods were used to characterise the hydrogen flame profile - a thermocouple method and a visual or photographic method, and have been described in Chapter 3. Data from both methods have been plotted and a correlation between temperature, flame dimensions and fuel flow was derived from trend lines fitted to the data. Appendix E2 contains the raw data for Figures 5.21 and 5.22.

5.5.1 Thermocouple Approach

Temperature profiles at different regions on the periphery of the flame were measured (Figure 5.20). The profile fluctuations are due to small air currents around the test set-up. Temperatures were highest at thermocouple one over the fuel velocity range tested except for a temperature decrease at fuel velocities greater than 0.4 ms^{-1} (>1600 mL min^{-1}). The decrease is because the increased fuel flow generates a larger coolant front (Figure 3.9). The maximum temperature recorded at any time during testing did not exceed 1200°C. The thermocouple centred in the flame recorded the higher temperatures, with a near parallel temperature profile to the thermocouple array. However, the temperature decreased at a lower fuel velocities (0.3 ms^{-1}) because the apex of the conical coolant front reached the thermocouple before affecting the lower placed peripheral, thermocouple number one. A second order polynomial equation was fitted to the average result of the two data sets to give trend lines (a) and (b), which can be written in the following form:

$$T_F \approx -4913(fv^2) + 4003(fv) + 281 + 273.15 \qquad (5.1)$$

where T_F is the approximate flame temperature, fv is the fuel velocity (ms^{-1}) and the 273.15 is used to convert the equation to Kelvin for computer modelling purposes.

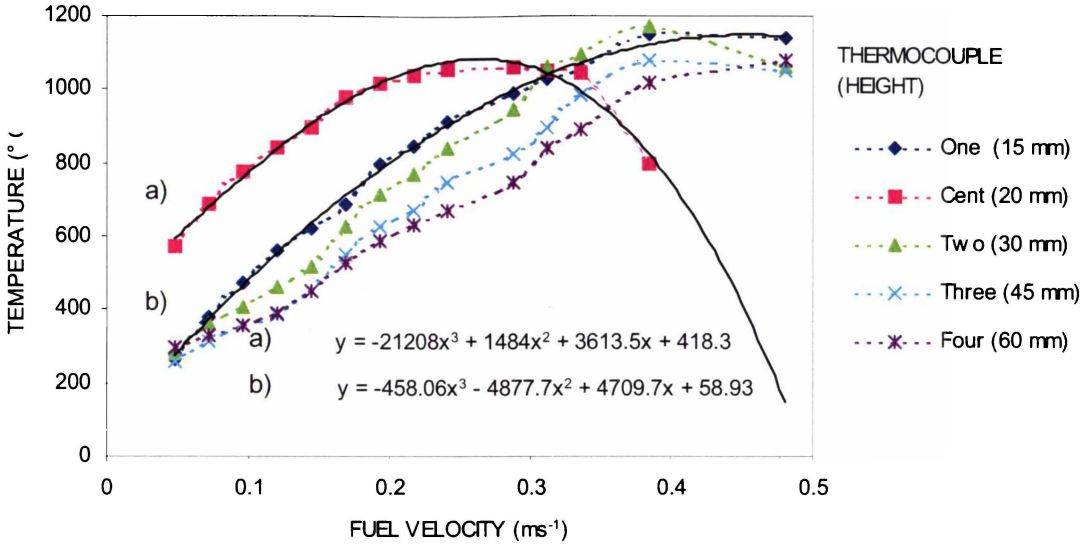

Figure 5.20 Temperature profiles for the peripheral thermocouple array (thermocouples one through four) placed 15, 30, 45 and 60 mm above the fuel tube orifice, and a single thermocouple centred (cent) 20 mm above the fuel tube orifice.

5.5.2 Visual Approach (Photographic)

Each of the flame dimension profiles have been correlated to a linear equation (Figure 5.21). Two equations will be applied in the computer modelling, which will provide an approximated area for the heat generated, in an attempt to simulate the heat from combustion. Equation 5.2 and 5.3 represent the relationship for the radiant flame height and radiant flame width respectively, which can be written in the following form:

$$czh \approx 0.0883(fv) + 0.0044 \tag{5.2}$$

$$czw \approx 0.0196(fv) + 0.0109 \tag{5.3}$$

where czh is combustion zone height (flame or heat generation zone height), and czw is combustion zone width. The fuel velocity is in ms^{-1} and dimensions are in metres.

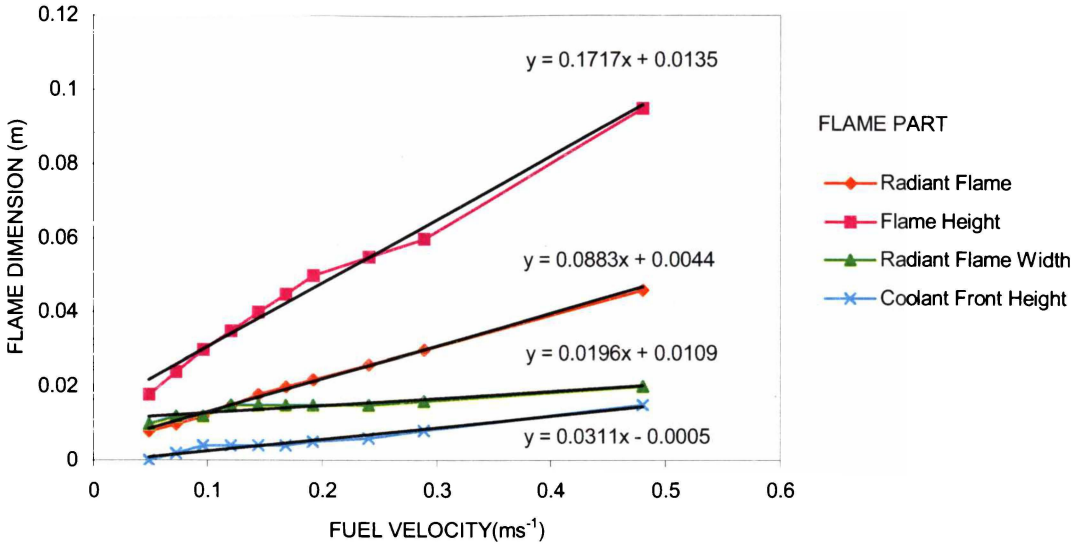

Figure 5.21 Flame dimensions as a function of fuel velocity.

5.6 Summary

The temperature rise from increasing fuel flow and applying insulation to the exterior of the verification cell has been characterised. Table 5.4 summarises the increase in temperature for the air and exhaust manifolds, and the outer exhaust stack. The data indicate that insulation reduces the bulk of the heat lost from the surface of the verification cell, at the exhaust stack. At the interior components14–22 % increase in temperature was recorded. The insulation is approximately equivalent to an additional 400 mL min^{-1} of fuel, in terms of increasing the temperature at the interior components.

Increasing the flue height from 100 mm to 300mm resulted in a change in the temperature distribution throughout the stack, with a decrease in temperatures in the combustion zone and at the exhaust outlet. This could be attributed to increased air flow at the air manifold inlet. At the exhaust outlet, temperature decrease could be due to the increased surface area of the flue. This increase in air flow may be desirable if a fuel cell stack were operating within this system.

Table 5.4 Impact of increasing the fuel flow and insulation, on the thermal profile, of the verification cell components (%)

	Air and Exhaust manifolds	Exhaust stack
Increasing Fuel Flow		
For non-insulated:		
800-1200 mL min^{-1}	21 %	30 %
1200-1600 mL min^{-1}	18 %	21 %
Impact of Insulation		
At fuel flow:		
800 mL min^{-1}	14 %	74 %
1200 mL min^{-1}	22 %	90 %

The % increase in temperature is = $(\Delta T/T_i)x100$, where $\Delta T = T_f - T_i$, T_i is the initial temperature, and T_f is the latter temperature.

Increasing the flue width decreased all temperatures. The averaged temperature for all solid components (air and exhaust manifolds, and exhaust stack) decreased by 7, 8 and 9% for fuel flows of 400, 800 and 1200 mL min^{-1} respectively. The following was thought to produce this temperature decrease:

- Increased heat lost through radiation from the top of the exhaust manifold, (combustion zone), which is more exposed to the surroundings,
- The larger surface area of the flue behaves as a heat sink,
- A larger volume of air is being drawn through the system (postulated).

The temperature distribution of the verification cell at thermocouple locations E4, E5, and E6 was axis-symmetric and the recorded temperatures were within 3°C.

A study of the steady state characteristics of the verification cell displayed that areas closer to the combustion zone reached steady state more quickly. The insulated system also took longer to reach steady state due to the increased heat capacity of the insulation. In contrast, a study on the rate at which the verification cell cooled displayed the opposite behaviour. The non-insulated system and the insulated system with the increased flue width cooled to approximately the same temperature, over 50 minutes (for the air and exhaust manifolds). The exhaust stack of the non insulated system cooled more quickly.

Restricting the flue (exhaust) outlet from a flow area of 1773 x 10^{-6} m^2 to 79 x 10^{-6} m^2, increased the temperature by 200 to 400°C in the combustion zone. When the exhaust outlet was further reduced to a flow area of 20 x 10^{-6} m^2, the temperature declined. The data indicate that the verification cell can operate with significantly reduced inlet and outlet flow areas.

The air flowing into the air manifold was approximately 100°C less than the air manifold walls.

An approximate relationship between fuel flow and the hydrogen flame temperature and dimensions (approximated as a cylinder) were determined using thermocouple and visual photographic methods:

$$T_F \approx -4913(fv^2) + 4003(fv) + 281 + 273.15 \quad (5.1)$$

$$czh \approx 0.0883(fv) + 0.0044 \quad (5.2)$$

$$czw \approx 0.0196(fv) + 0.0109 \quad (5.3)$$

T_F = Flame temperature

czh = Combustion zone height

czw = Combustion Zone width

fv = Fuel velocity.

REFERENCES - Chapter Five

1 R. J. Boersma, N. M. Sammes, and C. Fee, *J. Power Sources* 86, **2000**, pp. 369-375.

CHAPTER SIX

CHAPTER SIX

Modelling Results and Discussion

6.1 Introduction

This chapter presents the results obtained from the verification cell models. The discussion focuses on addressing the objectives (Section 4.2.1) to assess ANSYS® for modelling the verification cell, as a prelude to modelling SOFC stack housing configurations. The effect of the ANSYS® program options and how the model is configured are addressed. The approach to simulating the heat generated from combustion begins with a flame study followed by including the combustion codes (flame model) in the verification cell model. Experimental data are used to assess and calibrate the standard configuration of the verification cell model.* The effect of insulation, changes in flue height and width are investigated. Preliminary data for tracking mass fractions of individual gas species and the effect of radiation (instead of convection and conduction), are illustrated.

Chapter 5 presented a detailed explanation of the experimental data obtained from testing the verification cell. Therefore, this chapter will contain brief explanations of the modelling work highlighting comparisons between computer modelled, and experimental data.

Temperature profile plots are given in °C. Plots for steady state temperature solutions generated by ANSYS® are in K, as are all temperature data entered in the modelling codes.

Abbreviations used in this chapter include: ADI = adiabatic, HG = heat generation rate, htc = heat transfer coefficient, IN = insulated, N = numerical (computational) results, TC = temperature constraint.

* The standard configuration of the verification cell model is reviewed in Chapter 4, Section 4.4.

6.2 Program Specific Parameters

To assist in drawing conclusions from the computational data, parameters that are real and physical in nature must be distinguished from parameters arising from the modelling software. The problem type, mesh structure and size, number of iterations and type of solving methods (algebraic solver), are all solution options that can be selected or require input. The boundary conditions to apply need to be considered; the correct choice is not always intuitive. This section summarises the effect of each of the aforementioned options.

6.2.1 Problem Type

The type of problem has been characterised in Section 4.5.2. The solution options selected are:

- The fluid is compressible
- The flow is laminar
- The system is thermal (non-adiabatic).

The compressible option was required for modelling buoyant flows within the verification cell. The non-compressible option minimises heat transfer due to convection.

The fuel flow rates through the verification cell are low even when considering the increase in volume of the gas due to the increasing temperature. The comparison between solutions using the laminar option versus the turbulent option did not significantly affect temperature profiles.

6.2.2 Mesh

The thin walls of the verification cell were meshed using a mapped meshing procedure, ensuring regular elements throughout the solid regions of the model. Free mesh was applied in the gaseous regions. The aspect ratio between the solid regions and the gaseous regions led to the formation of poor elements in some areas of the free mesh. Retaining a consistent mesh across the boundaries was also problematic.

Variation in the free mesh gave small variations in data, especially at the fuel and air inlets. Various attempts were implemented to resolve the poor mesh in these regions, but with limited success. The effect on the overall data was insignificant compared to the other contributing factors, which are presented in the remainder of this chapter.

The mesh shape and size had a significant effect on data and the iterations required to achieve convergence for the same steady state result. Fewer iterations were required for finer meshes to achieve a given result. However, refining the mesh becomes important in areas where large gradients exist. In the verification cell, large temperature gradients are prevalent in the combustion zone, where mesh refinement had the most significant effect on results. Refining the entire model resulted in small variation in results compared to refining the combustion zone alone. Typically, the refined combustion zone mesh lowered temperature values and increased resolution of velocity plots. The lower limit on mesh size was set by factors such as computer memory, time required for post processing results and, at very small element size, computational limitations (discussed below).

6.2.3 Number of Iterations

Increasing the number of iterations reduced overall temperature and increased the heat transferred. The same effect is achieved with a refined mesh, typically about 5 to 10 % between simulations, but the effect depended on the type and distance from the heat source. Data for 50-150 iterations were comparable. At 300-600 iterations, the solution became unstable with reverse flows occurring down into the flue (which was not observed in the experimental work). This was attributed to numerical error such as truncation (rounding) error.

6.2.4 Solver Options

The tri-diagonal matrix algorithm (TDMA) is the default solver for the velocity equation (an approximate solver), requiring only the number of iterations (sweeps) to be specified. The other solvers available are described as exact methods and include the conjugate residual method and the preconditioned conjugate residual or gradient methods. The exact solvers iterate to a specified convergence criterion. In this work the TDMA was used for solving all but the energy equation, which was solved using

the conjugate residual method. The exact methods were investigated and required more parameters, such as relaxation and convergence criteria and search direction parameters, to assist the more direct solvers on their path to a solution. An improvement in convergence was not observed with the exact methods.

6.2.5 Convergence and Result Error Checks

The convergence monitor is displayed during an interactive session. An example of a multiple species solution being solved is displayed in Figure 6.1. The convergence monitor plots the normalised rate of change for the degree of freedoms of interest versus the number of iterations. An ideal solution's rate of change will decrease with the number of iterations. Typically, convergence is met when the normalised rate of change becomes very small (1.0E-07 or smaller), or when the plot levels out. All flame and the verification cell models investigated only achieved a weak convergence (normalised rate of change between 1.0E-01 to 1.0E-03). Convergence rarely improved beyond 50 iterations and depended on mesh (element) sizes, type of heat source and many other factors.

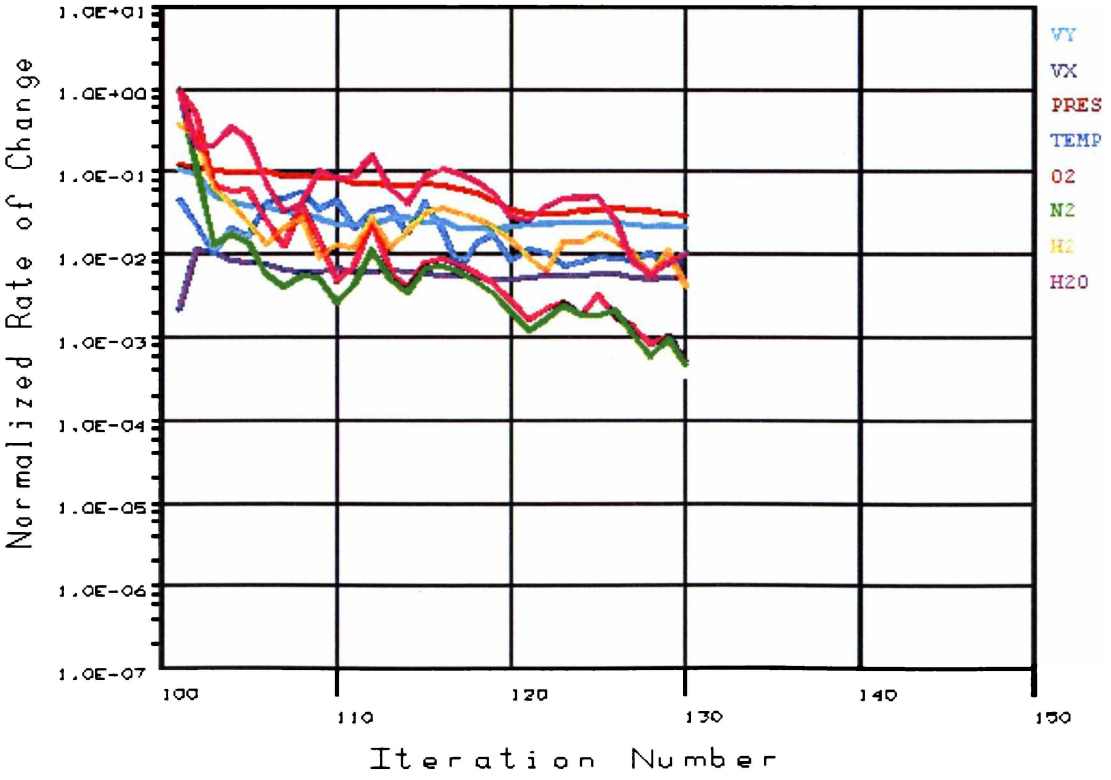

Figure 6.1 Snapshot of the ANSYS® convergence monitor (multiple-species problem being solved, first iteration number 101).

The *jobname.pfl* file generated by the ANSYS® program while solving a problem, includes a mass and energy balance, for mass flow and energy, entering and exiting the system. The values output in the *Jobname.pfl* file rarely balanced, for either the mass or energy when solving for the verification cell. This is expected because the TDMA solver relaxes the momentum equations to provide a stable solution and conservation laws are not strongly enforced. However, even with the more exact solver implemented, the final convergence was approximately the same. Other utilities for checking mesh quality were not available for checking models with FLOTRAN elements.

6.2.6 Summary

The low flow rates in the verification cell enable an unstructured mesh to be used and the laminar solution option to be selected. The results obtained from the computer models developed and presented in this thesis are very dependent on the mesh shape, size and quality, and the number of iterations. The extent that program specific parameters affect data were found to be as significant as selecting the correct boundary conditions (real world factors). It is worth stating that the finite element method is an approximate method, and radiative heat transfer has not been coupled. Thus care is required when comparing computational and experimental data.

6.3 Fuel Flow Rate and Heat Generation

The results for the flame model are presented in this section, along with the including the combustion code in the verification cell. Two methods are used for simulating the heat source, or flame:

1. Fixed heat generation rate (body load)
2. Fixed temperature (degree of freedom constraint).

The objective of the empirical flame study was to identify a relationship between fuel flow rate, flame temperature and flame profile. The parameters and data values derived from the experimental work are used for modelling the heat source (Table 6.1). Parameters for hydrogen-air combustion include fuel velocity (Fv), combustion zone width (czw), combustion zone height (czh), flame temperature (T_F), and heat put into the system (Hg). These parameters were determined empirically (see Section 4.5). Combustion zone parameters are representative of the empirically defined flame profile, or flame area as referred throughout this chapter.

Table 6.1 Heat source parameters and data

Flow rate (mL min^{-1})	Fv (ms^{-1})	czw (m)	czh (m)	T_F (°C)	Hg (w)
400	0.1	0.0064	0.0132	905	79
800	0.19	0.0073	0.0212	1137	132
1200	0.29	0.0082	0.0300	1301	202
1600	0.38	0.0092	0.0379	1365	264

6.3.1 Flame Model Study

The flame was simulated with either a heat source load (heat generation rate, Hg) or a temperature constraint applied to either a fixed area or a calculated area. The fixed area was equal to that calculated for a fuel flow rate of 1200 ml min^{-1} (0.29 ms^{-1}). Figures 6.2, 6.4, 6.6 and 6.8 show data derived from the axisymmetric flame model (described in Section 4.5.1).

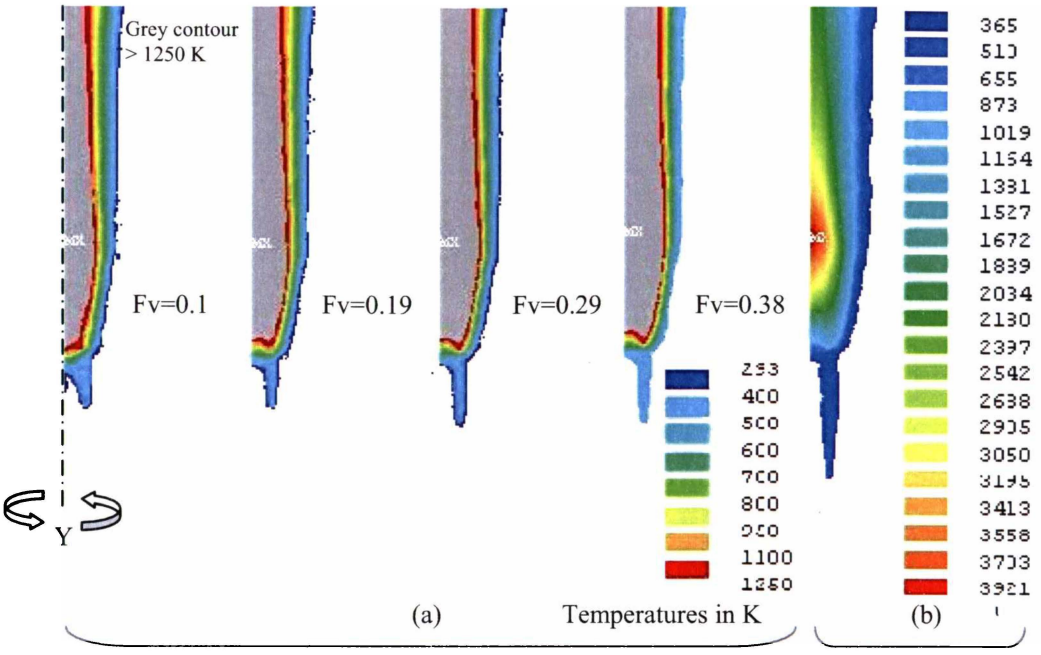

Figure 6.2 Temperature solutions with the calculated heat generation rate applied to a fixed flame area a) for Fv of 0.1, 0.19, 0.29 and 0.38 ms^{-1} represented by 9 contour plots and b) a 50 contour plot at Fv = 0.38 ms^{-1} (60 iterations).

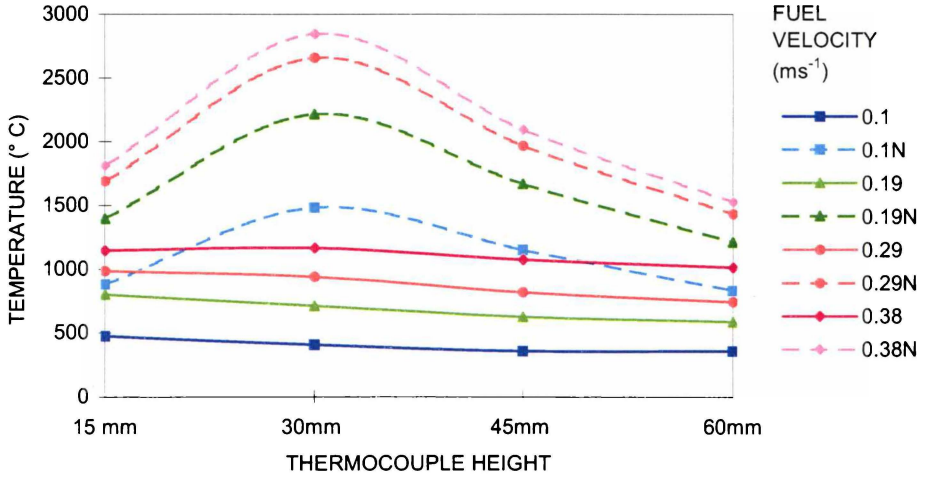

Figure 6.3 Temperature profiles of simulated flames illustrated in Figure 6.2, compared with experimental data at test flow rates. Note, 0.1N-0.38N refer to simulated (numerical) results.

When the heat generation rate was applied to a fixed flame area, theoretical temperatures were higher and did not vary as consistently with fuel velocity as the empirical results. Using a fixed flame area did not generate a temperature profile that agreed with the experimental data. Note the tail below the flame profile in Figure 6.2 is the thermal signature of the fuel tube.

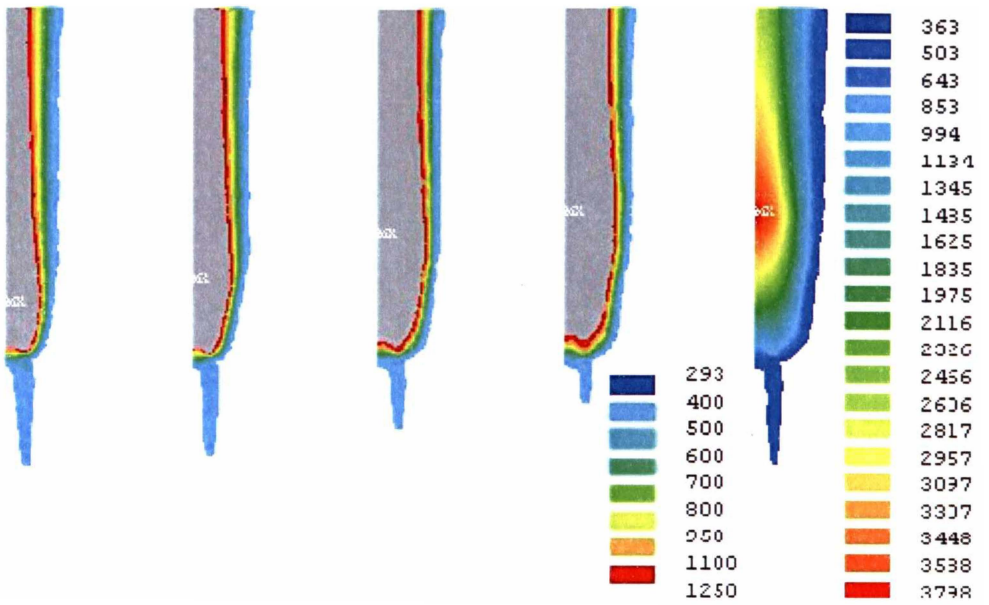

Figure 6.4 Temperature solutions using calculated heat generation rate applied to a calculated flame area, a) for Fv of 0.1-0.38 ms^{-1} represented by 9 contour plots, and b) a 50 contour plot at Fv = 0.38 ms^{-1}.

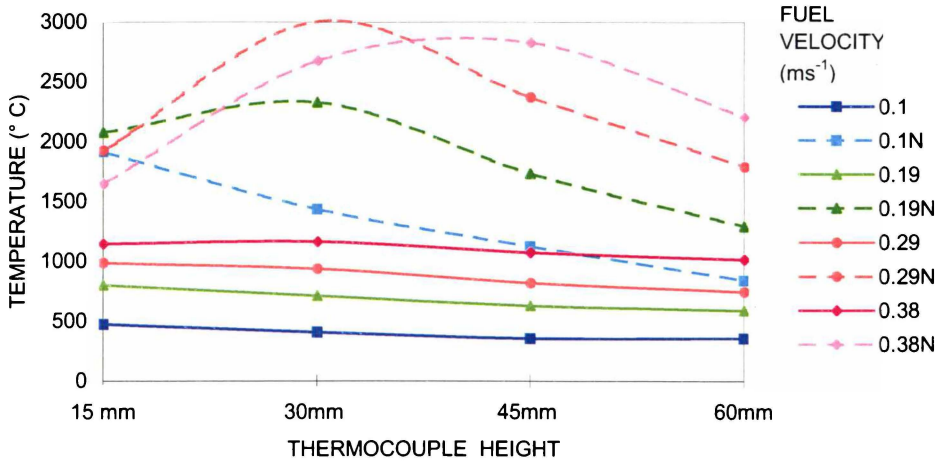

Figure 6.5 Temperature profiles for simulated flames illustrated in Figure 6.4, compared with experimental data, at Fv = 0.1-0.38 ms^{-1}.

Figures 6.4 and 6.5 illustrate simulated results for a heat generation rate applied to a calculated flame area. The temperatures are high, as observed in Figures 6.2 and 6.3, and have a unique temperature profile, the width of the flame area increases with increasing fuel velocity. The results indicate a maximum moving up through the flame with increasing fuel velocity, inconsistent with experimental data.

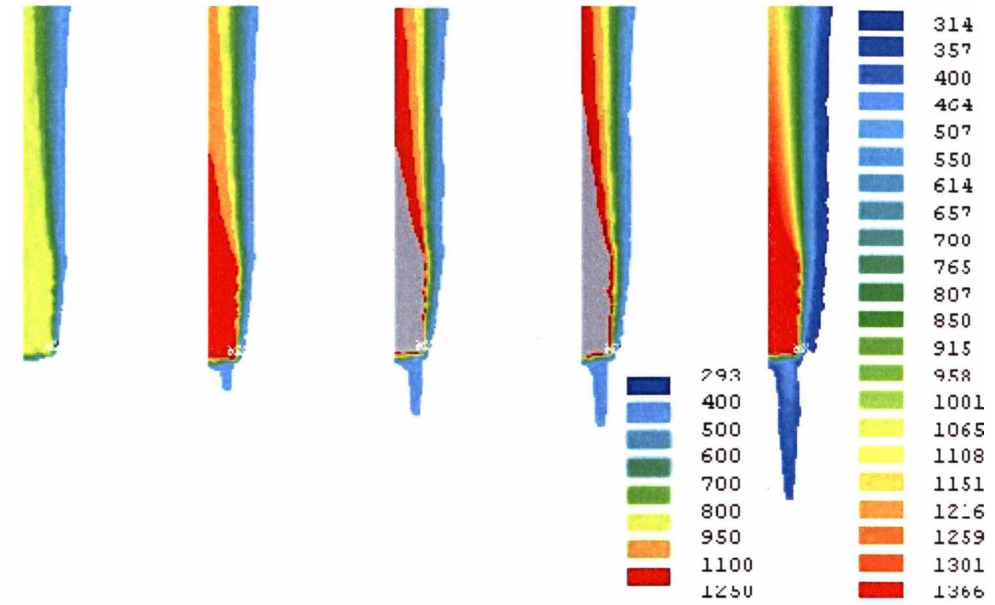

Figure 6.6 Plot of temperature solutions using calculated temperature constraint applied to a fixed flame area, a) for Fv of 0.1-0.38 ms^{-1} represented by 9 contour plots, and b) a 50 contour plot at Fv = 0.38 ms^{-1}.

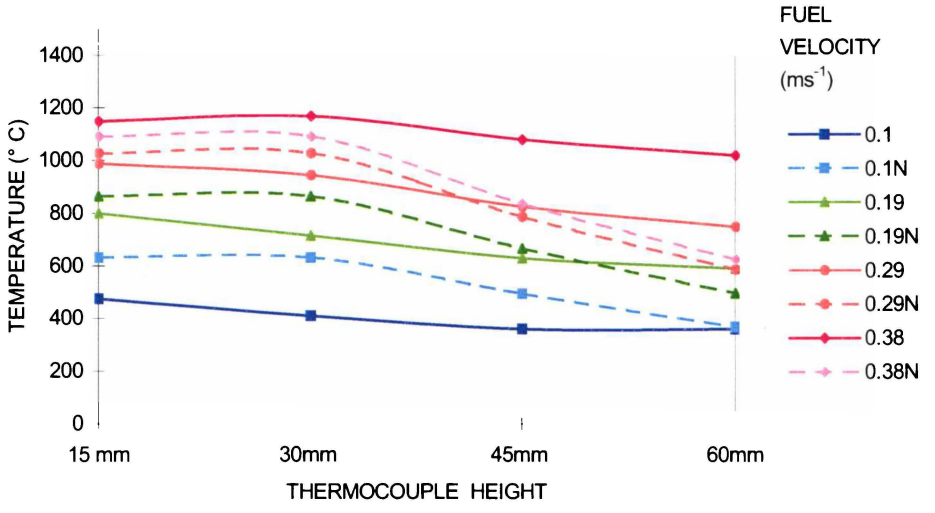

Figure 6.7 Temperature profiles for simulated flames illustrated in Figure 6.6, compared with experimental data, at Fv = 0.1-0.38 ms^{-1}.

Figures 6.6 and 6.7 illustrate the calculated temperature constraint, applied to a fixed flame area. The temperatures are lower than from the applied heat generation rate. A similarity with results in Figure 6.3 is the apparent peak temperature at 30 mm, a consequence of the fixed flame area. Visually, the fixed flame area approach does not represent the flame profile very closely (see photographs in Appendix E2).

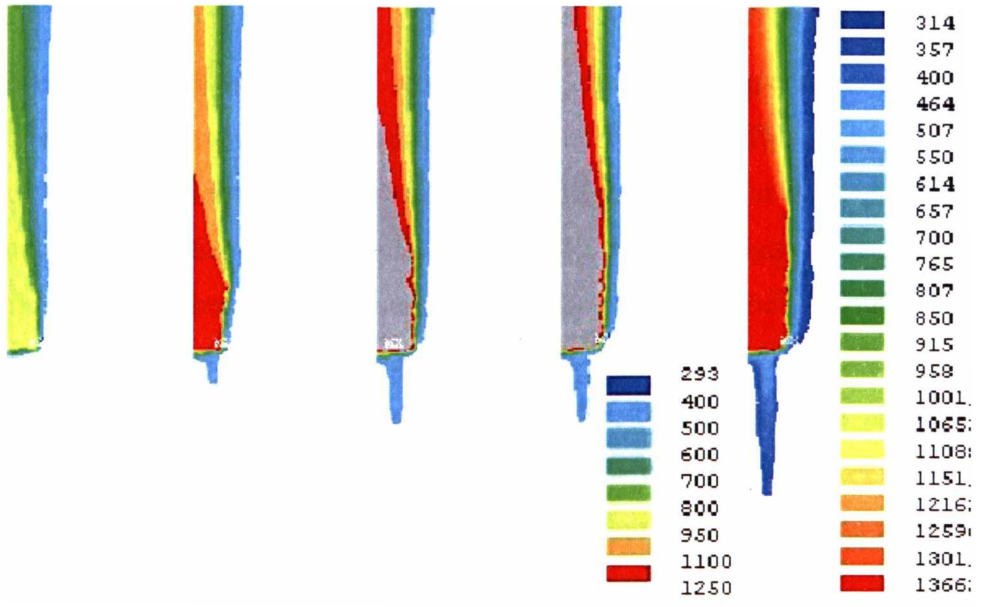

Figure 6.8 Temperature solutions using calculated temperature constraint applied to a calculated flame area, a) for Fv of 0.1-0.38 ms^{-1} represented by 9 contour plots, and b) a 50 contour plot at Fv = 0.38 ms^{-1}.

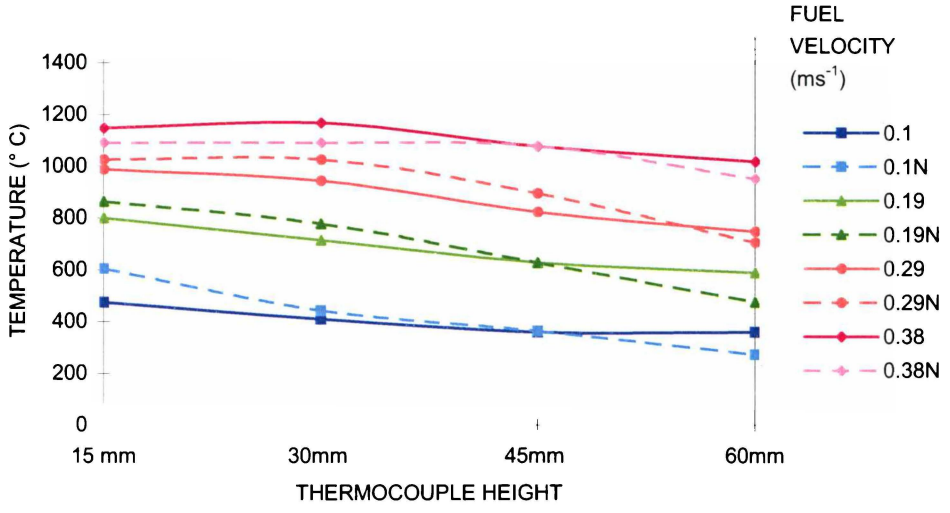

Figure 6.9 Temperature profiles for simulated flames illustrated in Figure 6.8, compared with experimental data, at Fv = 0.1-0.38 ms^{-1}.

Figures 6.8 and 6.9 illustrate the calculated temperature constraint applied to a calculated flame area. These results compare well with the experimental data. This is expected because the temperature constraint is derived from the experimental data to which the simulated results are being compared. Visually, the calculated flame area approach also represents the flame profile poorly. However, considering the uniform nature of the experimental data, the actual application of the calculated flame area approach is justified.

If the experimental approach is reconsidered, then the temperature data are not absolute either as they represent a cross section of the flame. The actual temperature at the flame periphery changes abruptly so a slight change in the position of any thermocouple in the thermocouple array could produce significant variation in recorded temperatures. This observation is also valid for the computer model if values are taken at slightly different locations to those previously used. Figure 10 displays the change in temperatures recorded when the data point is moved 1 mm nearer or away from the flame centre. At a fuel flow of 0.19 ms^{-1} (0.19N+), moving away from the flame centre decreases temperature in the mid regions of the flame (30 and 45 mm) by 200°C, using the calculated temperature constraint method. The result is similar if flame area is modified in a similar way.

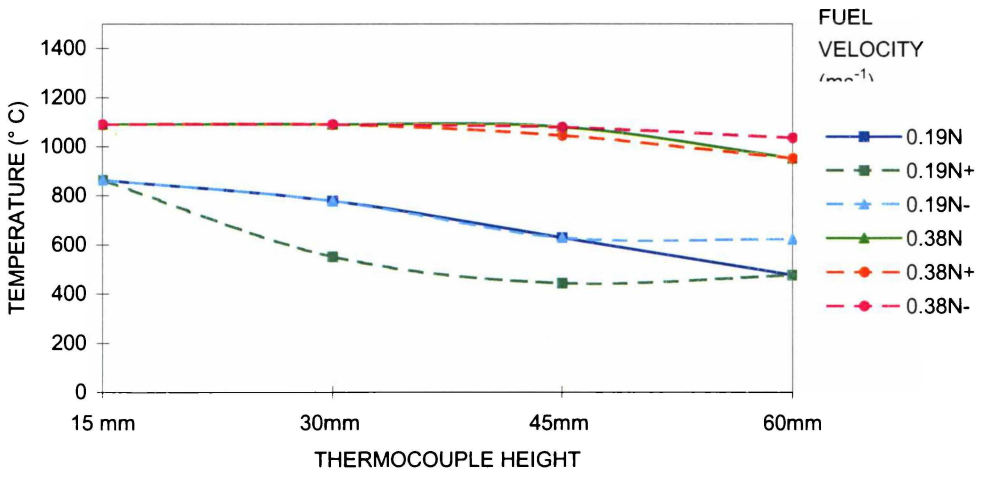

Figure 6.10 Temperature profiles for simulated flames at a Fv of 0.19 and 0.38 ms^{-1}, with thermcouple readings taken at 1 mm into the flame centre, N-, and at 1 mm further away from the flame centre, N+.

6.3.2 Applied Heat Generation Rate (Body Load)

Initial simulations of the verification cell (standard configuration) model, using the heat generation rate applied to a calculated flame area, produced higher temperature profiles than those recorded empirically. This trend is similar to the results generated in the flame model simulations (Section 6.3.1).

The calculation for the heat generation rate represents the maximum theoretical heat (enthalpy) generated by combusting hydrogen in air. To improve (approximately calibrate) the verification cell model results, the heat generation value (J m^{-3}) used in the model was reduced by a factor, referred to as the combustion efficiency, Ce. A Ce of 0.49 produced comparable results to empirical data (Figure 6.13). Thermal solutions for the verification cell at Fv =0.1, 0.19 and 0.29 ms^{-1} are in Figure 6.11 and the corresponding velocity plots are in Figure 6.12.

Unless otherwise indicated, all results presented in Sections 6.3 and 6.4 were solved with 150 iterations and the external wall of the verification cell set as an adiabatic boundary.

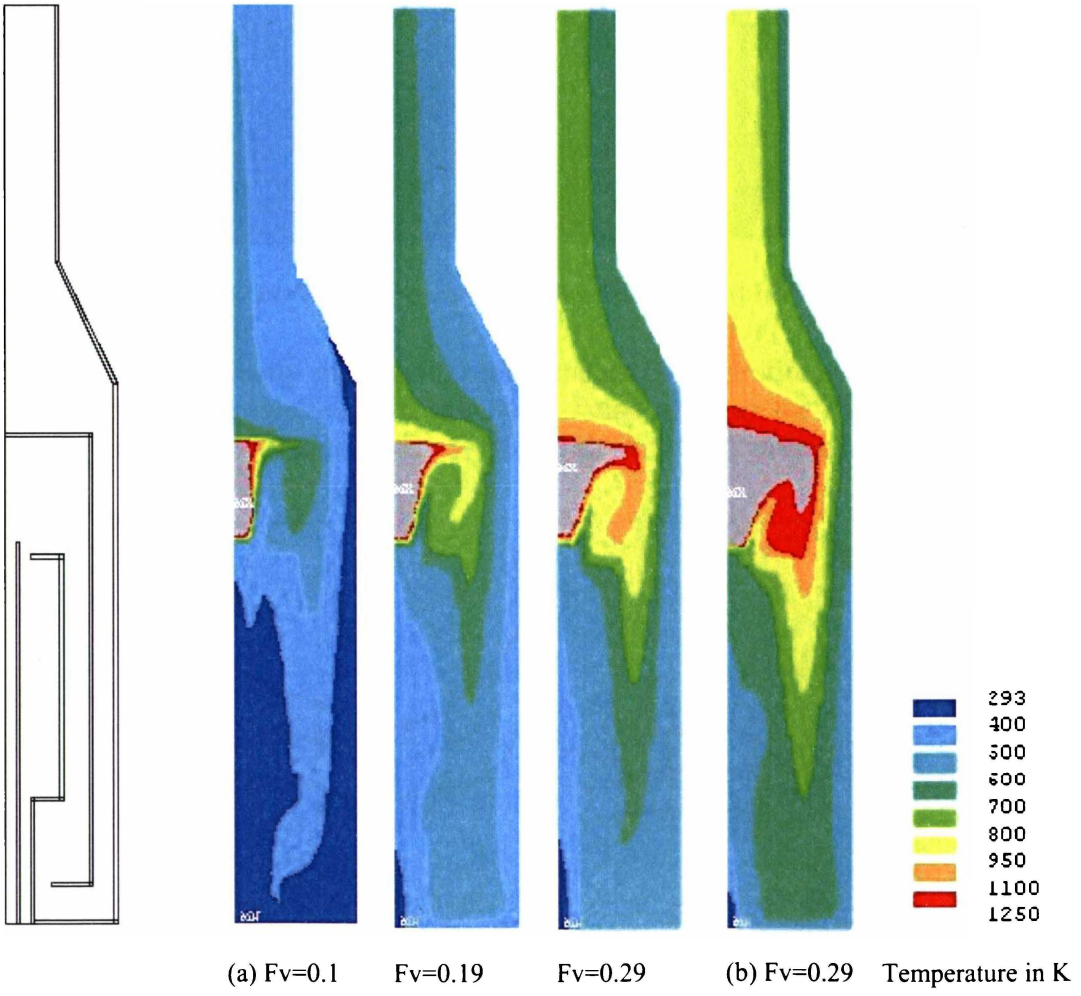

Figure 6.11 Temperature solutions for the standard configuration, with heat generation rate applied to a calculated flame area, a) for Fv of 0.1-0.29 ms^{-1}, Ce=0.49, and b) for Fv=0.29, Ce=1 (150 iterations).

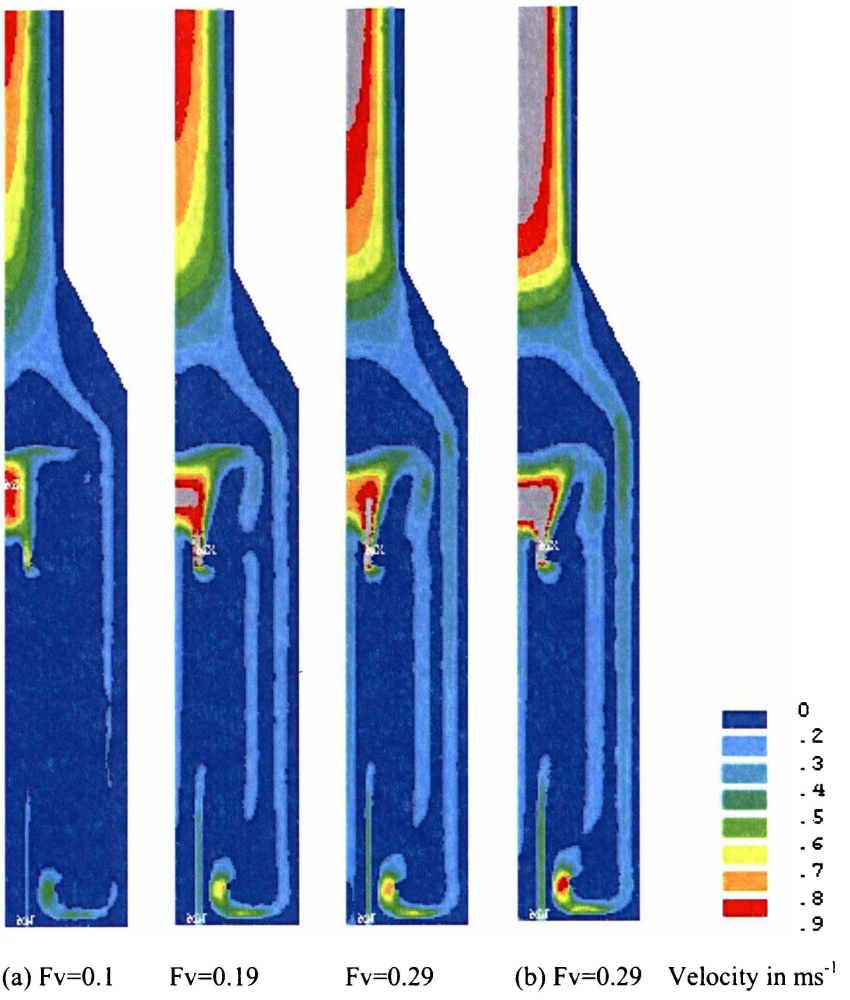

Figure 6.12 Velocity solutions for the standard configuration, with heat generation rate applied to a calculated flame area, a) for Fv of 0.1-0.29 ms^{-1}, Ce=0.49, and b) for Fv=0.29, Ce=1 (150 iterations).

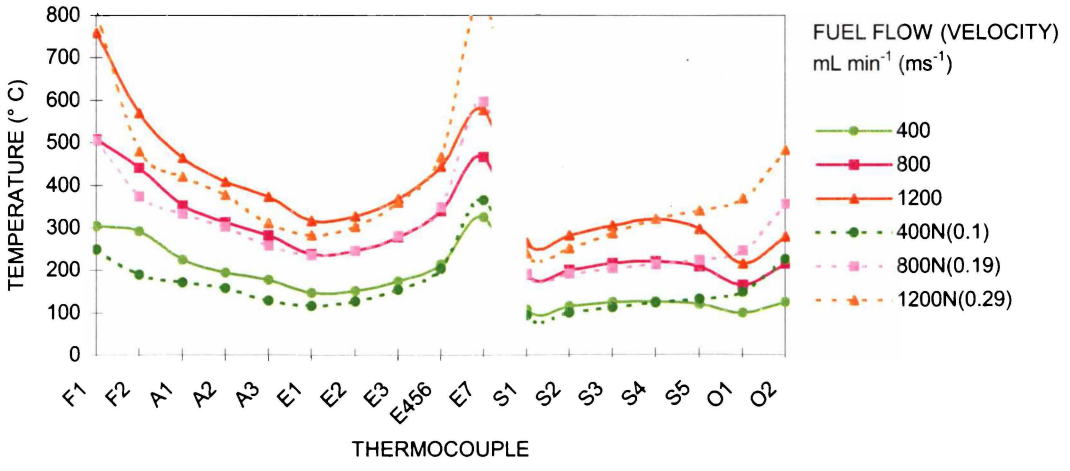

Figure 6.13 Temperature profiles for the standard configuration in Figure 6.11, compared with experimental data, at Fv =0.1-0.29. 400N(0.1), 800N(0.19) and 1200N(0.29) are simulated results.

6.3.3 Applied Temperature (DOF Constraint)

The temperature constraint applied to the calculated flame area produced lower temperature profiles than measured experimentally. The data trend was similar to data generated in the flame model simulations, with an expanded temperature distribution.

In an attempt to obtain a temperature profile that agreed better with empirical results, several parameters were modified; the combustion zone width was increased by a factor of 1.5 and 1.6 and T_F was increased by 400°C and 300°C. The effect of changing these parameters on the simulation and the empirical data, at Fv=0.19 ms^{-1}, are shown in Figure 6.14. Temperature profiles for the modified parameters, represented by 800N(a) and 800N(b), agreed with the experimental temperature profile.

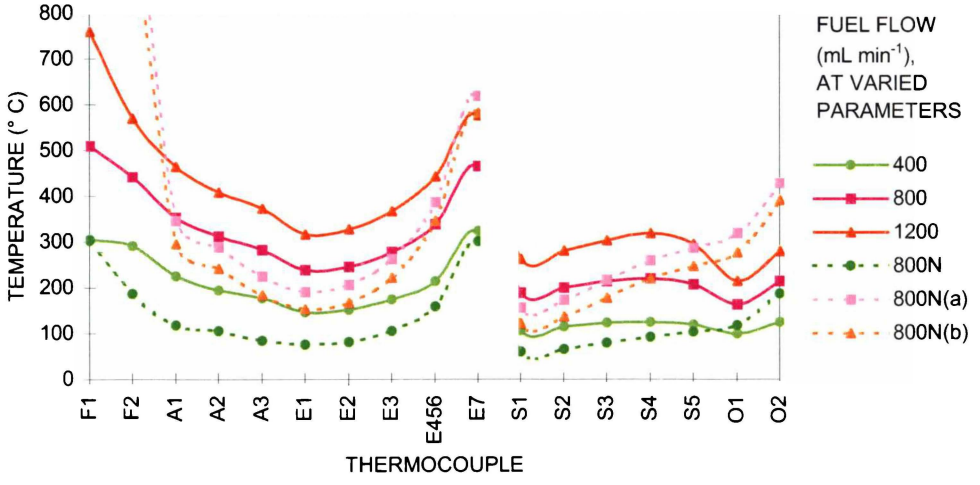

Figure 6.14 Temperature profiles for the standard configuration illustrated in Figure 6.15, 800N is the calculated temperature constraint, 800N(a) is czw*1.6, T_F+300°C, and 800N(b) is czw*1.5, T_F+400°C, compared to experimental data at Fv = 0.1-0.29 ms^{-1}.

Figure 6.15 displays the solutions for the temperature and velocity distributions at Fv=0.19 ms^{-1}.

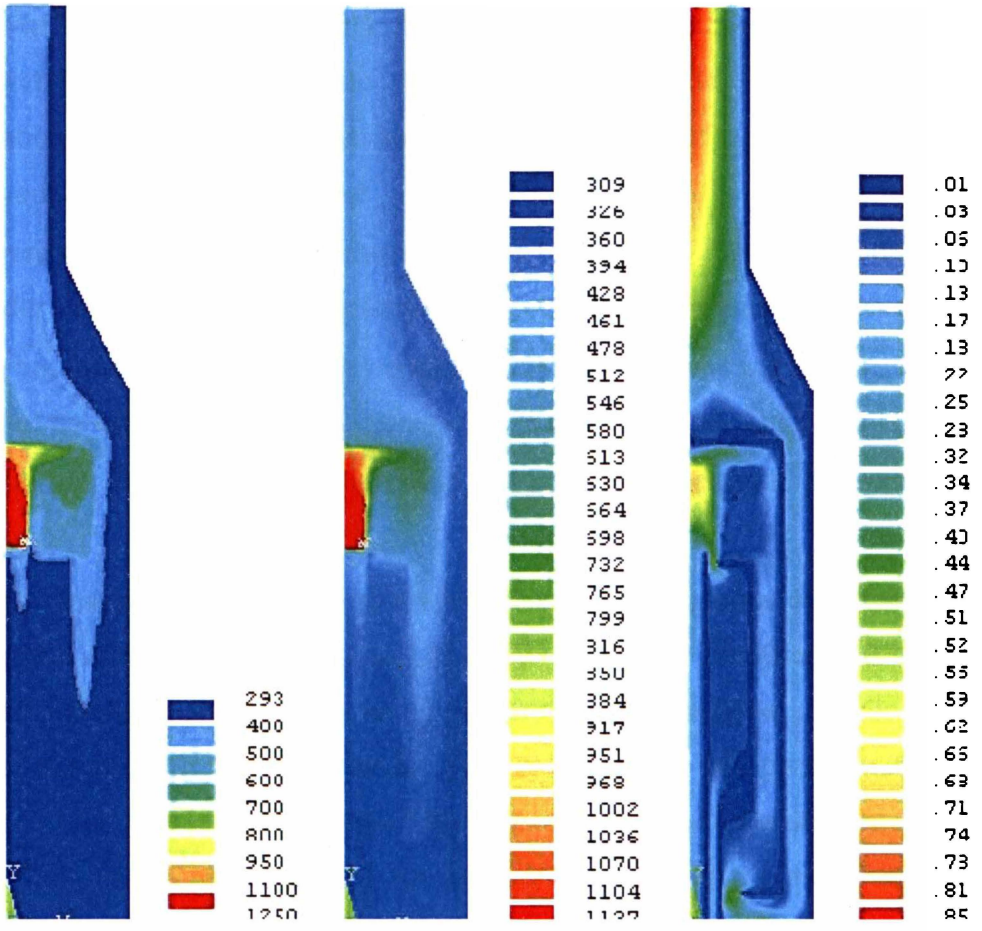

Figure 6.15 a) and b) 9 contour plot and 50 contour plot, respectively, of temperature solutions for the standard configuration, with temperature constraint applied to a calculated flame area, at a Fv =0.19 ms^{-1}, and c) velocity solution, represented by 50 contour plot.

6.3.4 Summary Discussion

The thermal trends exhibited by the flame model were retained when the flame model (combustion code) was included in the verification model (Thermal – Mass Flow model). The heat generation rate produced higher temperatures, and the temperature constraint code produced lower temperatures. The following adjustments to the codes produced better agreement between simulated and experimental data:

1. Applying a combustion efficiency factor to the heat generation rate, effectively reducing the amount of energy put into the verification cell.
2. Increasing the combustion zone width and the flame temperature, for the applied temperature constraint.

A consistent relationship between fuel flow rate and flame temperature profile was not accurately reproduced for the verification cell model. Three primary simplifications of the modelling codes contribute to lack of agreement between computational and experimental data:

1. The combustion code is a non-chemical model (empirically based) and does not consider chemical and thermodynamic behaviour of the combustion reaction.
2. Applying the flame model in the verification cell model does not account for the effect of the confined (enclosed) combustion manifold, on the flame profile .
3. Heat transfer by radiation is not included in the results presented in this section.

These simplifications contribute to the loss of an accurate representation of the flame properties and, consequently, the thermal characteristics of the modelled heat source. The overshoot observed at the centre of the heat generation zone was above the theoretical maximum for a hydrogen-air flame (Figure 6.2), and demonstrates the limitations of the flame model. Other factors that contribute to variation in results include having an accurate location for extracting data from the model and the modelling program issues discussed in Section 6.2.

6.4 Thermal – Mass Flow Model

The effect of insulation and increasing flue height and width on temperature distribution of the verification cell model are examined in this section. The first approach to modelling the insulation is to build the insulation into the model and apply a heat transfer coefficient to the external surface of the insulation. The second approach is to decrease the heat transfer coefficient on the external surface of the exhaust manifold, essentially simulating the effect of insulation. The first approach allows the heat distribution through the insulation to be studied while the second approach saves computational time, but at the expense of result detail. The verification cell model is parametric so changes in flue width (stack width) and flue height (stack height) are easily made.

6.4.1 Insulation

The effect of applying 2.54 cm of insulation to the external walls (surfaces) of the verification cell on the temperature profile is shown in Figure 6.16. The velocity solution (Figure 6.16a) provides information on gas velocities throughout the model, and indicates that gas flow is constricted at the air and exhaust manifold outlets. The velocity solution also identifies that the combustion zone and flue have high gas flows (also observed in Figures 6.12 and 6.15c). No experimental data was available to validate the velocity predictions. An example of a vector velocity plot is provided in Appendix F1

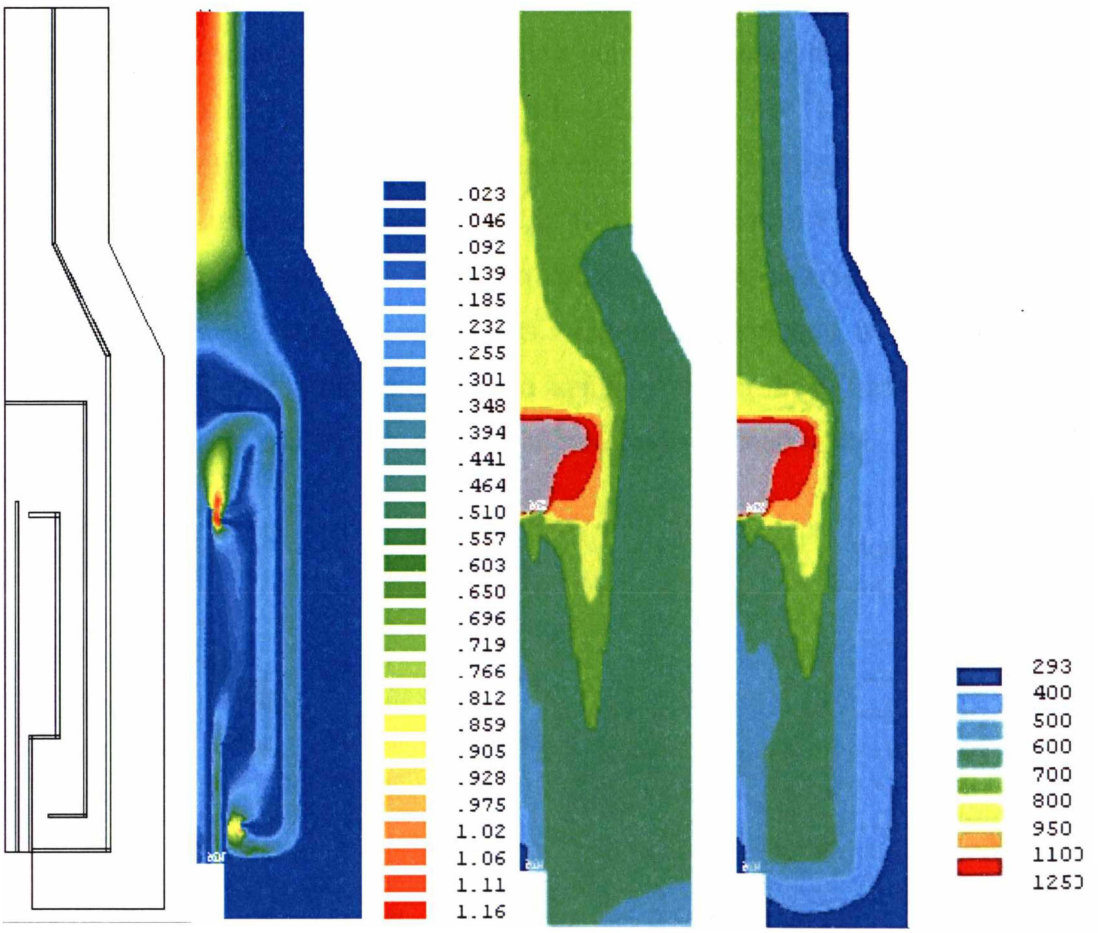

Figure 6.16 a) velocity and b) and c) temperature solution plots, for the standard configuration, with calculated temperature constraint applied to calculated flame area, insulated, at a Fv =0.19 ms^{-1}. Plot b), the standard configuration, with an adiabatic boundary condition, and c) heat transfer coefficient of 5 $Wm^{-2}K^{-1}$, applied to the external surface of the insulation.

Figures 6.16b and 6.16c show the effect of applying an adiabatic boundary condition and a heat transfer coefficient (5 $Wm^{-2}K^{-1}$) at the external surface of the insulation. The heat transfer coefficient lowers the overall temperature, and the adiabatic condition increases the temperature (Figure 6.17), as expected. The external boundary conditions affects mainly the exhaust stack (thermocouples S1-S5), with minimal increase at the interior components (air and exhaust manifolds, thermocouples A1-E5). The results for the insulated verification cell model are 100-200°C higher than the non-insulated verification cell model, with an adiabatic boundary condition at the external surface.

The difference in temperature profile for a non-insulated verification cell when heat transfer coefficients of 0 (adiabatic), 0.1, 0.5, and 5 $Wm^{-2}K^{-1}$ are applied to the external wall of the verification cell, and the insulated configuration (800N(IN-5)), with a heat transfer coefficient of 5 $Wm^{-2}K^{-1}$, are shown in Figure 6.18. The heat transfer coefficient has more effect on the temperature distribution of the exhaust stack, but less on interior components. Including insulation in the model gives significantly higher temperatures than applying lower heat transfer coefficients directly to the external surface of the non-insulated verification cell.

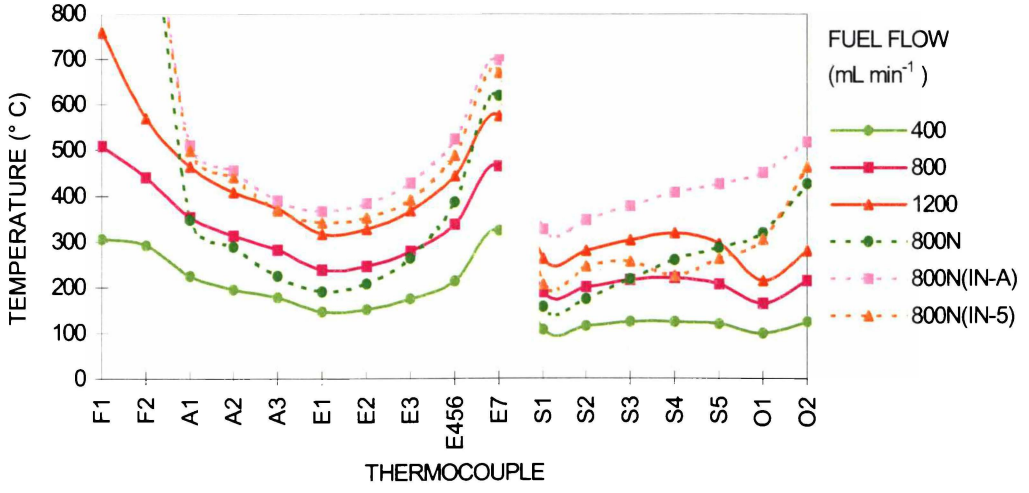

Figure 6.17 Temperature profiles for the standard configuration illustrated in Figure 6.16, compared to experimental data. 800N(IN-A) has the adiabatic wall boundary condition, and 800N(IN-5) has a heat transfer coefficient of 5 $Wm^{-2}K^{-1}$, applied to the external surface of the insulation.

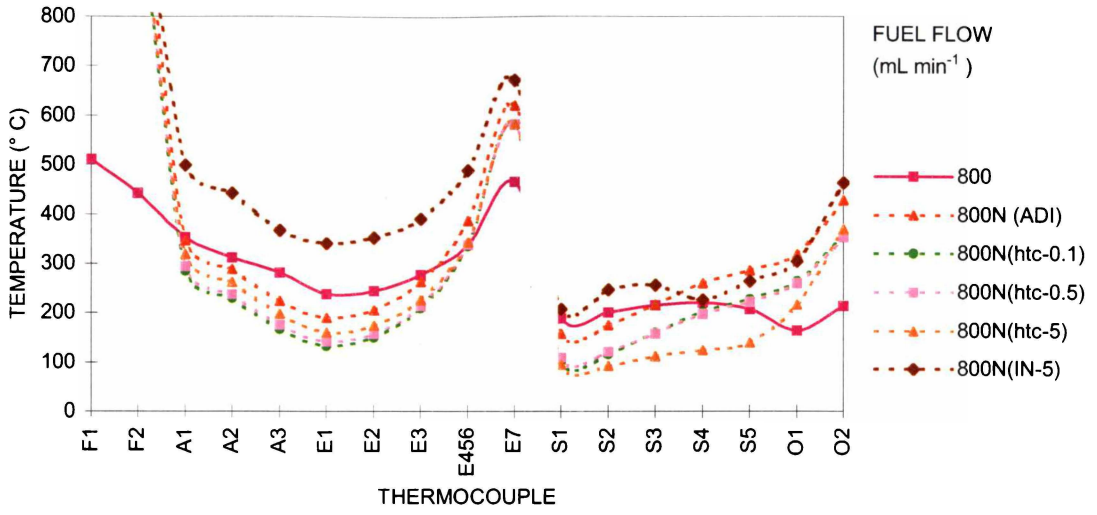

Figure 6.18 Temperature profiles for the standard configuration, with calculated temperature constraint, comparing insulated versus non-insulated, with adiabatic boundary condition and heat transfer coefficients of 0.1, 0.5 and 5 $Wm^{-2}K^{-1}$.

A closer examination of temperature data in Figure 6.18 show that increasing the heat transfer coefficient decreases temperatures in the exhaust stack region. However, the response for the interior is opposite; 800N(htc-0.1) has lower temperatures than 800N(htc-5). The interior temperatures are slightly lower because of lower heat loss at the exhaust stack. This may be because higher exhaust stack temperatures create more air flow, and introducing more cool air into the air manifold. Data from the adiabatic solution does not support this explanation.

6.4.2 Increasing Flue Height

The two approaches to simulating the heat source produced different results for the effect of increasing flue height in the verification cell. Velocity and temperature plots for the two heat sources are given in Figure 6.19. The heat generation rate (Figure 6.20; 800N(HG-300mm)) displays a similar trend in tempature profile data to the empirical data. The temperature constraint (800N(TC-300)) produces signficantly lower values, with an over temperature in the combustion zone due to the temperature constraint impinging on the region where thermocouple data (F1 and F2) is collected.

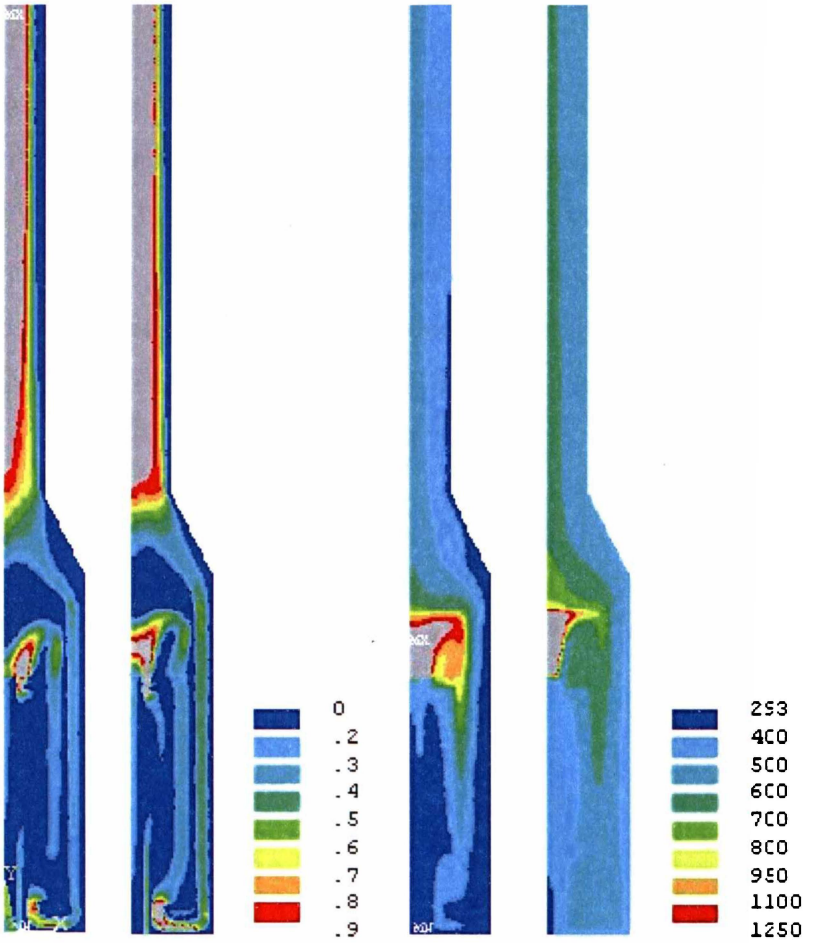

Figure 6.19 Velocity and temperature solutions for increased flue height to 300mm, at Fv =0.19 ms^{-1}, with adiabatic boundary condition at external surface. a) velocity, and c) temperature plots, for applied temperature constraint, b) velocity, and d) temperature plots, for applied heat generation rate, to calculated flame area.

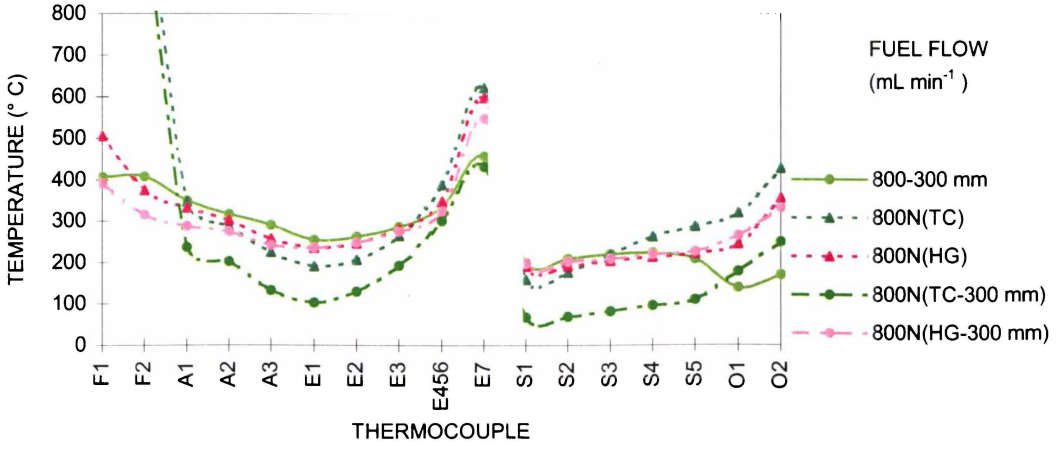

Figure 6.20 Temperature profiles for solutions of the standard configuration with a 200 mm flue extension (300 mm total flue height) illustrated in Figure 6.19.

6.4.3 Increasing Flue Width

Data generated using the two different heat sources used to model the effect of increasing flue width were contrary to empirical results. Increasing flue width increased (Figure 6.21, Figure 6.22), rather than decreased temperature, as predicted by the simulations. Applying the temperature constraint delivered the higher temperature. The heat generation rate produced unstable results, with gases flowing down the inside wall of the flue (Figure 6.21b).

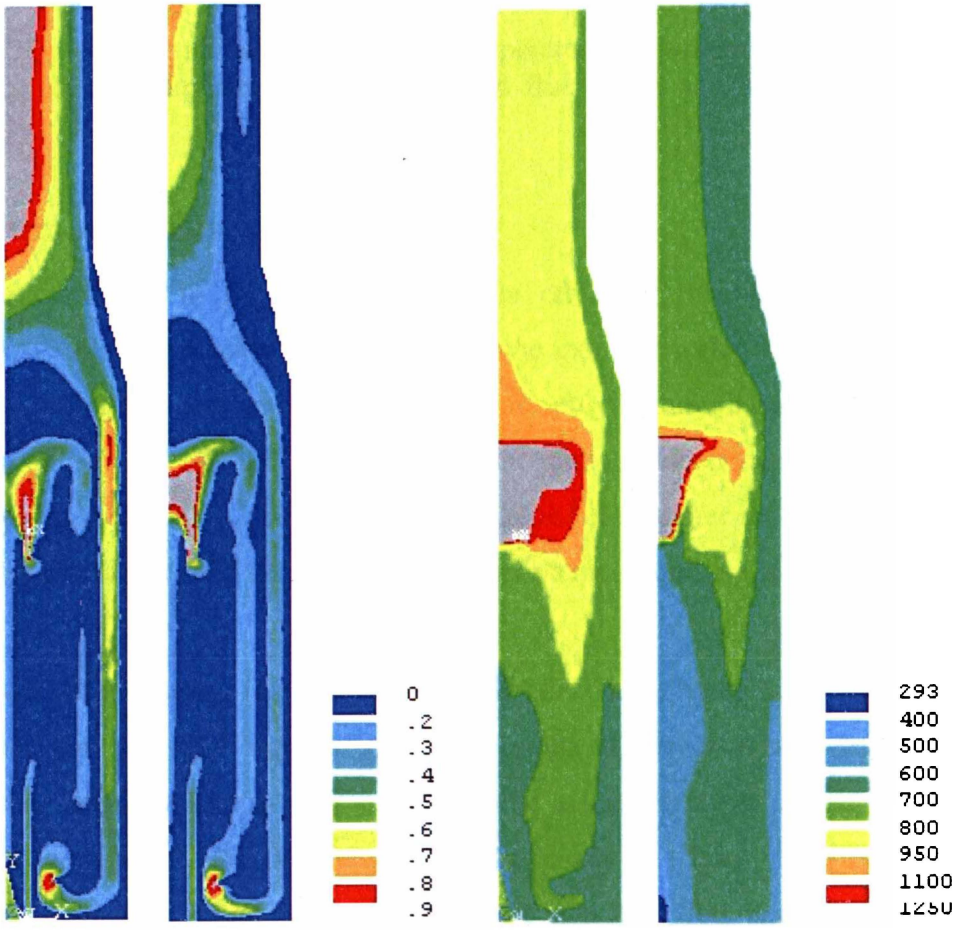

Figure 6.21 Velocity and temperature solutions for increased flue width to 76 mm, at Fv =0.19 ms^{-1}, with adiabatic boundary condition at external surface. a) velocity, and c) temperature plots, for applied temperature constraint, b) velocity, and d) temperature plots, for applied heat generation rate, to calculated flame area.

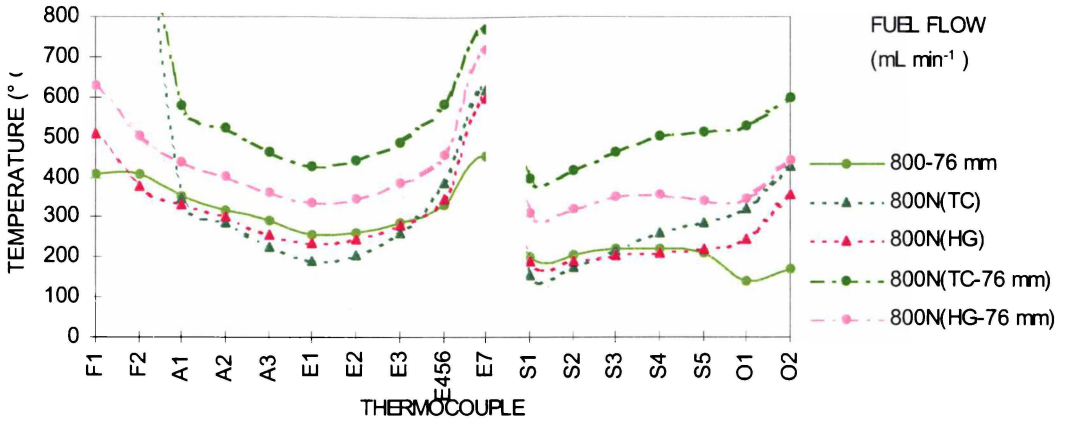

Figure 6.22 Temperature profiles for temperature solutions of the standard configuration with an increased flue width as illustrated in Figure 6.21.

6.4.4 Summary Discussion

Including insulation in the model allows the effect of insulation to be better represented. Insulation adds heat capacity to the external walls of the verification cell. Decreasing the heat transfer coefficient or applying an adiabatic condition to the external surface of the verification cell predicts lower temperatures than measured experimentally. Using only a lower value heat transfer coefficient does not capture the effect that insulation has on the overall temperature profile.

Simulations for increasing flue height and width also do not agree with experimental data, with the opposite temperature trend produced for increased flue width. Simplifying the heat source was not successful at delivering a simple utility to simulate heat generated by the flame, with increasing fuel flow. This conclusion reinforces those summarised in Section 6.3.4. Section 2.5 offers further explanation about combustion and flame characteristics. Further detail on assumptions and simplifications can be found in Section 4.5.5.

6.5 Multiple-Species Module

Results presented in this section demonstrate the multiple-species option and some other properties that are available for plotting from a simulation done using

ANSYS®. Opportunities for applying the multiple-species results to an SOFC model are illustrated.

6.5.1 Reactant and Product Gas Flows; H_2, O_2, N_2 and H_2O

The viscosity and density are calculated during a simulation (Figure 6.23a and b). During the solution, the values of these properties influence the temperature and velocity solutions, which in turn, influence the viscosity and density distributions. The solution process is iterative, solving and updating between fields.

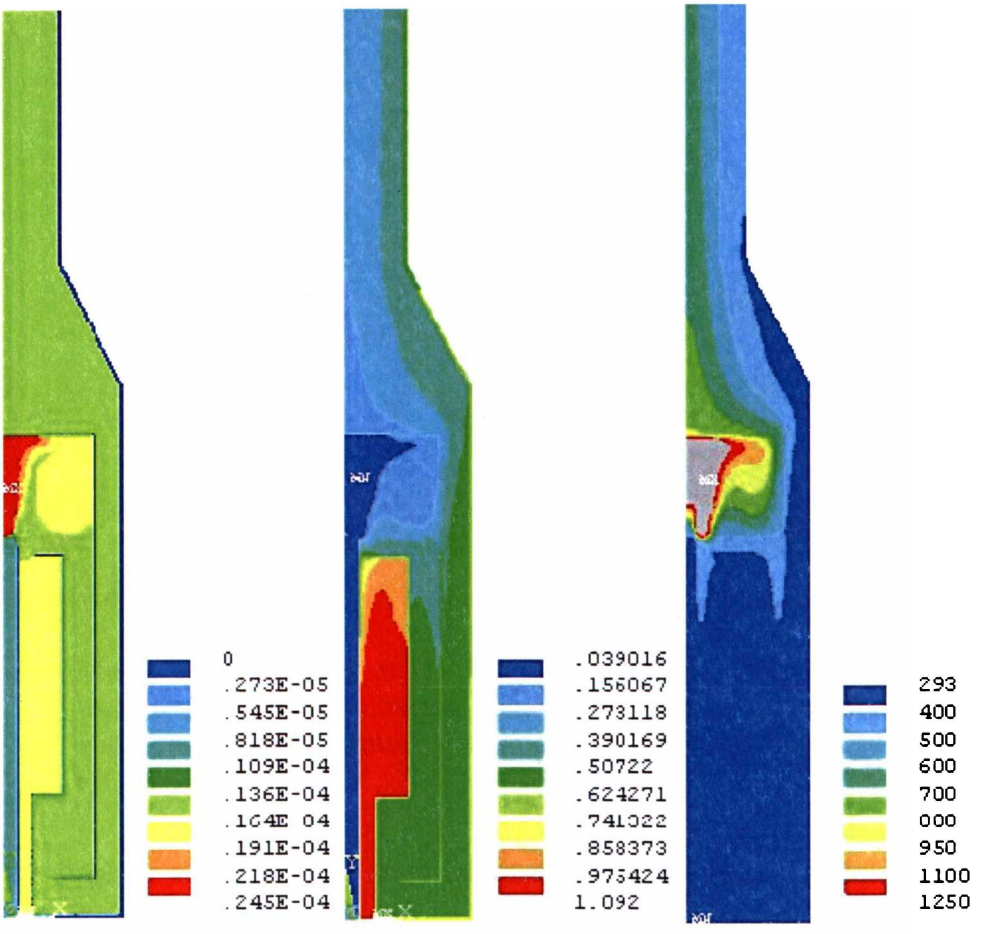

(a) Viscosity in kg m^{-3} (b) Density in kg m^{-3} (c) Temperature in K

Figure 6.23 Multiple-specie plots of; a) viscosity, b) density and c) temperature solution for the standard configuration, with temperture constraint applied to a calculated flame area, at a Fv =0.19 ms^{-1}.

The density distribution (Figure 6.23b) is related to the temperature distribution and gas properties. The similarity between Figure 6.23b and Figure 6.23c demonstrates how the decrease in density about the combustion zone (in and above) assists in

understanding buoyancy driven flow. The viscosity plot (Figure 6.23a) and the multiple-specie plots (Figures 6.24a-d) also exhibit similarity in distributions.

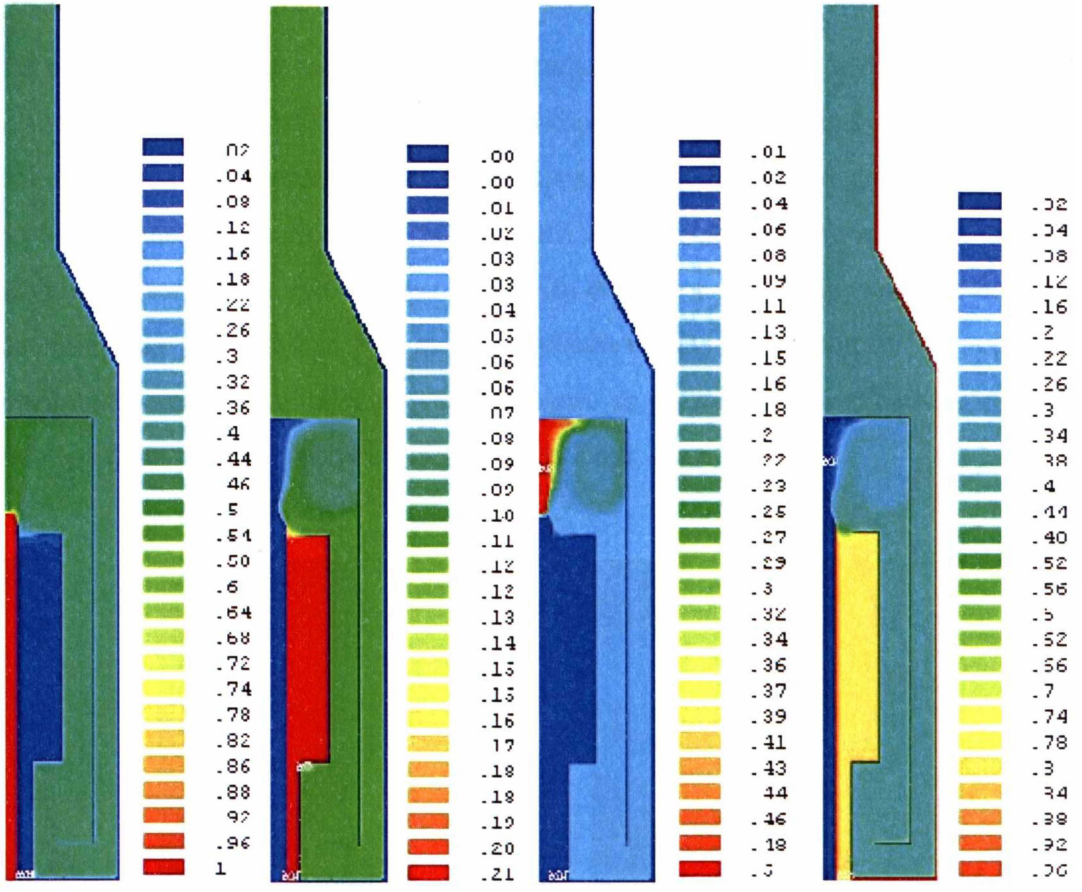

(a) H_2 – Mass fraction (b) O_2 (c) H_2O (d) N_2

Figure 6.24 Multiple-specie plots of; a) hydrogen mass fraction, b) oxygen c) water vapour, and d) nitrogen, solution for the standard configuration, with temperture constraint applied to a calculated flame area, at a Fv =0.19 ms^{-1}.

Figure 6.24 displays the change in mass fraction of the various chemical species flowing in the verification cell, and that are commonly used in an SOFC. The mass fraction of each species would be useful for studying reactants depletion and product formation during SOFC operation. The potential use of multiple-species results in an SOFC model are discussed in Section 4.6.

6.6 Radiation Module

The effect of radiative heat transfer is illustrated in this section. A solution is undertaken using a steady state analysis, and compared to the same analysis with the

radiation option included. These results are also compared to empirical results.

6.6.1 Effect of Radiation Matrix

The effect of including radiation in the simulations is illustrated in Figures 6.25a, c, e, and f, and compared to simulations without radiation in Figures 6.25b and d. Including radiant transfer reduces the temperature gradients and disperses the heat throughout the verification cell. The results agree well with the empirical results, particularly for the air and exhaust manifolds (Figure 6.26). The steady state result (no radiation) presented in Figure 6.27 indicates a more concentrated temperature distribution, with marginally higher temperatures at the air and exhaust manifolds and significantly lower temperatures at the exhaust stack.

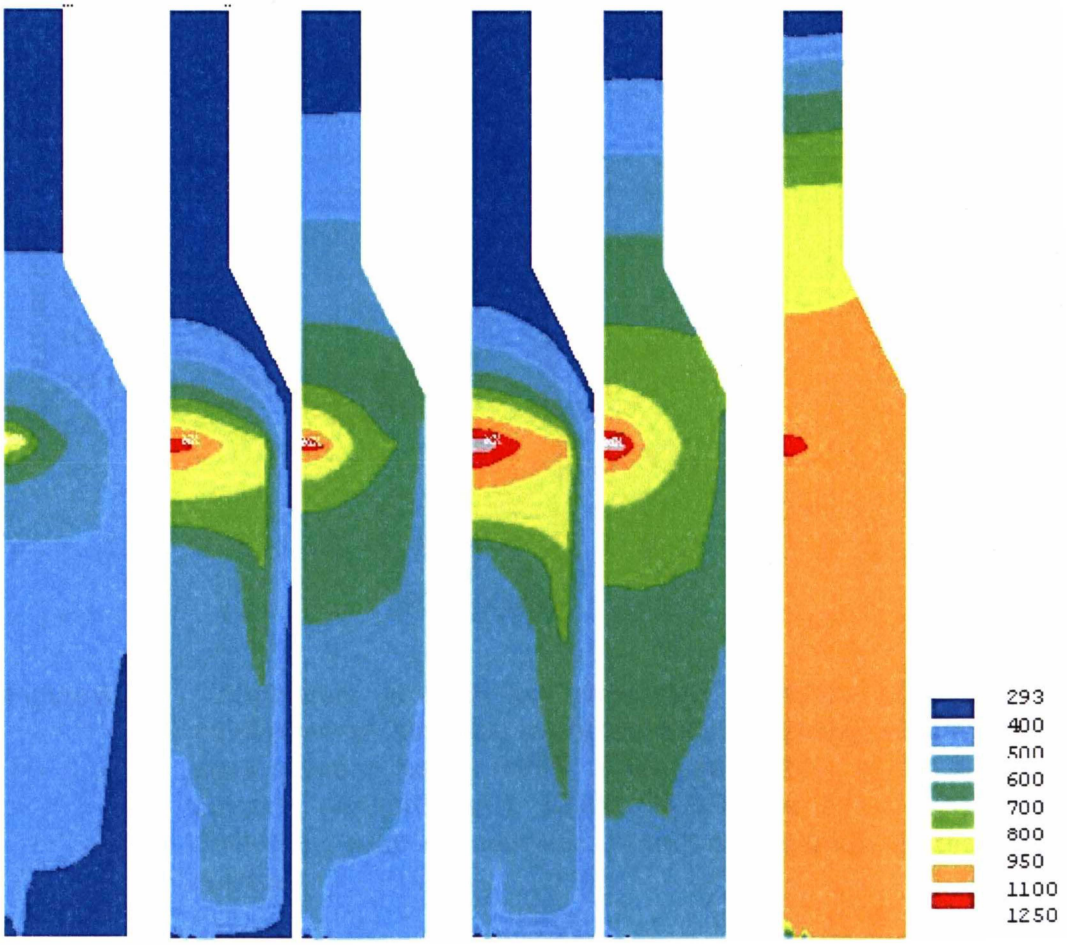

(a) R Fv=0.1 (b) NR Fv=19 (c) R Fv=0.19 (d) NR Fv=29 (e) R Fv=0.29 (f) R Fv=0.19 - adiabatic Temperature in K

Figure 6.25 Temperature solutions for the standard configuration, with temperature constraint applied to top of the exhaust manifold, comparing steady state solutions with radiative heat transfer, a), c), e), and f), and without radiative transfer, b) and d).

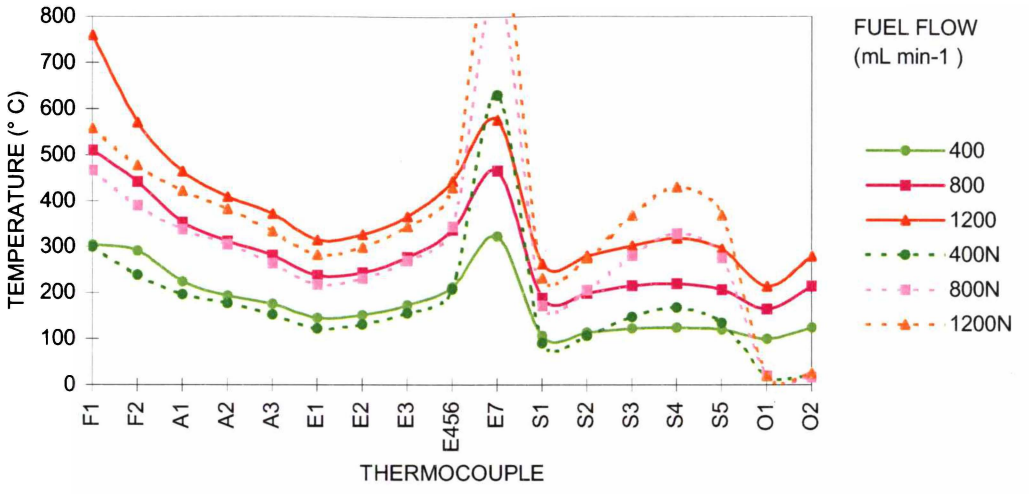

Figure 6.26 Temperature profiles for temperature solutions of the standard configuration illustrated in Figure 6.25, comparing empirical results (400,800 and 1200) to simulated steady state radiation results (400N, 800N and 1200N), at Fv = 0.1-0.29 ms^{-1}.

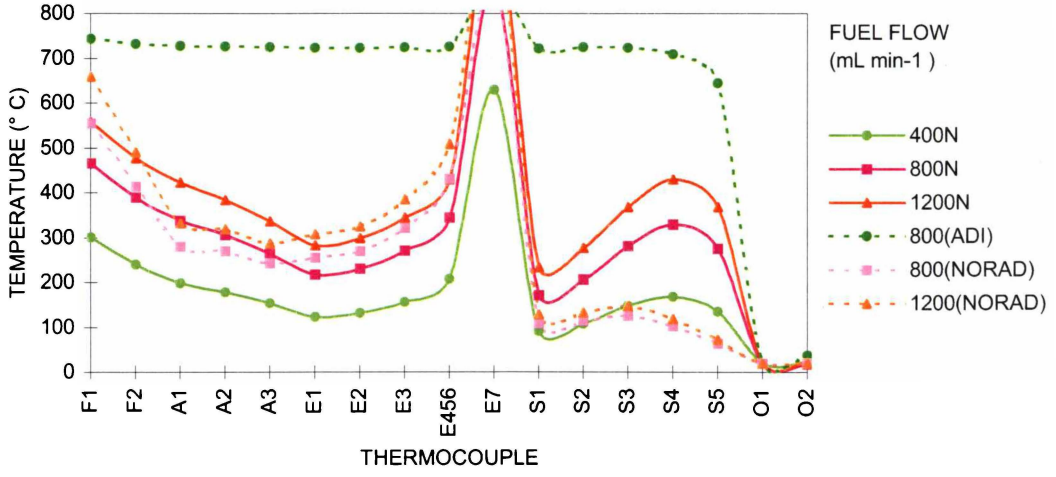

Figure 6.27 Temperature profiles for temperature solutions of the standard configuration illustrated in Figure 6.25, comparing simulated steady state radiation results (400N, 800N and 1200N), to the steady state solution (800(NORAD), 1200(NORAD)), at Fv = 0.1-0.29 ms^{-1}. 800(ADI) with an adiabatic boundary condition at the external surface.

The adiabatic option (800(ADI)) indicates a uniform temperature distribution (Figures 6.25 and 6.27) compared to other results produced when a heat transfer coefficient of 5 $Wm^{-2}K^{-1}$ is applied to the external surfaces of the verification cell. However, these results only consider conduction, radiation and convection in terms

of a set applied boundary condition; mass flows cannot be activated in the radiation module.

6.7 Summary

The following conclusions are drawn about results generated by the verification cell model:

1. The mesh shape and size affect temperature results in areas of high gradients.
2. Increasing the number of iterations reduces the overall temperature, increasing the temperature distribution.
3. The heat generation rate (body load) produced data that were typically higher than experimental data for both the flame study and when applied to the verification cell model.
4. The temperature (DOF) constraint produced temperature data that were lower than experimental data for both the flame study and when applied to the verification cell model.
5. The region in the model domain that data is extracted from has a significant effect on results.
6. The temperature profile of the verification cell model can be loosely correlated to a particular fuel flow rate by modifying the heat source (heat generation rate or temperature constraint) value and the area to which the heat source is applied.
7. The correlated temperature profiles do not translate for variable fuel flow rates.
8. Lack of agreement between modelling the heat source from combustion, computational and experimental data for the effect of fuel flow rate on resulting temperature profiles of the verification cell is attributed to three simplifications:
   a) The flame (combustion) model is non-chemical.
   b) The flame model does not take account for the confined space of the combustion zone.
   c) Radiation was not coupled with the Mass – Flow Model.

9. The multiple-species results offer insight into reactant and product flows through the verification cell, and has potential for being applied to a SOFC model.

10. The results for radiation (neglecting mass flow) show good agreement with empirical data for interior components of the verification cell.
11. Including radiant heat transfer reduces temperature gradients and increases the temperature distribution more uniformly through out the verification cell.

CHAPTER SEVEN

CHAPTER SEVEN

Conclusions and Recommendations

7.1 Summary and Conclusions

The main conclusions from the experimental and modelling studies developed to answer the goals and objectives described in Chapters 1, 2 and 4 are presented.

7.1.1 Experimental Data

1. The verification cell had an axisymmetric temperature profile with temperature decreasing from the combustion zone to the top of the air manifold, and therefore, temperature is not uniform throughout the air manifold.
2. Air flowing into the air-manifold was approximately 100°C lower than air at the manifold wall for fuel flow rates up to 1200 mL min^{-1}.
3. Hydrogen-air combustion was sustained in the verification cell with air being supplied by natural circulation via a chimney effect.
4. Insulating the verification cell increased the time required to obtain steady state and for cooling down. However, temperatures throughout the insulated verification cell were higher than in the uninsulated cell and temperature profiles were more uniform.
5. Increasing flue height caused temperatures to increase slightly throughout the verification cell except in the combustion zone and at the exhaust outlet; the higher temperatures were attributed to the increased air-flow (not validated).
6. Increasing flue width decreased temperatures in the verification cell because, the top of the combustion zone becomes more exposed. Heat lost from the system is a combination of radiation losses from the top of the exhaust manifold (combustion zone) and (postulated) the greater volume of air being drawn through the system.

7. The verification cell could function on significantly reduced inlet and/or outlet cross sectional areas (75% reduction of inlet and 95% reduction of outlet) than the standard system.
8. An empirical relationship between fuel flow rate, flame temperature and flame dimensions was obtained using thermocouples and photographic measurements of the flame.

Conclusion:

The verification cell operated successfully on hydrogen-air but the temperature was not high or uniform enough to support a fuel cell stack.

7.1.2 Computational Data

A base model (Thermal – Mass flow) and three modules (Combustion, derived from the Flame model, Radiation and Multiple-Species) were developed to calculate temperature profiles not easily measured experimentally. The process of developing these computer models enabled a more detailed understanding of the parameters to use for characterising the verification cell.

The following conclusions were obtained from modelling the verification cell:

1. Parameters such as mesh shape and size and number of iterations significantly affect accuracy of temperature predictions.
2. Temperature profile data from the Combustion module (flame study) using the heat generation rate were higher, while those produced from using a temperature-constraint as the heat source were lower, than the experimental (actual) temperatures measured.
3. The temperature profiles produced for a specific flow rate could not be translated to another fuel flow rate without decreasing accuracy.
4. Simplifying the combustion model decreased accuracy of predicting the flame properties (heat source).
5. The predicted temperatures for the insulated verification cell model were more accurate than for the non-insulated verification cell model.

6. Temperature gradients produced by the radiation module were more uniform than the Thermal – Mass Flow model and agreed well with the experimental data.
7. The combustion module applied in the Thermal – Mass Flow model did not model the effect of changing flue dimensions well.
8. The Multiple-Species module gave information on chemical distributions, indicating it has potential for modelling a SOFC cell or stack.

7.2 Recommendations

These recommendations involve further experimental work to improve the experimental test rig (verification cell) and discuss ways to improve the verification cell model. These two activities must be closely related if the computer modelling component is to benefit a physical outcome, and are outlined below.

7.2.1 The Verification Cell - Test Rig

1. A larger verification cell should be fabricated. This will reduce errors originating from sensor placements and from having large temperature gradients over small regions.
2. An electric heating element, which produces a known amount of heat and is more easily modelled than a gas flame, should be used to heat the verification cell.
3. Experiments should be done with a flame support (holder), such as a catalyst in the combustion zone to distribute the heat, thus removing the need to model heat from a flame. The distributed heat source would also simulate a fuel cell stack more closely.
4. Flue diameter could be reduced by 50% (to 25 mm) to reduce heat loss by radiation from the top surface of the combustion chamber.
5. The length of air-inlet should be adjustable so an optimum air preheat length can be determined. Increasing the length of the air inlet will improve heat transfer between outgoing exhaust gases and incoming air and fuel.
6. The effect of adding heat fins and/or decreasing component spacing, which will improve heat transfer, should be studied.

7. The effect of different gases, such as methane (natural gas), should be investigated to determine if the verification cell could operate on gases typically used for fuel cells. However, as the buoyancy-induced draft in the verification cell may not supply enough air for methane-air combustion, a premixed flow may be needed.
8. The amount of air for buoyancy driven flow should be determined by operating the verification cell with controlled forced air flow and comparing temperature profiles and differential pressures through components.
9. A gas analyser (oxygen sensor) could be used to analyse oxygen in the combustion products and hence determine the combustion characteristics.
10. Sensors (hot wire anemometer, differential pressure sensor) could be added to the verification cell to record inlet air-flows and pressure variances within the verification cell.

The final two recommendations focus on modelling a fuel cell in the verification cell:

11. Revisit the premise this research was based on, i.e., will natural convection supply the required air flow for a mini-tubular fuel cell stack to operate. Determine the validity of a natural draft SOFC, especially if the system is required to start up rapidly and to be efficient. If the excess heat from the system is to be used in combined heat and power applications then an efficient heat exchanger is required.
12. Design an experiment where the fuel tube of the verification cell is replaced with an electrically heated tube (e.g., resistance wire wrapped around the fuel tube). The fuel and steam should be mixed to simulate an actual fuel cell under full and part load, and air flow to the cathode controlled. The performance (heat exchange) over a range of flow conditions can then be investigated.

7.2.2 The Verification Cell - Model

The effect of the following variations in the model could be investigated to see if the model's accuracy can be improved:

1. Coupling the Mass – Flow and Radiation modules.

2. Carry out initial work on coupled code (point 1) with a simpler model to ensure a quality mesh. Eliminating uncertainties with the mesh will ensure quicker convergence and would enable the model to be further refined.
3. Have models that do not incorporate a flame profile (see points 1-3, Section 7.2.1).
4. Use models that include a flow driver such as the heated surfaces of the exhaust manifold rather than having to model a combustion zone.

7.2.3 ANSYS®

A conclusion on the suitability of using ANSYS® (FLOTRAN) for modelling SOFCs was not reached. Coupling electrochemical codes with ANSYS® steady state code (i.e., non-FLOTRAN) has been reported (Section 2.4.5) but the validity of the data is difficult to determine. The following advantages and disadvantages experienced when using ANSYS® for this research will help the reader form an opinion:

Advantages:

1. A complete set of pre-processing and post-processing conditions can be defined.
2. Useful plots of all data are generated. Because ANSYS® is a generic modelling program, other properties such as mechanical stresses in components can be investigated.
3. There is real time convergence monitoring.
4. ANSYS® can be coupled with custom codes (e.g., FORTRAN or C).
5. Newer versions of ANSYS® have more rigorous solvers, which enforce conservation laws more strictly.

Disadvantages:

1. The ANSYS® software is extensive and complex so significant time is required for training and to become proficient with the program structure and operation.
2. To achieve accuracy, mesh size and mesh quality has to be established through convergence studies and verification work. As in this thesis, validation has to be by comparing predicted data with experimental data. This refinement process takes time.

3. Adding sub-models or using coupled models increases model complexity, making it difficult to identify reasons for lack of agreement between computational and experimental data.

7.2.4 Closing Comments

A verification cell was built to represent a potential mini-tubular stack housing (Figure 1.13). The air-manifold of the verification cell is the fuel cell chamber. The base of the air-manifold needs to be modified for the fuel plenum and internal reformer. A uniform temperature distribution throughout the cells is required for safe and efficient SOFC operation. The current verification cell design does not deliver a uniform temperature. Recommendations have been given on how to improve thermal performance.

The modelling presented in this thesis indicates that heat source characteristics (intensity and profile) are very important for accurately simulating temperature distribution of the verification cell. Modelling a complex heat source coupled with buoyancy driven flow in an irregular geometry needs many software (program) specific variables. Data from the various models investigated were compared with experimental data for the verification cell. The Radiation module gave the best fit, with less than 10% variation between predicted and experimental data for the air and exhaust manifold components.

The challenge for designers and fabricators of SOFC systems is to obtain consistent temperature and chemical distributions, as well as increased power densities and volumes. The fabrication materials and techniques must also be economically viable. Computational modelling is becoming an increasingly useful tool in identifying these requirements.

APPENDICES

APPENDIX A

DEVELOPERS of SOFC TECHNOLOGY

Appendix A1 Web-sites

Acumentrics Corporation	http://www.acumentrics.com/
Argonne National Laboratory	http://www.anl.gov/
Ceramatec	http://www.ceramatec.com/
Ceramic Fuel Cells Ltd.	http://www.cfcl.com.au/
Consejo Superior de Investigaciones Cientificas	http://www.csic.es/
ETH Materials	http://ceramics.ethz.ch/
Federal Energy Technology Center	http://www.fetc.doe.gov/
FEV Motorentechnik GmbH	http://www.fev.com/
Forschungszentrum Julich	http://www.kfa-juelich.de/index-e.html
Fuel Cell Group	http://www.kla.dtu.dk/010/fcg1.htm
Gas Technology Institute	http://www.igt.org/
Gaz De France	http://www.gazdefrance.com/
GE Energy and Environmental Research Corp	http://www.eercorp.com/
Global Thermoelectric Inc.	http://www.globalte.com/
Hydrovolt Energy Systems	http://www.hydrovolt.com/
ICV-CSIC	http://www.icv.csic.es/
Lund Institute of Technology	http://www.vok.lth.se/
Massachusetts Institute of Technology	http://www.mit.edu/
Materials and Systems Research, Inc.	http://www.MSRIhome.com/
McDermott Technology, Inc.	http://www.mtiresearch.com/
Mitsubishi Heavy Industries, Inc.	http://www.mhi.co.jp/indexe.html
Netherlands Energy Research Foundation	http://www.ecn.nl/main.html
NexTech Materials, Ltd.	http://www.nextechmaterials.com/
Ontario Hydro Technologies	http://www.oht-inc.com/
Pacific Northwest National Laboratory	http://www.pnl.gov/
Siemens Westinghouse	http://www.siemenswestinghouse.com/en/fuelcells
Sulzer Hexis Ltd.	http://www.hexis.ch/
United States Department of Energy (main)	http://www.doe.gov/
Westinghouse Savannah River Company	http://www.srs.gov/general/srtech/srtc/srtchtm/wwdover.htm
ZSW, Center for Solar Energy & Hydrogen Research	http://www.zsw.uni-ulm.de/

REFERENCE:	http://www.fuelcell-eur.nl

APPENDIX B

LIST OF ABBREVIATIONS

Nomenclature	Description	Units
c	the molar density of the mixture	[mol m^{-1}]
C_{pi}	specific heat of species i, at constant pressure	[J kg^{-1} K^{-1}]
D_i	the effective diffusion coefficient of species i in a mixture	[m^2 s^{-1}]
F	Faraday constant (9.6485 x 10^4)	[C mol^{-1}]
ΔG	Standard Gibbs free energy change	[10^3 $Jmol^{-1}$]
h	heat transfer coefficient	[W m^{-2} K^{-1}]
H_W	enthalpy	[J mol^{-1}]
I	electric current	[A]
j	electric current density	[A m^{-2}]
n_e	electrons transferred per reaction	
Ni	mole flux of i	[mol S^{-1}]
P	electric power	[W]
P_i	pressure of species i	[Pa]
q	heat flux per unit area	[W M^{-2}]
R_G	universal gas constant (8.31451)	[J $K^{-1}mol^{-1}$]
ΔS	change in entropy	[$JmoL^{-1}$ K^{-1}]
T	temperature	[K]
E	cell voltage	[V]
E^o	Gibbs voltage	[V]
E_N	Nernst voltage	[V]
V	Electromotive force	[V]
$V_{rev,c}$	reversible electrode potential	
x_i	the mole fraction of component "i"	
z_{cell}	thickness of plate in z-direction	[m]
σ	electrical conductivity	[[Ω^{-1} m^{-1}]
η	overvoltage	[v]
ρ	resisitivity	[Ω m]
λ	thermal conductivity	[W $m^{-1}k^{-1}$]
∇	laplace operator	

Subscripts

i	species i
j	species j
rev,c	the reversible electrode potential for the cathode
rev,a	the reversible electrode potential for the anode

APPENDIX C

VERIFICATION CELL & THERMOCOUPLE PLACEMENT: - DIMENSIONS

Appendix C1 Verification Cell Dimensions (mm)

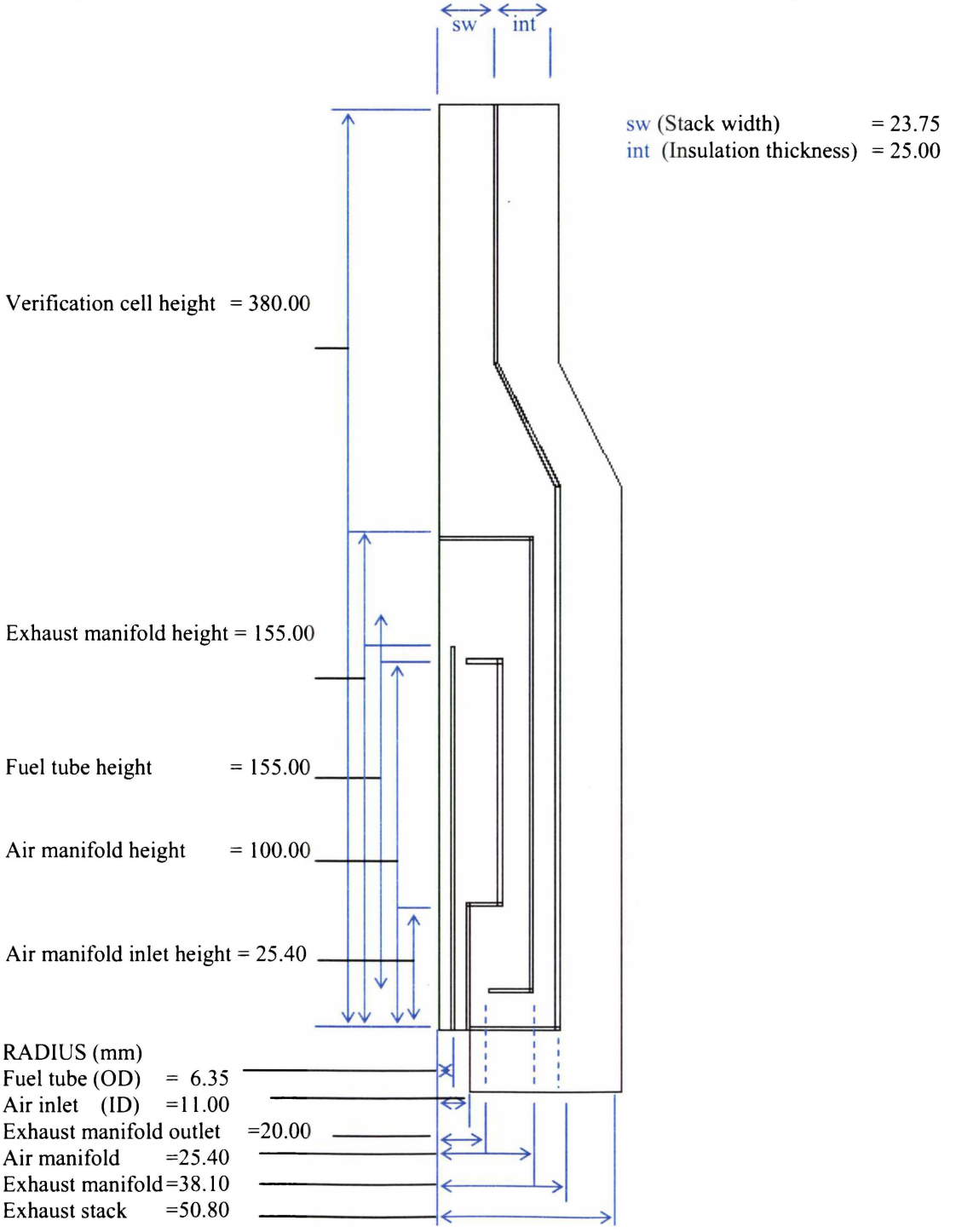

Appendix C2 Thermocouple Placement: - Dimensions

TAG	COMPONENT	LOCATION - DESCRIPTION	
(With reference to Figure 3.x)		X	Y
F1	Combustion zone	6mm from FT wall;	30 mm above AM top
F2	"	"	15 mm "
A1	Air manifold (near top)	outer-surface of AM wall;	10 mm below AM top
A2	" (middle)	"	40 mm "
A3	" (bottom)	"	85 mm "
E1	Exhaust manifold (bot)	outer-surface of exhaust manifold	170 mm below EM top
E2	" (mid-bot)	"	145 mm "
E3	" (mid)	"	100 mm "
E456	" (mid-top)	"	50 mm
E7	" (on top)	"	Top of EM / CZ
S1	" (bot)	outer-surface of exhaust stack	0 mm at ES bottom
S2	Exhaust stack (mid-bot)	"	50 mm above ES bottom
S3	" (mid-top)	"	150 mm "
S4	" (top)	"	200 mm at ES top
S5	" (top of reducer)	"	250 mm at top of reducer/ (flange)
O1	Exhaust outlet (near wall)	5 mm from stack wall	Top of stack
O2	" (centre)	Centre	"

KEY

Bot = Bottom
FT = Fuel Tube
AM = Air Manifold
EM = Exhaust Manifold
CZ = Combustion Zone
ES = Exhaust Stack
S = Stack (Flue)
O = Exhaust Outlet

Appendix C3 Thermocouple Map

FOLD OUT - Thermocouple placement

SIDE PERSPECTIVE

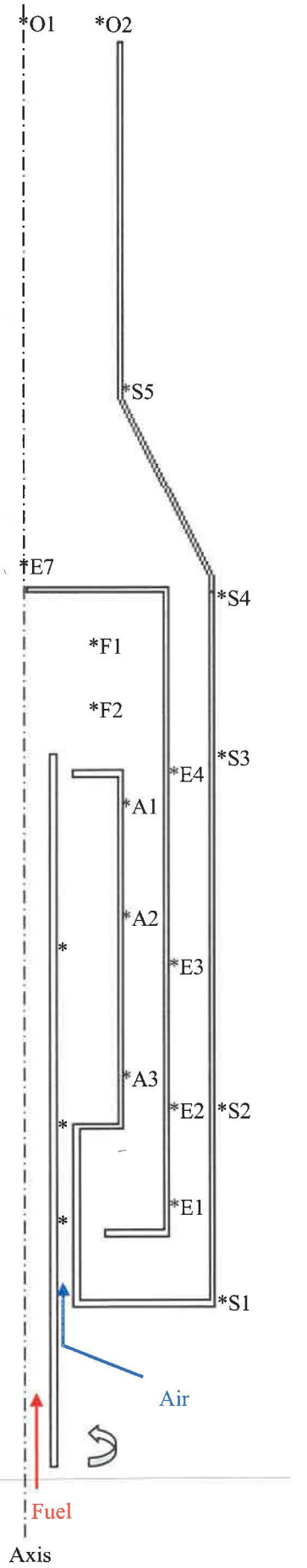

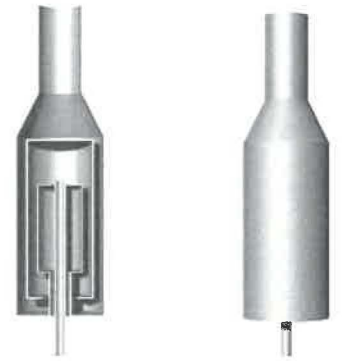

TOP PERSPECTIVE

AIR MANIFOLD

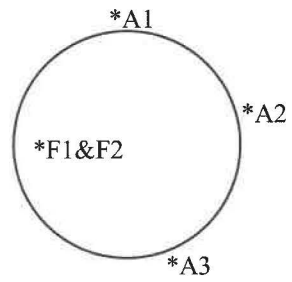

EXHAUST MANIFOLD

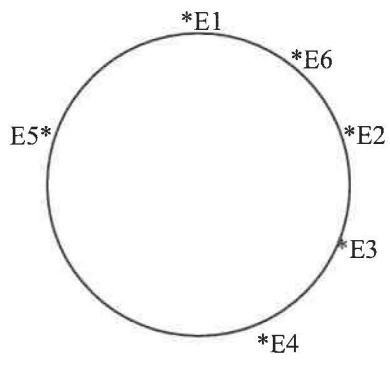

EXHAUST STACK,
Thermocouples, S1 – S5, are aligned vertically

KEY
*Tag = Thermocouple position on component
* (No Tag) = Insertion Probe

APPENDIX D

THE ANSYS® PROGRAM & MODELLING CODE

Appendix D1 On Line ANSYS® Help System – Documentation Description

Analysis Guides:	Description:
ANSYS Operations Guide:	Describes basic ANSYS operations (starting, Stopping, etc.) and use of the graphical uer Interface (GUI).
ANSYS Modeling and Meshing Guide:	Explains how to build a finite element model and mesh it.
ANSYS Basic Analysis Procedures Guide:	Describes tasks that apply to any type of analysis, including applying loads to a model, obtaining a solution, and using the ANSYS program's graphics capabilities to review results.
ANSYS Advanced Analysis Techniques Guide:	Discusses techniques commonly used for complex analyses or by experienced ANSYS users, including design optimization, submodeling, and substructuring.
ANSYS Structural Analysis Guide:	Describes how to perform structural analyses: static, modal, harmonic, transient, spectrum, buckling, non-linear, p-method, and explicit dynamics.
ANSYS Thermal Analysis Guide	Describes how to do to steady-state or transient thermal analyses.
ANSYS Electromagnetic Field Analysis Guide:	Explains techniques for doing transient, static, or harmonic magnetic analyses; current conduction analysis; and electrostatic and circuit analysis.
ANSYS CFD FLOTRAN Analysis Guide:	Describes how to perform fluid flow, acoustics, contained fluid, and dynamic fluid coupling analyses.
ANSYS Coupled-Field Analysis Guide:	Explains how to do indirect and direct coupled-field analysis (an analysis that accounts for the interaction between two or more engineering disciplines).

Command Manuals:	Description:
ANSYS Commands Reference:	Describes the syntax of all ANSYS commands and is organised alphabetically.
ANSYS Elements Reference:	Describe the ANSYS element library: figures, input data, output data, and other details of all ANSYS elements.
ANSYS Theory Reference:	Describe theory and ANSYS implementation of all ANSYS features: finite elements, solvers, postprocessors, elements, etc. This manual describes the relationship between input data and output results produced by the program and is essential for thorough understanding of how the program functions.

*The above list is referenced from the ANSYS Commands Manual, Chapter One.

ANSYS® MODELLING EQUATIONS

Appendix D2 Equations used by FLOTRAN

Appendix D2 overviews the fundamental equations used by ANSYS®/ FLOTRAN, which are relevant to the research presented in this thesis.

1. The equation of continuity — Equation (Eq.) (D1)
2. Conservation of momentum (Navier-Stokes equations) — Eq. (D6)
3. Compressible fluid energy equation — Eq. (D8)
4. Pressure equation — Eq. (D14)
5. Multiple species — Eq. (D16).

The continuity equation is simply the law of conservation of mass. That is the rate of mass accumulation is equal to the rate of mass into a defined volume, minus the rate of mass leaving the defined volume:

$$\frac{\partial \rho}{\partial t}+\frac{\partial}{\partial x}(\rho v_x)+\frac{\partial}{\partial y}(\rho v_y)+\frac{\partial}{\partial z}(\rho v_z)=0$$

Alternatively,

$$\frac{\partial \rho}{\partial t}+\nabla\cdot(\rho \underline{v})=0 \qquad \text{(D1)}$$

For incompressible flows (constant pressure), the continuity equation reduces to:

$$\nabla\cdot \underline{v}=0 \qquad \text{(D2)}$$

Where υ_i is the velocity vector component, and $i \in \{x,y,z\}$. To assist in solution of the finite element fluid flow problem, the rate of change of density is replaced by the rate of change of pressure, and the rate at which density changes with pressure. For a compressible gas, the derivative of the density, with respect to pressure, can be obtained from the ideal gas law, Equation D4, whereas an incompressible gas can be defined by a user specified value, β. A value of $\beta=10^{15}$, (default, $\partial\rho/\partial P \Rightarrow 0$), assumes a perfectly incompressible fluid.

$$\frac{\partial \rho}{\partial t} = \frac{\partial \rho}{\partial P}\frac{\partial P}{\partial t} \tag{D3}$$

$$\rho = \frac{P}{RT} \Rightarrow \frac{\partial \rho}{\partial P} = \frac{1}{RT} \tag{D4}$$

$$\frac{\partial \rho}{\partial P} = \frac{1}{\beta} \tag{D5}$$

The momentum per unit volume of a fluid with a velocity and density is, *momentum* = $\upsilon\rho$, and its rate of transfer defined, *rate* = $(\upsilon\rho)\upsilon$. Each component of the linear velocity depends on time and position. Momentum equations are also referred to as equations of motion, or the Navier-Stokes equations, and are the differential form of Newton's second law of motion. The conservation of momentum, is often expressed in the form of three momentum equations, represented here in rectangular co-ordinates (x, y, z), the x-component is given in Equation D6. Analogous expressions exist for the y- and z-components:

$$\frac{\partial \rho \upsilon_x}{\partial t} + \frac{\partial(\rho \upsilon_x \upsilon_x)}{\partial x} + \frac{\partial(\rho \upsilon_y \upsilon_x)}{\partial y} + \frac{\partial(\rho \upsilon_z \upsilon_x)}{\partial z} =$$

$$\rho g_x - \frac{\partial P}{\partial x} + \frac{\partial}{\partial x}\left(\mu_e \frac{\partial \upsilon_x}{\partial x}\right) + \frac{\partial}{\partial y}\left(\mu_e \frac{\partial \upsilon_x}{\partial y}\right) + \frac{\partial}{\partial z}\left(\mu_e \frac{\partial \upsilon_x}{\partial z}\right) + R_x + T_x \tag{D6}$$

Where g_x is the x-component of acceleration due to gravity, μ_e is the effective viscosity, R_x the distributed resistances, and T_x, is a viscous loss term, given in Equation D7. For laminar fluid flow, the effective viscosity is the dynamic viscosity, μ, (a specified fluid property value). R is optional and is a user specified source term, which may account for a complex geometric feature in the form of a distributed resistance, such as a flow through porous media, for example.

$$T_x = \frac{\partial}{\partial x}\left(\mu \frac{\partial \upsilon_x}{\partial x}\right) + \frac{\partial}{\partial y}\left(\mu \frac{\partial \upsilon_y}{\partial x}\right) + \frac{\partial}{\partial z}\left(\mu \frac{\partial \upsilon_z}{\partial x}\right) \tag{D7}$$

Other forms of the momentum equations for several conditions of fluid flow, such as, constant viscosity, constant viscosity and pressure, zero viscosity, for example, are reviewed elsewhere.* These forms of the momentum equations are available in FLOTRAN and depend upon solver options selected and solution settings.

The compressible (gas) energy equation, is given in Equation D8, in terms of the stagnation, or total temperature (explained below), applicable when solving thermal – fluid flow problems. Neglecting, pressure work, viscous work (W^v), kinetic energy (E^k), and viscous heat generation (Φ), the compressible energy equation reduces to the incompressible energy equation, which is a thermal transport equation for static temperature. The incompressible energy equation is also used for the solid regions of a fluid flow problem, the walls of the verification cell, for example:

$$\frac{\partial}{\partial t}(\rho C_p T_0)+\frac{\partial}{\partial x}(\rho \upsilon_x C_p T_0)+\frac{\partial}{\partial y}(\rho \upsilon_y C_p T_0)+\frac{\partial}{\partial z}(\rho \upsilon_z C_p T_0)=$$

$$\frac{\partial}{\partial x}\left(K\frac{\partial T_0}{\partial x}\right)+\frac{\partial}{\partial y}\left(K\frac{\partial T_0}{\partial y}\right)+\frac{\partial}{\partial z}\left(K\frac{\partial T_0}{\partial z}\right)+W^v+E^k+\ddot{q}+\Phi+\frac{\partial P}{\partial t} \quad \text{(D8)}$$

(Compressible)

$$\frac{\partial}{\partial x}\left(K\frac{\partial T}{\partial x}\right)+\frac{\partial}{\partial y}\left(K\frac{\partial T}{\partial y}\right)+\frac{\partial}{\partial z}\left(K\frac{\partial T}{\partial z}\right)+\ddot{q} \quad \text{(D9)}$$

(Incompressible)

Where:

C_p = specific heat,

T_0 = total (stagnation) temperature,

K = thermal conductivity,

W^v = viscous work term,

E^k = kinetic energy,

$\ddot{q}$ = volumetric heat generation (source), and

Φ = viscous heat generation term.

* S. M. Wales, *Modeling with Differential Equations in Chemical Engineering*, Butterworth–Heinemann, USA, **1991**, Chpt9, p251.

The temperature of the fluid after it has been brought isentropically to a zero velocity is referred to as the total (stagnation) temperature, T_0. Knowledge of the inlet conditions are applied to Equation D10, where T_{static}, is the static fluid temperature, and υ, the velocity magnitude, $|\upsilon|$, at the inlet, (T_{static} = 293 K for the verification cell):

$$T_0 = T_{static} + \frac{|\upsilon^2|}{2C_p} \tag{D10}$$

The viscous work term, presented in tensor form is:

$$W^v = u_j \mu \left[\frac{\partial}{\partial x_i} \frac{\partial u_j}{\partial x_i} + \frac{\partial}{\partial x_k} \frac{\partial u_k}{\partial x_j} \right] \tag{D11}$$

The kinetic energy term is:

$$E^k = -\frac{\partial}{\partial x}\left[\frac{K}{C_p}\frac{\partial}{\partial x}\left(\frac{1}{2}|\upsilon^2|\right)\right] - \frac{\partial}{\partial y}\left[\frac{K}{C_p}\frac{\partial}{\partial y}\left(\frac{1}{2}|\upsilon^2|\right)\right] - \frac{\partial}{\partial z}\left[\frac{K}{C_p}\frac{\partial}{\partial z}\left(\frac{1}{2}|\upsilon^2|\right)\right] \tag{D12}$$

The viscous heat generation term:

$$\Phi = \mu\left(\frac{\partial u_i}{\partial x_k} + \frac{\partial u_k}{\partial x_i}\right)\frac{\partial u_i}{\partial x_k} \tag{D13}$$

Pressure is obtained from the conservation of mass principle, whereby a pressure algorithm solves for a relative pressure, P_{rel}, rather than an absolute pressure, P_{abs}, for reasons of numerical accuracy. The reference pressure, P_{ref}, is calculated from the ideal gas law, and a user specified nominal temperature:

$$\rho \frac{D\underline{\upsilon}}{dt} = (\rho - \rho_0)\underline{g} - \nabla P_{rel} + \mu \nabla^2 \underline{\upsilon} \tag{D14}$$

$$P_{rel} = P_{abs} - P_{ref} + \rho_0 \underline{g} \cdot \underline{r} \qquad \text{(D15)}$$

The multiple species transport option is used to track several different fluids (gases), with different properties, through a common medium. An alternative application for this feature, is illustrated in the preceding, heat exchange example. The flow field is solved using a single momentum equation, with the properties being calculated from those of the individual species and their respective mass fractions. The mass balance equations for each of the species:

$$\frac{\partial(\rho Y_i)}{\partial t} + \nabla \cdot (\rho Y_i \upsilon) + \nabla \cdot (\rho D_{mi} \nabla Y_i) = 0 \qquad \text{(D16)}$$

Where Y_i is the mass fraction of ith species.

Further detail regarding the implementation of these equations within the ANSYS® program can be found in the online help manual "ANSYS Theory Reference", listed in Appendix D1.

VERIFICATION CELL MODELLING CODE

Appendix D3 Listing of Parameters and Description

NAME	DESCRIPTION		VALUE	UNITS
A1	Air manifold thermocouple (top)		468.4096	K
A2	Air manifold thermocouple (middle)		445.1858	K
A3	Air manifold thermocouple (bottom)		411.2958	K
AMHCC	Air manifold height		0.15	m
AMHI	Air manifold height, of inlet		5.00E-02	m
AMWCC	Air manifold width		2.38E-02	m
AMWI	Air manifold width of inlet (bottom of air manifold)		1.10E-02	m
AMWO	Air manifold width, of outlet (top of air manifold)		1.10E-02	m
CE	Combustion efficiency (calibration factor)		1	
CZH	Combustion zone height		3.00E-02	m
CZO	Combustion zone bottom (near top of fuel tube)		0.156	m
CZW	Combustion zone width		8.28E-03	m
E1	Exhaust manifold thermocouple (bottom)		383.7848	K
E2	Exhaust manifold thermocouple (bottom-middle)		392.4629	K
E3	Exhaust manifold thermocouple (middle)		423.2196	K
E4	Exhaust manifold thermocouples, (middle-top)		508.4006	K
E7	Exhaust manifold thermocouple (top of combustion zone)		745.505	K
ELSIZ	Element size		2.50E-03	m
ELSIZ2	Optional element size		2.50E-03	m
EMHCC	Exhaust manifold height		0.2	m
EMHO	Exhaust manifold height, of outlet (bottom em)		1.50E-02	m
EMWCC	Exhaust manifold width		3.65E-02	m
EMWO	Exhaust manifold width, of outlet		2.00E-02	m
ESHCC	Exhaust stack height		0.22	m
ESWCC	Exhaust stack width		4.92E-02	m
F1	Combustion zone thermocouple (top)		1236.663	K
F2	Combustion zone thermocouple (middle-top)		863.032	K
FT	Flame temperature	?	1478.389	K
FTH	Fuel tube height		0.155	m
FTW	Fuel tube width		4.70E-03	m
FV	Fuel velocity		0.29	ms-1
H	Enthalpy of combustion (hydrogen in air)		241000	$J.mol^{-1}$
HG	Heat generation (source)		30724807	$W.m^{-3}$
HGA	Heat generation area as applied to in model		2.48E-04	m^{-2}
HGAA	Heat generation volume, as applied to model		6.46E-06	m^{-3}
HGG	Actual heat generated from gas supplied		198.3586	W
HTC	Heat transfer coefficient		2	$W\ m^{-2}\ K^{-1}$
INT	Insulation thickness		2.50E-02	m
IP1	Insertion probe one (thermocouple)		398.1651	K
IP2	Insertion probe two		430.6357	K
IP3	Insertion probe three		465.232	K
MAXE	Maximum number of elements	?	6045	
MAXN	Maximum number of nodes		6181	
NDOF	Maximum number of Degrees of Freedom		6181	

NAME	DESCRIPTION	VALUE	UNITS
O1	Exhaust outlet thermocouple (near flue wall)	443.0904	K
O2	Exhaust outlet thermocouple (at flue centre)	515.5696	°C
OV1	Exhaust outlet velocity (near flue wall)	1.28E-02	ms^{-1}
OV2	Exhaust outlet velocity (at flue centre)	0.327045	ms^{-1}
P	Pressure	101325	Pa
PI	Pi	3.141593	
R	Gas constant	8.314	J mol^{-1} K
S1	Exhaust stack thermocouple (bottom)	356.3877	K
S2	Exhaust stack thermocouple (bottom-middle)	368.5098	K
S3	Exhaust stack thermocouple (middle-top)	399.1198	K
S4	Exhaust stack thermocouple (top, bottom of reducer)	416.07	K
S5	Exhaust stack thermocouple (top of reducer)	434.5747	K
SH	Stack height (flue height)	0.155	m
SHF	Stack height flange (reducer height)	5.00E-02	m
ST	Steel thickness	1.65E-03	m
STDIV	Number of steel divisions through width for mesh	3	
STKNUM	Number of areas (domains) which make up the model	20	
SW	Stack width (flue width)	2.38E-02	m
T	Temperature	298	K
TO	External or room temperature	300	K
V	Volume	2.01E-05	m^3
XO	Base of model on X-axis	0	
XOFF	Origin of model generation on X-axis	0	
YO	Origin of model generation on Y-axis	0	

PARAMETER STATUS - (71 PARAMETERS)
(INCLUDING 2 INTERNAL PARAMETERS)

KEY
w = width
h = height
t = top
b = bottom
s = stack
ft = fuel tube
am = air manifold
em = exhaust manifold
es = exhaust stack
i = inlet
o = outlet
f = fuel
a = air
e = exhaust

Comments:
- Parameters may appear as lower case in modelling codes
- Values given here are examples, and may not necessarily have been used
- Reference to thermocouple, refers to numerical result for thermocouple location
- SI units used through out.

Appendix D4 Combustion (Heat Generation) Code

The codes herein have had line numbers inserted, to assist in identifying where each model or sub model is amended into the base code (Appendix D5). The use of == and ===== indicates code being placed, also, the first line number indicates where the code is being placed in the Thermal – Mass Flow model. ! is a remark, or a commented out command in the ANSYS® program.

Additional comments have been inserted, *and are underlined, and italicised.*

Line number represents location where code begins when placed in Thermal – Mass Flow (base) model.

```
==
=====
25  !    *** PARAMETERS ***
26  *
**
34  !    LOADING PARAMETERS
35  !    (Note, constants for combustion calculations, under Heat Generation)

36  fv   =0.4            ! fuel velocity              (ms-1)
37  Ce   =1              ! combustion efficiency
38  T    =293            ! temperature                (K)
39  H    =241000         ! enthalpy of combustion     (Jmol-1)
=====
==
=====
62  !    *** HEAT GENERATION ***   (Combustion Code)

63  !    (Note, fuel velocity as a function of flame dimensions - empirical component)
64  !    Fuel velocity (mass flow) are 0.1 (400), 0.19 (800), 0.29 (1200) and 0.38 (1600)
65  !    ms-1, ml min-1

66  czo  =fth+0.001              ! combustion zone origin
67  czh  =(0.0883*fv)+0.0044     ! combustion zone height
68  czw  =((0.0196*fv)+0.0109))*0.5      ! combustion zone width, (*0.5 to get flame radius)

69  !    CONSTANTS

70  Pi   =(4.0)*ATAN(1.0)
71  P    =101325                 ! standard presure                          (Pa)
72  R    =8.314                  ! gas constant                              (J mol-1 K-1)
73  V    =(Pi*ftw**2)*fv         ! volume of gas combusted per second in VC(m3)

74  !    CALCULATIONS FOR HEAT GENERATION

75  HGG        =((V*P)/(R*T))*H*Ce    ! total heat generated; volume of gas per second
76  ! units for heat generation, Js-1 m-3, HGG is js-1                      (W)

77  HGA        =czw*czh          ! area HG applied to in model
78  HGAA       =(Pi*czw**2)*czh        ! volume to area application - seudo 3D applicaiton
79  HG =(1/HGAA)*HGG             ! heat generation value to be applied to HGA as a body force
***
```

```
240 !    *** LOADS AND BOUNDARY CONDITIONS ***
==
=====
```

1) Heat generated as per calculation, and applied to experimentally predicted and fixed flame areas

```
270 !    THERMAL
==
=====
271 NSEL,,LOC,Y,czo,(czo+czh)   ! apply heat generation (source)
272 NSEL,R,LOC,X,xoff,(xoff+czw)
273 ESLN
274 BFE,ALL,HGEN,,hg
275 ALLS
=====
==
```

2) Reducing heat generation as per calculation, and applied to experimentally predicted and fixed flame areas

```
==
=====
271 *DO,ycount,0.1,1,0.1            ! do loop, reduce hg by 10% per cycle
272     /gopr
273     Alls
274     NSEL,,LOC,Y,(czo),(czo+(czh-(czh*ycount)))
275     NSEL,R,LOC,X,xoff,((czw)-(czw*ycount))
276     ESLN
277     BFE,ALL,HGEN,,(hg*ycount)
278 *ENDDO
=====
==
```

3) Experimentally predicted flame temperature applied to experimentally predicted and fixed flame areas

```
==
=====
271 TF=(-4913*(fv**2))+4003*fv+281+273.15
272 NSEL,,LOC,Y,czo,(czo+czh)   ! apply heat generation (source)
273 NSEL,R,LOC,X,xoff,(xoff+czw)
274 D,ALL,TEMP,TF
275 ALLS
=====
==
==
```

Total number of lines in code listing NA.

Batch File Comments

- Fixed flame area; czw and czh set to a constant value.

Appendix D5 Thermal – Mass Flow Code

```
1  !  INSULATED VERIFICATION CELL

2  /TITLE, VERIFICATION CELL: THERMAL-MASS FLOW MODEL (INSULATED)
3  /PREP7
4  /UNITS,SI
   !(/FILENAME,filename)        !optional
5  ET,1,FLUID141      ! set 2D fluid element type
6  KEYOPT,1,1,0       ! species transport not activated
7  KEYOPT,1,3,1       ! axisymmetric about Y axis


8  !  *** KEY ***

9  !  w      = width
10 !  wcc    = width of cell component
11 !  h      = height
12 !  hcc    = height of cell component
13 !  t      = top
14 !  b      = bottom
15 !  s      = stack
16 !  ft     = fuel tube
17 !  am     = air manifold
18 !  em     = exhaust manifold
19 !  es     = exhaust stack
20 !  ~i     = inlet
21 !  ~o     = outlet
22 !  f      = fuel
23 !  a      = air
24 !  e      = exhaust


25 !  *** PARAMETERS ***

26 !  MODELLING PARAMETERS

27 yo  =0            ! x origin
28 xo  =0            ! y origin
29 xoff=0            ! offset
30 stdiv     =3      ! number of elements through steel
31 stknum    =20     ! number of areas within the stack (VC)
32 elsiz     =0.0025 ! default element size
33 elsiz2    =0.0025 ! optional element size

34 !  LOADING PARAMETERS
35 !  (Note, constants for combustion calculations, under Heat Generation)

36 fv  =0.4          ! fuel velocity              (ms-1)
37 Ce  =1            ! combustion efficiency
38 T   =293          ! temperature                (K)
39 H   =241000       ! enthalpy of combustion     (Jmol-1)

40 htc =             ! heat transfer coefficient
41 to  =293          ! bulk air temperature
42 int = 0.025       ! insulation thickness
```

```
43 !   DESIGN AND OPERATING PARAMETERS (GEOMETRY)
44 !   (Note, base is the bottom plate of es (exhaust stack))

45 st  =0.00165          ! steel thickness
46 ftw =0.0047           ! fuel tube
47 fth =0.155            ! fuel tube height

48 amwi      =ftw+st+0.00465 ! air manifold width inlet  = 0.011      (radius = (r))
49 amhi      =0.050          ! air manifold height inlet = 0.05       (length of air inlet)
50 amwo      =ftw+st+0.00465 ! air manifold width outlet = 0.011      (r)
51 amwcc     =ftw+st+0.0174  ! air manifold width        = 0.02375    (r)
52 amhcc     =amhi+0.10      ! air manifold height from base  = 0.15  (am height = 0.10)

53 emwo      =amwi+0.009     ! exhaust manifold width outlet  = 0.02  (r)
54 emho      =0.015          ! exhaust manifold height of outlet      (near base)
55 emwcc     =amwcc+st+0.01105 ! exhaust manifold width       = 0.03645    (r)
56 emhcc     =amhcc+0.05     ! exhaust manifold height        = 0.18       (from emho)
57 eshcc     =emhcc+0.02     ! exhaust stack height from base = 0.22  (es height = 0.20)
58 eswcc     =emwcc+st+.01105! exhaust stack width            = 0.04915    (r)

59 sh  =0.155                ! stack height (flue height, includes 0.055 for reducer/flange)
60 sw  =0.02375              ! 0.03645 stack width (3 inch)                (r)
61 shf =0.05                 ! stack height flange, concentric reducer height


62 !   *** HEAT GENERATION ***   (Combustion Code)

63 !   (Note, fuel velocity as a function of flame dimensions - empirical component)
64 !   Fuel velocity (mass flow) are 0.1 (400), 0.19 (800), 0.29 (1200) and 0.38 (1600)
65 !   ms-1, ml min-1

66 czo =fth+0.001            ! combustion zone origin
67 czh =(0.0883*fv)+0.0044   ! combustion zone height
68 czw =((0.0196*fv)+0.0109))*0.5   ! combustion zone width, (*0.5 to get flame radius)

69 !   CONSTANTS

70 Pi  =(4.0)*ATAN(1.0)
71 P   =101325               ! standard pressure                          (Pa)
72 R   =8.314                ! gas constant                       (J mol-1 K-1)
73 V   =(Pi*ftw**2)*fv       ! volume of gas combusted per second in VC(m3)

74 !   CALCULATIONS FOR HEAT GENERATION

75 HGG       =((V*P)/(R*T))*H*Ce   ! total heat generated; volume of gas per second
76 ! units for heat generation,  Js-1 m-3, HGG is js-1                  (W)

77 HGA       =czw*czh              ! area HG applied to in model
78 HGAA      =(Pi*czw**2)*czh      ! volume to area application - seudo 3D application
79 HG =(1/HGAA)*HGG                ! heat generation value to be applied to HGA as a body force


80 !   *** MODELLING DOMAIN - GEOMETRY ***

81 K,100,ftw,yo,0            ! A1 Fuel tube wall
82 K,101,ftw,fth,0
83 K,102,ftw+st,fth,0
84 K,103,ftw+st,yo,0
```

```
85  L,101,102,stdiv
86  L,103,100,stdiv
87  A,100,101,102,103

88  K,200,amwi,yo,0              ! A2-8 Air manifold
89  K,201,amwi,amhi,0
90  K,202,amwi,amhi+st,0
91  K,203,amwi+st,amhi+st,0
92  K,204,amwcc,amhi+st,0
93  K,205,amwcc,amhcc-st,0
94  K,206,amwo,amhcc-st,0
95  K,207,amwo,amhcc,0
96  K,208,amwcc,amhcc,0
97  K,209,amwcc+st,amhcc,0
98  K,210,amwcc+st,amhcc-st,0
99  K,211,amwcc+st,amhi+st,0
100 K,212,amwcc+st,amhi,0
101 K,213,amwcc,amhi,0
102 K,214,amwi+st,amhi,0
103 K,215,amwi+st,yo,0

104 L,201,202,stdiv
105 L,202,203,stdiv
106 L,203,214,stdiv
107 L,204,211,stdiv
108 L,205,208,stdiv
109 L,206,207,stdiv
110 L,208,209,stdiv
111 L,209,210,stdiv
112 L,211,212,stdiv
113 L,212,213,stdiv
114 L,215,200,stdiv

115 A,200,201,214,215
116 A,201,202,203,214
117 A,203,204,213,214
118 A,204,211,212,213
119 A,204,205,210,211
120 A,205,208,209,210
121 A,205,206,207,208

122 ASEL,,,,2,8
123 CM,Air_man,AREA
124 !A,200,201,202,203,204,205,206,207,208,209,210,211,212,213,214,215

125 K,300,xoff,emhcc-st,0          ! A9-13 Exhaust manifold
126 K,301,xoff,emhcc,0
127 K,302,emwcc,emhcc,0
128 K,303,emwcc+st,emhcc,0
129 K,304,emwcc+st,emhcc-st,0
130 K,305,emwcc+st,emho+st,0
131 K,306,emwcc+st,emho,0
132 K,307,emwcc,emho,0
133 K,308,emwo,emho,0
134 K,309,emwo,emho+st,0
135 K,310,emwcc,emho+st,0
136 K,311,emwcc,emhcc-st,0

137 L,300,301,stdiv
138 L,302,303,stdiv
```

```
139 L,303,304,stdiv
140 L,305,306,stdiv
141 L,306,307,stdiv
142 L,308,309,stdiv
143 L,304,311,stdiv
144 L,307,310,stdiv

145 A,300,301,302,311
146 A,302,303,304,311
147 A,304,305,310,311
148 A,305,306,307,310
149 A,307,308,309,310

150 ASEL,,,,9,13
151 CM,Exhaust,AREA
152 !A,300,301,302,303,304,305,306,307,308,309,310,311

153 ! A14-18 Stack manifold
154 K,400,xoff,yo,0              ! (A18 Stack, defined inside this feature, due to dependent kps)
155 K,401,eswcc,yo,0             ! (A19 Insulation, also defined here)
156 K,402,eswcc,eshcc,0
157 K,403,sw,eshcc+shf,0
158 K,404,sw,eshcc+sh,0
159 K,405,xoff,eshcc+sh,0

160 K,410,amwi+st,yo+st,0
161 k,411,eswcc-st,yo,0
162 k,412,eswcc-st,yo+st,0
163 k,413,eswcc,yo+st,0
164 k,414,eswcc-st,eshcc,0
165 k,415,sw-st,eshcc+shf,0
166 k,416,sw-st,eshcc+sh,0

167 L,410,215,stdiv
168 L,411,412,stdiv
169 L,411,401,stdiv
170 L,401,413,stdiv
171 L,413,412,stdiv
172 L,402,414,stdiv
173 L,403,415,stdiv
174 L,404,416,stdiv

175 A,215,411,412,410
176 A,411,401,413,412
177 A,412,413,402,414
178 A,414,402,403,415
179 A,415,403,404,416


180 K,500,sw+int,eshcc+sh,0
181 K,501,sw+int,eshcc+shf,0
182 K,502,eswcc+int,eshcc,0
183 K,503,eswcc+int,yo-int,0
184 K,504,amwi+st,yo-int,0

185 ASEL,,,,14,18
186 CM,Stack_wall,AREA           ! A18 Stack wall

187 A,500,404,403,402,413,401,411,215,504,503,502,501,500
188 ASel,,,,19                  ! A19 Insulation
```

```
189 CM,Insulation,AREA


190 A,400,401,402,403,404,405    ! A20 Stack_bulk
191 ASEL,,,,20,                  ! (fluid/gas region)
192 CM,Stack_bulk,AREA


193 !    BOOLEAN OPERATION - JOINING DOMAINS

194 ASEL,ALL
195 ASBA,stknum,all,,,KEEP       ! subtract areas
196 NUMCMP,AREA                  ! compress area numbers
197 !Areas are now 1=Fuel tube wall, 2-8=Air manifold, 9-13=Exhaust manifold,
198 !14-18=Stack_wall, 19=Insulation, 20=Stack_bulk
199 ALLS


200 !    *** MESHING ***

201 !    MATERIAL PROPERTIES (ASSIGN ATTRIBUTES)

202 mp,dens,2,7500,                ! density, material 2
203 mptemp,1,273,773,5000,         ! temperature property table
204 mpdata,kxx,2,1,15,25,25,       ! conductivity material property table
205 !mpdata,kyy,2,1,15,25,25,      !kyy,kzz automatic when kxx defined
206 !mpdata,kzz,2,1,15,25,25,
207 mp,c,2,500                     ! specific heat
208 ALLS

209 mp,dens,3,250                                  ! density of insulation
210 mptemp,1,273,473,673,873,1073,5000,           ! temperature property table
211 mpdata,kxx,3,1,0.07,0.07,0.09,0.12,0.15,0.19, ! conductivity
212 !mpdata,kyy,3,1,0.07,0.07,0.09,0.12,0.15,0.19,
213 !mpdata,kzz,3,1,0.07,0.07,0.09,0.12,0.15,0.19,
214 mp,c,3,1000                                    ! specific heat

215 !    MESHING

216 ALLS
217 ASEL,,,,1,(stknum-2)          ! select all but stack_bulk and Insulation
218 AATT,2,1,1,0,                 ! material 2 for walls       (stainless steel)
219 ESIZE,elsiz,0,                ! element size (see elsize parameter) !MSHAPE,0  for A5.4
220 ESHAPE,2                      ! element shape, mapped mesh - quads !MSHKEY,1 for A5.4
221 AMESH,1,(stknum-2),1          ! mesh all walls with mapped mesh

222 ALLS
223 ASEL,,,,stknum,               ! select stack_bulk, fluid region
224 AATT,1,1,1,0,                 ! fluid properties set (air/ or mix if multiple-species)
225 ESIZE,elsiz,0,                ! element size
226 ESHAPE,0                      ! element shape, mixture of tri and quads
227 AMESH,stknum                  ! mesh fluid regions
228 SHPP,WARN                     ! warning, poor element shape, overrides abort function

229 ALLS
230 ASEL,,,,stknum-1,stknum       ! select insulation
231 AATT,3,1,1,0,                 ! material 3 for walls (Kaowool)
232 SMRTSIZE,,,3,1.5,,,,,,5       ! smart (automatic) mesh option
233 AMESH,stknum-1                ! mesh insulation region
234 SHPP,WARN
```

```
!ALLS
!NSEL,,LOC,Y,czo,(czo+czh) ! Optional refinement of combustion zone
!NSEL,R,LOC,X,xoff,(czw)
!NREFINE,ALL,,,
ALLS

!    *** LOADS AND BOUNDARY CONDITIONS ***

!    VELOCITY

ASEL,,,,1,(stknum-1)          ! zero velocity at all solid walls
DA,ALL,VX,0,0
DA,ALL,VY,0,0
DA,ALL,VZ,0,0
DA,ALL,PRES,0,0
ALLS

LSEL,ALL
LSEL,,LOC,Y,0
LSEL,R,LOC,X,xoff,amwi
LSEL,U,LOC,X,ftw,ftw+st
LSEL,A,LOC,Y,eshcc+sh
LSEL,INVE
DL,ALL,,VX,0,1                ! zero velocity at walls, except at inlets and outlets

NSLL,,1
NSEL,U,LOC,X,xoff
D,ALL,VY,0
ALLS

!LSEL,,LOC,Y,ESHCC+SH
!LSEL,R,LOC,X,0,SW
!NSLL,S,1
!D,ALL,PRES,0                 ! zero pressure at outlet     (off)
ALLS

ACEL,O,9.81,0                 ! set flow environment, gravity
ALLS

LSEL,,LOC,Y,0                 ! set fuel velocity at fuel tube inlet
LSEL,R,LOC,X,0,ftw
DL,ALL,,VY,fv,0
ALLS

!    THERMAL

NSEL,,LOC,Y,czo,(czo+czh)  ! apply heat generation (source)
NSEL,R,LOC,X,xoff,(xoff+czw)
ESLN
BFE,ALL,HGEN,,hg
ALLS

SFL,64,CONV,htc,,to           ! apply convection (heat transfer) coefficient
SFL,63,CONV,htc,,to
SFL,62,CONV,htc,,to
SFL,61,CONV,htc,,to
SFL,60,CONV,htc,,to
SFL,59,CONV,htc,,to
```

```
282 !    *** FLOTRAN SETUP AND FLUID PROPERTIES ***

283 ALLS
284 FLDATA15,PRES,REFE,101325,
285 FLDATA16,BULK,BETA,1e+015,
286 FLDATA17,GAMM,COMP,1.3999999761581,
287 FLDATA14,TEMP,NOMI,293,
288 FLDATA14,TEMP,TTOT,293,
289 FLDATA14,TEMP,BULK,293,
290 TOFFSET,273,

291 FLDATA1,SOLU,COMP,1          ! compressible gas property on
292 FLDATA1,SOLU,TURB,0          ! turbulent solver off
293 FLDATA1,SOLU,TEMP,1          ! thermal solution selected
294 FLDATA2,ITER,EXEC,50         ! execution control, number of iterations (200)
295 FLDATA2,ITER,OVER,50
296 FLDATA5,OUTP,SUMF,50

297 FLDATA13,VARY,DENS,1         ! set fluid properties (air)
298 FLDATA7,PROT,DENS,AIR-SI
299 FLDATA13,VARY,VISC,1
300 FLDATA7,PROT,VISC,AIR-SI
301 FLDATA13,VARY,COND,1
302 FLDATA7,PROT,COND,AIR-SI
303 FLDATA8,NOMI,COND,-1
304 !FLDATA13,VARY,SPHT,1
305 FLDATA7,PROT,SPHT,AIR-SI

306 FLDATA18,METH,PRES,1         ! set FLOTRAN solver controls (TDMA)
307 FLDATA19,TDMA,PRES,50        ! number of TDMA iterations for pressure
308 FLDATA19,TDMA,TEMP,50        ! number of TDMA iterations for temperature
309 FINISH
310 /SOLU
311 SOLVE                        ! solve model

312 FLDA,SOLU,ENRG,T             ! solve temperature equation
313 FLDA,SOLU,FLOW,T             ! solve momentum and pressure equations
314 FLDA,SOLU,TEMP,T

315 FLDA,METH,ENRG,3             ! solve energy equation (using PCRM solver)
316 FLDA,ITER,EXEC,50
317 FLDA,RELX,TEMP,1.
318 /SOLU
319 SOLVE

!        *** (((MULTIPLE SPECIES MODULE INSERTED HERE))) ***

320 FLDA,ITER,EXEC,50            ! 50 global iterations
321 FLDA,CONV,OUTP,BLOC          ! adjust convergence monitor output style
322 SAVE
323 FINISH
324 /SOLU
325 SOLVE

326 /WAIT,1
327 /POST1
328 SET,LAST
329 /CONT,1,50,AUTO              ! set display to 50 colour contour
330 /GLINE,1,-1                  ! hide mesh lines
331 PLNSOL,TEMP                  ! plot temperature solution
```

```
332 !    *** EXTRACTION CODE - TEMPERATURES FROM RESULT FILE ***

333 /OUTPUT                          ! output to window

334 *GET,MAXE,ELEM,,NUM,MAX
335 *GET,MAXN,NODE,,NUM,MAX
336 NDOF=MAXN*1

337 ALLS

338 F1=NODE((ftw+st+0.006),(amhcc+0.03),0)     ! flame; at x=6 mm from ft side, 30 mm from am top
339 F2=NODE((ftw+st+0.006),(amhcc+0.015),0)    ! "                              , 15 mm from am top

340 A1=NODE((amwcc+st),(amhcc-0.01),0)        ! air manifold; at 10 mm below am top
341 A2=NODE((amwcc+st),(amhcc-0.04),0)        ! "                    40 mm "
342 A3=NODE((amwcc+st),(amhcc-0.085),0)       ! "                    85 mm "

343 E1=NODE((emwcc+st),(emhcc-0.17),0)        ! exhaust manifold; at 170 mm below em top
344 E2=NODE((emwcc+st),(emhcc-0.145),0)       ! "                     145 "
345 E3=NODE((emwcc+st),(emhcc-0.100),0)       ! "                     100 "
346 E4=NODE((emwcc+st),(emhcc-0.050),0)       ! "                      50 "
347 E7=NODE((0.0001),(emhcc),0)               ! "                      0 " (top of combustion zone)

348 S1=NODE((eswcc+st),yo,0)                  ! exhaust stack; at bottom
349 S2=NODE((eswcc+st),(yo+0.075),0)          ! "                at  50 mm, from bottom
350 S3=NODE((eswcc+st),(yo+0.15),0)           ! "                at 150 mm, "
351 S4=NODE((eswcc+st),(yo+eshcc),0)          ! "                at top of exhaust stack
352 S5=NODE((sw+st),(eshcc+shf),0)            ! "                at top of exhaust flange/reducer

353 O1=NODE((sw-0.005),(eshcc+shf+sh),0)      ! outlet (exhaust); 5 mm from stack wall (inside flue)
354 O2=NODE((sw-0.023),(eshcc+shf+sh),0)      ! "              23 mm from stack wall  (flue centre)

355 IP1=NODE((ftw+st+0.005),(yo+0.05),0)      ! insertion probe, base of am
356 IP2=NODE((ftw+st+0.005),(yo+0.075),0)     ! "                    25 mm into am
357 IP3=NODE((ftw+st+0.005),(yo+0.1),0)       ! "                    50 mm into am

358 OV1=NODE((sw-0.005),(eshcc+shf+sh),0)     ! outlet (exhaust); 5 mm from stack wall (inside flue)
359 OV2=NODE((sw-0.023),(eshcc+shf+sh),0)     ! "              23 mm from stack wall, (flue centre)

360 !NODE ID COMPLETE

361 /OUTPUT,TEMP EXT,inp,                    ! output results to file, titled, TEMP EXT.inp

362 ! temperatures extracted on predefined path through VC

363 *GET,F1,NODE,F1,TEMP,          !*GET,NTEM,NODE,F1,TEMP
364 *GET,F2,NODE,F2,TEMP,
365 *GET,A1,NODE,A1,TEMP,
366 *GET,A2,NODE,A2,TEMP,
367 *GET,A3,NODE,A3,TEMP,
368 *GET,E1,NODE,E1,TEMP,
369 *GET,E2,NODE,E2,TEMP,
370 *GET,E3,NODE,E3,TEMP,
371 *GET,E4,NODE,E4,TEMP,
372 *GET,E7,NODE,E7,TEMP,
373 *GET,S1,NODE,S1,TEMP,
374 *GET,S2,NODE,S2,TEMP,
375 *GET,S3,NODE,S3,TEMP,
376 *GET,S4,NODE,S4,TEMP,
377 *GET,S5,NODE,S5,TEMP,
```

```
378 *GET,O1,NODE,O1,TEMP,
379 *GET,O2,NODE,O2,TEMP,
380 *GET,IP1,NODE,IP1,TEMP,
381 *GET,IP2,NODE,IP2,TEMP,
382 *GET,IP3,NODE,IP3,TEMP,

383 *GET,OV1,NODE,OV1,V,SUM
384 *GET,O2V,NODE,OV2,V,SUM

385 *STATUS                          ! lists all parameters to output file, TEMP EXT.inp
386 /OUTPUT

387 !FINISH
```

Total number of lines in batch file ≈ 390 (Non insulated configuration).

Appendix D6 Multiple Species Code

```
==
=====
320 !    *** MULTIPLE SPECIES SETUP ***

321 /PREP7

322 FLDATA7,PROT,DENS,CMIX          ! composite mixture for density
323 FLDATA7,PROT,VISC,CMIX          ! composite mixture for viscosity

324 KEYOPT,1,1,4                   ! specify number of species =4

325 FLDATA1,SOLU,SPEC,T             ! turn on solution for multiple species transport
326 MSDATA,2                       ! specify species 2 (N2) as the algebraic species

327 !    FLUID (GAS) PROPERTIES

328 MSSPEC,1,O2,31.999                                    ! oxygen
329 MSPROP,1,DENS,GAS,1.2998,300,1.01325E+5
330 MSVARY,1,DENS,t
331 MSNOMF,1,0.2
332 MSPROP,1,VISC,CONSTANT,1.2067E-5
333 MSPROP,1,MDIF,CONSTANT,2.149E-5
334 MSPROP,1,COND,CONSTANT,0.02674
335 MSCAP,1,1

336 MSSPEC,2,N2,28.018                                   ! nitrogen
337 MSPROP,2,DENS,GAS,1.1138,300,1.01325E+5
338 MSVARY,2,DENS,t
339 MSNOMF,2,0.4
340 MSPROP,2,VISC,CONSTANT,1.786E-5


341 MSSPEC,3,H2,2.016                                    ! hydrogen
342 MSPROP,3,DENS,GAS,0.08,300,1.01325E+5
343 MSVARY,3,dens,t
344 MSNOMF,3,0.2
345 MSPROP,3,VISC,CONSTANT,8.94E-6
346 MSPROP,3,MDIF,CONSTANT,4.964E-5
347 MSPROP,3,COND,CONSTANT,0.02674
348 MSCAP,3,1

349 MSSPEC,4,H2O,18.03                                   ! water vapour - steam
350 MSPROP,4,DENS,GAS,0.4,300,1.01325E+5
351 MSVARY,4,dens,t
352 MSNOMF,4,0.2
353 MSPROP,4,VISC,CONSTANT,4E-5
354 MSPROP,4,MDIF,CONSTANT,0.06E-4
355 MSPROP,4,COND,CONSTANT,0.11
356 MSCAP,4,1

357 !    SOLVER SETTINGS

358 MSRELX,1,1.0
359 MSRELX,3,1.0
360 MSRELX,4,1.0
361 MSMETH,4,1                    ! 4 species, TDMA (versus PCRM)
362 FLDA,ITER,EXEC,50
```

```
363 MSSOLU,4,,,2,1.e-5
364 ALLS

365 !    LOADS

366 NSEL,S,LOC,X,ftw+st,amwi          ! air species mass fraction at air inlet
367 NSEL,R,LOC,Y,0
368 D,ALL,O2,0.21
369 D,ALL,N2,0.79
370 D,ALL,H2,0.0
371 D,ALL,H2O,0.0
372 ALLS

373 NSEL,S,LOC,X,xoff,ftw             ! fuel, mass fraction = 1
374 NSEL,R,LOC,Y,0,fth
375 D,ALL,O2,0.0
376 D,ALL,N2,0.0
377 D,ALL,H2,1.0
378 D,ALL,H2O,0.0
379 ALLS

380 NSEL,,LOC,Y,(czo+0.0025),(czo+czh) ! heat generation zone, make 0.5 H2 / 0.5 H20
381 NSEL,R,LOC,X,xoff,((czw)*0.5)      ! half of flame producing steam
382 D,ALL,H2O,0.5
383 D,ALL,H2,0.5
384 D,ALL,N2,0
385 D,ALL,O2,0
386 ALLS

387 !    *** MULTIPLE SPECIES COMPLETE ***
=====
==
```

Total number of lines in batch file ≈ 425 (Non insulated).

Batch File Comments

Appendix D7 Radiation Make Matrix Code

```
==
=====
5   !ET,1,FLUID141      ! set 2D fluid element type
6   !KEYOPT,1,1,0       ! species transport not activated
7   !KEYOPT,1,3,1       ! axisymmetric about Y axis

8   !********** RADIATION SPECIFIC BEGIN

9   ET,1,PLANE55,,,1,   ! set 2D thermal element
10  ET,2,LINK32,        ! heat conducting bar element (overlay)

11  !********** RADIATION SPECIFIC END

12  !    *** KEY ***
13  **
14  *
15  *
200 **  *** MESHING ***

201 !    MATERIAL PROPERTIES (ASSIGN ATTRIBUTES)

202 !********** RADIATION SPECIFIC BEGIN

203 mp,dens,1,1.2               ! density, material 1 (air)
204 mp,kxx,1,2.502E-3           ! conductivity of air
205 !mp,kyy,1,2.502E-3
206 !mp,kzz,1,2.502E-3
207 mp,visc,1,0.0004            ! viscosity of air (Sutherlands Formula)
208 mp,c,1,1004

209 !********** RADIATION SPECIFIC END

210 mp,dens,2,7500,             ! density, material 2
211 mptemp,1,273,773,5000,      ! temperature property table
212 mpdata,kxx,2,1,15,25,25,    ! conductivity material property table
213 !mpdata,kyy,2,1,15,25,25,
214 !mpdata,kzz,2,1,15,25,25,
215 mp,c,2,500                 ! specific heat
216 ALLS

217 !    MESHING

218 ALLS
219 ASEL,,,,1,(stknum-1)       ! select all but Stack_bulk and Insulation
220 AATT,2,1,1,0,              ! material 2 for walls      (stainless steel)
221 ESIZE,elsiz,0,             ! element size
222 ESHAPE,2                   ! element shape, mapped mesh - quads
223 AMESH,1,(stknum-1),1       ! mesh all walls with mapped mesh

224 !********** RADIATION SPECIFIC BEGIN

225 LSEL,S,EXT
226 LATT,2,1,2,0,              ! material 2, element 2 for walls, external
227 MAT,2
228 TYPE,2
229 ESURF                     ! link32 element overlaid on wall mesh
230 ESEL,S,TYPE,,2            ! select only link32 elements
```

```
231 !    *** ENTER RADIATION PROCESSOR ***

232 /AUX12                    ! calculate radiation view factors, make radiation matrix

233 ESEL,S,TYPE,,2,
234 NSLE,S
235 !NSEL,A,NODE,,10002       ! optional space node

236 GEOM,1,20                 ! number of zones
237 EMIS,2,0.7                ! emissivity
238 STEF,5.67e-008
239 VTYPE,0,400
240 !SPACE,10002

241 WRITE,RMATRIX,SUB         ! write file, for use in a typical thermal analysis
242 ALLSEL

243 FINISH

244 !********** RADIATION SPECIFIC END
=====
==
```

Total number of lines in batch file ≈ 240.

Batch File Comments

A radiation matrix file is generated and written to the working directory, titled RMATRIX.SUB. RMATRIX.SUB, is then read into a typical thermal analysis, illustrated by the Radiation Apply Matrix Code.

Appendix D8 Radiation Apply Matrix Code

```
==
=====
5   ET,1,FLUID141        ! set 2D fluid element type
6   !KEYOPT,1,1,0        ! species transport not activated
7   !KEYOPT,1,3,1        ! axisymmetric about Y axis

8   !********** RADIATION SPECIFIC BEGIN

9   ET,1,PLANE55,,,1,    ! set 2D thermal element

10  !KEYOPT,1,8,1
11  !R,1,0.4,0.4

12  !ET,2,LINK32,        ! heat conducting bar element (overlay)

13  !********** RADIATION SPECIFIC END


200 !    *** MESHING ***

201 !    MATERIAL PROPERTIES (ASSIGN ATTRIBUTES)

202 !********** RADIATION SPECIFIC BEGIN

203 mp,dens,1,1.2                ! density, material 1 (air)
204 mp,kxx,1,2.602E-2            ! conductivity of air
205 !mp,kyy,1,2.602E-2
206 !mp,kzz,1,2.602E-2
207 mp,visc,1,1.93E-5             ! viscosity of air (Sutherlands Formula)
208 mp,c,1,1004

209 !********** RADIATION SPECIFIC END
=====
==
==
=====
240 !    *** ENTER RADIATION MATRIX INTO MODEL  ***

241 !********** RADIATION SPECIFIC BEGIN

242 /PREP7

243 ET,2,MATRIX50,1,,,,,1         ! radiation substructure matrix
244 DOF,TEMP
245 TYPE,2
246 SE,RMATRIX,,,                 ! read in radiation super-element

247 ESEL,ALL
248 ESLN,U
249 !!EDELE,ALL
250 ALLSEL
251 FINISH

252 /SOLU

253 ANTYPE,STATIC                ! steady state thermal analysis
254 ! TOFFST,273.0                      ! temperature offset (?)
```

```
255 TUNIF,293                    ! starting temperature for non-linear solution

256 !    *** BOUNDARY CONDITIONS ***

257 ALLS
258 LSEL,S,LOC,Y,0,0
259 LSEL,R,LOC,X,xo,ftw
260 NSLL
261 D,ALL,TEMP,293
262 D,ALL,VY,0.5

263 ALLS
264 LSEL,S,LOC,Y,0,0   lsel,s,loc,y,0,0
265 LSEL,R,LOC,X,(ftw+st),amwi
266 NSLL,
267 D,ALL,TEMP,293
268 D,ALL,VY,0.5

269 ALLS
270 LSEL,S,LOC,Y,(eshcc+sh),
271 LSEL,R,LOC,X,xo,sw,
272 NSLL,
273 D,ALL,TEMP,293

274 ALLS
275 !LSEL,S,LINE,,26              ! fictional temperature to study impact of rad.
276 !NSLL,S,1
277 !D,ALL,TEMP,1200

278 ALLS
279 NSEL,S,LOC,Y,czo,(czo+czh) ! heat generation
280 NSEL,R,LOC,X,xoff,czw       ! THIS HAS BEEN CHANGED
281 ESLN
282 BFE,ALL,HGEN,,hg

283 ALLS
284 SFL,57,CONV,htc,,to          ! apply convection (heat transfer) coefficient
285 SFL,55,CONV,htc,,to
286 SFL,53,CONV,htc,,to
287 SFL,51,CONV,htc,,to
288 SFL,50,CONV,htc,,to
289 SFL,46,CONV,htc,,to
290 SFL,45,CONV,htc,,to
291 ALLS
292 SFTRAN

293 ALLSEL
294 SOLVE
295 FINISH
296 /POST1
=====
==
```

Total number of lines in batch file ≈ 360 (including extraction code).

Batch File Comments

This file reads in the RMATRIX.SUB (radiation superelement), which is then implemented in a typical thermal analysis.

Appendix D9 /AUX12: - Commands

The /AUX12 command activates a matrix generation processor, within the processor /AUX12 commands are used to calculate view factors and substructure matrices for radiation effects. The **COMMAND**, description and *value or action used in the modelling code,* is given below:

/AUX12 Enters the radiation matrix generation processor,
/AUX12; initial command

EMIS Specifies the emissivity as a material property,
EMIS,MAT,EVALU; material number as specified for stainless steel (316) as used in the construction of the verification cell, emissivity ~ 0.75

GEOM Defines the geometry specifications for the radiation matrix calculation,

GEOM,1,20; 2-D geometry, one 360 degree division ~ axisymmetric
(20 axisymmetric sectors should provide reasonable accuracy – pending element aspect ratios, chp4 – Anal manual)

MPRINT Specifies that radiation matrices are to be printed

SPACE Defines a space node for radiation
node selected to account for radiation losses (required for open systems)

STEF Specifies Stefan-Boltzmann radiation constant
5.67E-8 $Wm^{-2}K^{-4}$ (SI Units)

VTYPE Specifies the viewing procedure used to determine the form factors
VTYPE,0,NZONE; hidden procedure used, NZONE ~ number of zones defaults to 200 (maximum of 1000 for 2-D geometry)

WRITE Writes the radiation matrix file
WRITE,FNAME; defaults to jobname.sub

Referenced from Commands 2.10a AUX12 Commands for Radiation Substructures

APPENDIX E

SUPPLEMENTARY RESULTS & RAW DATA

Appendix E1 Supplementary Plots

E1(a) Supplementary plots for effect of fuel flow on temperature profiles

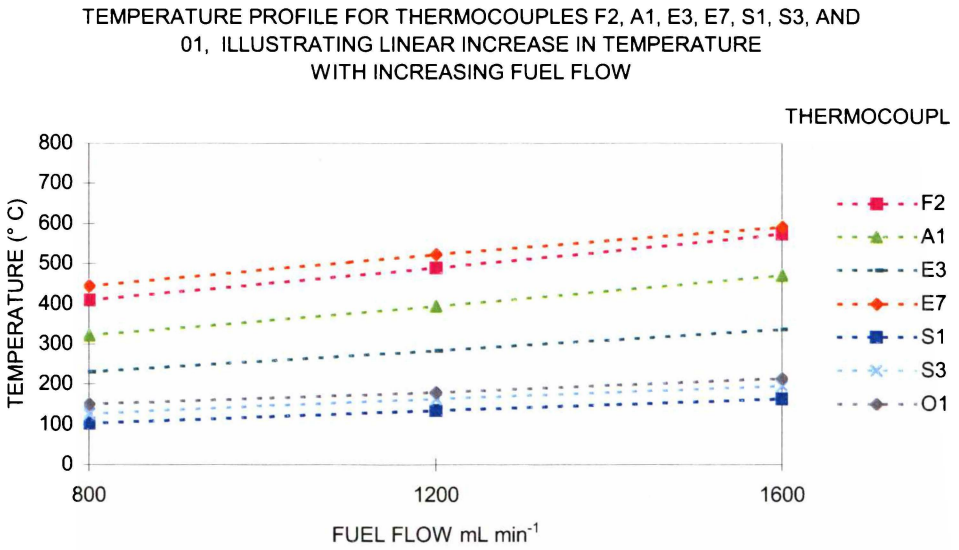

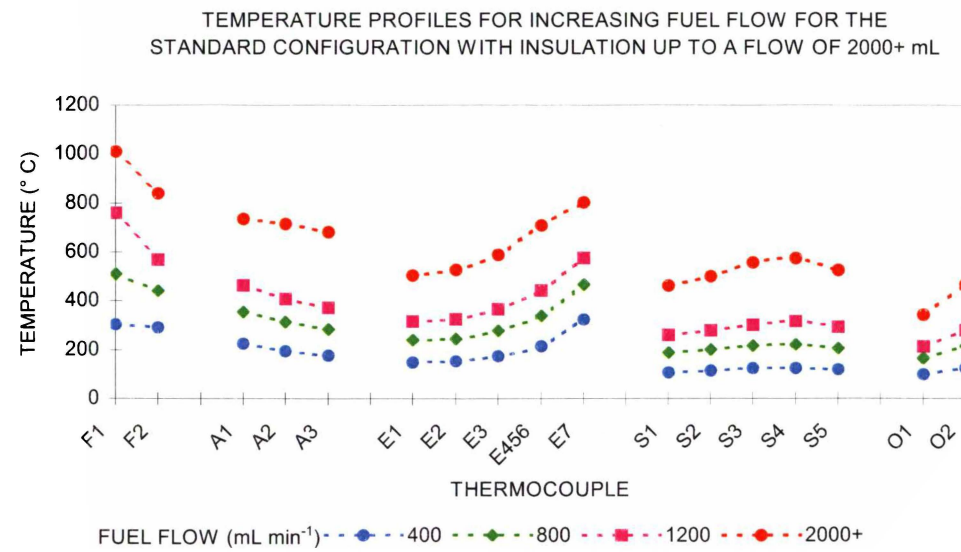

Appendix E2 Raw Data from Thermocouple and Flame Experiment

E2(a) Temperatures recorded for four-probe thermocouple array aligned on the periphery of the fuel tube wall, and above the fuel tube orifice

Fuel Flow (mL min^{-1})	One* (15 mm)**	Two (30 mm)	Three (45 mm)	Four (60 mm)
200	265	280	260	300
300	380	365	315	330
400	475	410	360	360
500	560	465	385	390
600	620	520	450	450
700	690	630	550	530
800	800	715	630	590
900	850	770	670	635
1000	915	840	750	670
1200	990	945	825	750
1300	1030	1060	900	840
1400	1055	1095	985	890
1600	1150	1170	1080	1020
2000	1140	1060	1050	1080

*Thermocouple number

**Thermocouple height above the fuel tube orifice (mm)

E2(b) Temperatures recorded for single-probe thermocouple centred in flame 20mm above fuel tube orifice

Fuel Flow (mL min^{-1})	Single (20 mm)
200	575
300	690
400	775
500	840
600	900
700	980
800	1020
900	1040
1000	1055
1100	1060
1200	1060
1300	1050
1400	1045
1600	800

E2(c) Measured height and width (m) of hydrogen flame for a range of fuel flows

Fuel Flow (mL min^{-1}) / Velocity (ms^{-1})

ml min^{-1} ms^{-1}	200 0.048	300 0.072	400 0.096	500 0.120	600 0.144	700 0.168	800 0.192	1000 0.240	1200 0.288	2000 0.480
Radiant Flame	0.008	0.01	0.012	0.015	0.018	0.02	0.022	0.026	0.03	0.046
Flame Height	0.018	0.024	0.03	0.035	0.04	0.045	0.05	0.055	0.06	0.095
Radiant Flame Width	0.01	0.012	0.013	0.015	0.015	0.015	0.017	0.018	0.018	0.022
Coolant Front Height	0	0.002	0.004	0.004	0.004	0.004	0.005	0.006	0.008	0.015

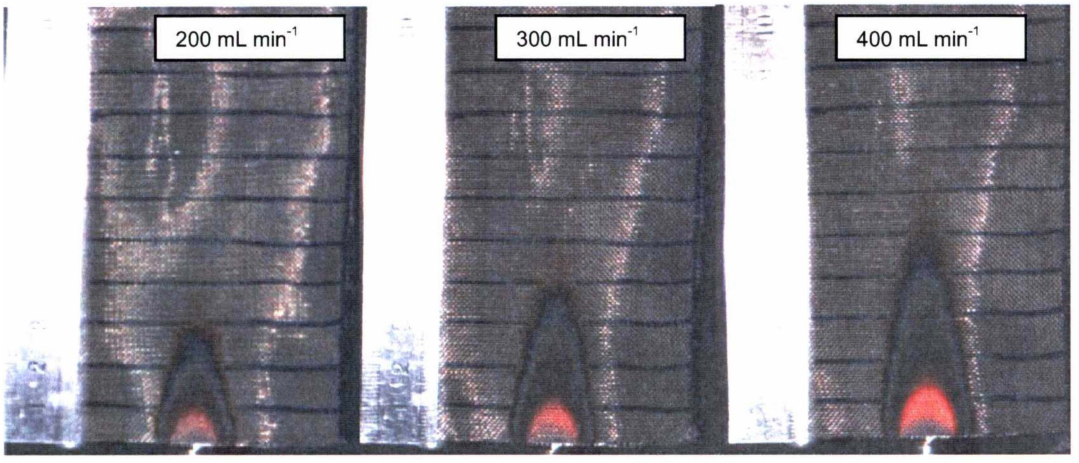

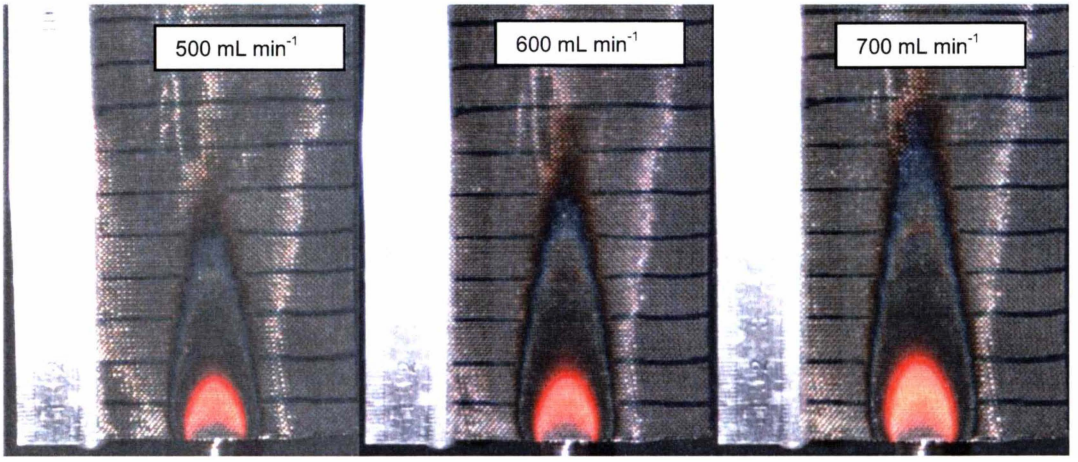

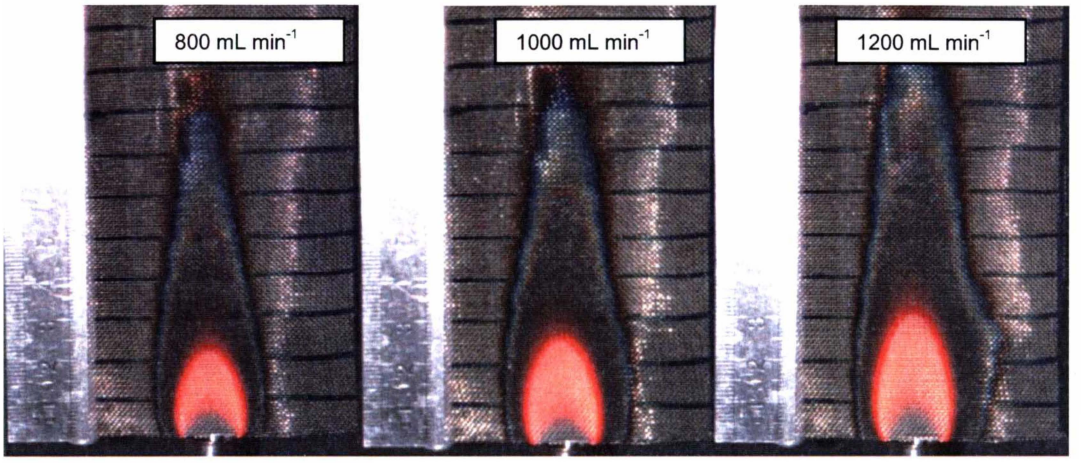
800 mL min-1
1000 mL min-1
1200 mL min-1

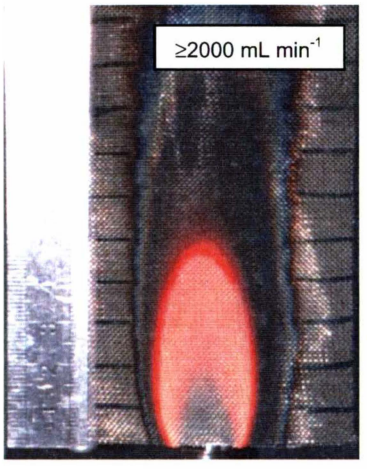
≥2000 mL min-1

APPENDIX F

SUPPLEMENTARY – COMPUTATIONAL RESULTS

Appendix F1 Verification Cell Model – Vector Velocity Plot